NAVAL POSTGRADUATE SCHOOL
Monterey, California

DISSERTATION

DEFORMATION BANDING AND GRAIN REFINEMENT IN FCC MATERIALS

by

Douglas Lee Swisher

March 2003

Dissertation Supervisor: T.R. McNelley

Approved for public release; distribution is unlimited

THIS PAGE INTENTIONALLY LEFT BLANK

REPORT DOCUMENTATION PAGE			*Form Approved OMB No. 0704-0188*

Public reporting burden for this collection of information is estimated to average 1 hour per response, including the time for reviewing instruction, searching existing data sources, gathering and maintaining the data needed, and completing and reviewing the collection of information. Send comments regarding this burden estimate or any other aspect of this collection of information, including suggestions for reducing this burden, to Washington headquarters Services, Directorate for Information Operations and Reports, 1215 Jefferson Davis Highway, Suite 1204, Arlington, VA 22202-4302, and to the Office of Management and Budget, Paperwork Reduction Project (0704-0188) Washington DC 20503.

1. AGENCY USE ONLY *(Leave blank)*	2. REPORT DATE March 2003	3. REPORT TYPE AND DATES COVERED Dissertation	
4. TITLE AND SUBTITLE: Deformation Banding and Grain Refinement in FCC Materials		5. FUNDING NUMBERS	
6. AUTHOR(S) Swisher, Douglas L.			
7. PERFORMING ORGANIZATION NAME(S) AND ADDRESS(ES) Naval Postgraduate School Monterey, CA 93943-5000		8. PERFORMING ORGANIZATION REPORT NUMBER	
9. SPONSORING / MONITORING AGENCY NAME(S) AND ADDRESS(ES) N/A		10. SPONSORING / MONITORING AGENCY REPORT NUMBER	

11. SUPPLEMENTARY NOTES The views expressed in this dissertation are those of the author and do not reflect the official policy or position of the Department of Defense or the U.S. Government.

12a. DISTRIBUTION / AVAILABILITY STATEMENT Approved for public release; distribution is unlimited.	12b. DISTRIBUTION CODE

13. ABSTRACT *(maximum 200 words)* Microscopy methods in the scanning and transmission electron microscopes have been employed to assess microstructures developed by deformation processing of selected face centered cubic (FCC) materials. Grain maps constructed from orientation data and analysis of transmission data illustrate the presence of fine grains and deformation bands in which the lattice orientation contains symmetric variants of a texture component. A banded, deformation microstructure is present to various degrees in FCC material systems irrespective of processing and material composition. The specific components of the deformation bands were observed to vary depending upon processing conditions of the material and the specific material. Single component and entire deformation textures from shear and plane strain, were both observed. The high-angle (40°-62.8°) interfaces or boundaries in the microstructure evolve from the interfaces between the bands while the lower-angle (2°-15°) boundaries tend to separate cells within the bands. Models of microstructural development that include deformation banding during cold working may be employed to describe both texture development and the origin of the high-angle grain boundaries.

14. SUBJECT TERMS Grain Refinement, Ultra-fine Grains, Deformation Banding, Plastic Deformation, Severe Plastic Deformation, Misorientation Angle, Orientation Imaging Microscopy, Electron Backscatter Diffraction, Equal-Channel Angular Pressing, Supral 2004, Nano Structures, Transmission Electron Microscopy	15. NUMBER OF PAGES 181
	16. PRICE CODE

17. SECURITY CLASSIFICATION OF REPORT Unclassified	18. SECURITY CLASSIFICATION OF THIS PAGE Unclassified	19. SECURITY CLASSIFICATION OF ABSTRACT Unclassified	20. LIMITATION OF ABSTRACT UL

NSN 7540-01-280-5500

Standard Form 298 (Rev. 2-89)
Prescribed by ANSI Std. 239-18

THIS PAGE INTENTIONALLY LEFT BLANK

DEFORMATION BANDING AND GRAIN REFINEMENT IN FCC MATERIALS

Douglas L. Swisher
Lieutenant Commander, United States Navy
B.S., United States Naval Academy, 1993
M.S., Naval Postgraduate School, 2000

Submitted in partial fulfillment of the
requirements for the degree of

DOCTOR OF PHILOSOPHY IN MECHANICAL ENGINEERING

from the

NAVAL POSTGRADUATE SCHOOL
March 2003

Author: _____
Douglas L. Swisher

Approved by:

_____   _____
Terry R. McNelley   Indranath Dutta
Professor of   Professor of
Mechanical Engineering   Mechanical Engineering
Dissertation Supervisor

_____   _____
Young W. Kwon   James Luscombe
Professor of   Professor of Physics
Mechanical Engineering

_____
Gamani Karunisiri
Professor of Physics

Approved by: _____
Young W. Kwon, Chairman, Department of Mechanical Engineering

Approved by: _____
Carson K. Eoyang, Associate Provost for Academic Affairs

iii

THIS PAGE INTENTIONALLY LEFT BLANK

ABSTRACT

Microscopy methods in the scanning and transmission electron microscopes have been employed to assess microstructures developed by deformation processing of selected face centered cubic (FCC) materials. Grain maps constructed from orientation data and analysis of transmission data illustrate the presence of fine grains and deformation bands in which the lattice orientation contains symmetric variants of a texture component. A banded, deformation microstructure is present to various degrees in FCC material systems irrespective of processing and material composition. The specific components of the deformation bands were observed to vary depending upon processing conditions of the material and the specific material. Single component and entire deformation textures from shear and plane strain, were both observed. The high-angle (40°-62.8°) interfaces or boundaries in the microstructure evolve from the interfaces between the bands while the lower-angle (2°-15°) boundaries tend to separate cells within the bands. Models of microstructural development that include deformation banding during cold working may be employed to describe both texture development and the origin of the high-angle grain boundaries.

THIS PAGE INTENTIONALLY LEFT BLANK

TABLE OF CONTENTS

THIS PAGE INTENTIONALLY LEFT BLANK

ACKNOWLEDGMENTS

THIS PAGE INTENTIONALLY LEFT BLANK

I.   INTRODUCTION

A.   HISTORY OF DEFORMATION PROCESSING

Throughout history the ability of metals to sustain plastic deformation has been put to use in the shaping of metallic materials and production of useful implements [Ref. 1]. It has also been long understood that plastic deformation strengthens metals, and that incorporating annealing treatments to soften the material during shaping processes may afford further control of both the process and the resulting material properties. For most of this history the mechanisms involved during deformation and annealing were not known and understanding of these processes was entirely empirical [Ref. 2]. The application of various microscopy techniques and X-ray diffraction methods [Refs. 3-6] to the study of microstructure in metallic materials has revealed the polycrystalline nature of most metallic materials. Deformation at low temperature results in distortion of the grain structure as dislocations are generated, move and become immobilized. This constitutes strain hardening and results in energy storage in the form of dislocation arrays. Annealing may result in recovery, i.e., softening associated with dislocation rearrangement, or in the formation and growth of new, strain free grains, i.e. recrystallization, within the microstructure [Ref. 7]. Thus, deformation and annealing treatments may allow control of the grain structure and grain size of metals. It is recognized that the study of deformation microstructures has encompassed an immense body of work prior to the 1980's. A selective review of recent research pertaining to the deformation features and mechanisms relevant to this study will be provided.

Grain size is an important factor in the mechanical properties of materials. Generally, refinement of the grain size results in improvements in both strength and toughness of metals [Refs. 8-9]. In alloys of metals such as iron and titanium the phase transformations that occur during cooling provide a significant degree of grain size control. In many other metals, such as aluminum, nickel and copper, grain size refinement in wrought alloys can only be achieved by deformation and recrystallization, but our understanding of these mechanisms during industrial processing is still largely

1

empirical [Ref. 2]. As recently as 1993 Haasen [Ref. 10] has observed that recrystallization is the last major unexplored frontier in physical metallurgy.

Grain sizes in the range of ~20-50μm are typical of engineering alloys commonly produced today. However recent research has demonstrated that grains can be readily refined to 1.0μm in size and still finer grain sizes of perhaps 100nm or less can also be achieved [Refs. 11-19]. Such ultra-fine grained materials may exhibit dramatic improvements in mechanical properties and many potential applications exist for the increased mechanical properties afforded by these materials. Applications include those requiring an increased strength to weight ratio, resistance to cyclic loads or those requiring increased fracture toughness.

Attainment of fine or ultra-fine grain sizes in wrought alloys that are not amenable to control by phase transformations may be achieved only through plastic deformation and recrystallization. The study of the deformation-induced microstructures has progressed rapidly in the last decade and this has contributed to the development and refinement of several theories of grain refinement.

1.   Deformation-Induced Microstructures

The low-energy dislocation structure (LEDS) theory of deformation-induced microstructures was developed and has recently been summarized by Kuhlmann-Wilsdorf [Ref. 20]. This and related theories have been developed to describe microstructures produced by deformation at low homologous temperatures. In conjunction with the LEDS hypothesis, descriptions of the dislocation boundaries formed during deformation have been developed [Ref. 21] from extensive investigations [e.g. Refs. 22-25]. In summary, dislocations generated during plastic deformation will adopt arrangements that reflect a state of lowest internal energy for the applied tractions. Some these dislocations will be part of dense dislocation walls that separate features that are termed 'cell blocks'. These dislocation walls are features that accommodate lattice curvature and realignment upon traversing from one cell block to an adjacent cell block and thus have been termed 'geometrically necessary boundaries' (GNBs). Other dislocations remaining within cell blocks form what are termed 'incidental dislocation boundaries' (IDBs) that comprise substructures within the cell blocks. With increased

2

plastic deformation, the distance separating GNBs becomes reduced more rapidly than the distance separating IDBs. This indicates that GNBs may be able to accommodate a larger proportion of the dislocations generated during plastic deformation than the IDBs [Ref. 22].

McQueen and coworkers [Refs. 26-28] have proposed the theory of geometric dynamic recrystallization to describe the deformation-induced microstructures that develop at moderately elevated temperatures and deformation strain-rates. It has been subsequently modified to include cases of severe plastic deformation. Doherty et al. [Ref. 2] have provided a detailed review. Briefly, plastic deformation causes the prior grains to elongate while equi-axed sub grains form within the prior grains. The subgrain size depends on the Zener-Hollman parameter, Z, given in Equation 1.1 as

$$Z = \dot{\varepsilon} \exp\left(\frac{Q}{RT}\right)$$
Equation 1.1

where $\dot{\varepsilon}$ is the strain rate, Q is the activation energy for deformation, R is the gas constant and T is the absolute temperature. With continued deformation, the thickness of the prior grains becomes reduced to the sub grain size. Then, the prior boundaries become serrated and may eventually pinch off, leading to the formation of smaller grains in the absence of a nucleation and growth process.

2. Deformation Banding

The phenomenon of deformation banding will have a prominent role in the current study. Deformation banding may commence at the initiation of and continue throughout large-strain plastic deformation and become the dominant mechanism of grain subdivision. As a consequence of this process, adjacent regions of a grain experience lattice rotation towards symmetrically related final orientations. These regions, or zones, of different lattice orientation become ribbon-like in shape during deformation and have been termed 'deformation bands'. The existence of deformation banding was suggested as early as 1940 by Barrett [Ref. 29] and Barrett and Levenson [Ref. 30]. Chin, et al. [Ref. 31], have also emphasized the importance of deformation banding.

Duggan, et al. [Refs. 32-37] have recently investigated the nature and origin of deformation banding in polycrystalline FCC metals. According to these authors, the occurrence of this phenomenon is dependent on the initial grain size and it predominates mainly in coarse-grained materials. The initial grain orientation and rolling reduction are also factors [Ref. 32] and deformation banding can commence either at the onset of plastic deformation or at some larger strain. Banding is favored by the simultaneous occurrence of dynamic recovery, which enables the rearrangement of the dislocations in the band interiors into low energy arrays, thereby reducing the stored energy [Ref. 33].

Compatible deformation under plane strain conditions for a structure of elongated deformation bands may occur with the activation of only two slip systems in each band due to the relaxation of constraints [Refs. 34, 38-39]. The Taylor model [Ref. 40] requires the operation of at least five independent slip systems for compatible deformation of a polycrystalline material composed of equi-axed grains having random lattice orientations. In a banded structure, there may be less strain hardening due to dislocation entanglement because there are fewer operative slip systems and therefore a lower flow stress since less work is done. In order for deformation banding to be energetically favorable, this decrease in plastic work during straining must exceed the additional energy required for the creation of the band interfaces plus the accommodation of shears at the band ends [Ref. 34].

As pointed out recently by Kulkarni, et al. [Ref. 41], "this phenomenon still remains remarkably enigmatic" despite the publication in recent years of several studies on deformation banding in a variety of different materials [Refs. 42-61]. Experimental evidence for deformation banding has been reported mainly in studies of pure metals and also in dispersion hardened materials [Refs. 42-56]. Recent studies have proposed a deformation banding model for specific types of deformation [Refs. 62-64]

B. DEFORMATION INDUCED MICROSTRUCTURES AND TEXTURES

1. Low Temperature Deformation

A review of early work on deformation microstructures and textures is provided by Gil-Sevillano et al. [Ref. 65]. A more recent review of observed textures in common deformation processes is provided by Hosford [Ref. 66] and Kocks et al [Ref. 67].

In general, plastic deformation processes occurring below $\sim 0.3T_m$ (less than 30% of the absolute melting temperature) result in microstructures with the following characteristics: elongated grains; reduced apparent grain size from that of the original; substantial increase in the dislocation density; increase in the fraction of low-angle (2°-15°) boundaries; and a preferred orientation (or texture) of the grains. These features are heavily influenced by the material and nature of the process imposing the plastic deformation.

2. High Temperature Deformation

Doherty et al. [Ref. 2] have recently reviewed the current understanding of the hot worked state, i.e., for deformation conducted at elevated temperatures. Briefly summarized, resulting microstructures can be interpreted in terms of dislocation arrangements and rearrangements associated with creep of the deformed materials although with some significant modifications. Notable modifications include the formation and retention of deformation bands that have large disorientations across band-band interfaces and the production (sub)grain boundaries that are apparently very stable.

C. RECRYSTALLIZATION

1. Current Theories of Recrystallization

The current understanding of recrystallization has also been reviewed recently [Ref. 2]. Smallman [Ref. 7] also provides a concise summary of the relevant theories in his text. In summary, the standard model for kinetic processes considers the formation of a nucleus of critical size by atom-by-atom construction from an embryo. This model is well suited for processes such as solidification and solid-solid phase transformation that involve large thermodynamic driving potentials. Thus, the free energy of formation, ΔG^*, of a critical nucleus is given in Equation 1.2 as

$$\Delta G^* = \left\{\frac{\alpha \gamma^3}{\Delta G_V^2}\right\} f\left(\cos\theta\right) \qquad \text{Equation 1.2}$$

where ΔG_V is the driving force in the form of volume free energy to continue growth; γ is the opposing surface (or interfacial) free energy; α is a parameter that varies with the shape of the nucleus, and is taken as $16\pi/3$ for a spherical nucleus; and the function $f(\cos\theta)$ varies between 0.1 and 0.5 depending on the contact angle θ for formation on a pre-existing interface. The density of the embryos capable of supporting growth, n_V^*, can be calculated using Equation 1.3,

$$n_V^* = N_V \exp\left(\frac{-\Delta G^*}{kT}\right) \qquad \text{Equation 1.3}$$

where, N_V is the number of atoms per unit volume, k is Boltzmann's constant, and T is the absolute temperature. If the volume free energy is taken to be due to the dislocation density, Equation 1.4 may be used to calculate ΔG_V.

$$\Delta G_V = \rho_\perp G b^2 \qquad \text{Equation 1.4}$$

where, $\rho_\perp$ is the dislocation density, G is shear modulus and b is the Burgers vector for dislocations. If the dislocation density is assumed to be that of a heavily cold worked metal, e.g., $\rho_\perp = 10^{16} \text{m}^{-2}$, it can be shown using the above equations that n_V^*, the density of stable grain nuclei, is essentially zero at any temperature up to the melting temperature. An alternative perspective is that the conventional theory cannot account for observed nucleation rates in deformed metals and alloys. Instead, it is now understood that recrystallization occurs when selected cells or substructures that were formed in the deformation microstructure become stable in size and are surrounded by boundaries that are able to migrate.

2. Continuous Recrystallization

Humphreys [Ref. 68] as well as Doherty et al. [Ref. 2] have reviewed the continuous recrystallization mechanism. The term 'continuous recrystallization' is a phenomenological description for a recovery-dominated microstructural transformation that occurs homogeneously throughout a deformation-induced microstructure in the absence of long-range high-angle boundary migration. Fine, second-phase particles are

believed to aid this process by hindering dislocation motion and rearrangement and the subsequent grain boundary migration. Materials that undergo the continuous recrystallization reaction generally retain well-defined deformation textures and develop bi-modal disorientation distributions [Refs. 69-71].

In many discussions of superplastic behavior in aluminum alloys, the deformation-induced microstructure at the conclusion of thermomechanical processing has been envisioned to consist of elongated prior grains that contain cells or subgrains of small disorientation. Several investigators have then suggested that continuous recrystallization consists of a recovery-controlled build up of the average disorientation angle for subgrains within such a structure [Refs. 2, 72-77]. However, the mechanism of this increase in disorientation is uncertain. It has been attributed to subgrain growth [Ref. 72], to subgrain coalescence [Ref. 73], to subgrain rotation [Ref. 74], to subgrain rotation and switching [Ref. 75] in a response to the tensile stress, or to the accumulation of dislocations in grain boundaries during elevated temperature deformation [Ref. 76-77].

In recent investigations of continuously recrystallized superplastic alloys, the presence of grain clusters or bands having lattice orientations corresponding to the symmetric variants of a texture component has been documented [Refs. 62-63]. The continuous recrystallization reaction during static annealing included the development of distinct boundaries accompanied by the retention and sharpening of the texture and development of a bimodal distribution of boundary disorientation angles. The high-angle boundaries (50º-62.8º) in the distribution were apparently the interfaces between the grain clusters while the lower-angle boundaries (2º-15º) corresponded to a cellular substructure within the clusters. It was suggested that the bands or grain clusters, and therefore the high-angle boundaries, might have formed as a result of deformation banding during the thermomechanical processing.

3.   Discontinuous Recrystallization

Doherty et al. [Ref. 2] have also given further detailed consideration to discontinuous, or primary, recrystallization. The discontinuous reaction can be viewed as conventional nucleation and growth in that it occurs heterogeneously in the deformation microstructure. Thus, discontinuous recrystallization may be viewed as the heterogeneous

formation of high-angle boundaries in the deformation microstructure, for example, in association with isolated cells or subgrains near prior boundaries or in the deformation zones surrounding hard second-phase particles. In general, it can be shown that the nucleation rate for such heterogeneous reactions is substantially greater than that of homogeneous nucleation as predicted by Smallman [Ref. 7]. The heterogeneous formation and migration of high-angle boundaries in the deformation zones surrounding hard particles has been termed 'particle-stimulated nucleation' in that the second phase particles apparently serve as nucleation sites in an alloy matrix.

The processing of aluminum alloys for particle-stimulated nucleation generally includes an overaging treatment followed by extensive plastic deformation at a low homologous temperature. This processing route provides numerous particles distributed throughout the material that may act as heterogeneous nucleation sites upon heating. A fine, equi-axed microstructure with a random texture is normally seen as a result. This microstructure and texture will then support elevated temperature deformation in a superplastic manner via dislocation motion and grain boundary sliding. The microstructures and textures after elevated temperature deformation vary with the final deformation conditions, i.e. strain rate and temperature.

D. PRODUCTION OF ULTRA-FINE GRAINS

1. Conventional Procedures

Conventional procedures for attaining a fine-grained material have included processes that incorporate phase transformations [Ref. 7] as well as deformation and recrystallization processes as described above [Ref. 2]. Most conventional plastic deformation procedures are limited in the amount of strain that may be imparted to a material. For example, rolling operations are typically limited to a true strains, $\varepsilon_{true}\sim3$, or a twenty fold reduction of the starting thickness to attain the final thickness. Grain sizes in rolled materials are typically 30–50μm. New and innovative deformation processing techniques may allow much larger strains to be attained and thereby enable finer grain sizes to be attained by deformation and recrystallization processing.

2.   Severe Plastic Deformation

Severe plastic deformation (SPD) techniques may offer alternative methods of producing fine grained structures in bulk material for material systems which are not amenable to traditional grain refinement techniques. SPD operations, as the name implies, can subject a material to plastic strains in excess of those produced by conventional means by up to an order of magnitude. Some SPD techniques will be reviewed briefly.

Equal-channel angular pressing (ECAP) was originally developed by Segal and coworkers as a method to homogenize the microstructures of cast billets [Ref. 78]. Valiev, et al., [Ref. 14] have shown that severe plastic deformation (SPD) by ECAP also offers the potential of achieving grain refinement, and of producing ultra-fine grained (UFG) or even sub-micron grained (SMG) structures, with corresponding improvements in mechanical properties. An ECAP die consists of two channels of equal cross-section intersecting at an angle through which a billet of material is pressed. Ideally, the material experiences a state of pure shear when passing through the intersection of the die channels. Because the cross-sectional area of a billet is unaltered during a single ECAP pass, very large strains may be achieved in bulk material by repetitive ECAP operations. ECAP will be fully reviewed in subsequent chapters.

High pressure torsion (HPT) was also developed in Russia [Refs. 17, 79] and has been recently reviewed [Refs. 80-82]. During HPT, a disc of material is placed between two plates and high pressure, normally in the GPa range, is applied. One of the plates is then rotated and the disc of material is deformed in shear through the frictional effects with the plates. The strain in the material is a function of location along the disc radius and number of rotations of the tool [Ref. 82], and hence is non-uniform throughout the sample. This procedure is limited to the formation of disc-shaped samples that are measured in millimeters. This process has been found to be effective in consolidation of nano-structured powders [Ref. 82-83].

Accumulative roll bonding (ARB) is a method that utilizes conventional rolling to induce severe plastic deformation into a material. ARB was developed in Japan [Ref. 18] and has been studied recently [Refs. 84-86]. This process uses conventional rolling with a 50% reduction in thickness during each pass to produce bulk material and the

corresponding doubling of the length in the rolling direction. The material is then cut in half after each pass, the surfaces to be bonded are prepared and the two plates are stacked on top of one another, returning the sample almost to the original length and thickness. Finally, the stacked plates are subjected to another rolling operation intended to bond the plates while again reducing the thickness of the stack. The process is repeated until the desired strain is achieved. This method can produce large sheets of material useful in many applications with currently available machinery. However, the surface preparation must include careful cleaning and surface preparation [Ref. 86]. Delamination and problems with contamination during bonding have also been reported [Ref. 86].

Asymmetric rolling was also developed in Japan [Ref. 19] and utilizes rollers of different sizes and thus different angular velocities, to produce a rolled sheet. The stress state experienced by the material has been examined and found to be more complex than that of plane strain found in conventional rolling procedures [Ref. 19]. This has been found to lead to the development of a microstructure influenced by the additional shear strains introduced [Refs. 87-88].

Friction-stir processing (FSP) is a technique adapted from the concepts of friction stir welding (FSW) [Ref. 89]. FSP is not intended to produce bulk material, however localized severe plastic deformation of a material and thus homogenization of microstructure and grain refinement can result in improved local material properties. This technique involves traversing a rotating tool under an applied force, across the surface of a material, producing intense plastic deformation associated with a "stirring" action in the material under the tool. Previous work has studied the effects of friction-stir processing on commercial aluminum alloys [Refs. 90-92]. These studies revealed that friction-stir processing resulted in grain refinement. Samples prepared from the thermomechanically affected zones (TMAZ) of processed material exhibited high strain rate superplasticity, as well as improved properties such as increased static strengths and increased ductility.

Material removed during a machining process may have been subjected to large plastic strains [Ref. 93] and if coolant was applied during the machining process, may not have been subject to recrystallization temperatures. Recently, techniques have been

investigated with the goal of recycling this "waste" material [Refs. 94-96] while taking advantage of the severe plastic deformation already imposed upon the material.

E.   RELEVANCE OF THIS RESEARCH

The current fundamental understanding of deformation-induced microstructures is based mainly on extensive characterization studies of deformed materials. Predictive models have yet to be developed that are applicable at all length scales to account for the effects of grain size and morphology as well as the micro- and macro-texture of the deformed materials. The crystal plasticity models currently used are based upon either: atomic scale dislocation interactions as provided in the text by Hirth and Lothe [Ref. 97]; macro-scale deformation described by the applied mechanics approach as provided by Hill [Ref. 98]; or a combination of the two. The current models do not take into account meso-scale, or intermediate-level, features that include: interactions among several grains; deformation behavior of groups or clusters of grains. In addition, these models do not consider lattice curvature that results from increased dislocation density. Recent developments in microscopy techniques have allowed the investigation and characterization of these meso-scale features. This may aid in bridging the gap between the micro- and macro-scale plasticity models by development of models to include meso-scale features, but these models have as yet to be applied.

Given the recent advances in techniques designed to introduce severe plastic deformation into material in order to achieve grain refinement, the underlying processes of plastic deformation must be understood at all length scales in order to take full advantage of this emerging technology. Thus, grain sub-division by deformation banding, which occurs on length scales corresponding to the grain size, has been largely ignored as a process that could lead to the development of sub-micron or nano-scale microstructures having large fractions of high-angle boundaries.

The microstructure of these and conventionally deformed materials has been extensively studied. This research differs in that it will primarily utilize microstructural characterization techniques that allow a quantitative measure of the grain-to-grain disorientation. These methods will utilize the analysis of diffraction patterns formed in

the scanning electron microscope (SEM) and transmission electron microscope (TEM). The orientation determination of the grains from the diffraction patterns will allow the location of various texture components to be identified as well as the location of high- and low-angle boundaries. This type of analysis of deformed materials has not been previously performed on the combination of alloy systems and deformation procedures in this study. The goal of this research is to further the fundamental understanding of plastic deformation mechanisms, specifically deformation banding and its role in the production and retention of high angle grain boundaries during conventional as well as severe plastic deformation processing.

II. BACKGROUND

A. EQUAL-CHANNEL ANGULAR PRESSING

Equal-channel angular pressing (ECAP) was originally developed by Segal and coworkers as a method to homogenize the microstructures of cast billets [Ref. 78]. Valiev, et al., [Ref. 14] have shown that severe plastic deformation (SPD) by ECAP also offers the potential of achieving grain refinement, and of producing ultra-fine grained (UFG) or even sub-micron grained (SMG) structures, with corresponding improvements in mechanical properties. Because the cross-sectional area of a billet is unaltered during a single ECAP pass, very large strains may be achieved in bulk material by repetitive ECAP operations. A schematic of an ECAP die is shown in Figure 2.1. The two die channels illustrated in Figure 2.1 are of equal cross section but intersect at an angle, Φ, which is equal to 90º for the die used for processing in the current study. The relief angle, Ψ, is also indicated in Figure 2.1, and is equal to 20° for this particular die. Reference axes are also indicated in Figure 2.1. The +x direction is aligned with the longitudinal axis of the as-pressed billet and it is directed opposite to the exit direction of the billet. Thus, during an ECAP pass the billet is pressed downward in the –z direction and is sheared as it passes through the die channel intersection before exiting the die in the –x direction. Then, the x, y and z planes are the transverse, flow and longitudinal planes, respectively. Ideally, plastic strain occurs by simple shear in the material as the billet is pressed through the intersection of the die channels. Iwahashi et al. [Ref. 99] have calculated the von Mises equivalent strain that accumulates during an ECAP pass and the result is given in Equation 2.1 in terms of the die angle Φ, and relief angle, Ψ:

$$\varepsilon_N = \left(\frac{N}{3^{1/2}}\right)\left[2\cot\left(\frac{\Phi}{2}+\frac{\Psi}{2}\right)+\psi\cos ec\left(\frac{\Phi}{2}+\frac{\Psi}{2}\right)\right] \qquad \text{Equation 2.1}$$

For the die of the current work the strain per pass is $\varepsilon_N = 1.055$ and hence the total accumulated strain after N passes is $\varepsilon_{Total} = 1.055N$.

Repetitive ECAP may be accomplished following various routes that may be distinguished by the amount and sense of rotation of the billet between successive pressing passes [Ref. 100]. The different routes are illustrated in Figure 2.2. For route A,

there is no rotation of the billet between successive passes. For route B_A, rotations are alternately 90° clockwise and 90º counterclockwise between successive passes. In route B_C, the rotation is always 90º in the same sense (i.e. always clockwise or counterclockwise). Finally, for route C the rotation is always 180° in the same sense.
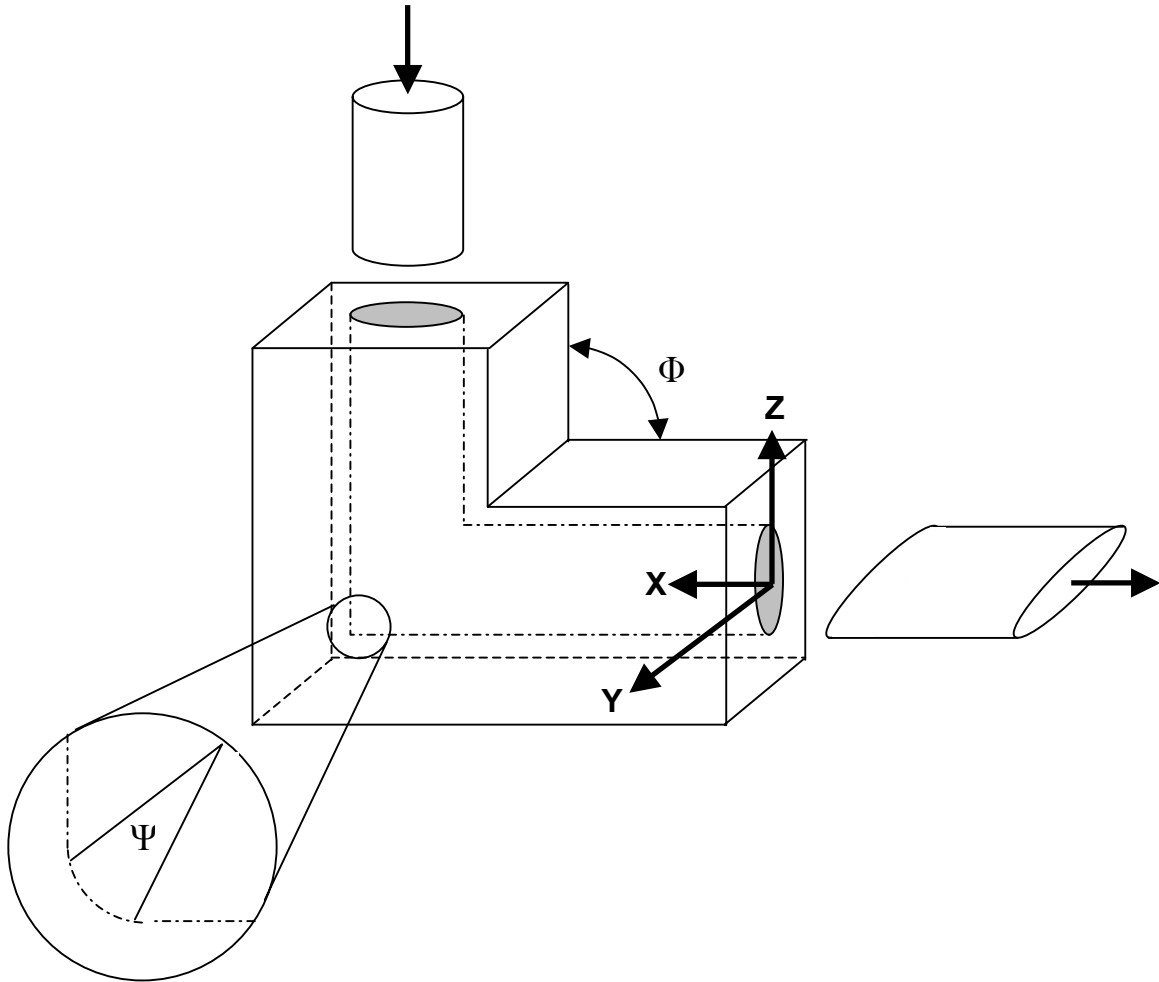
Figure 2.1. A schematic representation of an Equal Channel-Angular Pressing (ECAP) die. The angle between die channels is $\Phi=90°$; the shearing of a cylindrical billet during pressing is shown and the angles Φ and Ψ, which is the relief angle at the outer radius of the channel intersection, are defined.

Recently, attention has been given to the effectiveness of the various ECAP routes in producing grain refinement in bulk samples of various pure metals and alloys [Refs. 14-16, 100-103]. These investigations have relied mainly on transmission electron microscopy (TEM) and selected area electron diffraction (SAED) methods as a means of assessing the relative fraction of high-angle boundaries associated with grain refinement

by the various ECAP routes. These studies have all demonstrated that ECAP is capable of producing fine, equi-axed structures with large fractions of high-angle boundaries. Based on TEM observations of pure aluminum, it has been suggested that the optimum grain refinement after four ECAP passes may be achieved by following route B_C, and that routes A and C were less effective in achieving a high fraction of high-angle boundaries in the microstructure [Ref. 100]. Additional, related issues that have been examined recently include the effect of die angle on texture [Refs. 104-105] and microstructure [Ref. 106], analytical [Refs. 99, 107-108] and finite element [Refs. 109-110] modeling investigation of equivalent strains [Refs. 99, 107-108], adiabatic heating of billets during ECAP [Ref. 111], the capability of ECAP to enable superplasticity at high strain rates and low temperatures [Refs. 112-115], grain refinement mechanisms [Refs. 116-118], the characteristics of the grain boundaries after ECAP [Refs. 119-122] and the combined texture and microstructural modeling of ECAP [Ref. 123].
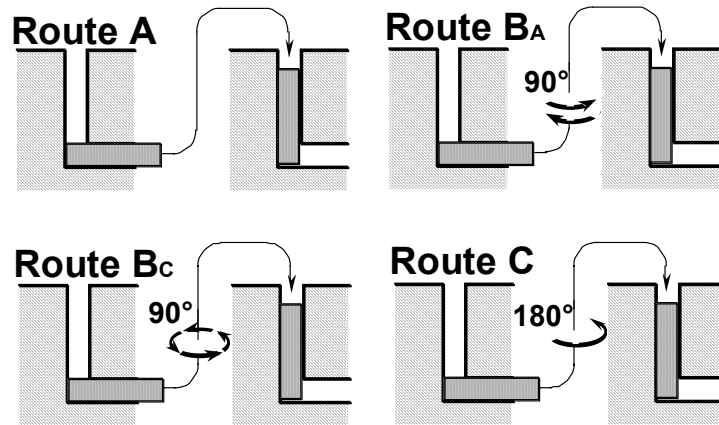
Figure 2.2. Schematic of the four defined Equal Channel-Angular Pressing routes for repetitive pressings. Route A involves no rotation between passes, Route B_A involves alternating 90° rotations, Route B_C has rotations of 90° in the same sense while Route C has rotations of 180° between successive passes. [From Ref. 101]

B.   ROLLING

Rolling has been and will continue to be one of the most important and extensively used techniques of deformation processing. Deformation during a rolling pass is illustrated in Figure 2.3 for the rolling of a sheet or plate material. Plastic deformation occurs as the material passes between parallel, counter-rotating rolls that are

15

separated by a gap that is less than the entering thickness of the material. The standard axis system that was utilized in this study is indicated in Figure 2.3 and consists of the rolling direction (RD), the transverse direction (TD) and the normal direction (ND).
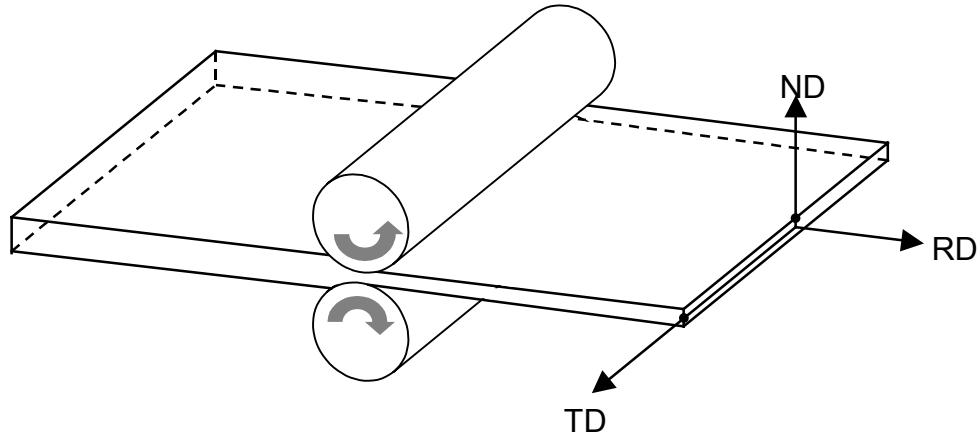
Figure 2.3. Schematic of the process of rolling. The axes are indicated as Rolling Direction (RD), Normal Direction (ND) and Transverse Direction (TD).

An idealized model of deformation during a rolling pass considers that the deformation is plane strain in nature. Thus, the material is elongated in the rolling direction (RD) while being reduced in the normal direction (ND). In reality, a true plane strain condition exists only near the center of the material. The stress state near the surfaces of the material is more complex due to friction at the roll / work piece interface and the effects of curvature of the rolls. Additionally, the assumption of plane strain conditions breaks down near the edges of the material and typically there is some elongation along the TD due to relaxation of the constraining effects of friction near the edge of the material. All rolled materials investigated in this study were examined near the mid-point along the ND and away from the TD edges of the sample. The rolling deformation is normally expressed in terms of a percentage reduction of the starting thickness. The corresponding true strain, ε_t, may then be calculated using Equation 2.2, where t_f is the final and t_o is the initial thickness.

$$\varepsilon_t = \left| \ln\left(\frac{t_f}{t_o} \right) \right|$$

Equation 2.2

16

C.   REVIEW: TEXTURE

1.   Texture Representation

Most engineering materials are polycrystalline in nature. Thus, each individual grain in a material will have a distinct lattice orientation. The lattice orientation is typically expressed in a fixed reference frame related in some way to the material. The presence or absence of a preferred or common orientation among numerous grains in the material defines the texture of the material under study. These orientations may be represented in a number of ways, using either discrete points for each measurement or by contour plots with each contour level corresponding to a density of points above the normalized background level. Randle and Engler [Ref. 124] have provided a thorough introduction to these topics as well as a background on the texture representations that have been used in this work. The first orientation representation used extensively in this study is by a stereographic projection, or pole figure, utilizing discrete points, each representing a single lattice orientation measurement.

The stereographic projection utilizes a sphere that is defined in a reference axis system. This axis system normally is chosen to coincide with a set of directions characteristic of the sample rather than of specific crystallographic directions. A texture may be described by a pole figure, which is constructed by, first, projecting a given family of crystal directions from an origin located at the center of the fixed sphere onto the surface of the sphere. The families of directions are normally chosen to be coincident with low index crystallographic directions, i.e. <002>, <022> and <111> and each family is represented by a separate pole figure. The points on the sphere surface are projected onto a plane normal to the sphere to obtain the actual pole figure. This projection plane is usually normal to one of the fixed axes of the reference frame so that the plane contains the other two fixed axes. The projections are normally accomplished stereographically (i.e. by a straight lines), or by either an equal-angle or equal-area method. These different representations are schematically shown in Figure 2.4. When examining pole figures it is important to bear in mind that the stereographic projection method causes the distance (or angle) between two points near the center of the plane to appear to be less than that of the

same points located further from the center of the plane. This can be seen in Figure 2.5, wherein the points are separated by 20°.

(a)

(b)

(c)
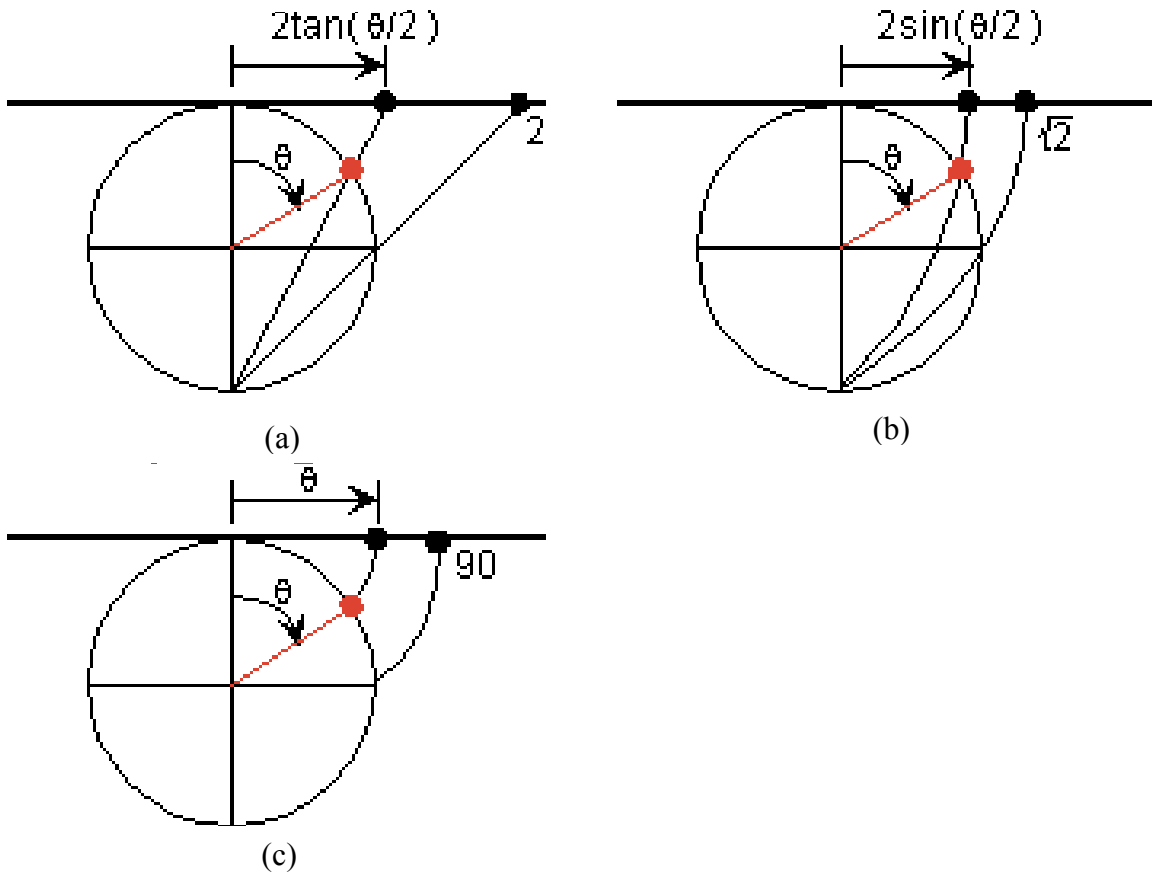
Figure 2.4.   Schematic representation showing the generation of a Stereographic Projection in (a), an Equal Area Projection in (b) and an Equal Angle Projection in (c). [After Ref. 125]

Pole figures representing the distributions of the <002>, <022> and <111> are widely used in this work. For cubic materials, these lattice directions correspond to the normals of the planes with the same indices, i.e. the [111] direction is collinear with the normal to the (111) plane. An example of a unit cube and the corresponding <002>, <022> and <111> pole figures is provided in Figure 2.6. These three pole figures represent the distributions of the cube planes, the slip directions and the slip planes, respectively, even though a single pole figure would be a complete description of the distribution of orientations (the texture) in the material.
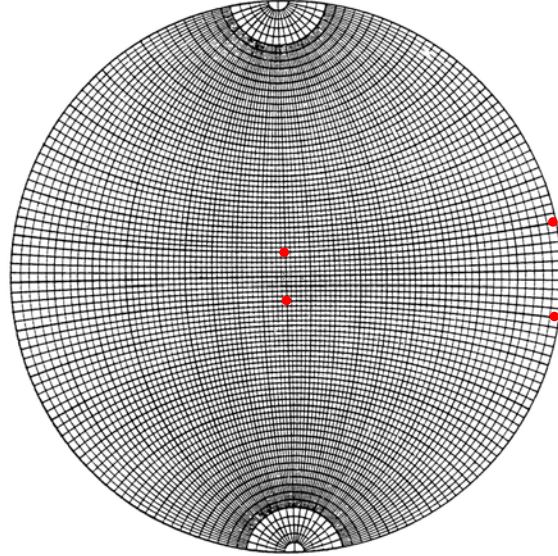
Figure 2.5. Stereographic projection on a Wolfnet, where the two points located near the center are separated by 20° and the two points located at the perimeter of the projection are also separated by 20°. It should be noted that while the angular separation distance is the same in both cases, the physical distances on the projection are not.

An alternative representation of texture consists of an inverse pole figure (IPF). The IPF is constructed in a similar manner to the pole figure with the exception that the reference axes are projected onto a plane that is referenced in turn to the grain or lattice orientation. Additionally, due to the symmetry of cubic materials, the IPF is normally presented in the form of a unit triangle with the apices being the <001>, <011> and <111> crystal directions; this may be seen in Figure 2.7.

The last method of texture representation in this work is the orientation distribution function (ODF). This representation of orientations is typically prepared by plotting three Euler angles, φ_1, Φ and φ_2, in a rectilinear coordinate system, which represent rotation angles needed to reorient the cube axes of the lattice into coincidence with the reference axes. The Euler angles are defined using Bunge's convention [Ref. 126]. Thus, φ_1 is the first rotation and it is about the x_3 (or Z) axis; the second rotation, Φ, is about the x_1 (or X) axis; and the final rotation, φ_2, is also about the x_3 (or Z) axis. These rotations are illustrated in the schematic in Figure 2.8. The ranges of the Euler angles necessary to represent all possible orientations depend on lattice symmetry. Thus, a triclinic lattice requires that the Euler angles have the following ranges: φ_1 from 0°-
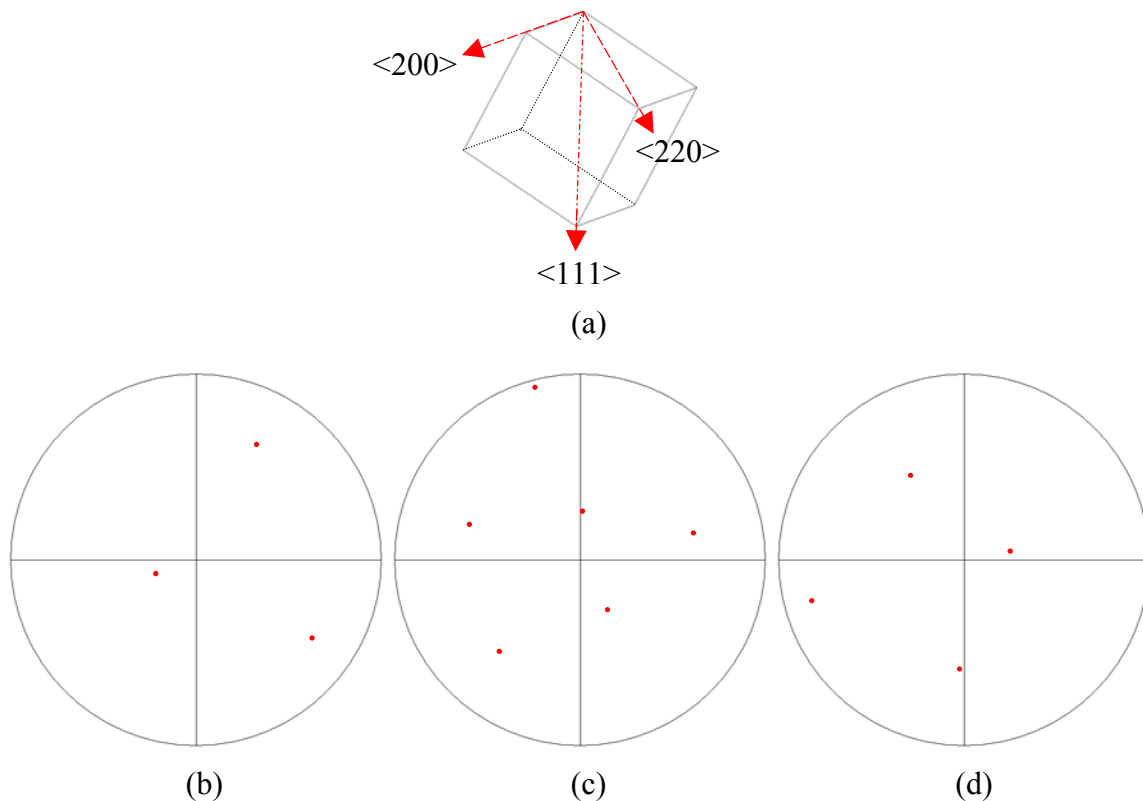
Figure 2.6. A unit cube with crystallographic directions <200>, <220> and <111> presented in (a) and the corresponding (200), (220) and (111) stereographic projections are presented in (b), (c) and (d) respectively.

360°, Φ from 0°-180°, and φ_2 from 0°-360°. Any cubic lattice orientation can be described with respect to the reference axis system by considering the ranges of φ_1, Φ and φ_2 each to be 0°-90°. The representation of a texture in Euler space is normally accomplished by plotting two angles, φ_1 and Φ, on constant φ_2 sections, as seen in Figure 2.9.

The Euler angles for the cubic lattice of a given grain may be used to obtain an orientation matrix, [A], as in Equation 2.3. This matrix represents the Euler rotations needed in order for the cube axes of the lattice to coincide with the reference axes of the material. If a similar orientation matrix is obtained for an adjacent grain, the disorientation matrix, [M], may then be computed using Equation 2.4. In practice there are up to 24 possible disorientation matrices and so determination of the disorientation angle, θ, involves a minimization operation among the crystallographically equivalent
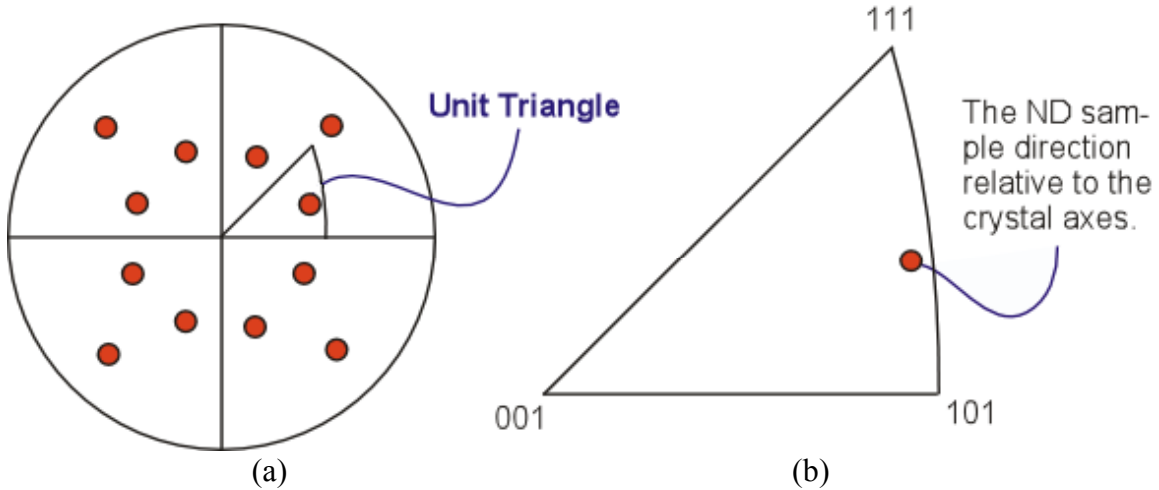
Figure 2.7. A representative schematic of an inverse pole figure (IPF), depicting the <100> directions in (a), corresponding to the reference axes RD (or [100]), TD (or [010]) and ND (or [001]) directions as projected onto the stereographic projection referenced to the crystal axes. In (b), the customary representation of the IPF utilizing only the unit triangle is shown. [From Ref. 125]

disorientation matrices. The disorientation angle, θ, is then found from Equation 2.5, where m_{11}, m_{22} and m_{33} are the diagonal terms of the [M] having the lowest rotation angle. For a cubic system symmetry considerations limit the range of θ to 0°-62.8°. In the simplest terms, the disorientation angle is the smallest rotation angle and its associated rotation axis that will bring the lattice of one grain into coincidence with the lattice of adjacent grain.

Equation 2.3

$$[A_1] = \begin{bmatrix} \cos\phi_1 \cos\phi_2 - \sin\phi_1 \sin\phi_2 \cos\Phi & \sin\phi_1 \cos\phi_2 + \cos\phi_1 \sin\phi_2 \cos\Phi & \sin\phi_2 \sin\Phi \\ -\cos\phi_1 \sin\phi_2 - \sin\phi_1 \cos\phi_2 \cos\Phi & -\sin\phi_1 \sin\phi_2 + \cos\phi_1 \cos\phi_2 \cos\Phi & \cos\phi_2 \sin\Phi \\ \sin\phi_1 \sin\Phi & -\cos\phi_1 \sin\Phi & \cos\Phi \end{bmatrix}$$

$$[M] = [A_1]^{-1}[A_2]$$

Equation 2.4

$$\theta_{12} = \min\left|\arccos\left[\frac{1}{2}\left(m_{11}^{12} + m_{22}^{12} + m_{33}^{12} - 1\right)\right]\right|$$

Equation 2.5
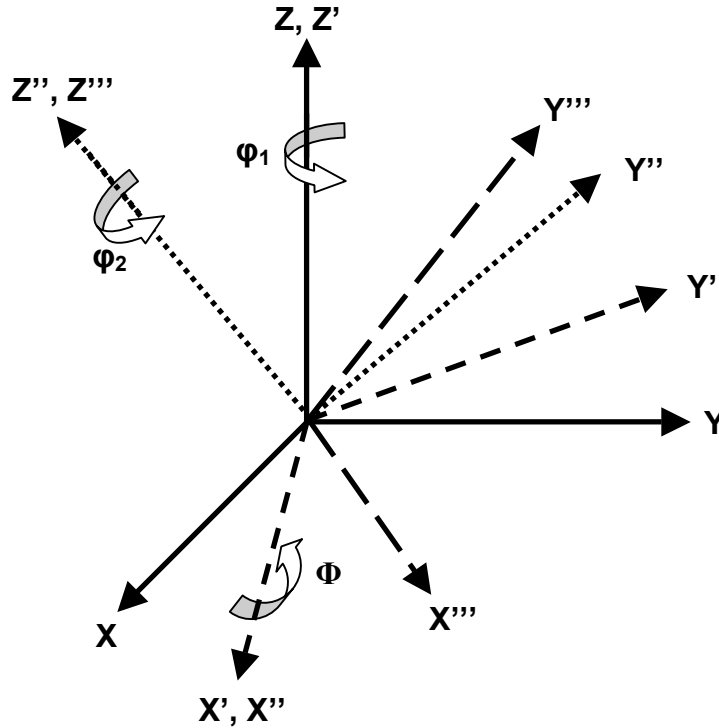
Figure 2.8. Schematic representation of the Euler angles φ_1, Φ and φ_2, using Bunge's convention, φ_1 is the first rotation about Z to arrive at X'Y'Z', Φ is the subsequent rotation about X' to arrive at X''Y''Z'', and the last rotation, φ_2, is about Z'' to arrive at X'''Y'''Z'''.

The disorientation angle associated with adjacent grains will be used to describe the grain boundary. Low angle boundaries (LAB's), or boundaries of small disorientation angle ($\theta \leq 5°$), are often the result of recovery following plastic deformation and may be thought of as arrays of dislocations so that there is a high degree of lattice registry across the boundary plane [Ref. 127]. Boundaries must be effective barriers to the motion of lattice dislocations in order to contribute to strengthening, e.g. as envisioned in the Hall-Petch [Refs. 8-9] model for grain size strengthening. Low angle boundaries would be relatively ineffective due to lattice registry across the boundary, and so the characterization of grain-to-grain disorientations is as important as determination of grain size.

2.   Texture Data Acquisition

The texture of materials was first investigated using x-ray diffraction [Refs. 3-4] by von Laue in 1912. In 1913, Bragg described the interaction of x-rays with the crystal
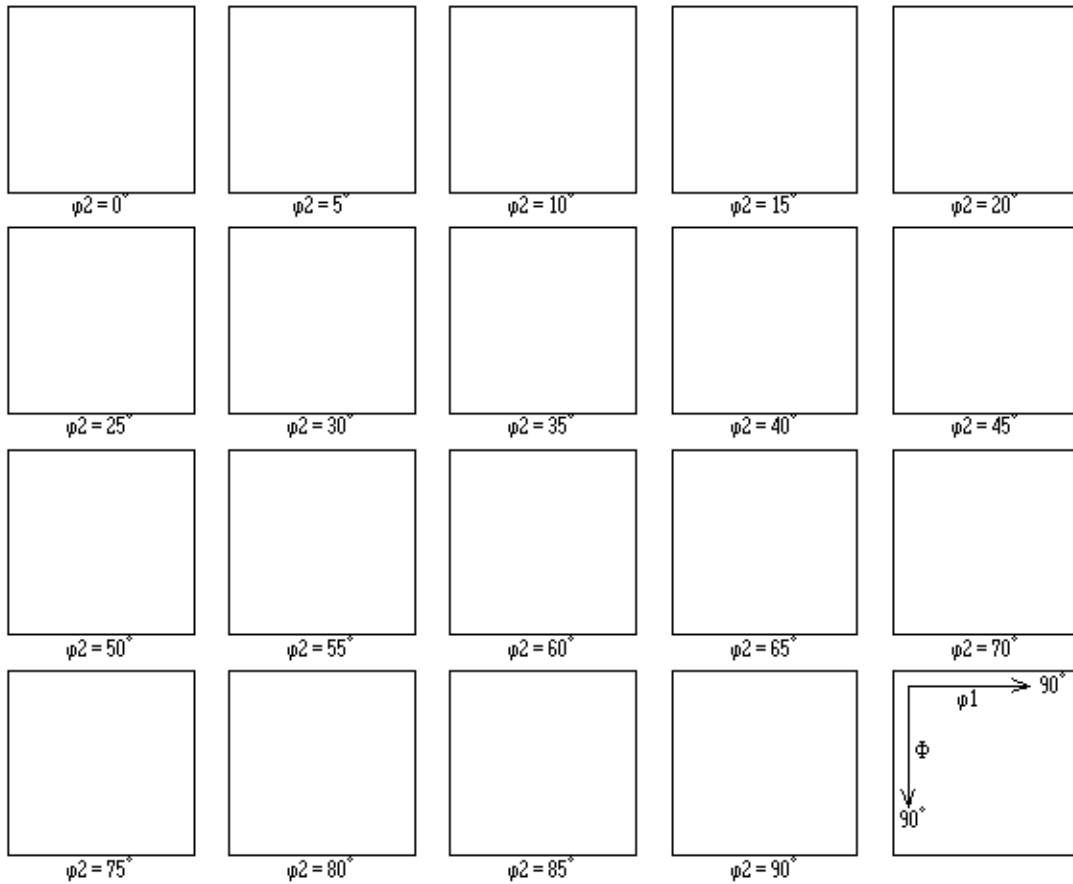
Figure 2.9. Example of an Euler space plot where a rectilinear 3-D coordinate system is presented in "slices" of constant angle, φ_2. The slices are normally set to present data that falls half way below and above the slice label, i.e. the $\varphi_2=40°$ slice would represent data $37.5° < \varphi_2 < 42.5°$ in this example.

lattice and derived Equation 2.6 [Ref. 5-6] wherein n is the order of reflection, λ is the x-ray wavelength, d is the interplanar spacing of the diffracting planes and θ is the corresponding Bragg angle.

$$n\lambda = 2d \sin\theta$$ Equation 2.6

Typically, x-ray diffraction measurements are conducted over large surface areas, sometimes encompassing several thousand grains. This technique lends itself to determination of the macro- or bulk texture of a material. However the computation of grain-to-grain disorientations is practically impossible since the x-rays illuminate all grains simultaneously, making the distinction of individual grain orientations infeasible.

23

In addition, symmetrically equivalent variants of orientations in some textures cannot be distinguished by x-ray methods. For example, the Brass (or B texture) component is often observed in rolled material and may be specified as {110}<112>, meaning a <112> direction aligns with the rolling direction and a {110} plane lies in the rolling plane. As can be seen in Figure 2.10, there are two distinct variants of the B texture, which are disoriented by a 60° rotation about a <111> aligned with the transverse direction. The individual variants are indistinguishable by x-ray diffraction methods so that each variant is equally weighted when computing fractions of dominant orientations. The same problem arises in neutron diffraction of a bulk material.

The use of electron diffraction in the transmission electron microscope (TEM) and scanning electron microscope (SEM) to determine micro texture has evolved more
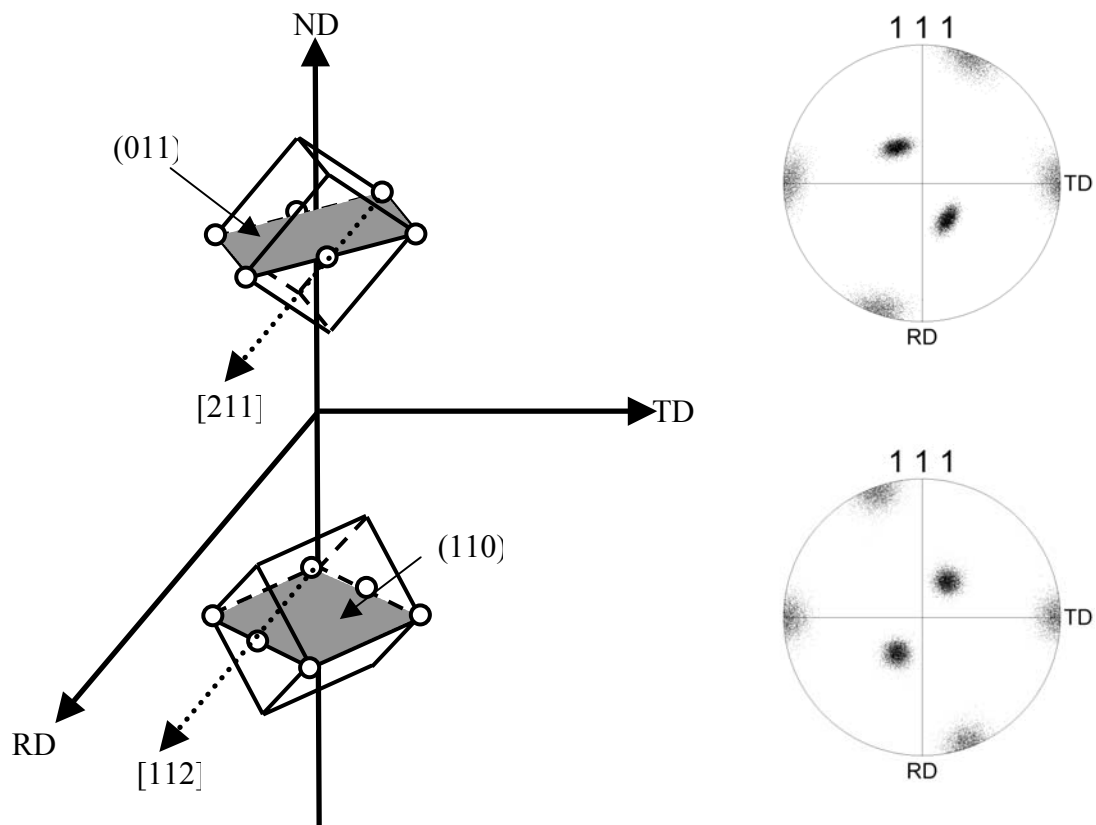

Figure 2.10. A schematic representation of the two B (or Brass) texture variants and the corresponding (111) pole figures, where the <112> directions are aligned with RD and the (110) planes are parallel to the RD-TD (rolling) plane.

recently. Starting in the late 1940's, the TEM became widely available for use as a practical scientific tool [Ref. 128]. This invention allowed electrons to be used for investigations on a finer scale than was available through optical microscopy and x-ray diffraction methods. This was due to the electron's wave-like characteristics and very short wavelength when accelerated through a large potential drop. Neglecting relativistic effects, the electron wavelength, λ, may be calculated by the de Broglie relationship [Ref. 129], as given in Equation 2.7:

$$\lambda = \frac{h}{\left(2m_o eV\right)^{1/2}}$$

Equation 2.7

where V the applied accelerating voltage, m_o is the rest mass of an electron, e is the charge of an electron and h is Planck's constant. If relativistic effects are included, Equation 2.7 can be modified as in Equation 2.8, with the only new variable being c, the speed of light in a vacuum.

$$\lambda = \frac{h}{\left[2m_o eV\left(1 + \frac{eV}{2m_o c^2}\right)\right]^{1/2}}$$

Equation 2.8

Since, the wavelength, λ, is inversely proportional to the square root of the accelerating voltage, V, the higher the applied voltage, the shorter the wavelength. If the wavelength of the electron is shorter, the resolution of the technique is improved and atomic resolution has become possible now. The practical limitations of electron microscopy are defined by the ability lens system in the microscope to focus the electron beam.

By taking advantage of the scattering of electrons and the wavelike characteristics of the electrons, Bragg diffraction, given in Equation 2.6, is possible in electron microscopes. Kikuchi recognized this possibility in 1928 by considering only geometric considerations, well before the invention of any electron microscope [Ref. 130]. Kikuchi also recognized that line patterns may be formed from incoherently scattered electrons that travel in all directions from an inelastic scattering event while loosing only minimal

energy. This is depicted schematically in Figure 2.11(a). These electrons have also been termed diffusely scattered electrons. A diffusely scattered electron can then undergo Bragg diffraction from the various planes of atoms in the material, as seen in Figure 2.11(b). The combination of electrons having many incident directions and energies near the energy of the incident beam results in the formation of diffracted cones of electrons emerging from the sample. These 'Kosel cones' [Ref. 128] will intersect the Ewald sphere, and be observed as lines, shown in Figure 2.11(c). If the radius of the Ewald sphere is large, the projection of the cones will be in the form of straight lines rather than parabolas. These straight lines can then be used to unambiguously determine the orientation of the crystal lattice. The material must not absorb the diffusely scattered electrons; otherwise, no 'Kikuchi' lines will be observed. For electrons that are diffusely scattered back in the general direction of the incident beam (backscattered electrons) this means that Kikuchi patterns will be observed only for regions near the free surface. Conversely, for diffuse scattering in the forward sense the material must be in the form of a thin foil to avoid absorption of the diffusely scattered electrons.

The observation of backscattered electrons in an SEM following Kikuchi diffraction was first reported in 1954 [Ref. 131]. These resulting diffraction patterns were termed backscatter Kikuchi diffraction (BKD) patterns. In the 1970's, tools were developed to capture and index these patterns in SEM's [Ref. 124]. Through the past two decades, this phenomenon has also been termed electron backscatter pattern (EBSP) analysis and electron backscatter diffraction (EBSD). Kikuchi diffraction methods have been used extensively in this research in the SEM, through Orientation Imaging Microscopy (OIM), developed by TexSEM Laboratories in Draper, UT (a subsidiary of EDAX, Mahwah, NJ). The OIM system will be described in detail in a later section.

Kikuchi diffraction is also utilized for orientation measurements in the transmission electron microscope (TEM) [Refs. 124, 128]. When the electron beam penetrates the sample, most of the electrons will be scattered in the forward direction. This produces many electrons available for Bragg diffraction with the various atom

(a)　(b)

(c)
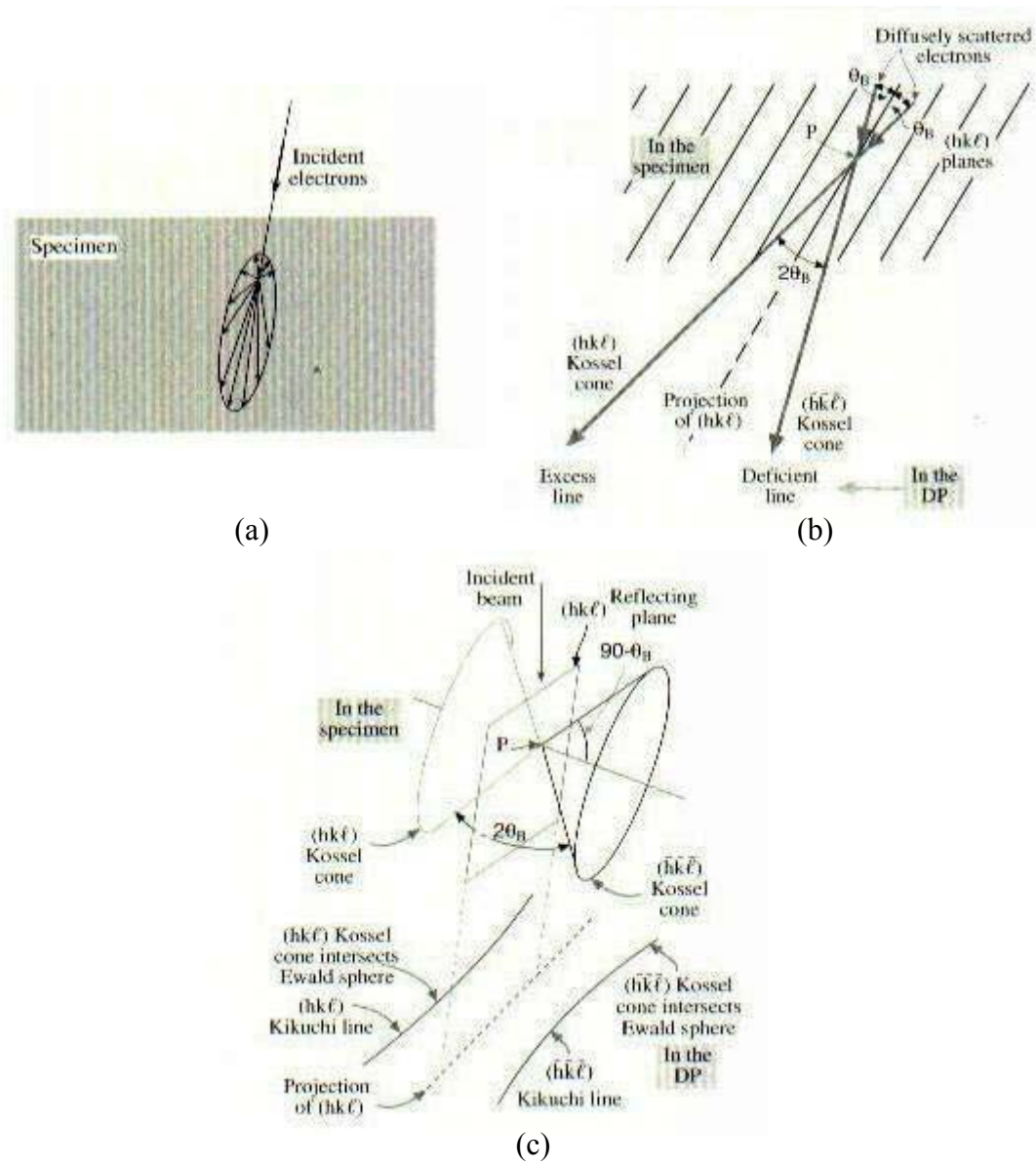
Figure 2.11 Schematic representation of all electron scattering localized at a single point in (a). In (b), some of the diffusely scattered electrons undergo Bragg diffraction from certain atom planes. In (c), Kossel cones are formed and projected onto the Ewald sphere, creating parabolas which approximate to straight Kikuchi lines. [From Ref. 128]

planes. Additionally, due to the high voltages used in TEM's, inelastically scattered electrons loose only a fraction of their incident energy through sample interaction and contribute to the formation of diffraction patterns along with the elastically scattered incident electrons. The TEM may also be operated in convergent beam mode to increase the number of incident electrons available for Kikuchi diffraction. The converging electron beam will be able to satisfy the Bragg diffraction condition more readily than a

conventional, parallel electron beam that is used for normal imaging and production of selected area diffraction (SAD) patterns. The convergent beam electron diffraction (CBED) patterns are consequently produced with very distinct Kikuchi lines that are readily usable in the indexing of the crystal lattice orientation. The convergent beam may also be focused to achieve nanometer sized probes, typically 1–50nm in diameter. This feature of the TEM will allow the investigation of very fine grained materials, while still producing readily indexed diffraction patterns.

The analysis of CBED patterns in this work was performed using Tools for Orientation and Crystallographic Analysis in the TEM (TOCA) software developed by TexSEM Laboratories in Draper, UT (a subsidiary of EDAX Inc., Mahwah, NJ). A detailed description of the TEM hardware and TOCA software will also be provided in a subsequent section.

3. Common Textures Presented in This Work

The following are descriptions and schematic representations of some common textures observed in this work in rolled materials. The notation commonly associated with these orientations is {hkl}<uvw>, meaning that the {hkl} plane is parallel to the rolling plane and the <uvw> direction is parallel to the rolling direction (RD). The single orientations include: Cube {001}<100>, Goss {110}<001>, B or Brass {110}<112>, C or Copper {112}<111>, T or Taylor {4 4 11}<11 11 8> and the S {123}<634>orientation. The cube and Goss orientations have only one variant while the B, C and T have two and the S has four, as in the schematic of Figure 2.12.

Another common texture encountered is the fiber texture. A fiber texture results when a crystallographic direction tends to be common to all grains but there exists rotation about that direction. Two common fiber textures encountered in this work were the <100> and <111> fibers, meaning that those crystallographic directions were aligned with known directions found in the sample or reference axis system. An example of a <111> fiber texture aligned with ND is provided in Figure 2.13.

4. Deformation and Torsion Textures

During deformation processing, e.g. by cold rolling, groupings of the orientations listed in the previous section can develop. The specific orientations and their distribution

28
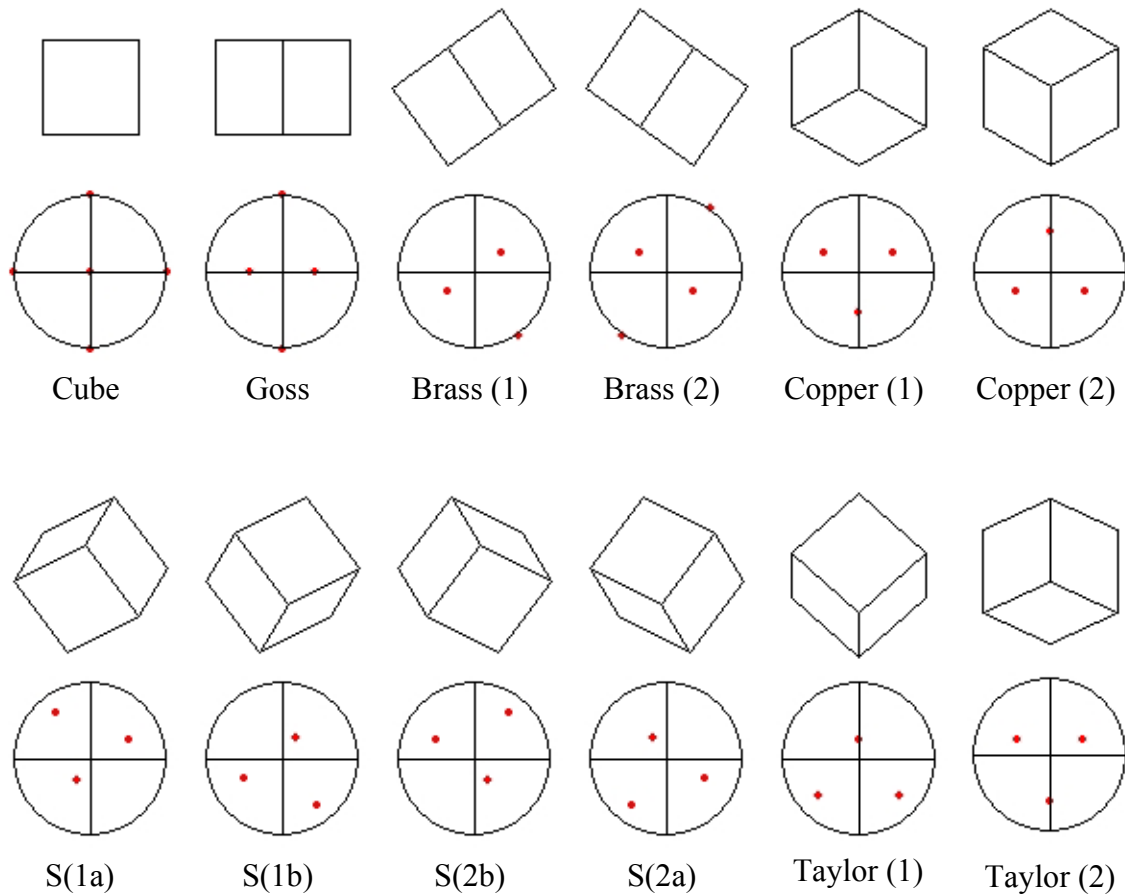
Figure 2.12. Schematic representations of a unit cube and the associated (200) pole figure, using the convention of RD being the vertical axis and TD the horizontal, for some common single orientation variants seen during rolling of fcc materials.

in the material depend on alloy constitution and processing history, mainly the strain and the temperature of deformation. An example of a deformation texture formed during cold rolling of copper is provided in the pole figures of Figure 2.14. If these orientations are plotted in Euler space, they fall along the lines, or orientation fibers, that are illustrated schematically in Figure 2.15. Two of these, the α and β fibers, are of particular importance in rolled face centered cubic metals. The α fiber connects the Cube, Goss and Brass orientations, while the β fiber connects the Brass, S, T and Copper orientations. As with individual orientations, the fibers themselves comprise symmetric variants. The α fiber may also be thought of as having two variants but the orientations are crystallographically identical and therefore indistinguishable from one another. This is because the α fiber lies on along the edge of the fundamental zone of Euler space for

29
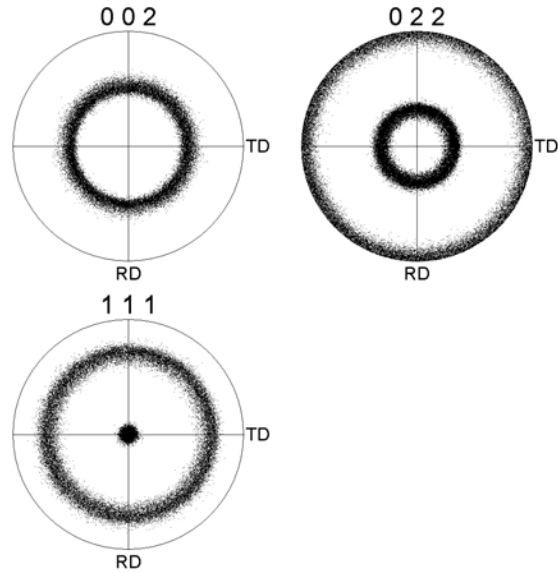
Figure 2.13. Example of a <111> fiber texture aligned with the sheet normal (ND). The rotational axis of symmetry is the <111> as can be seen in the (111) pole figure.

cubic systems. The relationships among such orientations are the same as the symmetry relationships of the crystal structure itself. The β fiber has two distinct and distinguishable variants and there will exist disorientation between the two variants. These fibers are normally associated with plane strain deformation, i.e. rolling, in face centered cubic (fcc) materials such as aluminum and copper [Ref. 126].

Axial torsion of a thin-walled cylinder produces a state of pure shear, which in turn is characterized by unique deformation textures. Canova et al. [Ref. 132] have examined torsion texture development and given a theoretical treatments of torsion textures for cubic materials. Briefly, depending on the constraints imposed different orientations or partial fiber texture components are observed to develop. The different texture components were termed the A, B and C type shear textures. The A type shear texture is a partial fiber texture of the form {111}<hkl> (the notation refers to {plane parallel to the shear plane}<direction parallel to the shear direction>). The B type shear texture is also a partial fiber texture of the form {hkl}<110>. Lastly, the C type shear texture component is a single orientation, {100}<110>, which lies at one end of the B component. A schematic representation of each, and A + B + C components together, are presented in Figure 2.16.

30
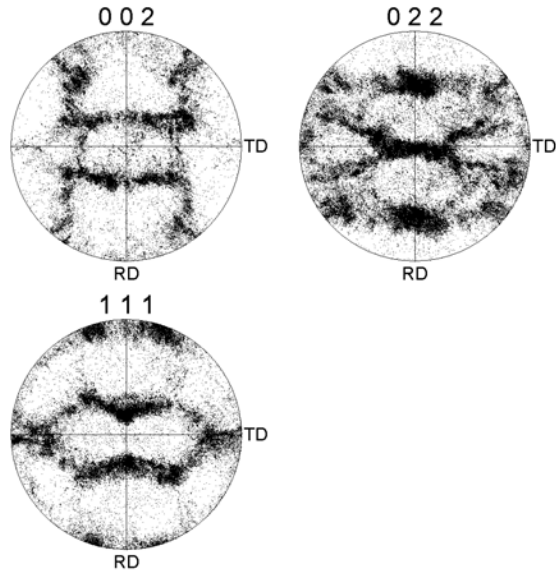
Figure 2.14. Representative example of a deformation texture from a rolled fcc material.
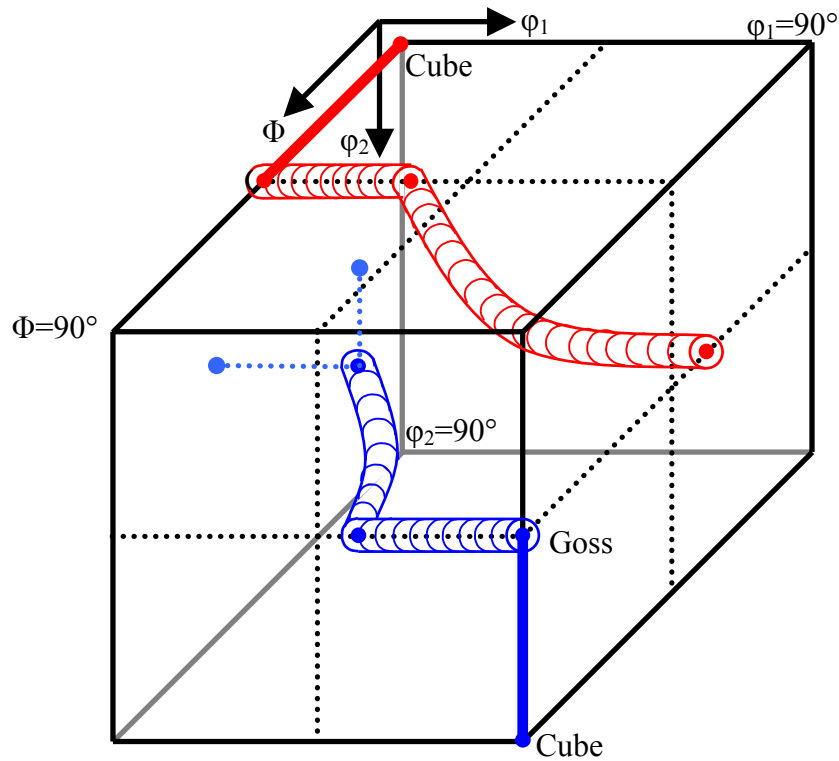
Figure 2.15. Schematic representation of Euler space depicting the locations of the variants of the texture components associated with rolling an fcc material along each variant of the α and β fiber.
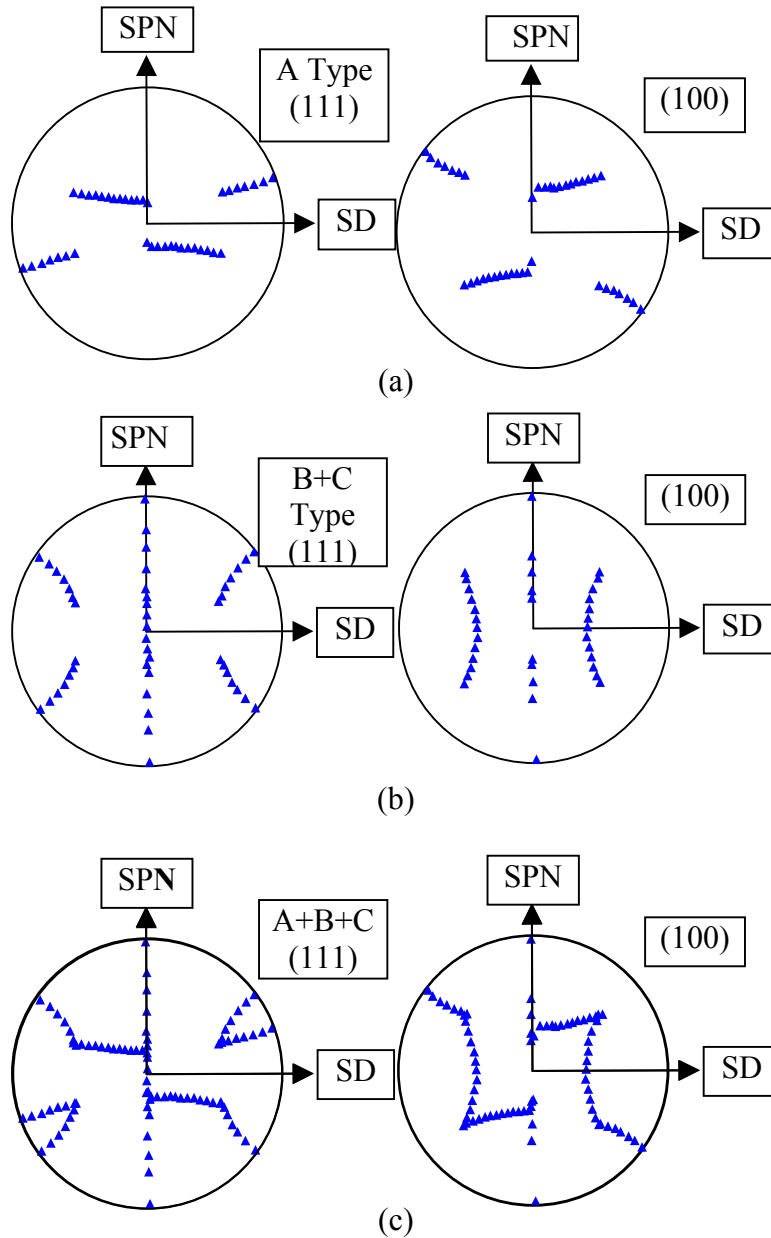
Figure 2.16. Stereographic projections, (111) and (100), of theoretical shear textures developed by Canova et al. [Ref. 132] where SD is the shear direction and SPN is the shear plane normal. A type shear texture: {111}<hkl> is presented in (a), and the B type: {hkl}<110> plus C type: {100}<110> shear textures in (b). The combined A + B + C shear textures are represented in (c). [After Ref. 132]

D.   ORIENTATION IMAGING MICROSCOPY (OIM)

1.   Introduction

Microtexture measurements were performed using electron backscatter diffraction (EBSD) methods and OIM.   Again, Randle and Engler [Ref. 124] provide a thorough introduction to EBSD and OIM and so only a brief overview of the system used in this study will be given.

A TOPCON SM-510 SEM equipped with a tungsten filament and operating at an accelerating voltage of 20kV was used for data collection and analysis. The system is shown in Figure 2.17. After polishing, the samples were placed into the SEM in a holder that inclines the sample surface at 70° to the horizontal. This was done in order to utilize the EBSP analysis capability of the Orientation Imaging Microscopy (OIM) hardware and software provided by TexSEM Laboratories (TSL Inc., Draper, UT), a subsidiary of EDAX Inc., Mahwah, NJ. The SEM was operated in spot mode with an electron beam diameter of about 100nm. The electrons interact within the first 30–50nm of the sample surface, undergoing Bragg diffraction and thereby providing orientation information from a region approximately 100nm in diameter. The backscattered electrons impinge upon a phosphor screen, thus illuminating it. A low-light level camera captured the image of the diffraction pattern, seen in Figure 2.18(a), on the phosphor screen. The OIM software
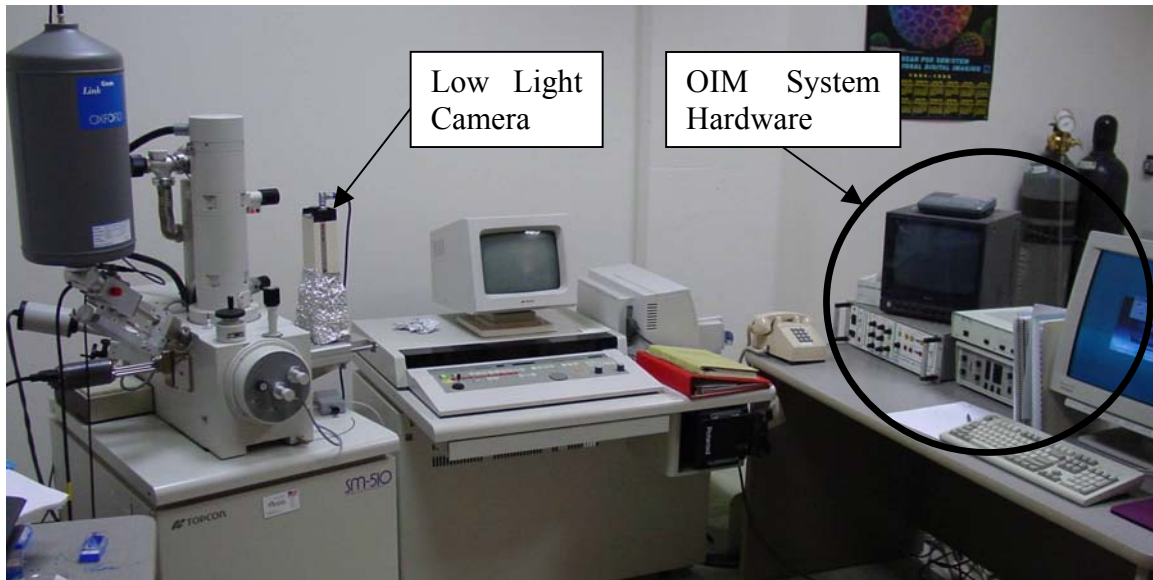
Figure 2.17. Picture of the TOPCON SM-510 scanning electron microscope with the major components of the OIM system indicated.

was employed to capture, analyze and index the pattern to determine the corresponding lattice orientation. The corresponding indexing of the pattern of Figure 2.18(a) may be seen in Figure 2.18(b).

(a)   (b)
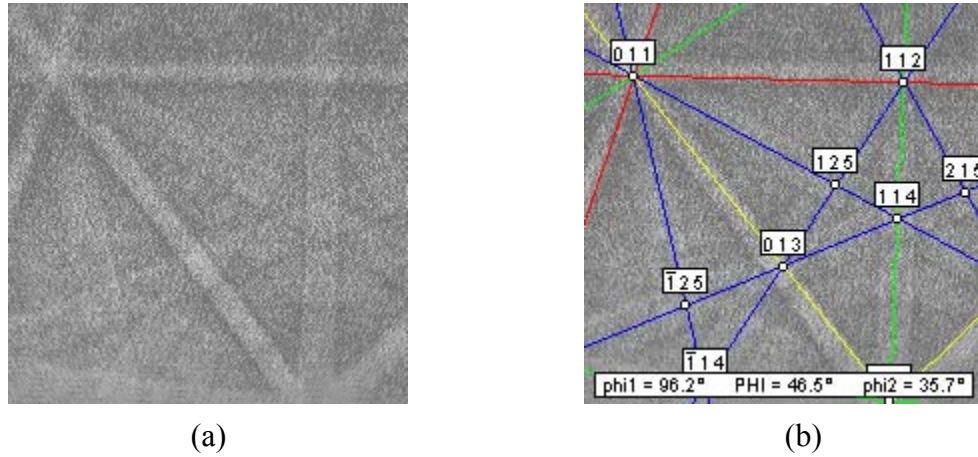
Figure 2.18. Sample Kikuchi pattern and indexing. In (a), an actual Kikuchi pattern obtained on the video screen is shown; (b), an indexed pattern showing several low-index poles [011], [112], [125], etc.; and Euler angles phi1 (φ_1), PHI (Φ) and phi2 (φ_2) for this orientation.

In practice, each pattern is analyzed several times, and resulting solutions, in the form of the Euler angles φ_1, Φ, and φ_2, are then ranked in the software. The pattern is then assigned a best-fit solution and an indication of the goodness of the solution, which is called the Confidence Index (CI). A CI value greater than 0.1 corresponds to a 95% probability correct indexing. The pattern index was then saved in the following format: the Euler angles φ_1, Φ, and φ_2, the coordinate location x and y on the sample surface, the image quality (IQ), or sharpness of the pattern, and the assigned CI value. OIM is accomplished by progressively displacing the electron beam over a preselected area on the sample surface in a raster pattern, as depicted in Figure 2.19. The local lattice orientation at each successive beam position in the raster pattern is obtained as described above. The point-to-point step size is based on the expected microstructure and size of the region being examined. Scans over larger areas, using larger step sizes, were also employed to examine meso-scale features.
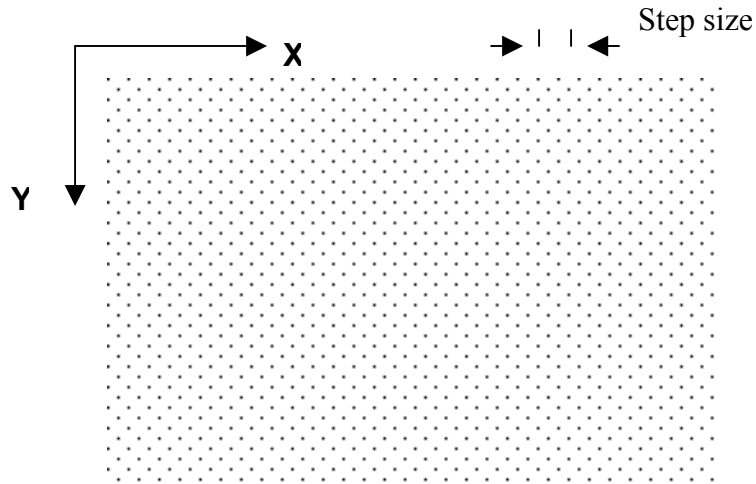
Figure 2.19. Illustration of a typical hexagonal raster scan of a sample surface with the OIM coordinate system and step size indicated.

Poor diffraction patterns may be obtained from regions of severe lattice curvature due to stored strain energy, or where the electron beam is incident on a grain boundary so that overlapping patterns are produced on the viewing screen. Data clean up procedures are included in software and were performed in two successive steps to alleviate such problems. First, the highest CI for a grain is assigned to all points in that grain. Second, a data point (orientation) with a CI less than 0.1 is compared to its nearest neighbors and the orientation of the neighbor with the highest CI is assigned to such a point. This effectively incorporates the point into a grain. This procedure assumes that the low CI points are associated with grain boundaries or regions of high dislocation density and that nearby points with higher CI values are the true orientations. It should be noted that any single orientation with a CI value greater than 0.1 will not be altered. Grains with good quality EBSPs will be kept no matter what the grain size. The elimination of low CI points is done in order to obtain a higher fidelity picture of the grain boundary regions and thus a more accurate determination of the disorientation angle between grains. Accepted accuracy of individual grain orientations in OIM is ± 1° or better; on this basis, the resolution of grain-to-grain disorientations here is taken to be 2°.

After the clean up procedures are completed, the OIM software allows the production of OIM unique grain color maps, pole figures representing the texture, disorientation distribution histograms, and various other representations of the data. The

35

OIM unique grain color maps are produced by assigning neighboring points to the same "grain" if the point-to-point disorientation differed by less than a user-specified amount (2° in the current work). A schematic representation is provided in Figure 2.20(a). The entire "grain" may not have a common orientation. A gradual lattice reorientation due, for example, to curvature associated with residual strain, may accumulate in a traverse across a grain and not be apparent in a grain color map if point-to-point disorientations are always < 2°. Images can also be plotted using CI values, image quality represented in Figure 2.20(b), or other factors that result in contrast within the resulting image. Images may also be plotted superimposing another parameter, such as IQ, over a unique grain color map as illustrated schematically in Figure 2.20(c). Plotting of the orientation data on stereographic projections allows the data to be represented in the form of discrete pole figures. Highlighting features of OIM may be employed to identify the location of various texture components and grain boundaries within various disorientation ranges in the microstructure. This is also indicated in the schematic of Figure 2.20(d).

2.   Errors in Histograms of Disorientation Data

There are two main sources of error in histograms representing the data for the distribution of grain-to-grain disorientations. The first is a standard error due to the number of disorientations in a data set, SE_N, as given in Equation 2.9.

$$SE_N = \sqrt{\frac{x_i(1-x_i)}{N}}$$

Equation 2.9

Here, N is the number of disorientations in the data set and x_i is the fraction of N that are contained in the ith bin of the disorientation distribution. The second is a standard error due to the resolution limit of disorientation measurement, SE_θ, as given in Equation 2.10.

$$SE_\theta = \frac{\theta_{resolution}}{\theta_{MAX}}$$

Equation 2.10

In this relationship $\theta_{resolution} = 2°$ for OIM and $\theta_{MAX} = 62.8°$, which is the maximum disorientation possible for cubic lattices. The total standard error, SE_{Total}, is then given in Equation 2.11.

$$SE_{Total} = \sqrt{(SE_N)^2 + (SE_\theta)^2}$$
<div align="right">Equation 2.11</div>

For all cases examined in this study by OIM, $N \geq 2000$, and so $SE_{Total} \approx SE_\theta = 0.032$.

(a)

(b)

(c)

(d)
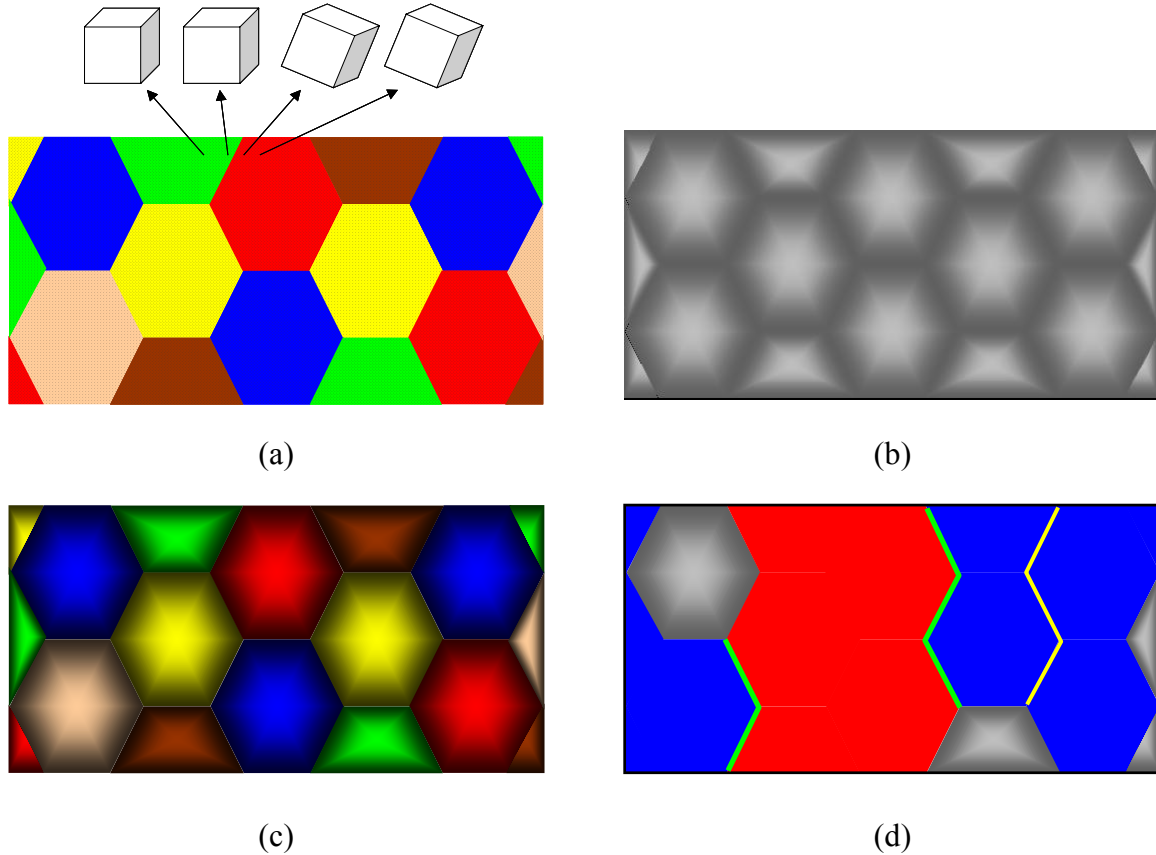
Figure 2.20. OIM grain map representations. (a) Unique grain color map where each color represents a unique grain, defined by a user defined grain tolerance angle and the dots represent individual data points. The cubes illustrate how a grain boundary between grains is based on change in orientation. (b) Image Quality (IQ) grayscale map. Grain boundaries appear dark because they are regions of high lattice imperfection at therefore result in more diffuse, lower quality patterns. (c) Illustrates ability to superimpose Unique Grain Color Maps and IQ grayscale map. (d) Is an IQ grayscale map depicting the highlighting of similar orientations from an associated pole figure or Euler space plot, high- (green) and low-angle (yellow) grain boundaries.

E. TOOLS FOR ORIENTATION AND CRYSTALLOGRAPHIC ANALYSIS IN THE TEM (TOCA)

A TOPCON EM-002B TEM, shown in Figure 2.21, equipped with a LaB$_6$ filament and operated at 200kV, was used for data collection. TEM images and

convergent beam electron diffraction (CBED) patterns were captured by a Gatan DualView300 (DV300) digital camera, installed on the TEM and controlled by Digital Micrograph (DM) software. Tools for Orientation and Crystallographic Analysis in the TEM (TOCA) was developed by TexSEM Laboratories (TSL Inc., Draper, UT) a subsidiary of EDAX Inc., Mahwah, NJ. The TOCA system was installed on the same computer as the DM software to allow file sharing between the two programs. The TOCA program was used to perform crystallographic measurements based on the orientation and phase determination of the CBED patterns.

It should be noted that the TOCA system may also be used to index spot patterns formed from selected area diffraction (SAD) measurements in the TEM. The resolution limit of orientation determination from an SAD spot pattern is ~5° while the CBED patterns will be indexed to within 0.1°. This means that the same pattern, either SAD or
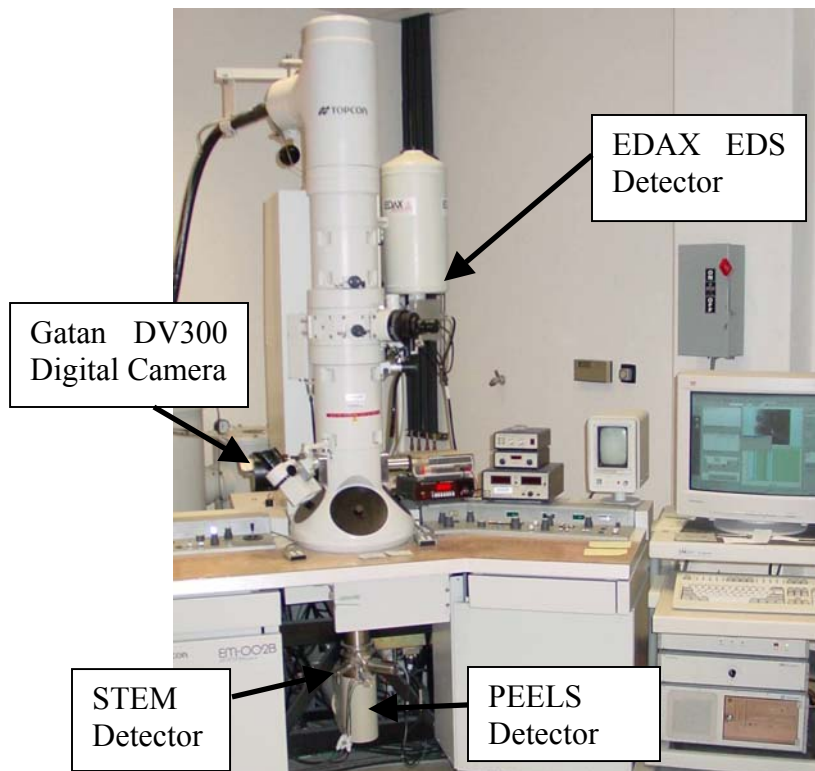
Figure 2.21. Picture of the TOPCON EM-002B transmission electron microscope with the detectors indicated for the following analytical tools: Scanning Transmission Electron Microscope (STEM), Parallel Electron Energy Loss Spectroscopy (PEELS), Energy Dispersive x-ray Spectroscopy (EDS) and Gatan DualView 300 (DV300) digital camera.

CBED, when indexed multiple times will be determined to have an orientation within the stated limits. Additionally, the smallest SAD apertures available on most TEM's is several microns. Hence, this was the smallest area that could be investigated using SAD and would cover several grains in a material with a ~1μm grain size making grain-to-grain disorientation measurements extremely difficult if not impossible.

The process of collecting and indexing of patterns in the TEM is summarized as follows. A TEM bright field image was focused and captured using the DV300 and DM. The sample was then moved to center a specific region of interest. This region of interest could be a grain, sub-grain or second phase particle. A CBED pattern was then formed in the TEM using a probe diameter or spot size of 16nm and a camera length of 56cm. These patterns were captured using the DV300, saved and automatically numbered using DM. The bright-field image was annotated with the location where the pattern had been obtained and the specific pattern number assigned by DM. The process was repeated until CBED patterns from all regions of interest in the bright field image had been collected. The sample was then displaced to an adjacent location and another bright field image was captured along with the CBED patterns as described before. This was done to allow a montage of TEM images to be assembled that would cover a large region of the sample.

The CBED patterns were collected and stored so that they could then be indexed using TOCA. In order to accomplish this, TOCA was started and loaded with the TEM operating conditions (i.e. accelerating voltage and camera length) and the possible crystal phases in the sample. CBED patterns were then loaded in sequence into the TOCA program. An example of such a CBED pattern is provided in Figure 2.22(a). The user then "measured" the Kikuchi line pairs, one bright and one dark, by drawing parallel lines over the CBED image, as shown in Figure 2.22(b). Normally, three Kikuchi line pairs, associated with three different poles, were used to quickly and accurately index a CBED pattern. The program was then told to "Index" the measured lines and, based on the crystal data available, generate a list of possible matches. If multiple solutions resulted for a given crystal orientation, the user could add more Kikuchi line pairs in order to eliminate erroneous solutions. Finally, the TOCA system can also displayed the "ideal"

Kikuchi diffraction pattern as an overlay to the captured pattern for comparison, shown in Figure 2.22(c).
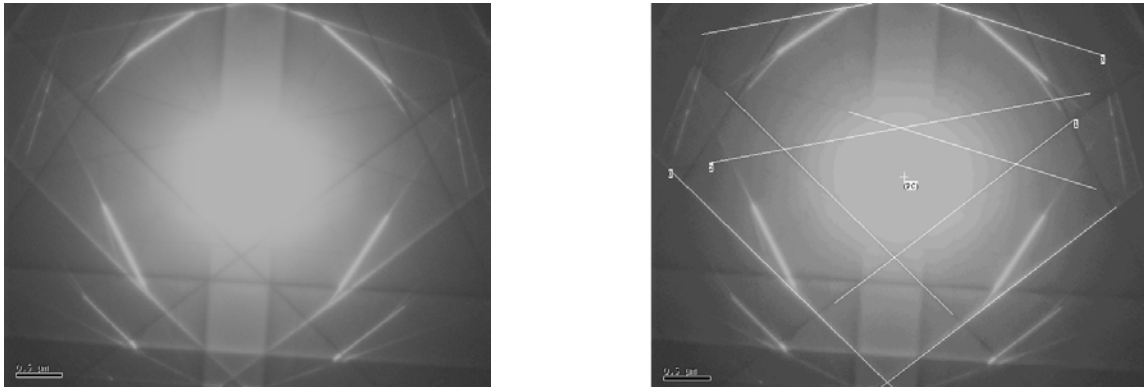
<div align="center">(a)</div>

<div align="center">(b)</div>
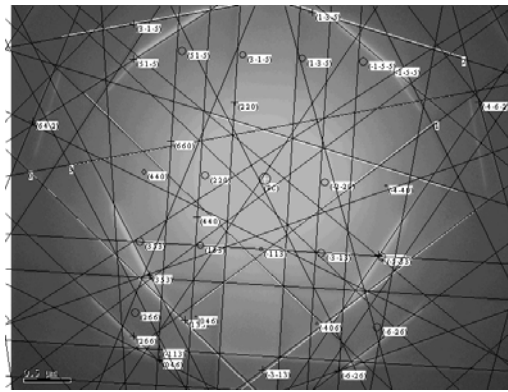
<div align="center">(c)</div>

Figure 2.22. Sample TEM CBED Kikuchi pattern and indexing using TOCA. In (a), an actual Kikuchi pattern is obtained and captured by the Gatan DV300 and Digital Micrograph; (b), the user "measured" Kikuchi line pairs; (c) an indexed pattern showing the "ideal" Kikuchi overlay.

Disorientation determination was accomplished by loading multiple crystals of the same type (i.e. several pure aluminum crystals with identical lattice parameters) during start-up. The following procedure would be repeated until the disorientation between all neighboring grains had been determined: the first CBED pattern would be loaded and indexed; one crystal would be turned "off" (i.e. the system would save the current orientation); a neighboring grain CBED pattern would be loaded and indexed; the

<div align="center">40</div>

program's disorientation function would be used to determine the disorientation between the two indexed patterns.

The disorientation distributions obtained by analysis of CBED patterns using the TOCA software include the same two sources of error that were noted earlier in the section on Orientation Imaging Microscopy. The standard error due to the total number of disorientation measurements, SE_N, and the standard error due the resolution limit, SE_θ, may both be calculated using Equations 2.1 and 2.2 respectively. For the TEM data, SE_N is now a significant source of error in the TEM measurements due to the smaller number of CBED patterns indexed, normally ~100 per montage of images, while SE_θ has improved due to the finer resolution of the TEM orientation determination technique. The corresponding total standard error, SE_{Total}, associated with the TEM measurements, was calculated using Equation 2.3.

Using the Kikuchi diffraction patterns, the TOCA software provided the ability to quickly conduct accurate orientation determination, disorientation measurements and simultaneous phase identification if required. The phase identification not only included crystals of different lattice types (i.e. fcc, bcc, etc.) but also differentiation between similar crystal lattices (i.e. copper and aluminum). An experienced operator could be expected to index ~50 CBED patterns per hour and determine ~200 disorientations per hour, depending upon the average number of nearest neighbors for each grain.

F.   ADDITIONAL ANALYTIC TOOLS OF THE TEM

Scanning Transmission Electron Microscopy (STEM) and Energy Dispersive x-ray Spectroscopy (EDS) were also performed on selected samples. A thorough discussion of each technique is provided by Williams and Carter [Ref. 128]. In STEM mode, the TEM focusing coils are used to deflect the electron beam in a raster pattern over the sample surface while operating the TEM in a diffraction mode. This allows the production of images much like those obtained in a scanning electron microscope. Additionally, while operating in STEM mode, the electron beam is focused to a point, 0.5nm-48nm in diameter. This facilitates the simultaneous use of the EDS system to collect, point-by-point, elemental imaging of the sample surface.

G. EXPERIMENTAL PROCEDURES COMMON TO ALL SYSTEMS EXAMINED

Samples were sectioned from all materials using a Buehler low-speed saw with a diamond-wafering blade. With reference to the axes defined in Figure 2.1 for ECAP material, a disc of 2mm thickness having the ± x direction as its normal was sectioned from the as-pressed billet. A second cylindrical section ~10mm in length was also cut from the ECAP billet. This latter piece was then reoriented for further sectioning that was intended to provide a planar surface containing the center line of the billet and whose normal is the ± y direction. These sections are represented schematically in Figure 2.23. With reference to the axes defined in Figure 2.3 for rolled material, the samples were sectioned to examine the plane whose normal is either the transverse direction (TD) or normal direction (ND). A schematic is shown in Figure 2.24 for a sectioned rolled sheet whose normal is TD.
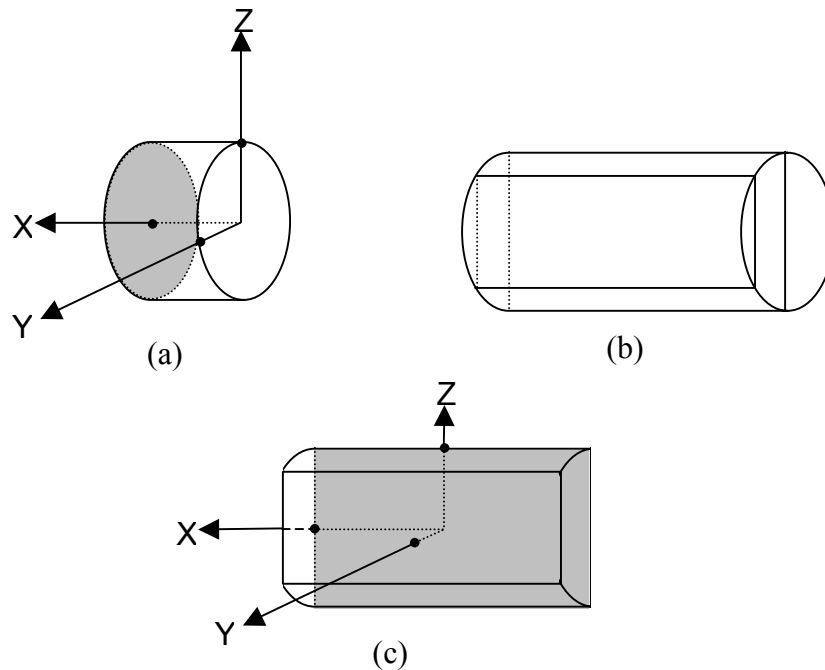
Figure 2.23. Schematic showing the sectioning of ECAP samples for EBSD analysis. In (a), the approximate shape of the samples after sectioning is illustrated for the X plane and in (b) the sectioning to be performed on the second cylinder cut from the sample after reorientation and (c), the final approximate Y Plane section shape. The shaded regions indicate the actual surface examined.
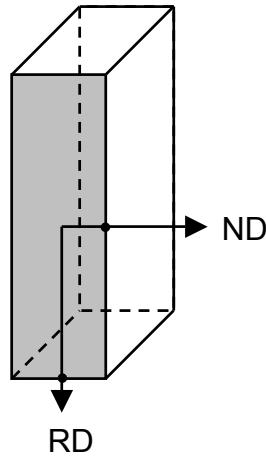
Figure 2.24. Schematic of a rolled sheet after sectioning, the shaded surface indicating the plane examined.

Mechanical polishing of the samples was accomplished by carrying out the steps outlined in Table 2.1 for the indicated times. Fixed silicon carbide (SiC) abrasive papers were used, with water as the lubricant, and grinding was conducted in one direction until all evidence of the prior grinding step had been eliminated. The sample was then rotated 90° and the process was repeated on the next paper. Rotating wheels with microcloth were used for polishing with the Metadi suspension, and Chemomet I was used with colloidal silica. Care was exercised to employ dilute diamond abrasive suspensions and a dilute colloidal silica suspension to avoid surface contamination with these abrasives. After each mechanical polishing step, an ultrasonic cleaning was performed for 10 minutes in ethanol.

A distortion-free final polish was required due to the very small interaction volume near the surface of the sample associated with formation of the diffraction patterns by the electrons in the scanning electron microscope. Hence, the final polishing step was an electropolish conducted in a Buehler Electromet 4 apparatus. Specific electrolytes, voltages and times for each system examined will be provided in the Experimental Procedures section of each chapter. All samples were examined in the as-polished condition.

Step	Abrasive	Time	RPM
1	500 Grit SiC Paper	30 sec.	180
2	1000 Grit SiC Paper	30 sec.	180
3	2400 Grit SiC Paper	30 sec.	180
4	4000 Grit SiC Paper	30 sec.	180
5	3 μm Metadi Diamond Suspension	10 min.	180
6	1 μm Metadi Diamond Suspension	10 min.	180
7	0.05 μm Colloidal Silica	10 min.	40

Table 2.1. Mechanical Polishing for SEM Sample Preparation

Thin foils for selected materials and conditions were prepared utilizing a similar procedure. The low speed saw was used to section a slice ~1000μm thick from the sample. Mechanical polishing was conducted on both sides of the slice using the silicon carbide papers listed in Table 2.2. The goal was to produce a foil ~100μm in thickness. A 3mm disc was then punched from the sample and electropolished in a Fischione Twin Jet Polisher. Specific electrolytes and polishing conditions will be provided in each Experimental Procedures section for the material as required.

Step	Abrasive	Final Step Thickness	RPM
1	500 Grit SiC Paper	500 μm	100
2	1000 Grit SiC Paper	250 μm	100
3	2400 Grit Sic Paper	150 μm	100
4	4000 Grit SiC Paper	100 μm	100

Table 2.2. Mechanical Polishing for TEM Sample Preparation

III. MICROSTRUCTURE OF ROLLED COPPER

A. INTRODUCTION

Deformation-induced microstructures and the associated textures that develop during rolling have long been studied and characterized. A review of early work on deformation microstructures and textures was provided by Gil-Sevillano et al. [Ref. 65]. Hosford [Ref. 66] and Kocks et al. [Ref. 67] have provided a more recent review of textures found in association with common deformation processes. Rolling deformation of an fcc metal at low homologous temperatures generally results in the formation of band-like features aligned with the rolling direction (RD), a (sub)grain structure within each band, and a distinctive deformation-induced texture. The texture of the material typically falls on or near the β fiber in the orientation distribution function in Euler space representation. The β fiber comprises two crystallographically equivalent variants. Each variant connects B (or Brass), {110}<112>, S, {123}<634> and C, or Copper, {112}<111>, orientations in Euler space. This notation refers to {plane parallel to the rolling plane defined by the RD and TD}<direction parallel to the rolling direction RD>. The observed orientation distribution along the β fiber will depend upon the material and the degree of rolling reduction.

Orientation Imaging Microscopy (OIM) data will be presented that illustrates the presence of these band-like features in the as-cold-rolled condition of pure Cu, as well as in material deformed in tension below the recrystallization temperature. Microstructure evaluation was conducted for material in annealed and deformed conditions as well as in the as-rolled state. Furthermore, the bands will be shown to correspond to material having lattice orientations along one or the other of the variants of the β fiber. Also, the lattice orientation along the ND tends to alternate back and forth between the two symmetrically equivalent β fiber orientations. High-angle boundaries will be shown to be the interfaces separating the symmetric variants of the β fiber in the as-rolled condition, as well as during tension tests conducted below the recrystallization temperature.

B. EXPERIMENTAL PROCDURES

The material of this study was designated Copper 101 OFE, which has a minimum 99.99% purity and is oxygen free electrical grade metal [Ref. 133]. The pure copper was obtained in the form of round-corner square bar stock, 31.8mm square. Detailed chemical analysis data are provided in Table 3.1. Annealing was performed at 600°C (0.64T_m) for 1hr in air, after allowing for an additional 15mins of soak time to achieve thermal equilibrium, to obtain an annealed and recrystallized microstructure having an average grain diameter of ~50μm. Following the work of Duggan and Lee [Ref. 32], a grain size of ~50μm was anticipated to result in formation of deformation bands accompanying the development of a strong deformation texture in fcc Cu rolled to 80% reduction. After the initial annealing, 1.27mm was machined from all sides to remove the oxide layer that had formed during annealing. This resulted in an initial thickness, t_o = 29.2mm, prior to rolling.

Zn	Pb	Bi	Cd	O	P	S	Se	Te	Sb	As	Fe	Mn	Ni	Ag	Sn	Cu
0.3	1	0.2	0.2	2	2	8	2	0.5	1	1	4	0.3	1	8	1	Bal.

Table 3.1. Composition (ppm) for the as received Copper 101 OFE

Rolling was conducted at room temperature, with sufficient interpass time to allow the material to return to room temperature after the adiabatic heating that resulted from the plastic deformation of each successive rolling pass. The rolling schedule was based on a reduction per pass of 0.1 (true strain definition). Separate billets were rolled to nominal true strains, ε_{true}~1.0, 1.5, 2.0, 2.5 or 3.0. Copper rolled to ε_{true}~2.5 (~92% reduction) will be the main focus of this study. The recrystallization temperature was determined for this material and, subsequently, tension tests were performed both above and below this temperature.

Tensile coupons having a 12.5mm gage length were machined from this rolled material such that the tensile axis was parallel to the rolling direction (RD). Tensile tests were performed at a constant nominal strain rate. Test temperatures were 150°C or

250°C. Sample preparation for microscopy consisted of mechanical polishing as outlined in Chapter II. Samples for SEM examination were electropolished in a 33% nitric acid, 67% methanol electrolyte solution at 20VDC for 15sec with the electrolyte initially cooled to a temperature of –25°C.

C.   RESULTS

Data corresponding to the following conditions will be presented for this material: prior to rolling; as-rolled; rolled and annealed; and rolled and deformed in tension at elevated temperature. Figure 3.1 presents data for the pure copper after the initial annealing treatment at 600°C for 1hr. Figure 3.1(a) is an OIM grain map constructed by superposition of unique grain colors and gray tones that correspond to the image quality (IQ) of the Kikuchi diffraction patterns. The grain tolerance angle was set at 2°, which means that adjacent points disoriented by more than 2° will be assigned different random colors.   This grain tolerance angle will be used in all subsequent unique grain color images in this study. Figure 3.1(b) is an optical micrograph of this same material after mechanical polishing following the procedure outlined in Chapter II, and then etching for two mins with a solution having a nominal composition of 18.75% hydrochloric acid, 6.25% $FeCl_3$ and 75% methanol [Ref. 134] .   Comparison of Figures 3.1(a) and (b) reveals that OIM and optical microscopy results are mutually consistent. Annealing twins and a grain size of ~50 μm are apparent in these data. This initial grain size is sufficiently large to allow for the development of deformation bands [Ref. 32].

Discrete pole figures that represent the ~12,000 individual orientation measurements corresponding to Figure 3.1(a) are shown in Figure 3.1(c). From these data the starting texture of this annealed material is predominantly random. The disorientation distribution data in Figure 3.1(d) were obtained by binning angular disorientations of adjacent points laying along grain boundaries and representing the results in the form of a histogram. The peak near 40° is consistent with a random texture component in a cubic material (following the definition of MacKenzie [Ref. 135]), while the 60° peak is associated with the boundaries of the annealing twins.

47
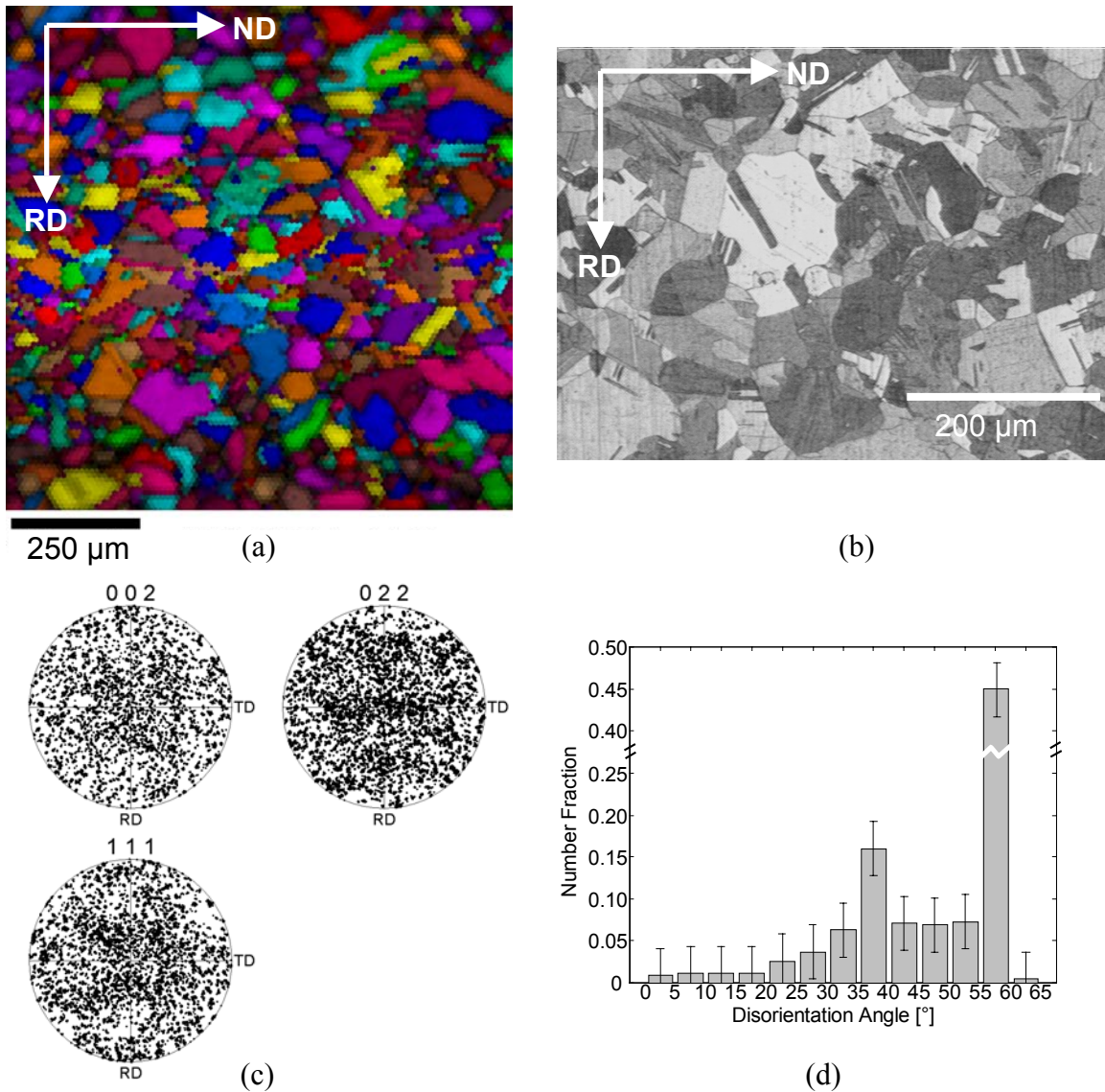
Figure 3.1. Pure copper after 1hr anneal at 600°C taken from the bar to be rolled. In (a), an OIM grain map and in (b), an optical micrograph show the initial average grain diameter to be ~50μm. In (c), the discrete pole figures are presented to ensure a random starting texture which is verified by the disorientation histogram (d), showing a peak near 40°-45° which corresponds to that predicted by MacKenzie. The peak near 60° is due to the annealing twins formed during the heat treatment.

Figure 3.2 shows data for the copper rolled to ε_{true}~2.5. A unique grain color map with superimposed IQ is presented in Figure 3.2(a). The darker regions correspond to a lower IQ and are the result of diffuse or overlapping diffraction patterns that normally occur in regions of high dislocation density, or in locations nearby grain boundaries. The apparent grain elongation and the dark overall appearance of Figure 3.2(a) is consistent

with the high stored strain energy due to dislocation storage in this cold rolled material. The discrete pole figure data in Figure 3.2(b) correspond to the same region as shown Figure 3.1(a), and depict a deformation texture in an fcc metal deformed in plane strain [Refs. 66-67]. The backscattered electron (BSE) image in Figure 3.2(c) may be used as a qualitative measure of grain orientations if the operating conditions in the SEM are adjusted to give orientation contrast. The orientation contrast does not give quantitative orientation data but only indicates differences from region to region by the brightness
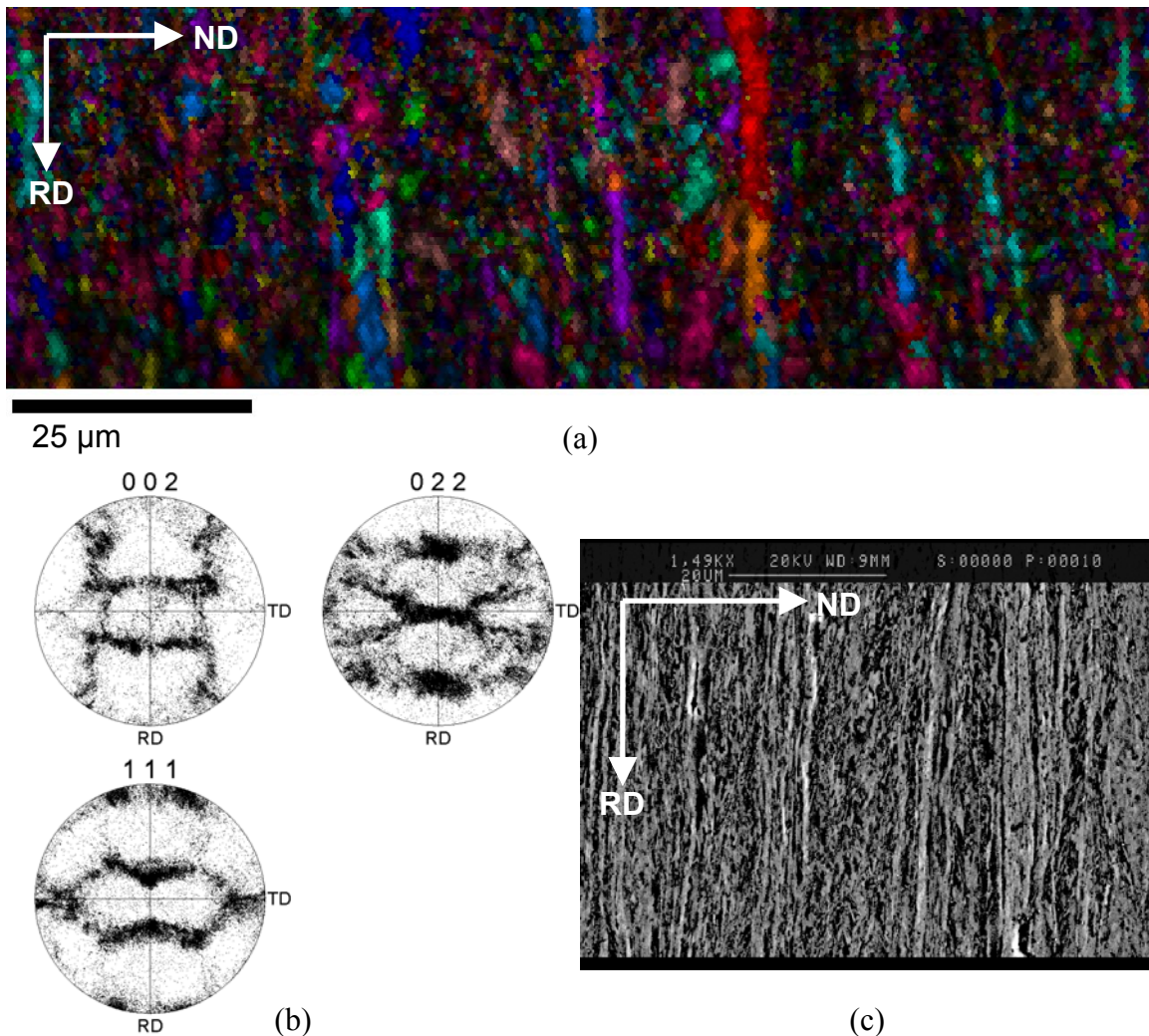
Figure 3.2. OIM grain map in (a) with the grain tolerance angle set to 2° and the corresponding discrete pole figure in (b) which illustrates a common deformation texture seen in rolled fcc metals. The image in (c) is a BSE image illustrating the orientation contrast, no etchant. Both the OIM map and BSE image show elongated grains of similar orientation aligning with RD.

49

level observed in the micrograph. As such, it can be seen in Figure 3.2(c) that there are bands of similar orientation aligned with RD.

Figure 3.3 is shows alternative representations of the data from Figures 3.2(a) and (b) (the axes have been omitted for clarity). In Figure 3.3(a), an IQ map was constructed using gray levels, and was then highlighted with random superimposed colors to show the spatial distributions in the microstructure of the symmetric variants of, separately, the B, S and C β-fiber components. The locations of the Goss and cube texture components are also indicated. In Figure 3.2(b) highlighting has been done differently in order to illustrate the spatial distributions of the two distinct variants of the entire β fiber (in either red or blue), as well as the Goss (green) and cube (yellow) orientations. The locations of boundaries of disorientation > 40° are also highlighted (white). It should be noted that the high-angle boundaries tend to align with RD and tend to separate regions belonging to the two β fiber variants. The discrete pole figures in Figure 3.3(c) show the highlighted orientations corresponding to those in (b). The large number of low-angle boundaries in the 0°-5° bin of the disorientation histogram in Figure 3.3(d) is indicative of a deformation-induced microstructure.

Annealing of the rolled material was conducted at various temperatures. The initial recovery stage of annealing involves only dislocation rearrangement or annihilation and thus a slight softening of the material. More severe annealing temperature will result in nucleation and growth of new, strain-free grains and therefore have a more dramatic effect on hardness. Figure 3.4 is a plot of hardness (Rockwell F Scale) versus time for annealing of this material at various temperatures. It can be inferred that the recrystallization temperature is ~200°C ($0.35T_m$) for annealing times of up to 5hrs from examination of these data. Microstructural investigations for selected annealing conditions were also conducted to confirm this.

Figure 3.5 presents unique grain maps for selected annealing conditions. The material in Figure 3.5(a) had been annealed for 5hrs at 150°C. The elongated features in the microstructure suggests the predominance of recovery by dislocation re-arrangement and annihilation for this annealing treatment [Ref. 97]. The microstructure after annealing for 5hrs at 200°C is distinctly different as shown in Figure 3.5(b). Coarser, equi-axed

grains due to recrystallization have replaced the elongated structure of the as-rolled material. Grain growth does not become apparent until this material is annealed at 450ºC {compare Figures 3.5(b), (c) and (d)}.

Area-weighted average grain area values were also determined for this annealing

(a)

25 µm

(b)

25 µm

(c)

(d)
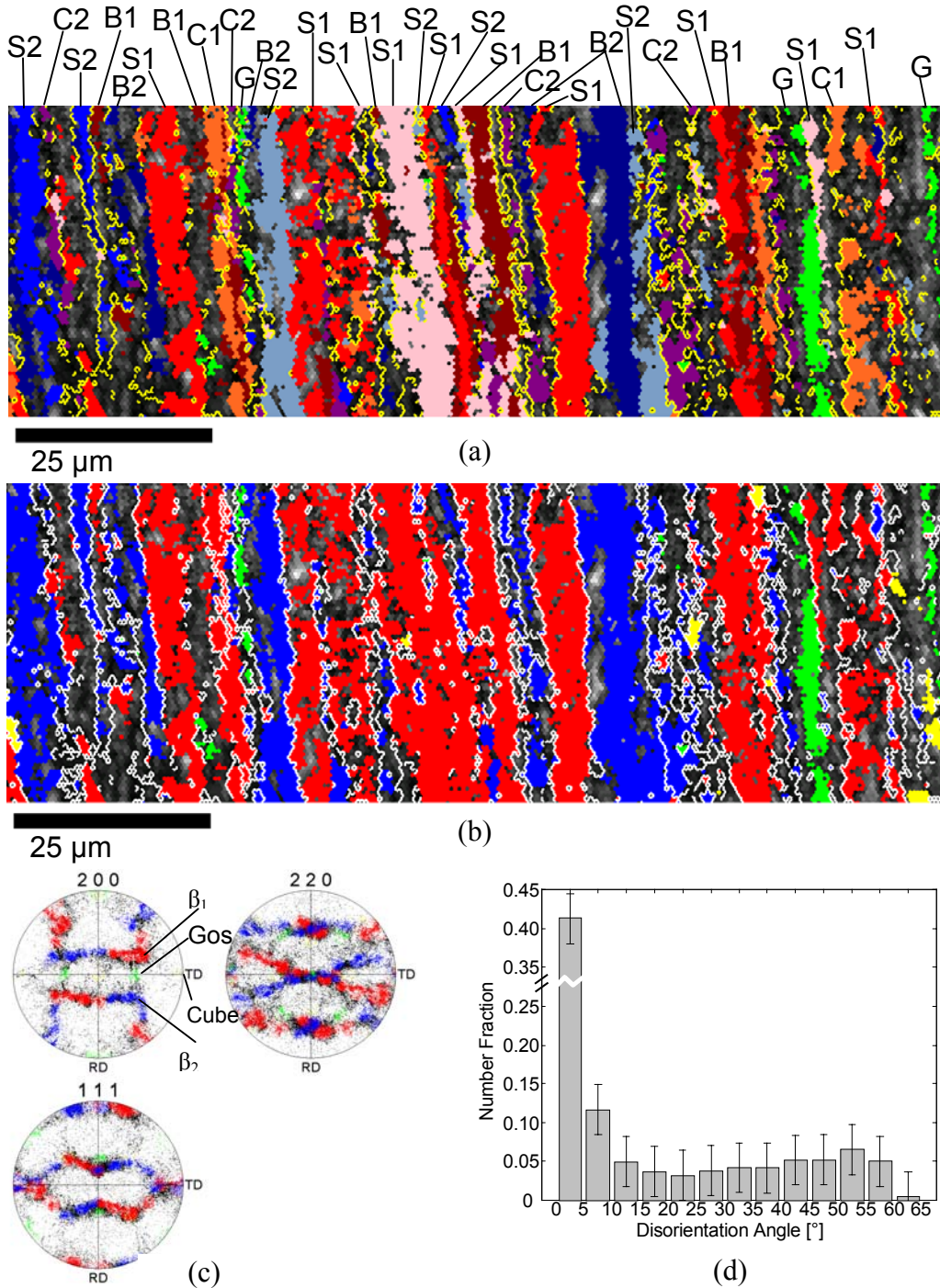
Figure 3.3. Highlighted OIM grain map of rolled copper from Fig. 3.2. In (a), individual texture components have been highlighted and annotated. In (b), the β_1 (red) and β_2 (blue) fibers, Goss (green) and Cube (yellow) textures have been highlighted along with boundaries $\theta > 40°$. In (c), the corresponding highlighted discrete pole figure is provided. In (d), the disorientation distribution shows a predominance of low-angle boundaries

study. The data of Figure 3.6 indicate a distinct change in grain area upon increasing the annealing temperature from 150ºC to 200ºC, but no grain area difference in material annealed at 200°C as compared to that annealed at 300°C. Significant grain growth at temperatures exceeding 450°C is also evidenced by the order of magnitude increase in grain area for annealing at this temperature.

Texture data for this annealing study are shown Figure 3.7. Discrete pole figures corresponding to the regions examined in Figures 3.5(a)-(d) are shown in Figures 3.7(a)-(d). These data provide further support for the predominance of recovery up to 150ºC, in that the deformation texture of the as-rolled condition is retained, and that
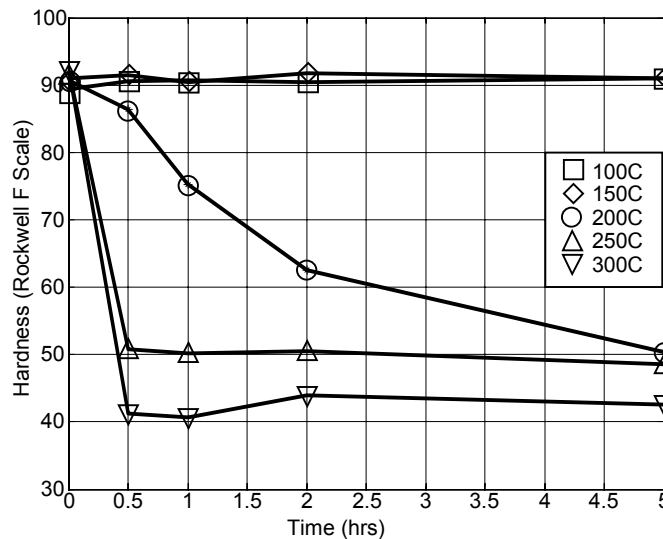
Figure 3.4.   Hardness of rolled copper as a function of time and temperature.   The recrystallization temperature is ~200°C ($0.35T_m$), below which, recovery dominates.

recrystallization occurred during the 200°C anneal, in that a more nearly random texture developed. An accurate assessment of the presence or absence of a preferred recrystallization texture could not be made in the material annealed at 450°C due to the limited number of grains present in Figure 3.7(d). Therefore a larger area (1mm X 1mm in extent) was subsequently scanned in this same material and found to exhibit have the two C (or Copper) and four S texture variants as the preferred orientations after recrystallization. Very little of the cube orientation is evident in Figure 3.7(e). A similar region was examined for material annealed at 600°C and was found to have a sharpened C and S variants and, again, almost none of the cube orientations, seen in Figure 3.7(f).

53

These results are consistent with other published recrystallization texture data for pure copper [Ref. 135].

The disorientation distributions for the rolled and annealed conditions were also investigated and the results are presented in Figure 3.8. A predominantly recovered state is indicated in Figure 3.8(a) for material annealed at 150°C for 5hrs by the large number of low-angle boundaries. Recrystallization but with little grain growth is evident in (b) and (c) for material annealed at 200°C and 300°C, respectively, by the appearance of a more random distribution and the large high-angle peak resulting from annealing twins. The effects of the preferred recrystallization orientations on the disorientation distributions can be seen in the higher temperature anneals of 450°C and 600°C in (d) and (e), respectively, along with the retention of the annealing twins.

Tension tests were conducted at either 150°C or 250°C, and at a constant nominal strain rate of 10^{-3} sec^{-1} in order to investigate the effects of uniaxial elevated temperature deformation on microstructure and, especially, on the texture. These deformation temperatures were selected to be either below or above the recrystallization temperature for this material, and grain growth following recrystallization was avoided by conducting tensile deformation at 250ºC. The stress-strain data are illustrated in Figure 3.9 for each condition. The material deformed at 150°C exhibited a peak in flow stress at a strain of about 0.02, followed by strain softening accompanied by diffuse necking. Localized necking began at a strain of about 0.12 and was followed by failure. The material deformed at 250ºC exhibited a much reduced yield strength and therefore substantial strain hardening and elongation prior to the onset of necking. Uniform elongation for material deformed at 250°C corresponded to a true strain of approximately 0.45.

Microstructure and texture data for tensile deformation parallel to RD at 150°C are presented in Figure 3.10. This sample was deformed to failure and diffuse necking had commenced at ~0.02 plastic strain. Comparison of Figure 3.10(a) to Figure 3.5(a) reveals that deformation results in a more nearly equi-axed fine structure. The deformation texture of the as-rolled material, or of the rolled and annealed material, is still evident, as seen in Figure 3.10(b). The characteristic low-angle peak in the disorientation distribution for a deformation-induced microstructure is seen in Figure
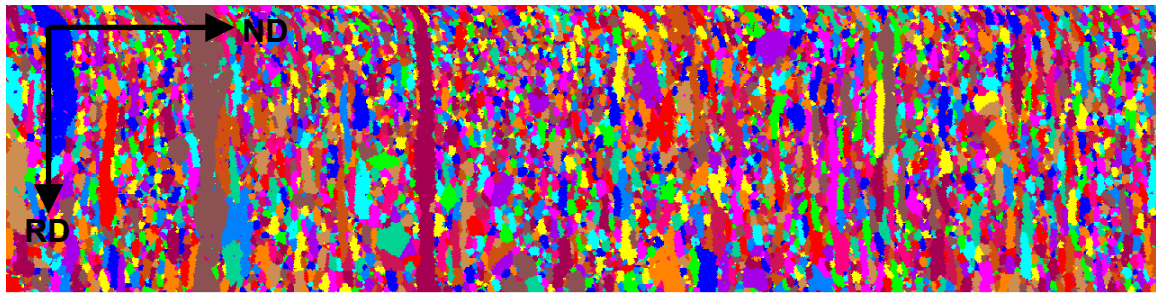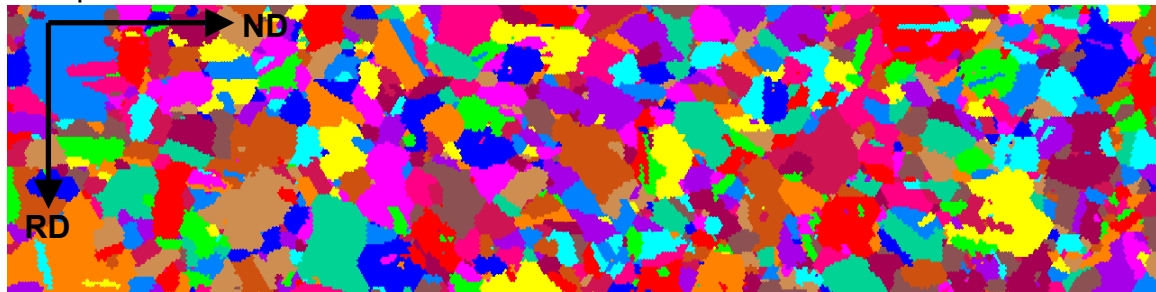
Figure 3.5. OIM grain maps, with a 2° grain boundary tolerance, for pure copper after rolling to $\varepsilon_{true}\sim 2.5$ and annealing for 5hrs. at (a) 150°C, the deformation microstructure is retained; (b) 200°C, recrystallization has occurred; (c) 300°C, little grain growth is apparent; and (d) 450°C, showing substantial grain growth.

3.10(c). Examination of the highlighted IQ map in Figure 3.10(d) reveals that the grains
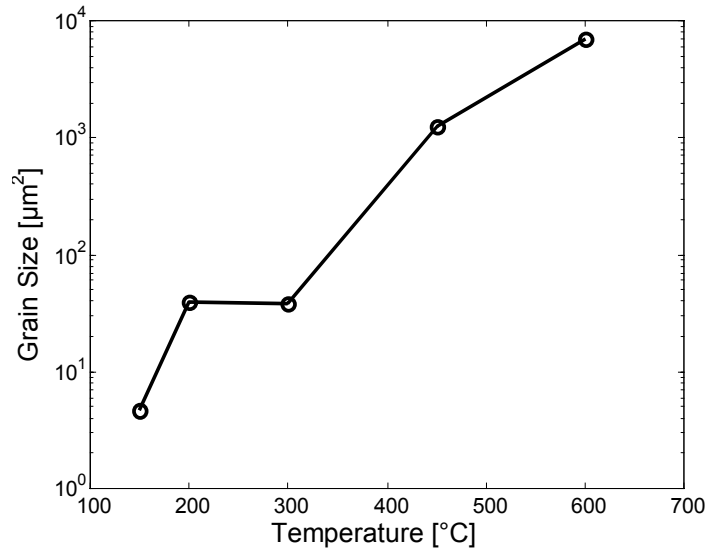
Figure 3.6. Area weighted average grain size [μm^2] of pure copper after rolling to ε_{true}~2.5 and annealing for 5hrs at various temperatures.

still tend to be elongated in the RD, and the banding of the structure developed during rolling and retained during annealing alone is also retained during deformation. High-angle boundaries separate the variants of the β fiber. Altogether these data indicate the predominance of recovery during deformation of the material under these conditions. The band structure is retained and the bands are similar in thickness as those seen in material in the as-rolled condition {Figure 3.3(b)}. A build-up of low-angle boundaries within the bands is evidenced by the more nearly equi-axed appearance of the grain map in Figure 3.10(a). Low-angle boundaries of > 2° disorientation will give a color change in the OIM grain map and so the more equi-axed structure after deformation may reflect a build-up of dislocations within boundaries transverse to the RD. It should be noted that a gradual lattice curvature resulting in a build up of disorientation over a long range may not be detected in grain maps with a 2° tolerance angle.

Tension tests were also conducted to failure at 10^{-3} sec^{-1} and 250°C with the tensile axis aligned with RD. Elongation to the onset of necking was ~57% ($\varepsilon_{truePLASTIC}$~0.45). The resultant microstructure, seen in Figure 3.11(a), is similar to that produced during static annealing. However, the weak texture of the recrystallized condition has been replaced by a double fiber texture having <002> or <111> components (where the notation is <direction aligned with the fiber axis>). Grains having

56

orientations corresponding to either of these two fibers have many equally stressed slip systems under uniaxial tension. There are six equally stressed <110>{111} fcc slip systems for the <111> fiber and eight equally stressed <110>{111} fcc slip systems for the <002> fiber orientation. Grains having either of these orientations will therefore exceed the Taylor requirement of at least five slip systems for compatible deformation [Ref. 40]. The peak at 60° in the disorientation distribution, Figure 3.11(c), can be attributed to annealing twins. Comparison of the highlighted IQ map, Figure 3.11(d), to the unique grain color map of Figure 3.11(a) reveals that the (sub)grains form clusters that are contained within a fiber and the (sub)grains are separated by a low-angle boundary, highlighted in green, thus resulting in the low-angle peak in (c). The high-angle boundaries seen in (d) are generally the boundaries between the grains oriented in one or the other of the two fibers. It should be noted that the disorientation distribution for an ideal, single-component fiber texture has a constant number fraction equal to 0.077. Thus, there is a statistical probability that some high-angle boundaries will always be present even with such a fiber texture.
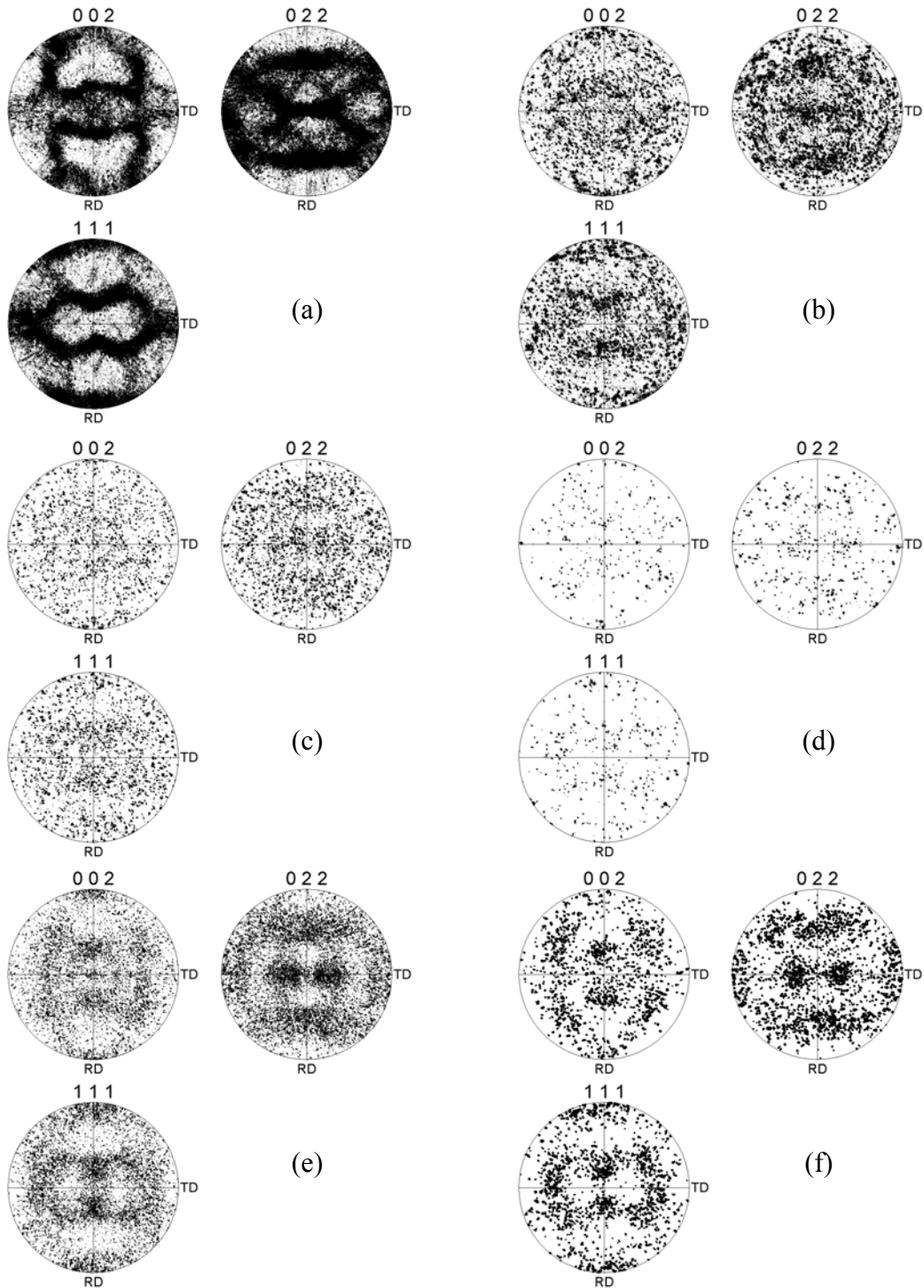
Figure 3.7. Discrete pole figures corresponding to Figures 3.4(a)-(d) for pure copper after rolling to $\varepsilon_{true}\sim2.5$ and annealing for 5hrs. at (a) 150°C, the deformation texture is retained; (b) 200°C; (c) 300°C; and (d) 450°C, all showing a diffuse deformation texture. Discrete pole figures from a 1mm X 1mm area investigated for the rolled copper after a 5hr. anneal at (e) 450°C and (f) 600°C showing remnants of the deformation texture with an increased concentration near the C texture orientations.
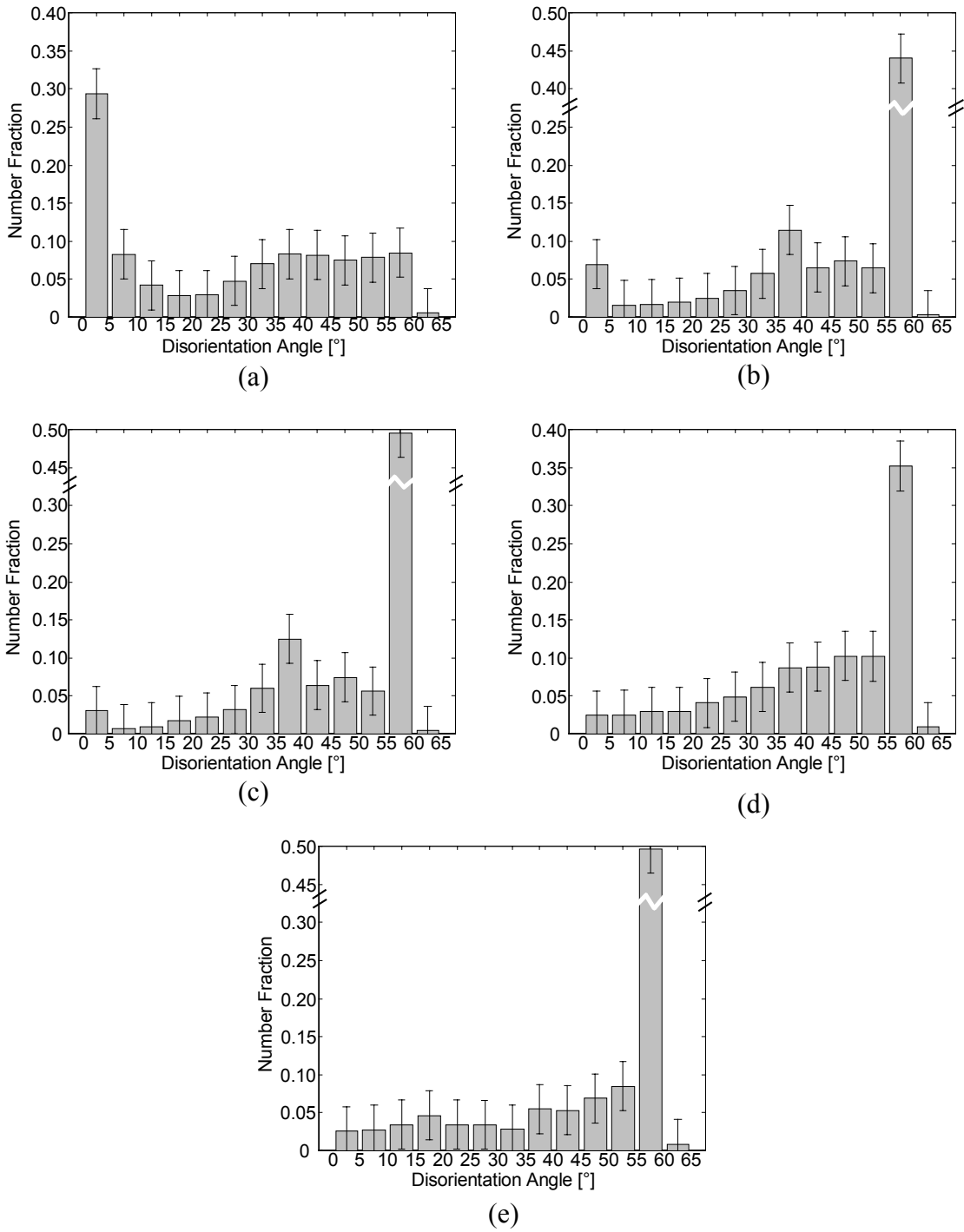
Figure 3.8. Disorientation distributions for pure copper after rolling to ε_{true}~2.5 and annealing for 5hrs at (a) 150°C showing a deformation induced distribution with many low-angle boundaries; (b) 200°C, (c) 300°C, (d) 450°C and (e) 600°C all showing evidence of recrystallization.
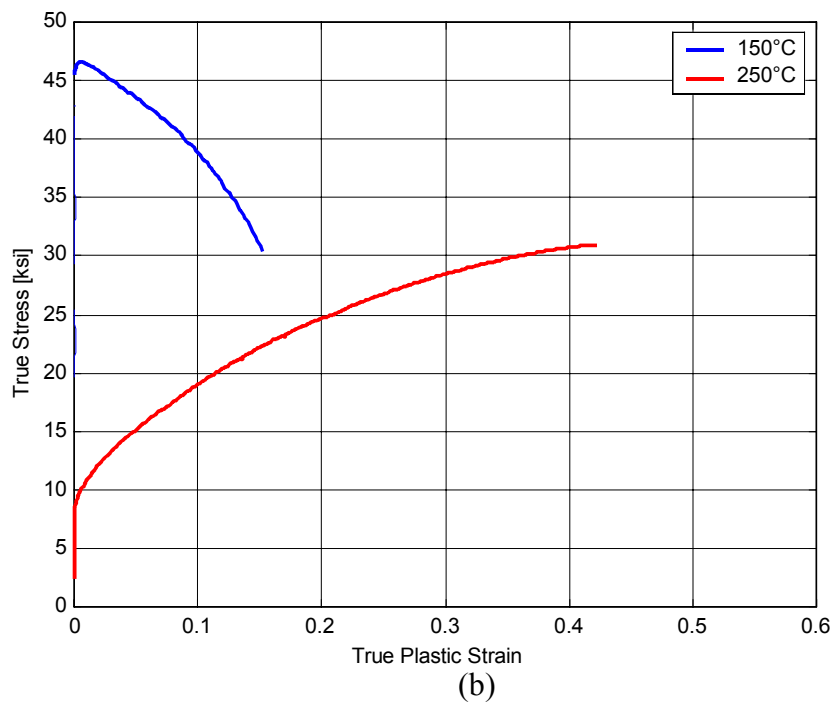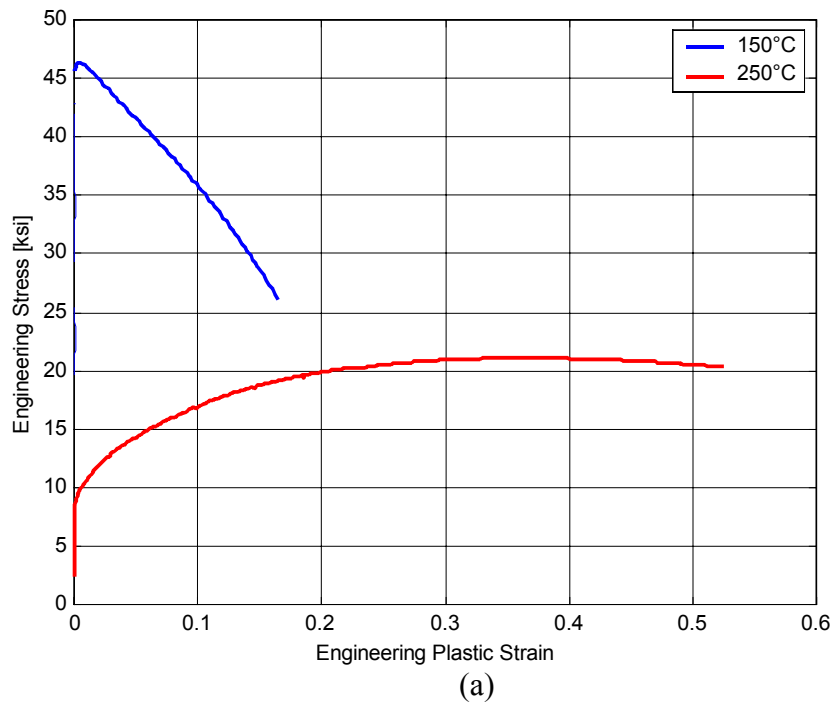
Figure 3.9.   Stress-Strain plots for pure copper deformed at 10^{-3} sec^{-1} at constant temperatures.   In (a), the engineering stress-strain curves associated with plastic deformation are presented for 150°C and 250°C; in (b), the true stress–true plastic strain curves are presented for the same temperatures.

60

D. DISCUSSION

1. As-Rolled Pure Copper

As-rolled copper exhibits elongated grains and banded microstructure as well as the presence of a distinct deformation texture; such a microstructure and texture are characteristic of fcc metals deformed by rolling at low temperatures [Refs. 66-67]. Within the tolerances employed in the orientation highlighting, the lattice orientation of the bands tends to alternate between the two symmetric β fiber orientations during a traverse along the ND. Then, the high-angle boundaries tend to separate bands corresponding to the variants of the β fiber. The thickness of the bands is ~5μm based on the intersections of high-angle interfaces when traversing in the normal direction (ND).

A more complete analysis of deformation banding and the stability of the microstructure and texture will be treated in a subsequent chapter. Briefly, the presence bands having lattice orientations corresponding to the alternating variants of the same texture component will allow plane strain deformation on a macroscopic level while requiring fewer slip systems to be active within an individual band during rolling deformation. This is less than the five independent slip systems required by the Taylor criteria for compatible plastic deformation [Ref. 40]. However, by arranging deformed and elongated regions belonging to the entire β fiber in an alternating pattern, the residual shear terms in each variant average out and a region having such a pattern may deform macroscopically in plane strain.

Grain subdivision, with lattice rotation toward a β fiber texture variant orientation on one side of a developing boundary and a different β fiber variant orientation on the opposite side of the boundary, would lead eventually to the microstructure illustrated in the OIM data of Figures 3.2 and 3.3. Thus, a deformation banding model for the deformation microstructure of an fcc metal includes grain subdivision during the deformation processing with the development of bands of lattice orientations that alternate between various β fiber variants of the deformation texture. The bands that are apparent in Figure 3.2(a) are ~5μm in thickness, which is approximately the thickness expected if the starting grain diameter is ~50μm and rolling reduced the thickness by ~92% (ε_{true}~2.5). However, investigations into deformation banding have generally

shown that the process of grain subdivision begins at much smaller strains and involves formation of several bands within each prior grain [Refs. 32-37]. The prior boundaries are indistinguishable in Figure 3.2(a) and so it would be necessary to examine the evolution of deformation banding during rolling in order to assess the interaction between the bands and the prior grains.

2. As-Rolled and Annealed Condition

Results similar to those presented for as-rolled material were obtained following annealing below the recrystallization temperature (~200°C). Details will not be presented here and the results will be summarized; briefly, the band structure was essentially unaltered from that of the as-rolled condition although a more equi-axed cellular (sub)structure became apparent during annealing. The (sub)grains appear to be 1–2μm in size and can be observed in Figure 3.5(a). Thus, dislocation rearrangement has taken place and this is evident in the form of more distinct low-angle boundaries within each band. The large disorientations associated with interfaces between variants having β fiber orientations are still present after annealing. These high-angle boundaries are a direct result of the prior rolling deformation and did not develop during subsequent annealing of the material.

Annealing of the deformed copper above the recrystallization temperature resulted in nucleation and grain growth by long-range migration of high-angle boundaries. The retention of orientations associated with the prior rolling deformation is still evident at the highest annealing temperatures in this work. The absence of a large volume fraction of cube-oriented grains in this annealed copper may be attributed to a lack of suitable cube nuclei [Ref. 136]. Then, the retention and development of prominent C type orientations is observed [Ref. 67].

3. Deformation of a Banded Microstructure

After deformation the microstructure remains banded and the deformation texture is retained. The microstructure still includes high-angle interfaces between bands and a cellular structure within the bands. During deformation at temperatures below the recrystallization temperature, recovery-controlled rearrangement of dislocation structures and processes such as glide and climb allows the band or cell to remain in a stable

orientation. The major change in the microstructure is the increase in the population of sub-grain boundaries. The lattice orientation within the bands or cells on either side of such an evolving structure is envisioned to be unaffected during such a process, which is consistent with the stability of the texture.

Deformation occurring above the recrystallization temperature results in larger microstructural and microtextural changes in the material. The results (Figure 3.11) suggest that the deformation is predominately by dislocation deformation processes. Under dislocation creep conditions a distinct <111> fiber texture formed during deformation of a 5083 alloy, which had a fine, recrystallized grain size and a random initial texture after TMP to make this material superplastic. A weak <002> fiber was also reported [Ref. 137]. Examination of the discrete (002) and (111) pole figures in Figure 3.11(b) reveals that <002> and <111> fibers are both distinct. Texture modeling will be employed later in this study to examined texture evolution during uniaxial deformation of various initial textures.

THIS PAGE INTENTIONALLY LEFT BLANK

IV.   MICROSTRUCTURE OF ROLLED PURE ALUMINUM

A.   INTRODUCTION

Orientation Imaging Microscopy (OIM) data will be presented that demonstrates the presence of deformation bands but at a coarser scale than observed in the rolled copper portion of this research (Chapter III).   Nominally pure aluminum will be examined in the as-rolled condition and after subsequent annealing treatments.   High-angle boundaries will be shown to be the interfaces separating the symmetric variants of the β fiber in the as-rolled condition.

B.   EXPERIMENTAL PROCEDURES

The aluminum obtained for this study was commercially pure, nominally greater than 99% purity [Ref. 138].   This material was obtained in plate form, from which bars, 29.2mm square and 150mm in length, were machined.   Chemical analysis of the composition is provided in Table 4.1.   Recrystallization annealing was performed at 330°C ($0.64T_m$) for 1hr in air, with an additional 15min soak time to assure temperature equilibration.   The thin, protective oxide layer was not removed after annealing.   The initial thickness, t_o, prior to rolling, was 29.2mm.

Al	Si	Fe	Cu	Mg	Zn
99.72	0.04	0.20	0.01	0.01	0.02

Table 4.1. Composition (wt.%) for the as-received aluminum.

Rolling was conducted at room temperature ($\sim 0.31T_m$) with sufficient interpass time to allow the material to return to room temperature following heating due to adiabatic deformation during each rolling pass. The rolling schedule corresponding to a reduction of 0.1 (true strain) per pass.   The aluminum was rolled to $\varepsilon_{true} \sim 2.5$ for comparison with the copper data that was presented in Chapter III. A sample of the rolled aluminum was also subsequently annealed at 330°C for 5hr., again for comparison

with the copper and with accepted recrystallization textures [Ref. 67]. Sample preparation consisted of mechanical polishing outlined in Chapter II. SEM samples were electropolished in a 20% perchloric acid, 80% ethanol electrolyte solution at 35VDC for 20sec. The electrolyte was initially cooled to –25°C.

C.   RESULTS

Data will be presented for pure aluminum in the following conditions: prior to rolling; as-rolled; and rolled and annealed.

Figure 4.1 represents data from pure aluminum after the initial annealing treatment at 330°C for 1hr. Figure 4.1(a) is an OIM unique grain color map with a tolerance angle set to 2°. This map includes superimposed IQ gray tones. The average grain diameter was found to be ~100μm, and, following the work of Duggan and Lee [Ref. 32], should be sufficient to support the formation of deformation bands upon rolling. The discrete pole figures in Figure 4.1(b) show the presence of a weak cube texture, which is common in recrystallized aluminum [Ref. 67]. The disorientation distribution in Figure 4.1(c) is consistent with the presence of a weak recrystallization texture and appears to consist of a random disorientation component (as defined by MacKenzie [Ref. 135]) with additional populations of low (0˚-10˚) and high (55˚-65˚) boundaries.

Figure 4.2 illustrates the data obtained from the aluminum in the as-rolled condition for a reduction corresponding to ε_{true}~2.5. A unique grain color map is presented in Figure 4.2(a), which shows the grain elongation in the RD. The discrete pole figures in Figure 4.2(b) depict an incomplete fcc deformation texture [Refs. 66-67, 126]. A complete deformation texture was found, but only when the sample was examined over distances in excess of 1000μm in ND. These data are not included here. The disorientation distribution, Figure 4.2(c), exhibits a low-angle peak at 0˚-5˚ that is consistent with the presence of subgrains in a deformation-induced microstructure. Figure 4.2(d) is an IQ map with superimposed highlighting (in red or blue) to illustrate the spatial distributions of the texture components belonging to the β fiber. The separate variants of the β fiber are highlighted in different colors. Finally, the white lines indicate
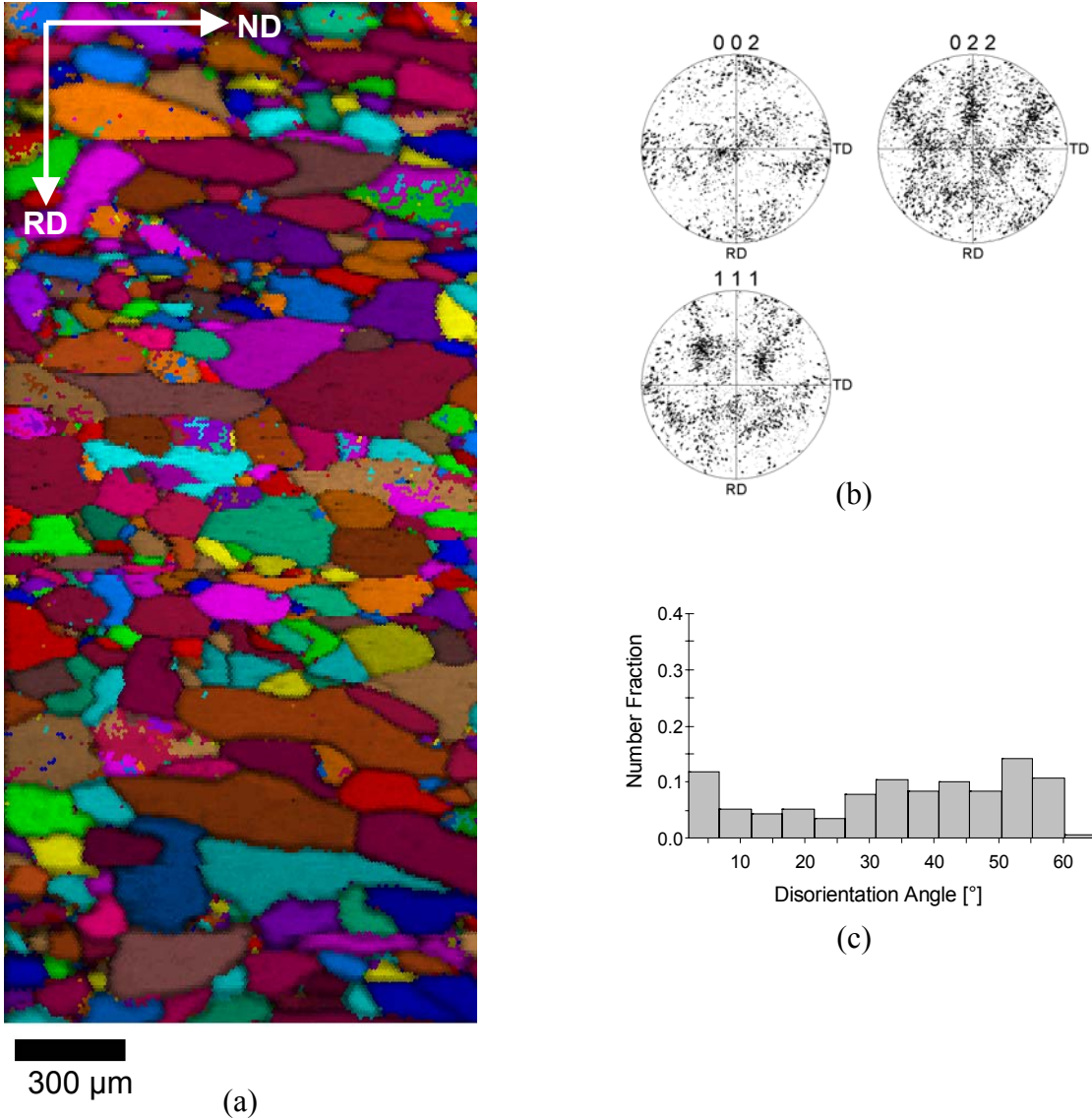
Figure 4.1. OIM data of pure aluminum after annealing for 1hr at 330°C prior to rolling. In (a), a unique grain color map with a grain tolerance angle of 2°; (b) discrete pole figures showing a weak cube recrystallization texture; and (c) disorientation distribution histogram. The average grain diameter is ~100μm.

the locations of boundaries of >50° disorientation. The high-angle boundaries tend to align with RD and to separate β fiber variants.

Annealing of this rolled aluminum was conducted at 330°C ($0.64T_m$) for 5hrs. A large area (1mm X 1mm) was examined and found to have prominent cube and weaker C texture components. Figure 4.3(a) is a unique grain color map showing a recrystallized grain structure with an average grain diameter ~50μm. The discrete pole figures in Figure 4.3(b) have been highlighted to show the cube (green) and two C (red or blue)
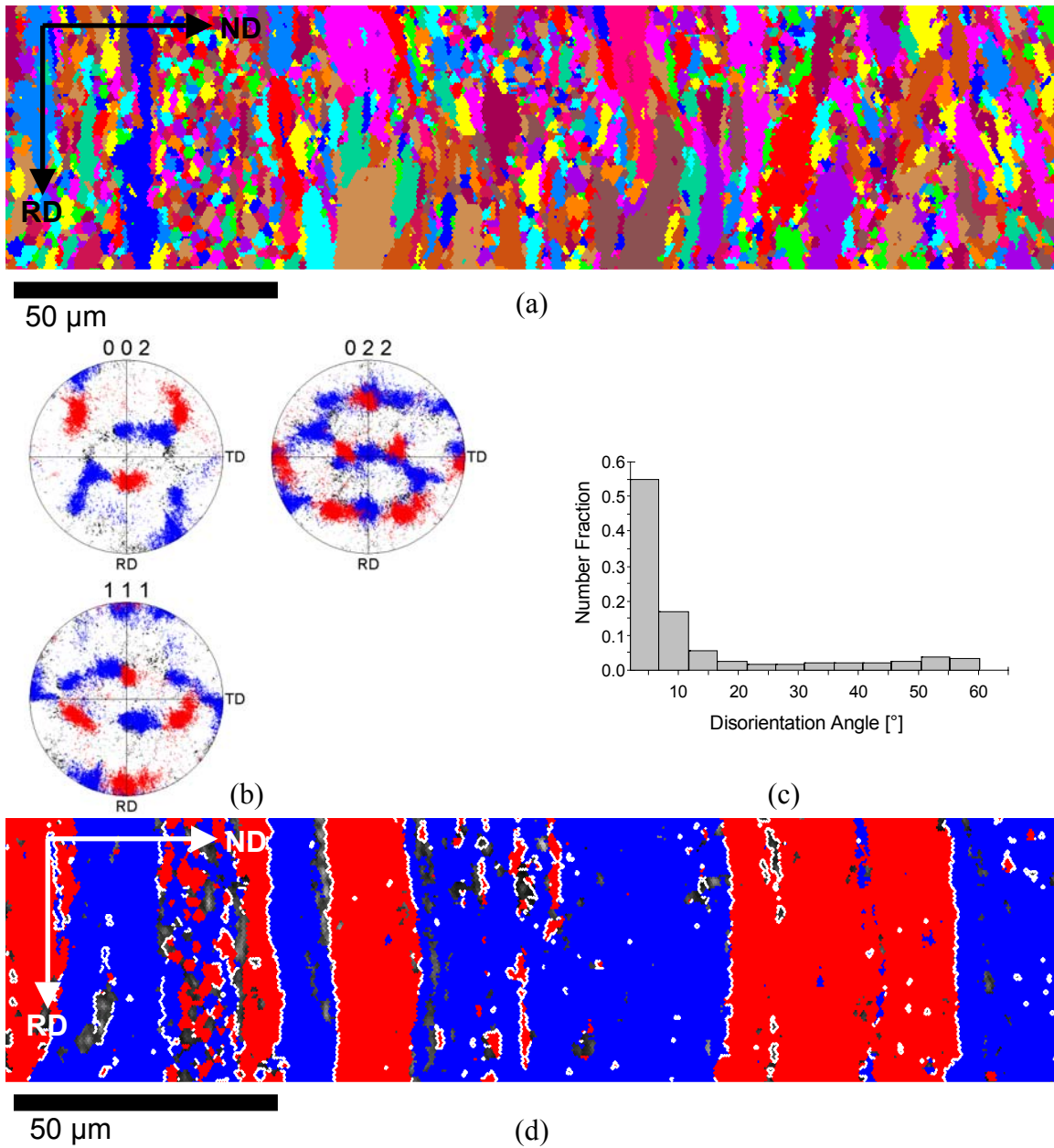
Figure 4.2. OIM data for pure aluminum after rolling to $\varepsilon_{true}{\sim}2.5$. In (a), unique grain color map with a 2° tolerance; (b) discrete pole figures with the present components of the symmetric β fibers highlighted in either blue or red; (c) disorientation histogram with the low-angle peak indicating a deformation structure; (d) IQ only map with the locations of the symmetric variants of the β fibers corresponding to the pole figures in (b), highlighted blue or red and white highlighting boundaries in excess of 50° disorientation. A complete deformation texture observed when traverse in excess of 1000μm in ND.

texture components. The cube component is generally expected after annealing aluminum [Ref. 67]. The positions of the texture components have been correspondingly

highlighted on the IQ map in Figure 4.3(c) along with the locations of the high-angle ($50°<\theta<62.8°$) boundaries, which have been highlighted in white. The high-angle boundaries are now seen to have no preferred alignment direction. The disorientation distribution histogram in Figure 4.3(d) is almost exactly that predicted by MacKenzie [Ref. 135].
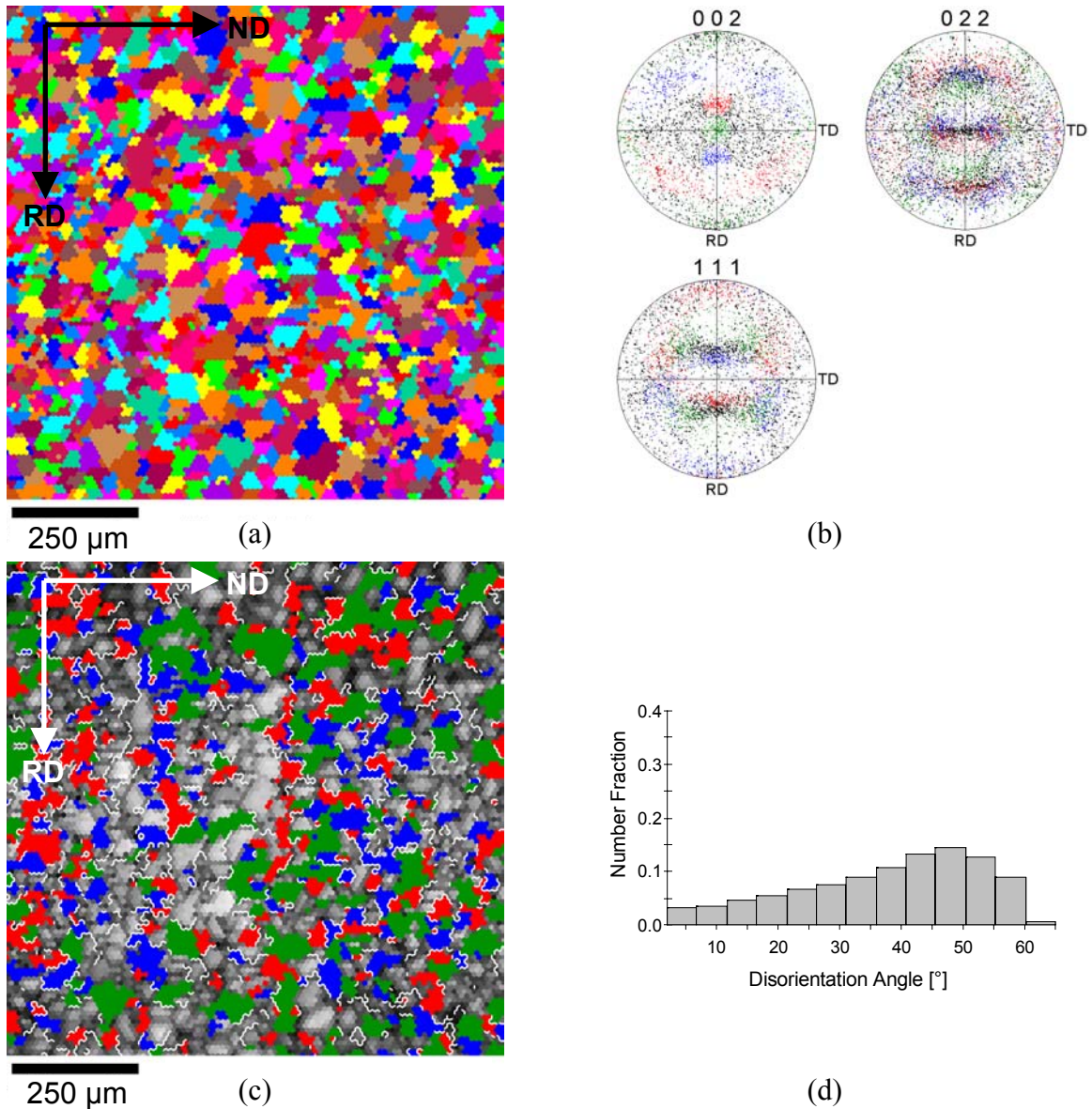
Figure 4.3. OIM data for pure aluminum after rolling to ε_{true}~2.5 and annealing at 330°C for 5hrs. In (a), unique grain color map with a 2° tolerance; (b) discrete pole figures with the symmetric variants of the C texture component highlighted in either blue or red and the cube component in green; (c) IQ only map with the locations of the symmetric C variants and cube component corresponding to the pole figures in (b), highlighted and white highlighting boundaries in excess of 50° disorientation; (d) disorientation histogram tending toward the MacKenzie distribution for random cubes.

70

D.   DISCUSSION

1.   As-Rolled Pure Aluminum

The as-rolled aluminum exhibits grain elongation in the rolling direction (RD) and a banded microstructure in which the bands are also aligned with the RD. A deformation texture which is characteristic of fcc metals deformed by rolling at low temperatures [Refs. 66-67, 126] is also evident although a complete and symmetric deformation texture is not observed unless areas extending at least 40% of the sample dimension along ND are evaluated. This is in contrast to the copper data of Chapter III. Complete rolling textures were observed in relatively smaller volumes and the thickness of the bands that correspond to the alternating variants of the β fiber is about 0.1 of the band thickness observed for the pure aluminum even though the rolling reductions were identical. However, the aluminum and copper data both include the alternating lattice orientation of the bands along the ND wherein the lattice orientation alternates between the orientations of the two symmetric β fibers, and that these symmetric variants of the β fibers are separated by a high-angle boundary.

The differences between aluminum and copper suggest that a deformation-banding model will have to include material-specific parameters that would affect the final band thickness for a given strain. These parameters should include a terms relating to the stacking fault energy of the material and a temperature dependent parameter relating the deformation temperature to the absolute melting temperature.

2.   As-Rolled and Annealed Condition

Following annealing of aluminum at a homologous temperature of $0.64T_m$ to the most severe annealing temperature of the copper study, also $0.64T_m$, a large volume fraction of cube oriented material was found to be present, which is expected for this material [Ref. 67].   Thus, this material exhibited the development of a cube recrystallization texture with the retention of diffuse preferred orientations near the C component variants. Finally, examination of the pole figures of Figure 4.3(b) and disorientation histogram in Figure 4.3(d) reveals the presence of a large random component to the recrystallization texture.

THIS PAGE INTENTIONALLY LEFT BLANK

V.   MICROSTRUCTURE OF ROLLED SUPRAL2004

A.   INTRODUCTION

Highly refined and stable grain sizes and grain boundaries that resist tensile separation during elevated temperature deformation are required for superplasticity. In wrought aluminum alloys, grain refinement for superplasticity can only be achieved by deformation and recrystallization. At least two distinct thermomechanical processing (TMP) routes have been developed to enable superplastic response in aluminum alloys. The current understanding of the microstructural transformations associated with such TMPs has recently been reviewed [Refs. 64, 137]. The process of interest in the present work involves the continuous recrystallization (CRX) reaction in Supral 2004 [Refs. 139-140]. For as-cast material, the TMP consists of severe deformation by hot and cold rolling under conditions that allow the retention of fine second-phase particles of the Al_3Zr phase. These particles hinder dislocation rearrangement and the formation and migration of boundaries, thereby leading to a predominance of recovery in the continuous recrystallization reaction [Ref. 68]. Materials that undergo continuous recrystallization, such as Supral 2004, generally retain well-defined deformation textures and develop bimodal disorientation distributions [Refs. 69-71]. The phenomenon of deformation banding has received only limited attention in alloys of high solute content and its role in the development of grain boundaries during continuous recrystallization has not been addressed.

Orientation Imaging Microscopy (OIM) and transmission electron microscopy (TEM) data will be presented that demonstrates the presence of deformation bands in as-processed and processed and annealed Supral 2004. The high-angle boundaries that support superplasticity in this material will be shown to form as the interfaces between bands having lattice orientations corresponding to the symmetric variants of the main texture component. This work provides support for the role of deformation banding formation of high-angle boundaries during continuous recrystallization of superplastic aluminum alloys such as Supral 2004. Furthermore, the macro- and micro-texture data as well as the disorientation results cannot be interpreted in terms of conventional models

for development of superplastic microstructures in such alloys [Refs. 141-143]. Finally, the DB model will be extended to interpret the response evolution of such a banded microstructure during deformation within the superplastic regime.

B.   EXPERIMENTAL PROCEDURES

Supral 2004 material was obtained as 2.0mm sheet in the as-processed condition from Superform-USA, Inc. Chemical composition data are provided in Table 5.1. Details of processing are proprietary; chill casting is employed to avoid formation of primary Al_3Zr and subsequent homogenization treatments are conducted at lower than normal temperatures to inhibit precipitation of Zr. Deformation processing by hot rolling to a strain of about 2.0 is then followed by cold cross rolling to an additional strain of about 1.0. The as-processed material exhibits a tensile elongation of about 800% upon heating and straining at 450°C and strain rates up to 10^{-2} sec^{-1}.

	Cu	Zr	Fe	Si	Zn	Mn	Mg	Ti	Li	Al
Cast # 2004F013	5.66	0.37	0.14	0.06	0.29	0.013	0.003	0.005	0.0001	Bal.

Table 5.1. Alloy composition (wt.%) for the as-received Supral 2004

Tensile coupons with 12.5mm gage length were machined from the rolled sheet with the tensile axis parallel to either the final cold rolling direction of the sheet (RD) or the final transverse direction (TD). Tensile tests were performed along at a constant strain rate of 10^{-2} sec^{-1} at 450ºC, ensuring superplastic deformation. Sample preparation consisted of mechanical grinding presented in Chapter II. The final step for SEM examination consisted of electropolishing with perchloric acid (20%) and ethanol (80%) solution at 35V for 20s cooled to an initial temperature of -25ºC. The TEM samples were thinned to perforation using the Fischione Twin Jet Polisher operated at 15V with a 33% nitric acid and 67% methanol electrolyte solution cooled to -25°C.

C.   RESULTS

Microstructural and texture data for Supral 2004 will be summarized for material in the following conditions: as-received; annealed at 450˚C for 6 hours; and deformed in the superplastic regime at 450˚C and a strain rate of 10^{-2} sec^{-1} to either 110% or 200% elongation in the RD, and 107% in the TD. Figure 5.1(a) illustrates the as-received microstructure of this material. This OIM grain map reflects severe cold deformation in the final stage of the TMP [Refs. 144-146] and the formation of elongated grains aligned with the RD. A coarse dispersion of $\theta(Al_2Cu)$ particles ranging in size from 0.5μm to 4μm is also evident where there is low Kikuchi image quality (i.e. dark gray regions). The particles also tend to be elongated in the rolling direction. The OIM grain maps are consistent with previously published backscatter electron micrographs [Refs. 145-146]. Figure 5.1(b) illustrates the bimodal distribution of disorientations.

In Figure 5.1(c), the pole figure data are plotted and orientations that are within 15˚ of each of the two variants of the main B texture component, which are $(110)[1\bar{1}2]$ and $(011)[2\bar{1}1]$, are highlighted in either red or blue. Figure 5.1(d) is an alternative representation of the grain map of Figure 5.1(a) in the form of an image quality (gray tones) map that has been plotted with the highlighted locations corresponding as well with these same two variants of the B texture component. Altogether, these data show that the microstructure is formed by adjacent bands of alternating lattice orientations corresponding to the two variants of the main, B texture component that are separated by distinct high-angle ($50°>\theta>62.8°$) boundaries also highlighted in Figure 5.1(d), or by a narrow transition region. The transition region may represent an area of continuous lattice curvature associated with dislocations arrays of like sign, or this region may contain smaller, discrete cells separated by low-angle boundaries. The limit of resolution of the OIM technique is approximately 0.2μm and so definite conclusions cannot be made regarding the details of the transition region. However, as indicated in Figures 5.1(e) and (f), which were obtained by linear queries in the normal direction (ND) at positions 1 and 2 on Figure 5.1(d), the lattice orientation varies throughout these regions and tends to be substantially different than either texture variant.
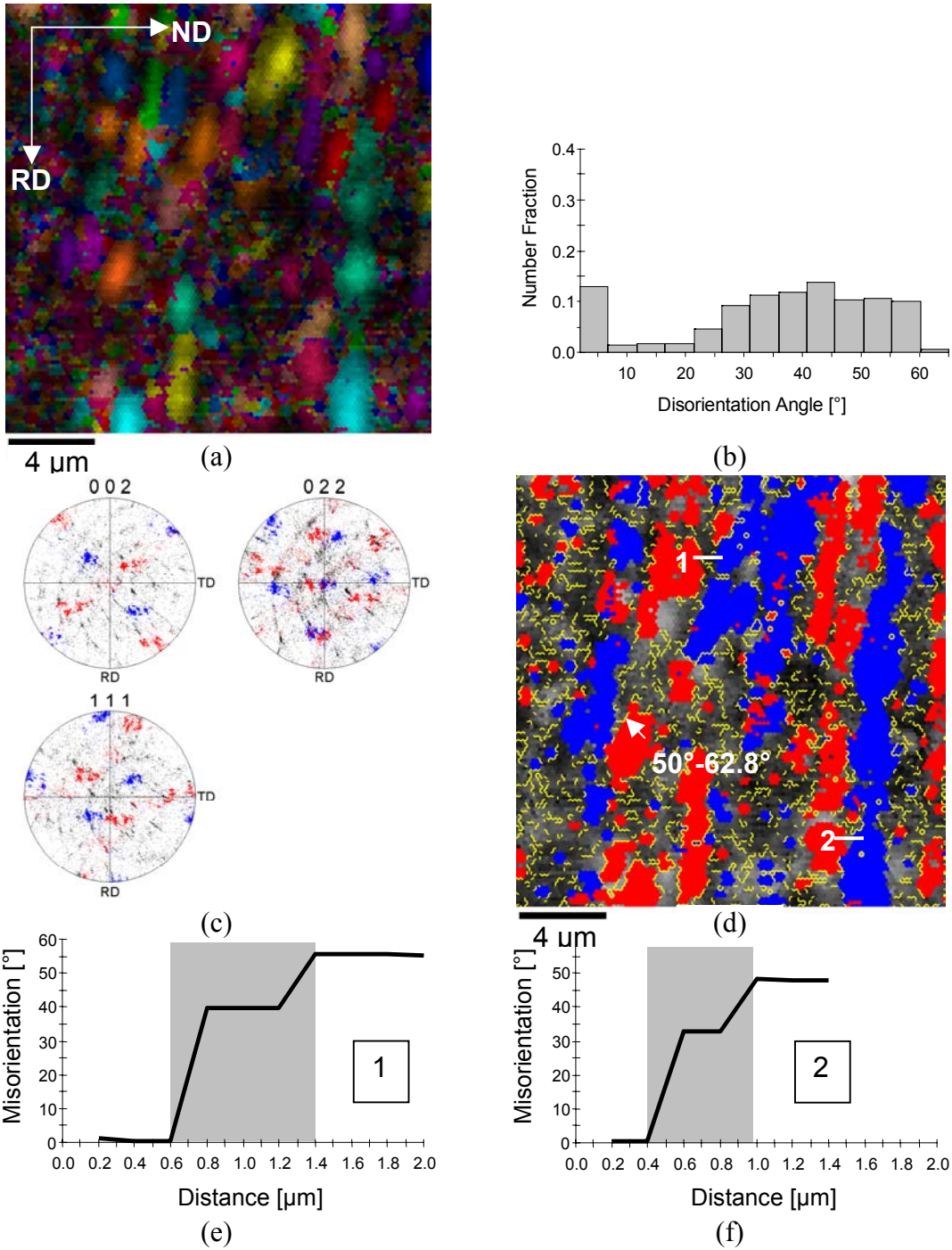
Figure 5.1. (a) An OIM unique grain color map, wherein neighboring pints of disorientation <2° are assigned the same grain color, with superimposed image quality. (b) Disorientation histogram for the region examined. (c) Discrete pole figures, with the symmetric variants of the B texture component highlighted in either red or blue. (d) IQ only map with the positions of the symmetric variants highlighted corresponding to the pole figure, in addition to boundaries >50° disorientation are highlighted in yellow. (e) and (f) are misorientation plots corresponding to the linear traverses, 1 and 2, seen in (d).

Annealing of the as-received material for 6hrs at 450˚C resulted in the development of a uniform, fine (sub)structure, of 2.0-2.1μm mean linear intercept, and which exhibited slight elongation in the rolling direction. Microtexture data indicated that the deformation texture of the as-received material remained stable during this annealing treatment and no new components appeared. While several components along the β-fiber, including S and {123}<634>, were present, the Brass (B) component, {110}<211>, and nearby orientations related to B by rotations about the sheet normal (i.e. orientations lying along the α-fiber) were most prominent and will be of particular concern here.

Figure 5.2(a) illustrates that the microstructure of the material after an annealing treatment at 450°C for 6hrs consists of a (sub)grain structure that is slightly elongated in the RD and has a mean linear intercept of about 2.0μm. The pole figure data are plotted and orientations that are within 15˚ of each of the two variants of the main B texture component, which are $(110)[1\bar{1}2]$ and $(011)[2\bar{1}1]$, are highlighted in either red or blue in Figure 5.2(b). A predominant B component is evident in the (220) pole figure in the concentration of orientations along ND and in the (111) pole figure in the concentration of orientations near the transverse direction (TD). The corresponding IQ grain map, Figure 5.2(c), has been plotted with orientations that are highlighted corresponding as well with these same two variants of the B texture component in Figure 5.2(b). These data show that the microstructure is formed by adjacent bands of alternating lattice orientation corresponding to the two variants of the main, B texture component. The bands are elongated along the RD and have a width of about 3μm. The lattice orientation of the bands alternates along the ND according to the pattern ….. B_1, B_2, B_1, B_2, ..., where B_1 is $(110)[1\bar{1}2]$ and B_2 is $(011)[2\bar{1}1]$.
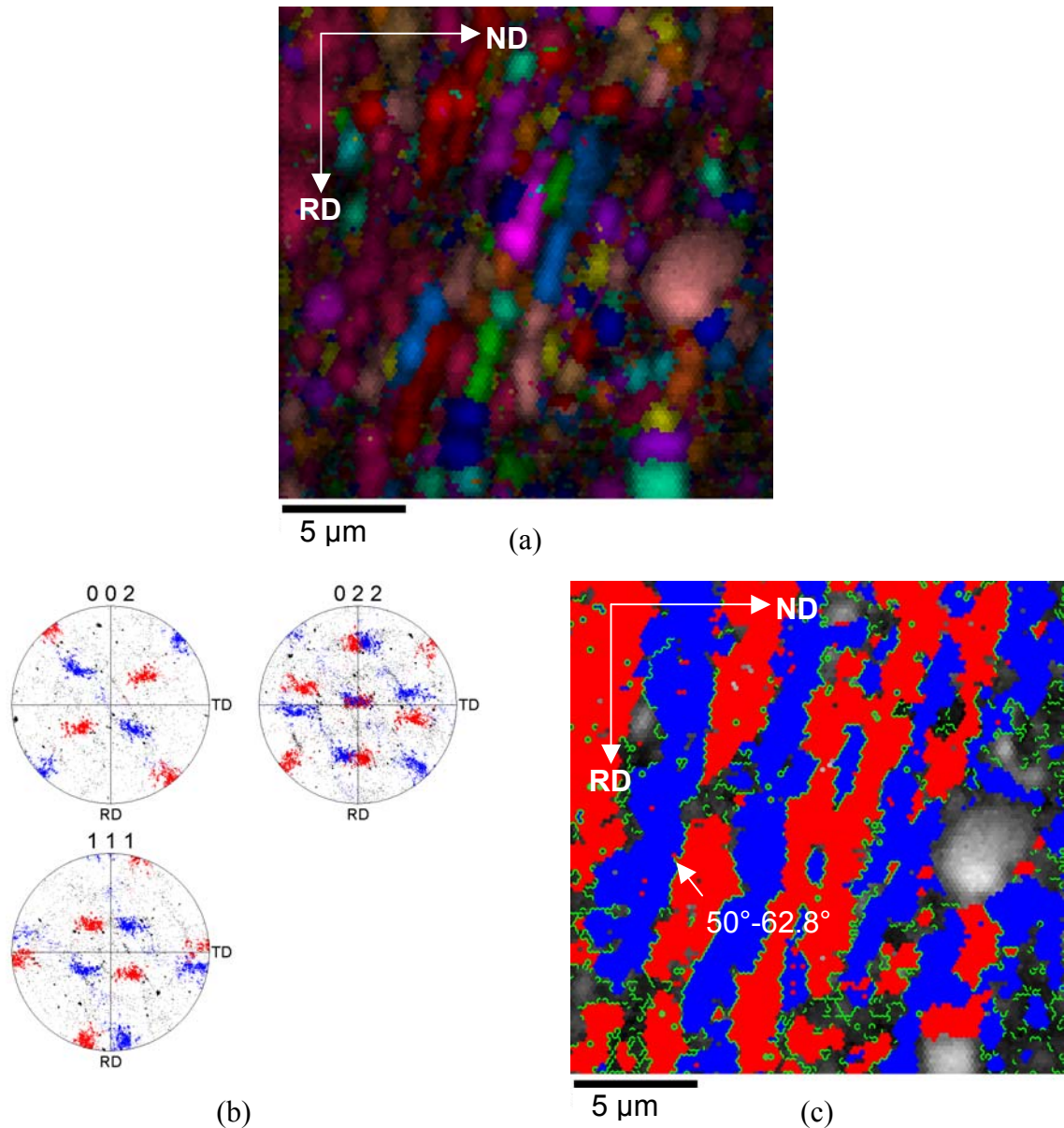
Figure 5.2. OIM data for Supral 2004 after annealing at 450°C for 6hrs. In (a), an OIM grain map with superimposed IQ. The pole figure in (b) has been highlighted in red and blue to correspond to the two B texture variants. An IQ only map in (c) is highlighted to show the positions of the variants and high-angle boundaries.

Also of note is the reduction in width of the transition regions, or even absence of such regions, separating the B texture components. Accordingly, the texture highlighted grain maps of this same region are presented with the high- (50˚-62.8˚) and low-angle (2˚-15˚) grain boundaries also highlighted in Figures 5.2(c) and 5.3(a) respectively. It can be seen that the high-angle boundaries tend to separate adjacent bands when the

transition regions are absent. The low-angle boundaries separate regions (cells) within those bands. It is also apparent that there are one to three cells along the width of each band, and the cells range in size from about 0.5μm to 2μm. The cell walls tend to be aligned mostly perpendicular to the RD while the high-angle boundaries tend to align with RD. When transition regions are present, as annotated in regions 1 and 2 of Figure 5.3(a), a linear traverse in the ND again indicates orientations that are rotated away from the main texture components, as shown in Figures 5.3(b) and (c).

Figure 5.4 illustrates the TEM investigations of the annealed material. The band structure is observed: the symmetric variants of the B-texture component are separated by

(a)

(b)

(c)
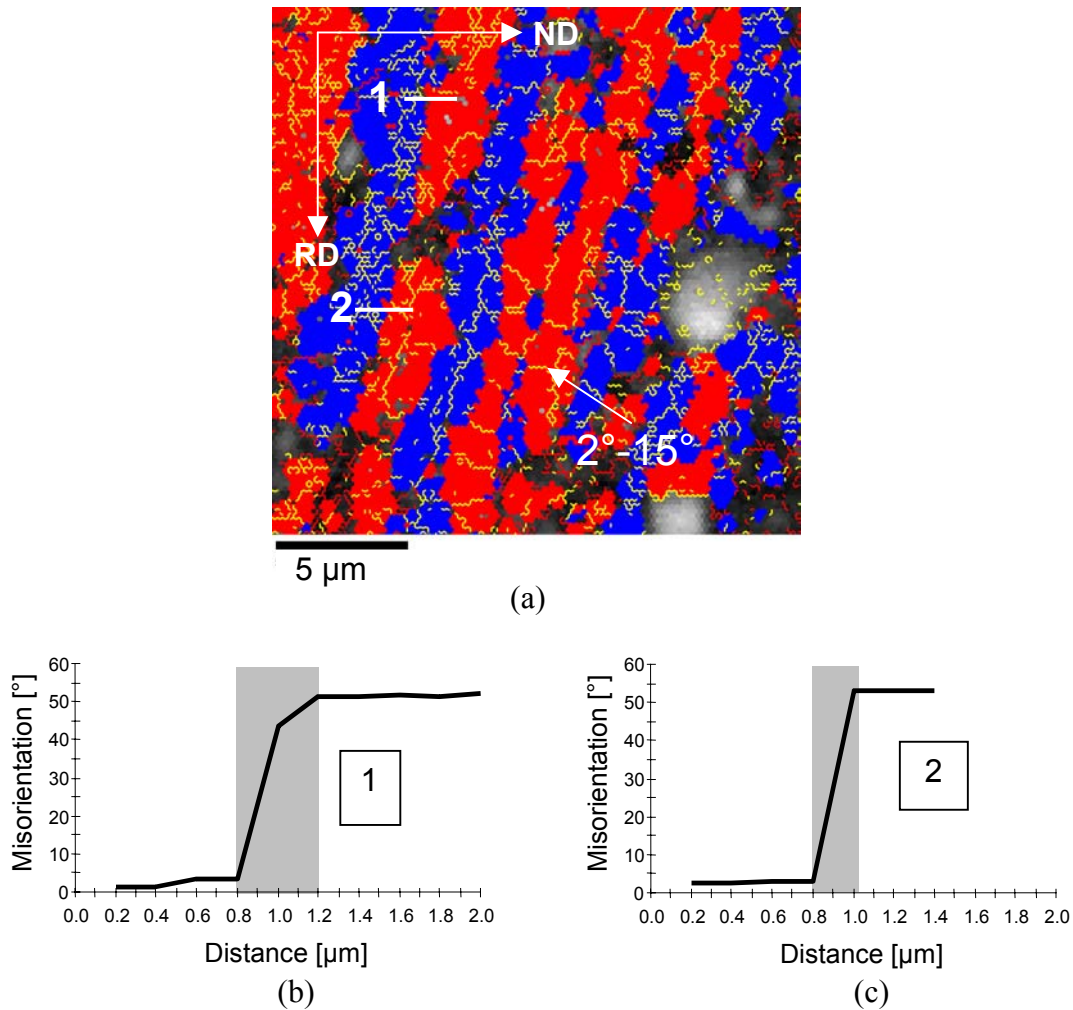
Figure 5.3. OIM grain map in (a) of the same area as in Fig. 5.2 with the low-angle boundaries highlighted in yellow. (b) and (c) are misorientation plots corresponding to the linear traverses, 1 and 2, seen in (a).
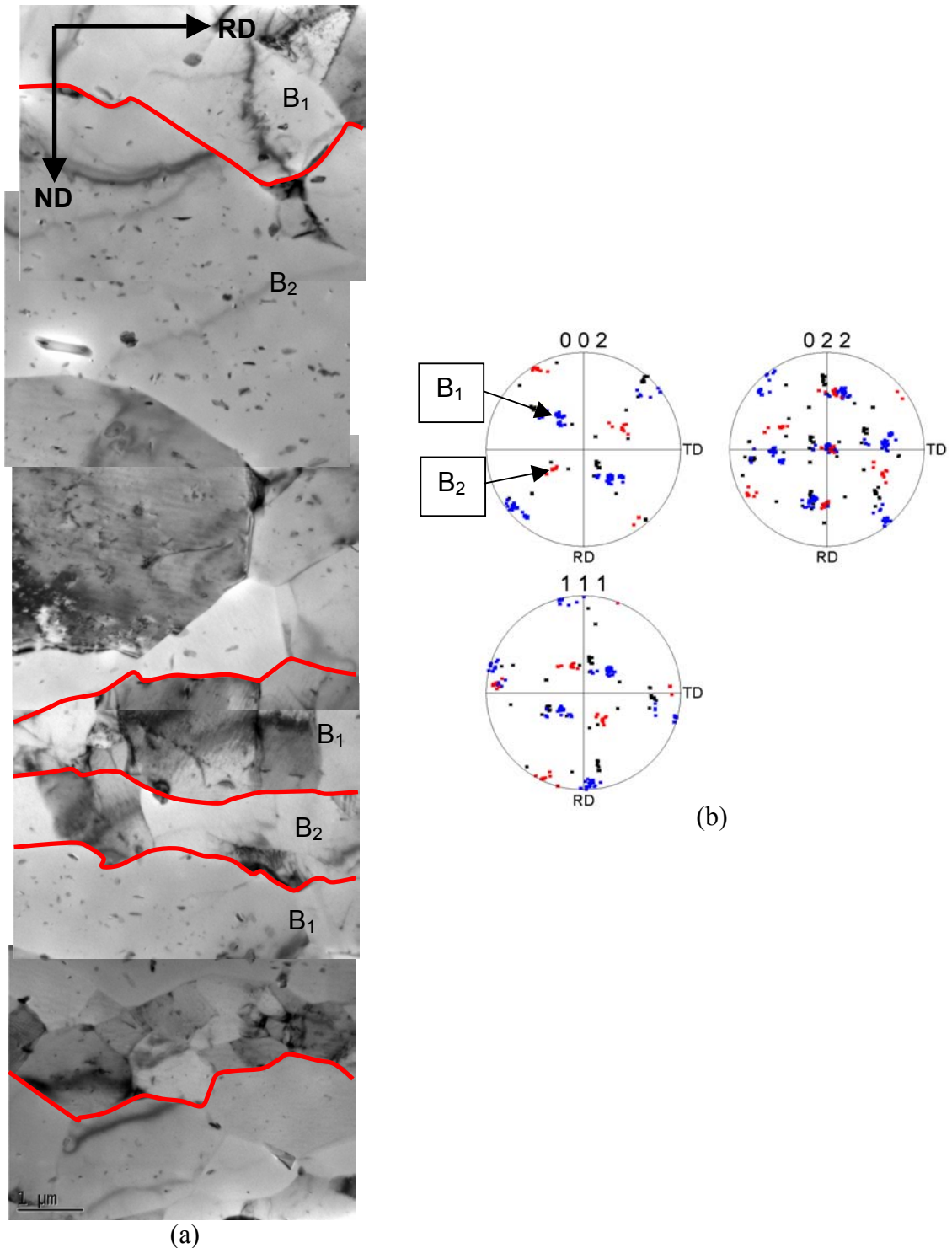
Figure 5.4. TEM montage in (a) of Supral 2004 after annealing at 450°C for 6hrs. The positions of the symmetric variants of the B texture corresponding to the highlighted discrete pole figures in (b) are indicated in (a) along with the high-angle (θ>50°) boundaries, indicated by red lines.

high-angle boundaries roughly aligned with the RD. These bands are of similar thickness as those apparent in the OIM investigation. The bands of Figure 5.4 range from 1-5μm in width and there is clearly a sub-structure within each band. The sub-structure comprises low-angle boundaries. Transition regions were not apparent readily in the region of the sample investigated.

A distinct bimodal distribution of grain-to-grain disorientation angles is presented in Figures 5.4(a) and (b). Figure 5.4(a) is data obtained by TEM investigation and Figure 5.4(b) by SEM methods. The significant difference in the lowest bin is due to the angular resolution afforded by CBED in the TEM. The population of boundaries of 0°-5° disorientation is larger than that reported previously for this material, but otherwise these data consistent with previous work [Refs. 144-145].
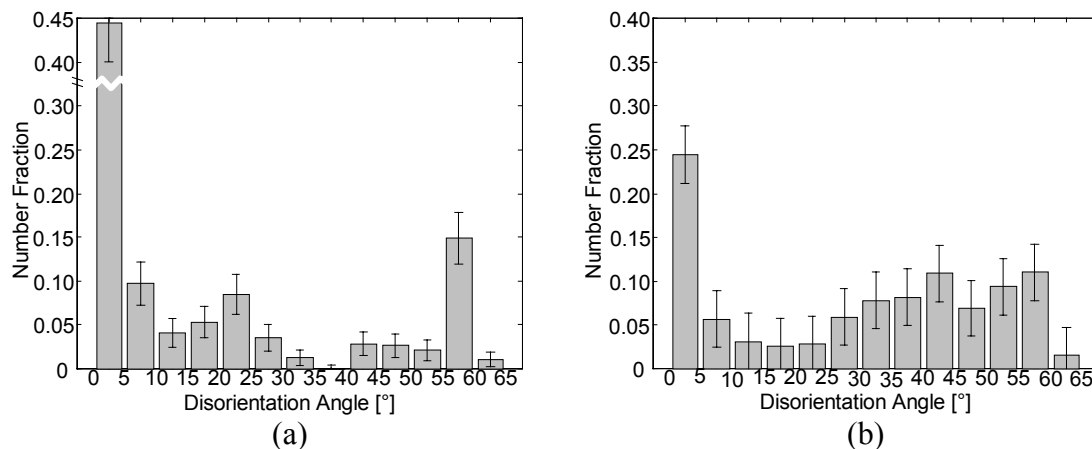
Figure 5.5.   Disorientation distributions from Supral 2004 after being annealed at 450°C for 6hrs from (a) TOCA in the TEM and (a) OIM in the SEM.

Deformation of as-processed material was conducted on samples at a strain rate of 10^{-2} sec^{-1} and at a test temperature of 450°C. The test coupons were machined such that the tensile axis during deformation was parallel to either the final processing cold rolling direction or transverse direction. Samples were tension tested to 110% and 200% elongation in RD and 107% in TD, which is substantially below the failure elongation of approximately 1000% for these conditions.

The OIM grain map for the sample elongated 110% in the RD is provided in Figures 5.6(a). The representative pole figures (highlighted in red and blue) and the IQ

the grain map of the 110% RD elongation study are provided in Figures 5.6(b) and (c), respectively. It should be noted that the size of the region investigated is larger than that in the cases of the as-received and annealed materials due to grain coarsening of the material at the elevated deformation temperature. Also apparent is the spreading of the orientations about the main texture components. The corresponding color-coded grain map in Figure 5.6(c) also has the high-angle grain boundaries highlighted. This map indicates that the bands evidently do not coarsen when compared to the as-received condition, but instead remain essentially the same in width. Transition regions are still evident. These transition regions (Figures 5.6(d) and (e)) may now be the result of the more random nature of the texture that is evident in the pole figures (Figure 5.6(b)). The TEM data also confirm the retention of the band structure, with high-angle boundaries separating the bands as seen in Figure 5.7. Second phase particles are also seen to lie along these high-angle boundaries. These results are consistent with a prominent contribution random grain rotation associated with deformation by grain boundary sliding.

The histograms presented in Figure 5.8, indicate a significant decrease in the relative number of low-angle grain boundaries from the as-received [5.12,5.13] and annealed conditions [5.15]. The TEM data {Figure 5.8(a)} illustrates the retention of the bimodal disorientation distribution while the SEM data indicate an increase in the relative number of grain boundaries that are oriented from 35˚-50˚ {Figure 5.8(b)}. It should be noted that the area investigated in the SEM in the RD is four times that investigated in the TEM. This peak in the SEM disorientation histogram is in the same range as predicted by MacKenzie for randomly oriented cubes [5.16]. This indicates a slight randomization of the texture due to deformation occurring by grain boundary sliding.

The sample deformed 107% in the TD was also characterized in a similar manner but with the exception of linear traverses. Figures 5.9(a)–(d) represent the unique grain color map, disorientation histogram, highlighted pole figures and IQ map with the high-angle boundaries highlighted in yellow. This condition differs slightly from the deformation condition aligned with RD in that a <111> is already nearly aligned with the
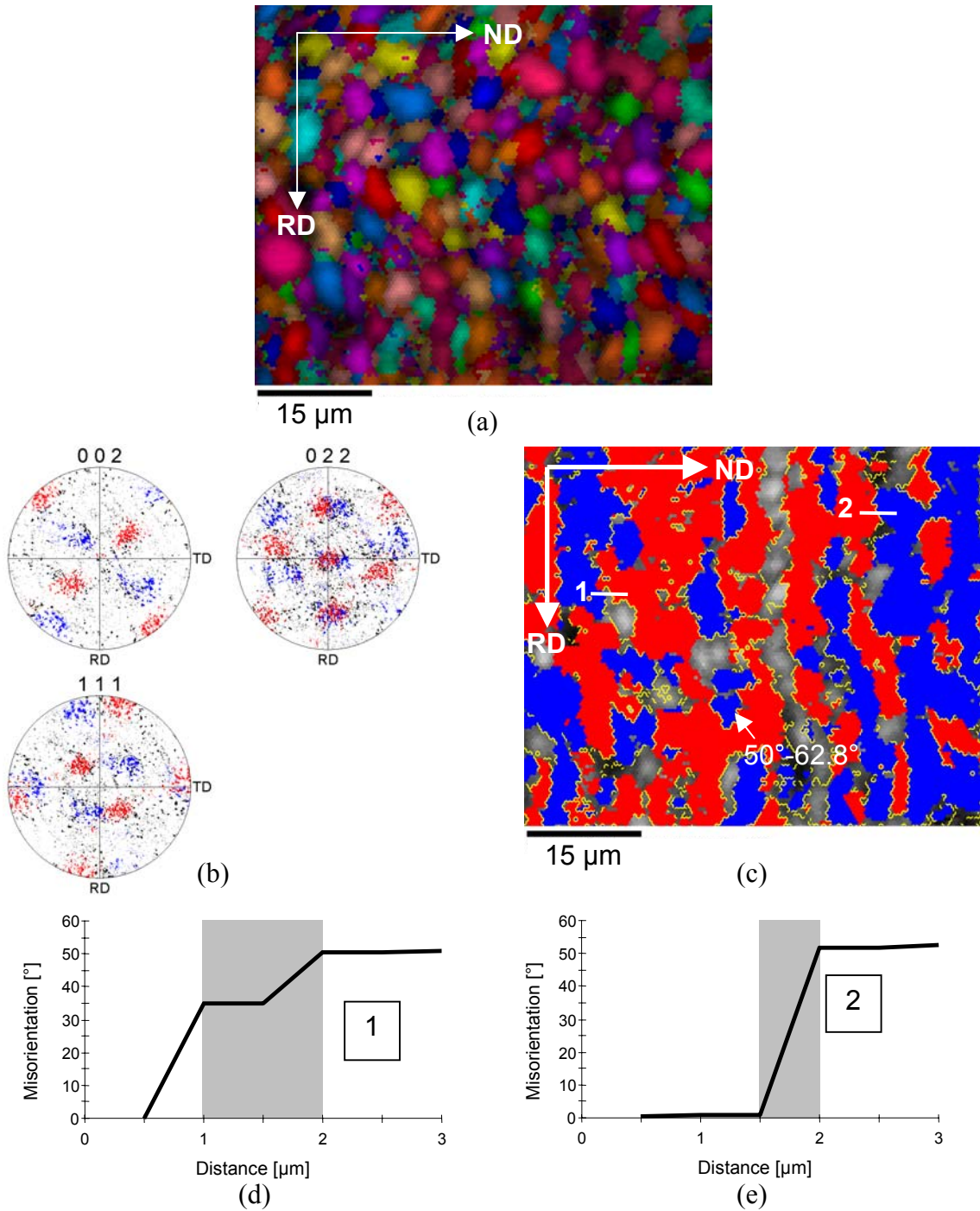
Figure 5.6. (a) OIM unique grain color map for Supral 2004 deformed to 110% elongation at 10^{-2} sec^{-1} and 450°C. (b) Discrete pole figures with the symmetric variants of the B texture highlighted in either red or blue. (c) IQ only map with the positions of the symmetric texture variants highlighted corresponding to the pole figure in addition to boundaries >50° disorientation are highlighted in yellow. (d) and (e) are misorientation plots at the positions labeled in (c).
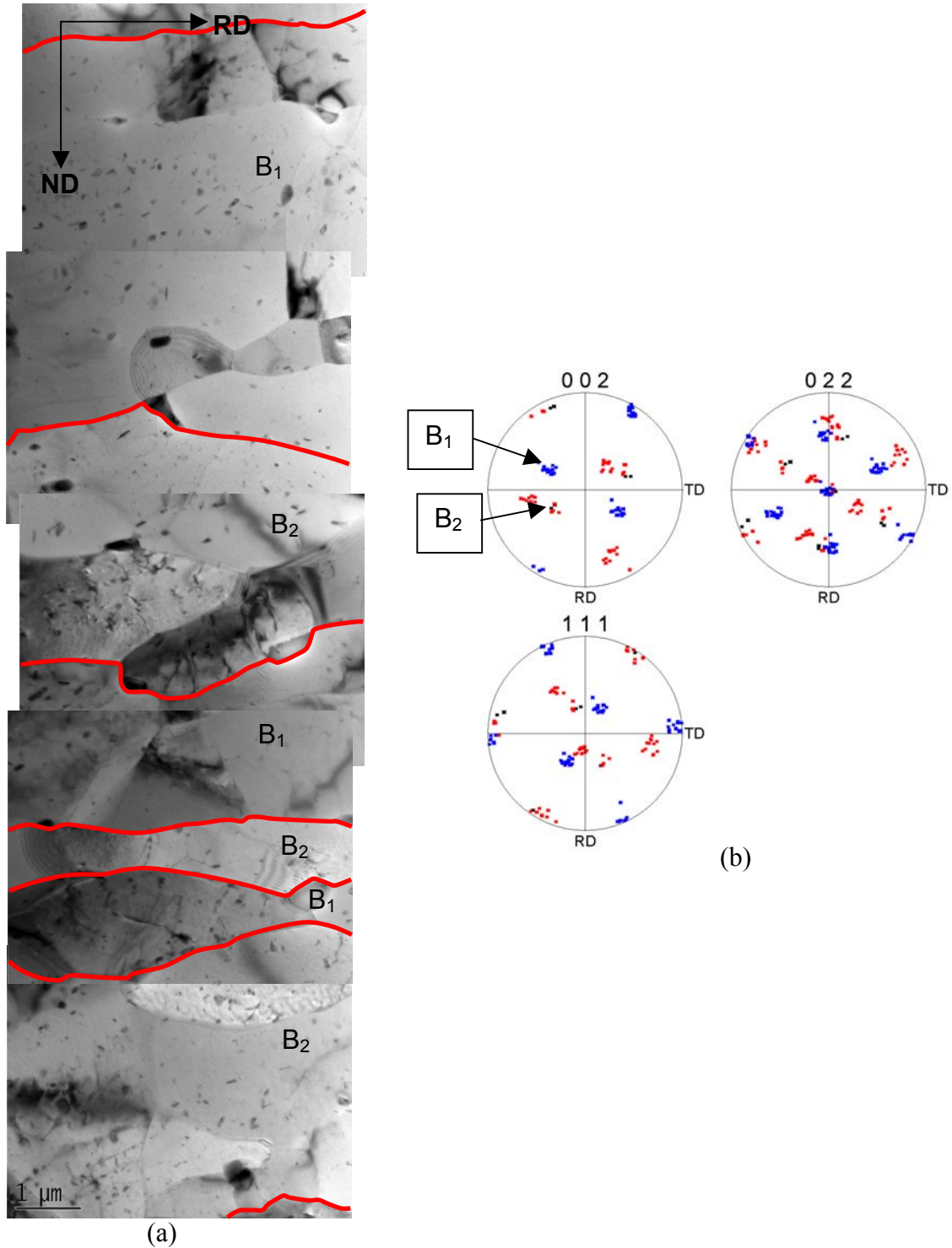
Figure 5.7. TEM montage in (a) of Supral 2004 after deformation at 450°C and 10^{-2} sec^{-1} to 110% elongation in RD. The positions of the symmetric variants of the B texture corresponding to the highlighted discrete pole figures in (b) are indicated in (a) along with the high-angle ($\theta > 50°$) boundaries are indicated by red lines.

tensile axis. This allows for a sharpening and stabilization of the texture. Each band will be able to deform through three equally stressed slip systems.

(a)   (b)
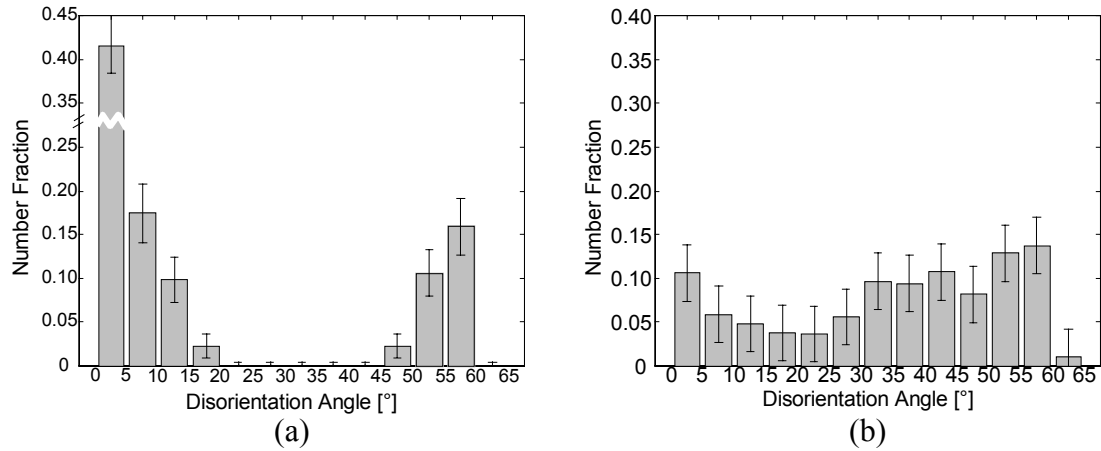
Figure 5.8. Disorientation distributions from Supral 2004 after being deformed to 110% elongation at 10^{-2} sec^{-1} and 450°C from (a) TOCA in the TEM by CBED analysis and (a) OIM in the SEM.

The sample deformed 200% in the RD was also examined in the same manner. Figures 5.10(a)-(d) correspondingly represents the orientation grain map, disorientation histogram, pole figures and texture highlighted grain map with the additional highlighting of the high-angle boundaries. A more diffuse distribution of orientations is evident in the pole figures but the predominant B-type texture is still evident. The grain coarsening previously noted in material deformed 110% along the RD has apparently ceased, which is in keeping with the low mobility of HABs in a continuously recrystallized material. Additionally, the band widths tend to remain unaltered. However, a break-up of the well-defined bands is taking place, presumably due to the contribution of grain boundary sliding. This is associated as well with the further increase in the randomness of the grain boundary disorientations in this microstructure. The predominantly HAB structure also supports the evidence of grain boundary sliding as a deformation mechanism during superplasticity.

An example of a STEM image and elemental map for Zr are provided in Figure 5.11(a) and (b) respectively, illustrating the presence of the coarse, second phase particles aligning with the RD in the annealed condition. Another investigation on deformed material revealed similar findings, namely that the large second phase particles evidenced
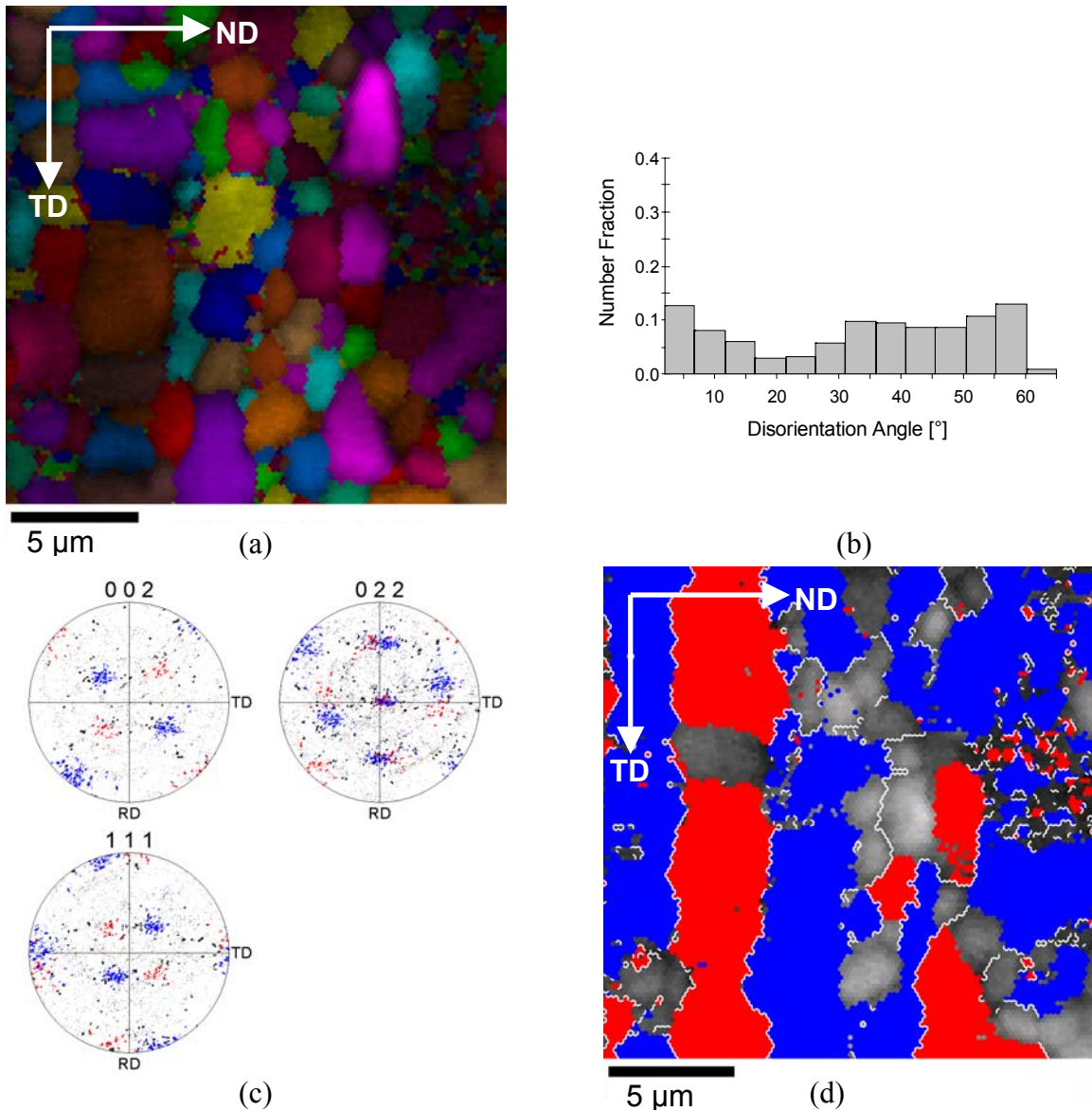
Figure 5.9. Supral 2004 deformed at 450°C and 10^{-2} sec^{-1} with the tensile axis parallel to the TD direction. (a) An OIM grain map; (b) Misorientation histogram with the bimodal distribution; (c) Discrete pole figures with the B texture components highlighted in red or blue; (d) IQ only grain map with the red and blue highlighting corresponding to the pole figures in (c) with the high-angle (50°<θ<62.8°) highlighted in white.

in Figure 5.7(a), tended to align with the original RD with some coarsening and that Zr containing regions were found at the high-angle boundaries. The exact composition was not determined.
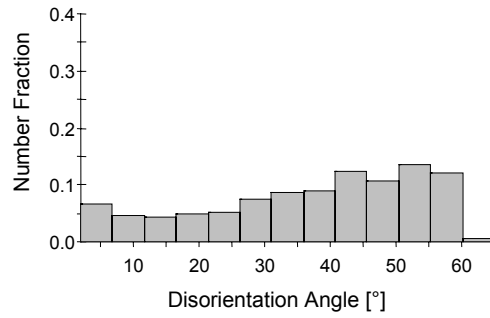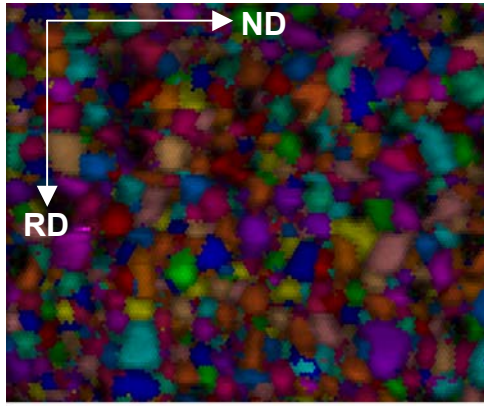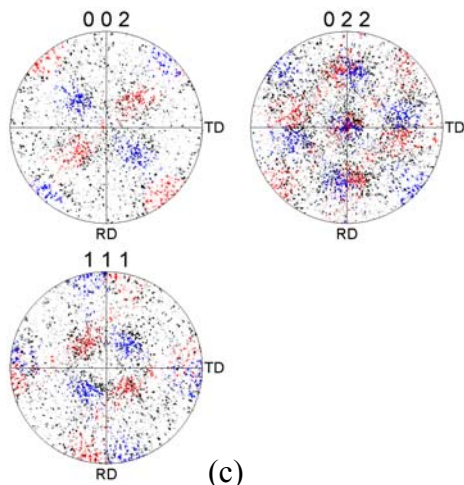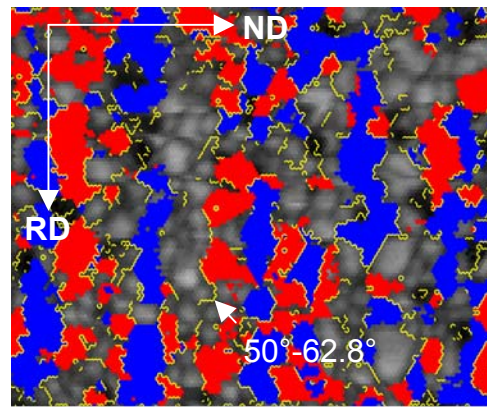
Figure 5.10. (a) OIM unique grain map of Supral 2004 deformed to 200% elongation in RD. (b) Disorientation histogram showing an increased fraction of high-angle boundaries corresponding to the MacKenzie random distribution. (c) Discrete pole figures showing the B texture components becoming more diffuse. Additionally, the texture components are highlighted in red and blue. (d) IQ only grain map corresponding to the highlighted pole figures of (c) with high-angle boundaries highlighted in yellow.
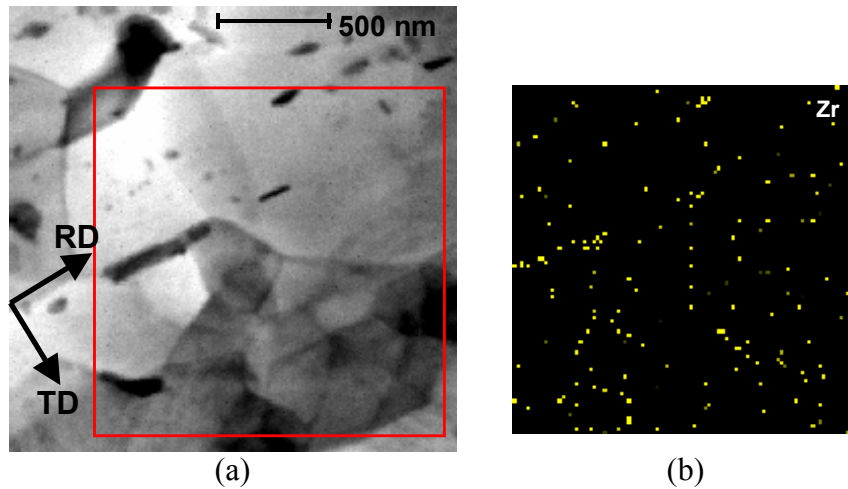
Figure 5.11. STEM image in (a) of Supral 2004 after annealing at 450°C for 6hrs. Zr elemental map in (b), from the region in (a) indicated by the red square, showing the tendency of the Zr concentrations to lie along the grain boundaries.

D.   DISCUSSION

Superplasticity requires both a fine, stable grain structure and high angle boundaries for GBS and its accommodation mechanisms, and thermomechanical processes involving large-strain deformation and recrystallization are necessary in order to realize such microstructural features and enable superplasticity in aluminum alloys. The phenomenon of continuous recrystallization apparently provides the necessary microstructures and results in highly superplastic response in alloys such as Supral 2004. However, the mechanisms involved in this phenomenon have remained unclear and approaches to achieve and control continuous recrystallization have been mainly empirical in nature. The OIM and TEM data of this research have illustrated the importance of a particular mechanism, deformation banding, in grain refinement and development of high-angle boundaries in association with continuous recrystallization after TMP.

1.   As-Rolled Material

The as-rolled Supral 2004 exhibits an elongated and banded microstructure and a deformation texture with a predominant B component; such a texture is characteristic of FCC metals deformed by rolling at low temperatures. The microtexture data for the as-received material are consistent with X-ray data [Ref. 63] and, furthermore, band-like features are apparent in the OIM and TEM data. Within a tolerance of 15º, the lattice orientation of the bands alternates along the ND according to the pattern ….., B_1, B_2, B_1, B_2, ..., where B_1 is $(110)[1\bar{1}2]$ and B_2 is $(011)[2\bar{1}1]$, in traverses along the ND on the RD/ND plane. Here, B_1 and B_2 refer to the symmetric variants of the B texture component.

The analysis of Hirsch and Lücke [Ref. 147] and McNelley et al. [Ref. 63] will be treated in a subsequent chapter. Briefly, these authors illustrate the crystallography of the two distinct variants of the B texture component in a cubical volume of fcc material having B-type lattice orientations and deformed in plane strain. Deformation conditions are such that the material deforms on only two slip systems under a Tucker-type of stress state ($\sigma_{ND,ND} = -\sigma_{RD,RD}$) and, except for an additional shear strain $\varepsilon_{RD,ND}$, exhibit plane strain deformation ($\varepsilon_{ND,ND} = -\varepsilon_{RD,RD}$; $\varepsilon_{TD,TD} = 0$). Thus, by arranging deformed and

elongated regions having the B_1 and B_2 variant orientations in an alternating pattern as illustrated in Figure 5.1(a), the shear terms average out and a region having such a pattern may deform macroscopically in plane strain.

Grain subdivision, with lattice rotation toward the B_1 variant orientation on one side of a developing boundary and the B_2 variant orientation on the opposite side of the boundary, would lead eventually to the microstructure illustrated in the OIM data of Figure 5.1(a). Thus, a deformation banding model for the deformation microstructure of Supral 2004 includes grain subdivision during the prior TMP with the development of bands of lattice orientations that alternate between the symmetric variants of the deformation texture. The bands that are apparent in Figure 5.1(a) are about 2.5μm in thickness, which is approximately the thickness expected if prior grains that are initially 50μm in size prior to rolling are reduced by a true strain of 3.0. However, investigations into deformation banding have generally shown that the process of grain subdivision begins at much smaller strains and involves formation of several bands within each prior grain [Refs. 32-37]. The prior boundaries are indistinguishable in Figure 5.1(a) and so it would be necessary to examine the evolution of deformation banding during rolling in order to assess the interaction between the bands and the prior grains.

2.   Annealed Material

Following annealing, the bands have a thickness-to-length aspect ratio of 10:1, or more, and an equi-axed cellular structure, comprising many boundaries of 2º-15º disorientation, has become apparent within the bands (Figure 5.3(a)). The cells appear to be 1.0μm – 2.0μm in size. Thus, from one to three cells are encountered in a traverse along the ND across each band. The presence of the Al_2Cu particles and the shear strain $\varepsilon_{RD,ND}$ at the ends of the bands must be accommodated by additional local strains within the bands. These accommodation strains account for the presence of the cellular substructure within the bands. The large apparent disorientations associated with the cell walls reflect a high dislocation density developed during TMP as well as low rates of recovery due to the high solute content and presence of the Al_3Zr particles. The main B texture component reflects deformation banding during the prior TMP of the material

90

while the presence of a cellular substructure due to accommodation accounts for the spread about the B texture component.

3. Superplastic Deformation of a Banded Microstructure

The disorientations immediately after TMP correspond to features of the deformation microstructure, including interfaces between bands and a cellular structure within the bands. The presence of transition regions, wherein lattice orientation changes gradually from one band orientation to the next, suggests that the band/band interfaces are extended regions of high dislocation density rather than distinct boundaries. The details of such regions require higher spatial resolution than attainable in OIM. Figures 5.2 - 5.4, represent the effect of annealing. The annotations 1 and 2 of Figure 5.1(d) represent the transition regions between bands or cells in the deformation microstructure. Reorientation of the lattice from one band or cell to the next takes place gradually through the transition region (Figure 5.3). Thus, recovery-controlled rearrangement of dislocation structures and processes such as cell wall or subgrain boundary coalescence within a transition region allows the band or cell to grow at the expense of the transition region. The lattice orientation within the bands or cells on either side of such an evolving structure is envisioned to be unaffected during such a process, which is consistent with the stability of the texture. Eventually the transition regions are replaced by distinct boundaries seen in Figure 5.4.

The OIM results (Figures 5.5, 5.7 and 5.8) suggest that the processes of boundary development from these transition regions occur progressively at 450ºC with concurrent straining under superplastic conditions. The retention of the B texture component and the band structure after a strain of 110% in RD and 107% in TD suggests that few boundaries have become able to slide at this point and so deformation is predominately by dislocation creep processes despite the apparent refinement of the grain structure. Under dislocation creep conditions a distinct <111> fiber texture formed during deformation of a 5083 alloy, which had a in a fine, recrystallized grain size and a random initial texture after TMP to make this material superplastic [Ref. 137]. Examination of the discrete (111) pole figure in Figures 5.5(c) and 5.7(c) reveals that a <111> is nearly aligned with the RD and TD respectively, which are also the tensile axes, in both the B_1 and B_2

variants of texture. Thus, only small lattice rotations would be required during uniaxial tensile extension along either RD or TD and this is reflected in the apparent stability of this orientation here.

At a strain of 200% the randomizing of the texture and grain boundary disorientation distribution suggest that boundary development from the band and cell boundaries is essentially complete and GBS is now contributing a large proportion of the total superplastic strain. A mean linear intercept grain size of 3.0μm allows superplastic response over a wide strain rate range. Comparison of the disorientation distributions in Figures 5.5(b) and 5.8(b) shows that the populations of low-angle (2º-5º) and high-angle (50º-62.8º) are decreasing. However, a peak at 40º-45º in the disorientation histogram of Figure 5.8(b) is in the same range as predicted by Mackenzie for randomly oriented cubes [Ref. 135], and this is consistent with the random grain rotations associated with GBS.

VI.   MICROSTRUCTURE OF ROLLED AL-5%CA-5%ZN

A.   INTRODUCTION

Several investigations over a long period of time have provided results for certain superplastic metals that exhibit a pattern of microstructural transformation generally referred to as continuous recrystallization [Refs. 69, 148-169] during heating and deformation. Thus, in some of these alloys, deformation texture components that had developed during prior thermomechanical processing (TMP) were retained during superplastic deformation, or other texture components were observed to form. Anisotropy of superplastic deformation has been observed in other materials [Refs. 69, 148-166]. Furthermore, transmission electron microscopy (TEM) studies have provided evidence of dislocation activity in the form of slip lines that were observed in samples following superplastic deformation [Refs. 167-169]. These observations have led some authors to suggest that dislocation creep and grain boundary sliding may contribute jointly and simultaneously to the total strain during superplastic deformation, and do so over a wide range of diffusion-compensated strain rates. This is in distinct contrast to the behavior reported for the superplastic 5083 aluminum alloy, in which grain refinement has been accomplished by discontinuous recrystallization in association with coarse second phase particles. It is also in contrast to the predictions of phenomenological models that are based on the independent, additive contributions of these mechanisms to the total deformation rate [Ref. 137].

These observations are common to superplastic aluminum alloys that exhibit continuous recrystallization, either during static annealing or during superplastic straining. The term 'continuous recrystallization' is a phenomenological description for a recovery-dominated microstructural transformation that occurs homogeneously throughout a deformation-induced microstructure in the absence of long-range high-angle boundary migration [Ref. 170].

In many discussions of superplastic behavior in aluminum alloys, the deformation-induced microstructure at the conclusion of TMP has been envisioned to consist of elongated prior grains that contain cells or subgrains of small disorientation.

Several investigators have then suggested that continuous recrystallization consists of a recovery-controlled build up of the average disorientation angle for subgrains within such a structure [Refs. 2, 72-77]. However, the mechanism of this increase in disorientation is uncertain. It has been attributed to subgrain growth [Ref. 72], to subgrain coalescence [Ref. 73], to subgrain rotation [Ref. 74], to subgrain rotation and switching [Ref. 75] in a response to the tensile stress, or to the accumulation of dislocations in grain boundaries during elevated temperature deformation [Refs. 76-77].

A more complex picture of deformation-induced microstructures has emerged in recent investigations of large-strain, low-temperature deformation of pure metals [e.g. Ref. 171]. Grain elongation with cell/subgrain formation at small strains gives way as the strain increases to processes of grain subdivision. A classification of resulting boundary types and glossary of terms employed in description of deformation microstructures has recently been provided [Ref. 171]. At large strains, highly elongated, banded or ribbon-like grain structures are seen to develop. These structures may include large fractions of high-angle boundaries although the initial grain size, the deformation temperature, the solute content and the presence of second phase particles all strongly influence the resulting structure.

During annealing of such deformation-induced microstructures, recovery processes involving local dislocation rearrangements and short-range boundary migration may lead to the development of a fine grain structure that also comprises a large fraction of high-angle boundaries. In the absence of long-range migration of high-angle boundaries these processes would constitute continuous recrystallization. Recent investigations into the behavior of the Al-5%Ca-5%Zn alloy [Ref. 69] of this research and of Supral 2004 [Refs. 63-64, 71], have examined this perspective on continuous recrystallization using computer-aided electron backscatter diffraction (EBSD) pattern analysis methods. These microtexture studies have shown that the boundary disorientation distribution in as-processed material is that of a fine, deformation-induced cellular structure. The cell walls likely consist of dislocation arrays of high density due to the severe cold working typical of the final processing stages for such materials. The grain boundary disorientation distributions after annealing corresponded closely to the

distribution observed in the cellular structure in the as-processed material. Therefore, it has been suggested that continuous recrystallization during annealing consists mainly of the development of boundaries by evolution of the dislocation arrays of the cell walls. Also, many of the resulting grain boundaries were retained during annealing while others were eliminated, altogether in a manner consistent with retention of the deformation texture.

In the present work, texture and mechanical property data for the Al-5%Ca-5%Zn alloy will be used as an example of a material that exhibits continuous recrystallization. These results suggest a distinctly different pattern of elevated temperature deformation behavior than observed in 5083 aluminum [Ref. 137].

B.   EXPERIMENTAL PROCDURES

The Al-5%Ca-5%Zn alloy was prepared by Alcan, Inc. using aluminum of 99.99% purity. Details of the composition are provided in Table 6.1. Cast ingots were hot rolled and subsequently cold rolled to a 3.2 mm thick sheet [Ref. 172].

Ca	Zn	Fe	Si	Mg	Al
5.0	4.95	0.18	0.1	0.042	Bal.

Table 6.1. Alloy composition (wt.%) for Al-5%Ca-5%Zn

Annealing was performed at 520°C and 400°C and tensile tests were performed at a strain rate of 10^{-2} sec^{-1} at 400°C. Test coupons, with a 12.5mm gage length, were prepared with tensile axes aligned either with the rolling or transverse direction (RD or TD) of the as-processed sheet. Details of the sample geometry and testing procedure have been provided elsewhere [Ref. 157]. Microtexture measurements as well as microstructure examination were performed in the mid-layer of the sheet alloy following the procedures explained in Chapter II. The final step for SEM examination consisted of electropolishing with nitric acid (20%) and methanol (80%) solution at 35V for 20sec cooled to an initial temperature of -25ºC.

C. RESULTS

Macro and microtexture measurements have been previously performed in Al-5%Ca-5%Zn alloy in the as-received condition [Refs. 64, 69, 157, 173]. The X-ray results indicated that the material exhibits a weak but distinct deformation texture. The most prominent orientation is {225}<554>, which is located just 5º away from the C component, {112}<111> [Refs. 124, 173]. The {225}<554> component lies close to the β fiber, which connects the C and the B ({011}<211>) orientations in Euler space, and therefore is typical of a deformed fcc metal [Refs. 126, 147]. The microtexture data reported in [Ref. 69] also show the presence of a weak deformation texture in the as-received material and indicate as well a predominant population of apparently random orientations. The disorientation distribution histogram exhibits a maximum near 45º [Ref. 69] and is similar to the MacKenzie distribution for randomly oriented cubes [Ref. 135]. The present EBSD examination is consistent with previous results. Figure 6.1 shows the OIM data corresponding to the microstructure Al-5%Ca-5%Zn alloy in the as-received condition. Figure 6.1(a) is a grain color map in which (sub)grains disoriented more than 2° or more have been randomly assigned different colors. It can be noted that the average (sub)grain size is around 0.5μm. Figure 6.1(b) illustrates the (200), (220), and (111) discrete pole figures in which the two symmetric variants of the C-type texture component, have been colored in blue and red. A tolerance of ±15° around the ideal orientations has been used. The significant scattering of the data reveals the weakness of the texture. The spatial location of (sub)grains oriented as these two symmetric variants is represented in Figure 6.1(c). It is important to note that some clustering of (sub)grains belonging to the same variant can be appreciated. The regions colored in black or gray tones correspond to other orientations.

The effect of annealing at 520°C on this alloy has been described previously [Ref. 69]. It was shown that the weak C-type component that was present in the as-received material is retained and strengthened with annealing time. Simultaneously, the grain size increased. The retention of a deformation texture component during annealing is commonly associated with the occurrence of continuous recrystallization [Ref. 2]. A
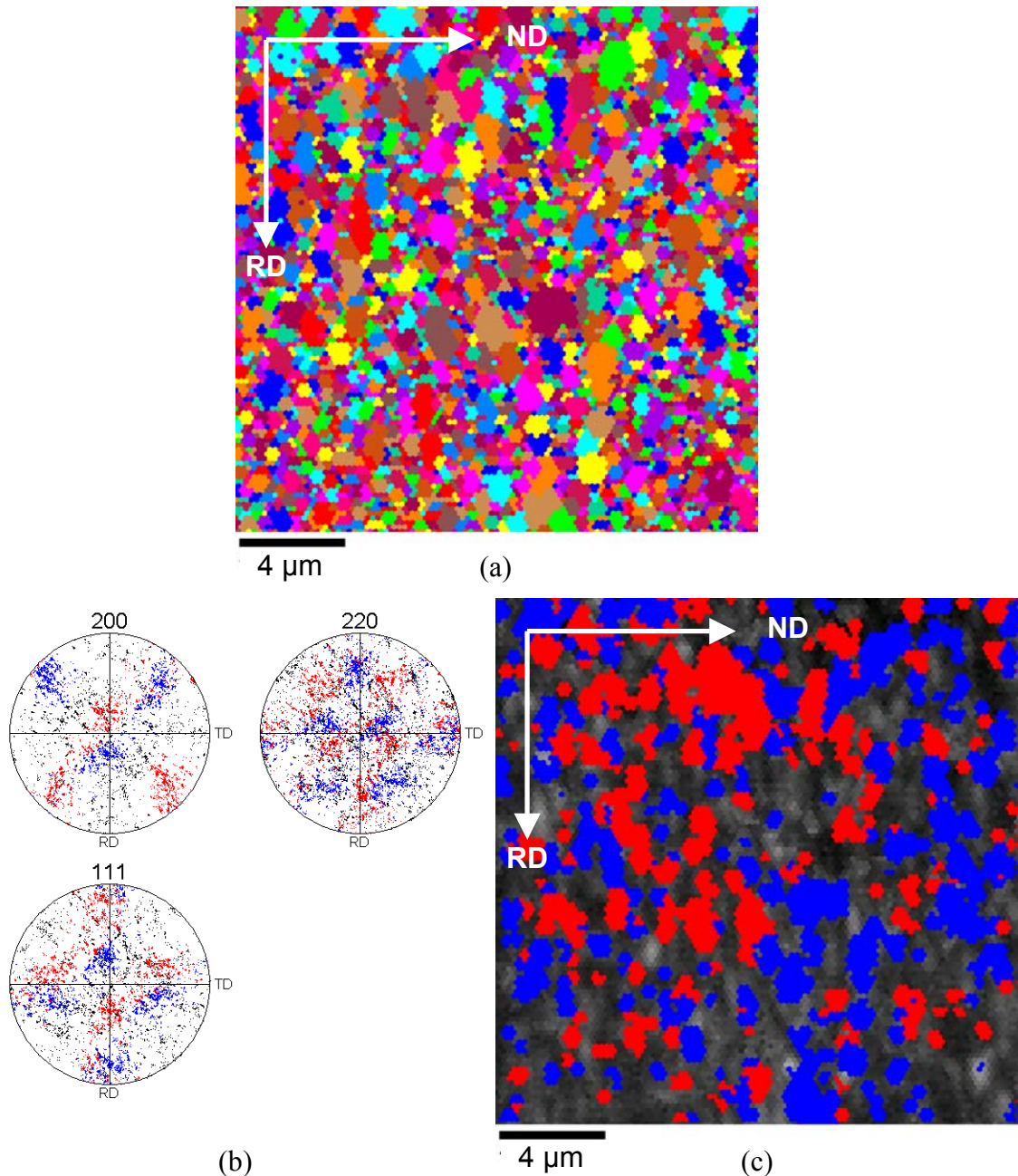
Figure 6.1. OIM data for the Al-5%Ca-5%Zn in the as received condition: (a) an OIM unique grain color map for (sub)grains disoriented more than 2°; (b), discrete pole figures in which the two symmetric variants of the C texture component have been highlighted in either red or blue; (c) an IQ only grain map plotted with the positions of the two C texture variants highlighted in red and blue corresponding to (b).

bimodal misorientation distribution becomes apparent after short annealing times (7min) indicating the predominance of boundaries misoriented in the range between 5º-15º and 50°-55°. It was suggested [Ref. 69] that the high angle boundaries separate (sub)grains

belonging to the two symmetric variants of the main texture component and moderately misoriented boundaries separate (sub)grains within each texture variant. The bimodal character of the misorientation distribution becomes increasingly pronounced with time of annealing.

Figure 6.2 illustrates direct microstructural evidence of these annealing-induced changes. The OIM data presented in this figure were obtained from the RD-ND plane of the Al-5%Ca-5%Zn alloy after annealing at 520°C for 15 minutes. Figure 6.2(a) is an OIM grain color map in which (sub)grains disoriented more than 2° or more have been randomly assigned different colors. Average (sub)grain size after this short annealing treatment has increased to 2μm. The (sub)grain size is consistent with that observed by TEM [Ref. 64]. Figure 6.2(b) show the (200), (220), and (111) discrete pole figures, in which the two variants of the C-type texture, and orientations within 15° of the ideal C-variant orientations, are color coded in blue and red, respectively. A distinct sharpening of the texture with respect to that of the as-received material can be appreciated. This is consistent with previous studies [Ref. 69]. Figures 6.2(c) and 6.2(d) are image quality (IQ) only OIM maps, corresponding to the same region as that of Figure 6.2(a), showing the spatial location of (sub)grains oriented as the two symmetric variants of the main texture component. In contrast to Figure 6.1(a), it can be seen now that the microstructure is formed by grains oriented as the two symmetric variants of the main C-type texture component. Also, clustering of (sub)grains belonging to each of the two variants is now clear and the clusters belonging to different variants are intermingled in the microstructure. As mentioned above, previous studies [Ref. 69] have detected the predominance of boundaries misoriented in the range between 5º-15º and 50°-55° in the annealed microstructure of the Al-5%Ca-5%Zn. Figures 6.2(c) and 6.2(d) also show the location of the high- ($50°<\theta<62.8°$) and low-angle ($2°<\theta<15°$) boundaries, respectively. It can clearly be observed here that the high-angle boundaries, in green in Figure 6.2(c), separate (sub)grains belonging to the two variants and the low-angle boundaries, in yellow in Figure 6.2(d) separate (sub)grains within each variant.
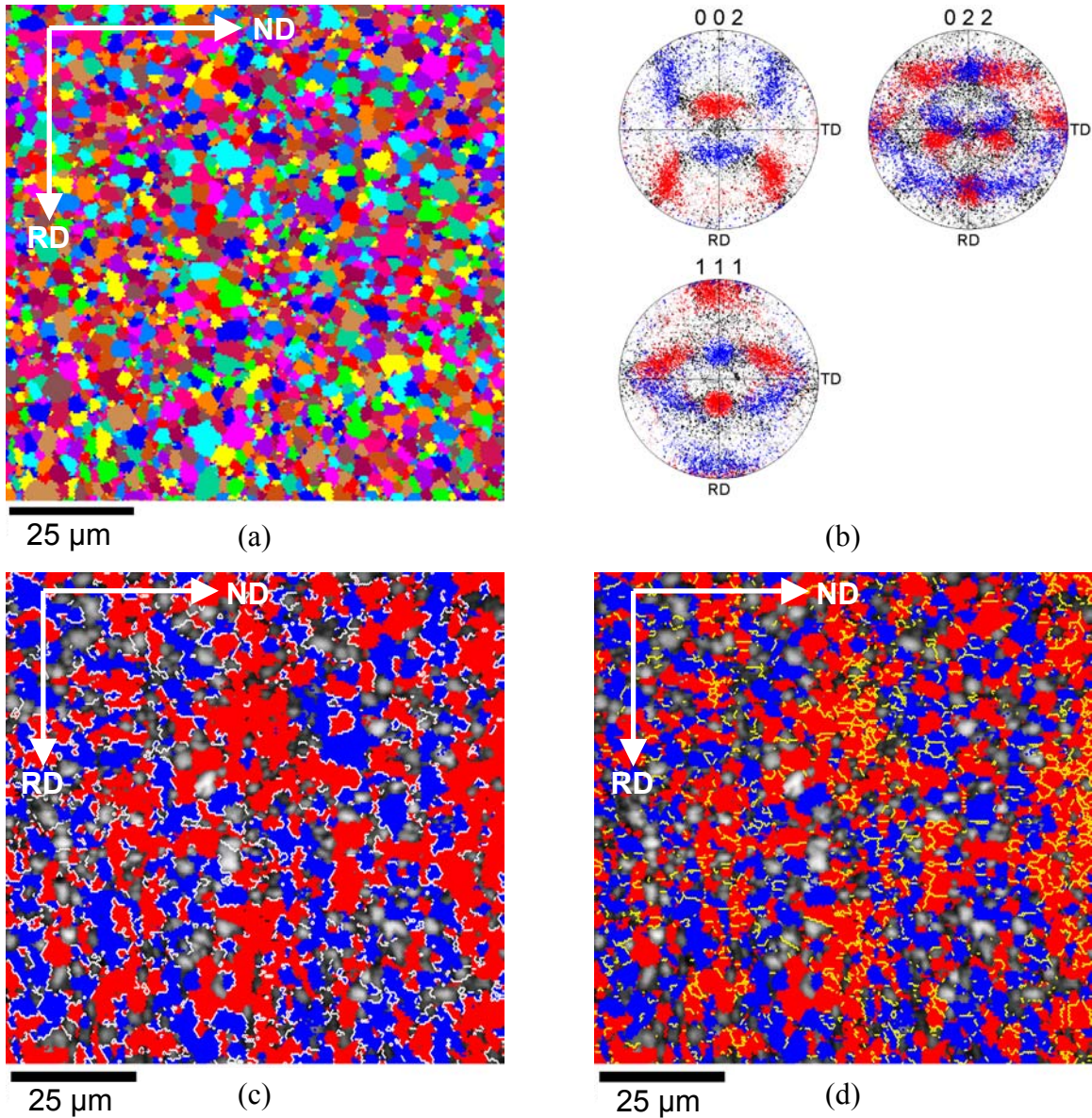
Figure 6.2. OIM data for Al-5%Ca-5%Zn after annealing at 520°C for 15min.: (a) an OIM unique grain color map for (sub)grains disoriented more than 2°; (b), discrete pole figures in which the two variants of the C texture component have been highlighted in either red or blue; (c) and (d) IQ only maps plotted with the positions of the high-angle (50°<θ<62.8°) and low-angle (2°<θ<15°) boundaries highlighted in white and yellow respectively along with the locations of the two C texture components highlighted in red and blue corresponding to (b).

The OIM data presented in Figure 6.3 correspond to the RD-ND plane of the Al-5%Ca-5%Zn alloy annealed at 520°C for 6 hours. Figure 6.3(a) is an OIM grain color map in which (sub)grains disoriented more than 2° or more have been randomly assigned
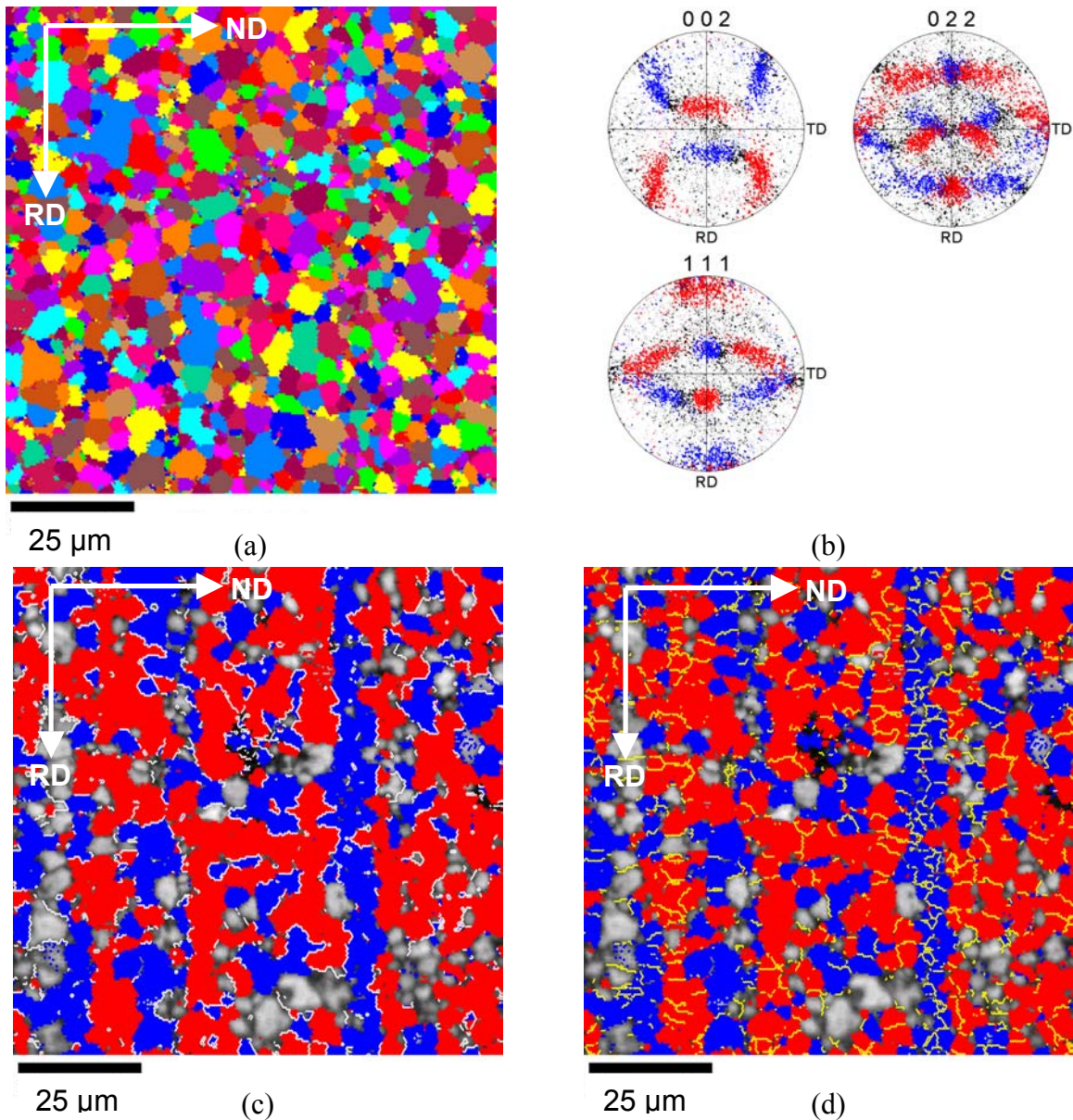
Figure 6.3. OIM grain map of Al-5%Ca-5%Zn after annealing at 520°C for 6hrs.: (a) and OIM grain color map for (sub)grains disoriented more than 2°; (b), discrete pole figure in which the two symmetric variants of the C texture component have been highlighted in either red or blue; (c) and (d), IQ only grain maps with the positions of the high-angle (50°<θ<62.8°) and low-angle (2°<θ<15°) boundaries highlighted in white and yellow respectively along with the corresponding locations of the C type texture shown in (b).

different colors. Figure 6.3(b) illustrates the discrete pole figures, in which the two variants of the C-type texture are color coded in blue and red, respectively. The result of the previous thermomechanical processing is evidenced by a distinct band-like

100

appearance of the two texture components in which the bands are aligned with the RD. Figures 6.3(c) and 6.3(d) are image quality (IQ) OIM maps, corresponding to the same region as that of Figure 6.3(a), that are also highlighted to show the spatial location of the two symmetric variants of the C texture component. Figures 6.3(c) and 6.3(d) also include highlighting to illustrate separately the locations of the high- and low-angle boundaries. It can be observed here that, clearly, the high-angle ($50°<\theta<62.8°$) boundaries, in white in Figure 6.3(c), separate (sub)grains belonging to each of the two variants and low-angle ($2°<\theta<15°$) boundaries, in yellow in Figure 6.3(d), separate (sub)grains within each variant.

The OIM data presented in Figure 6.4 correspond to the RD-ND plane of the Al-5%Ca-5%Zn alloy annealed at 400°C for 6 hours. Figure 6.4(a) is an OIM grain color map with a 2° disorientation tolerance. The discrete pole figures in Figure 6.4(b), have been color coded in blue and red corresponding to the C texture variants. Although not truly banded, the image quality (IQ) only OIM maps in Figures 6.4(c) and 6.4(d) that are highlighted corresponding to the pole figures of Figure 6.4(b), show the location of the two symmetric variants of the C texture component. Figures 6.4(c) and 6.4(d) show the location of the high- ($50°<\theta<62.8°$) and low-angle ($2°<\theta<15°$) boundaries, respectively. The high-angle boundaries, white in Figure 6.4(c), separate (sub)grains belonging to each of the two variants and low-angle boundaries, yellow in Figure 6.4(d), separate (sub)grains within each variant. Comparison of Figures 6.4(a) and 6.4(d) show that the grains of similar orientation tend to cluster, align with the final rolling direction and are separated by low-angle boundaries.

The elevated temperature deformation behavior of this alloy was investigated by Pérez-Prado et al. [Ref. 64] and superplastic response was observed over the range of deformation temperatures and strain rates for the samples considered in this study. Figure 6.5 shows OIM data corresponding to the Al-5%Ca-5%Zn alloy deformed in tension at 400°C and 10^{-2} sec^{-1} along the rolling direction. Figure 6.5(a) is an OIM grain color map illustrating an equi-axed (sub)grain structure. The microtexture is represented in Figure 6.5(b) by means of (200), (220), and (111) discrete pole figures in which the two variants of the main C component have been highlighted in either blue or red. Figure 6.5(c) is an

101
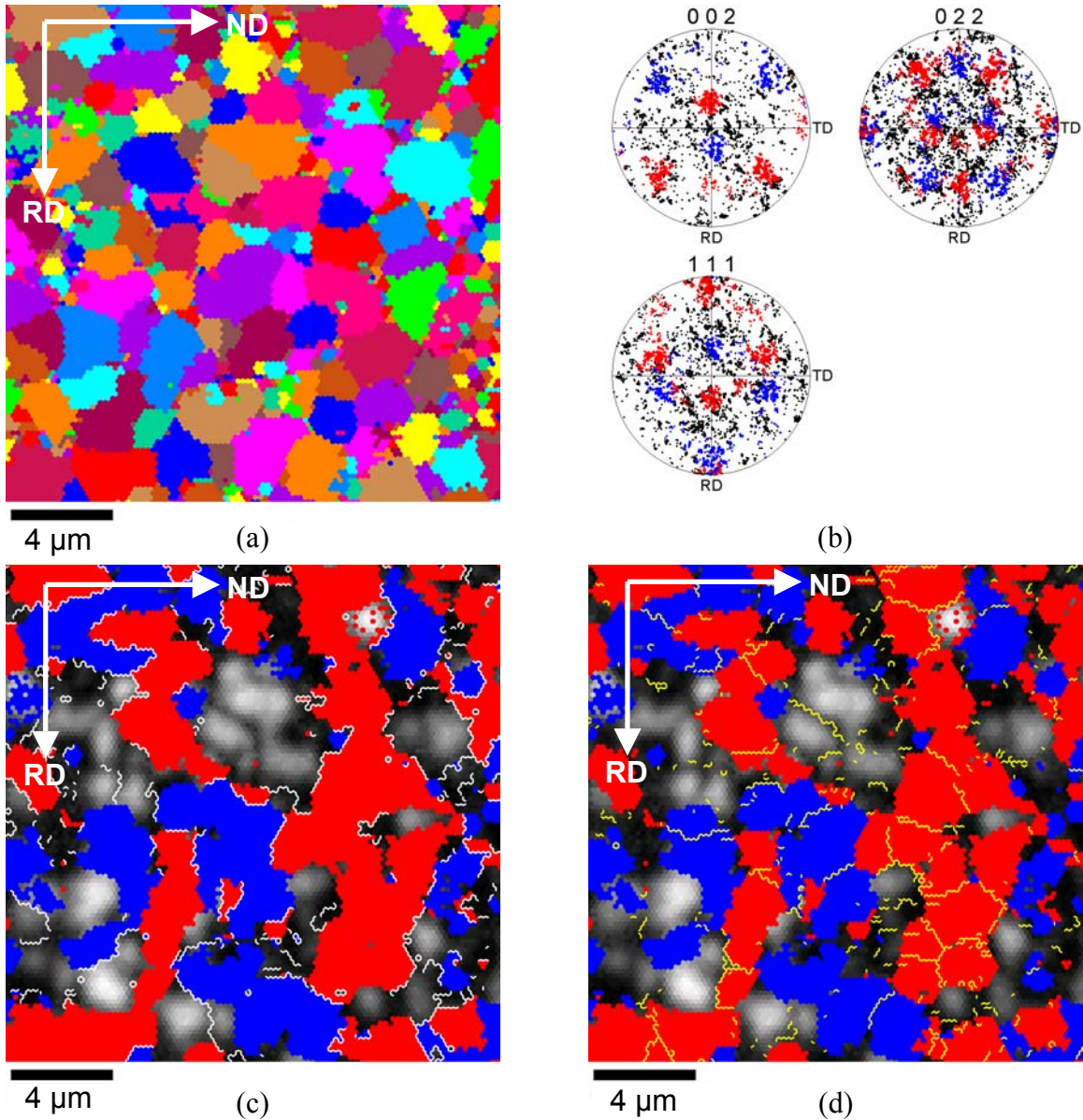
Figure 6.4. OIM data for Al-5%Ca-5%Zn after annealing at 400°C for 6hrs.: (a), an OIM unique grain color map with a 2° disorientation tolerance; (b), discrete pole figures highlighted in either red or blue corresponding to the two C texture variants; (c) and (d), IQ only grain maps showing the positions of the high-angle ($50° < \theta < 62.8°$) boundaries in white and low-angle ($2° < \theta < 15°$) boundaries in yellow, respectively, and the locations of the two C texture components.

OIM map corresponding to the same region as that in Figure 6.5(a), but showing the spatial distribution of these two symmetric texture variants (in blue and red) as well as the high-angle ($50° < \theta < 62.8°$) boundaries in green. Adjacent clusters of (sub)grains belong to different variants. Clusters of (sub)grains are elongated along the rolling
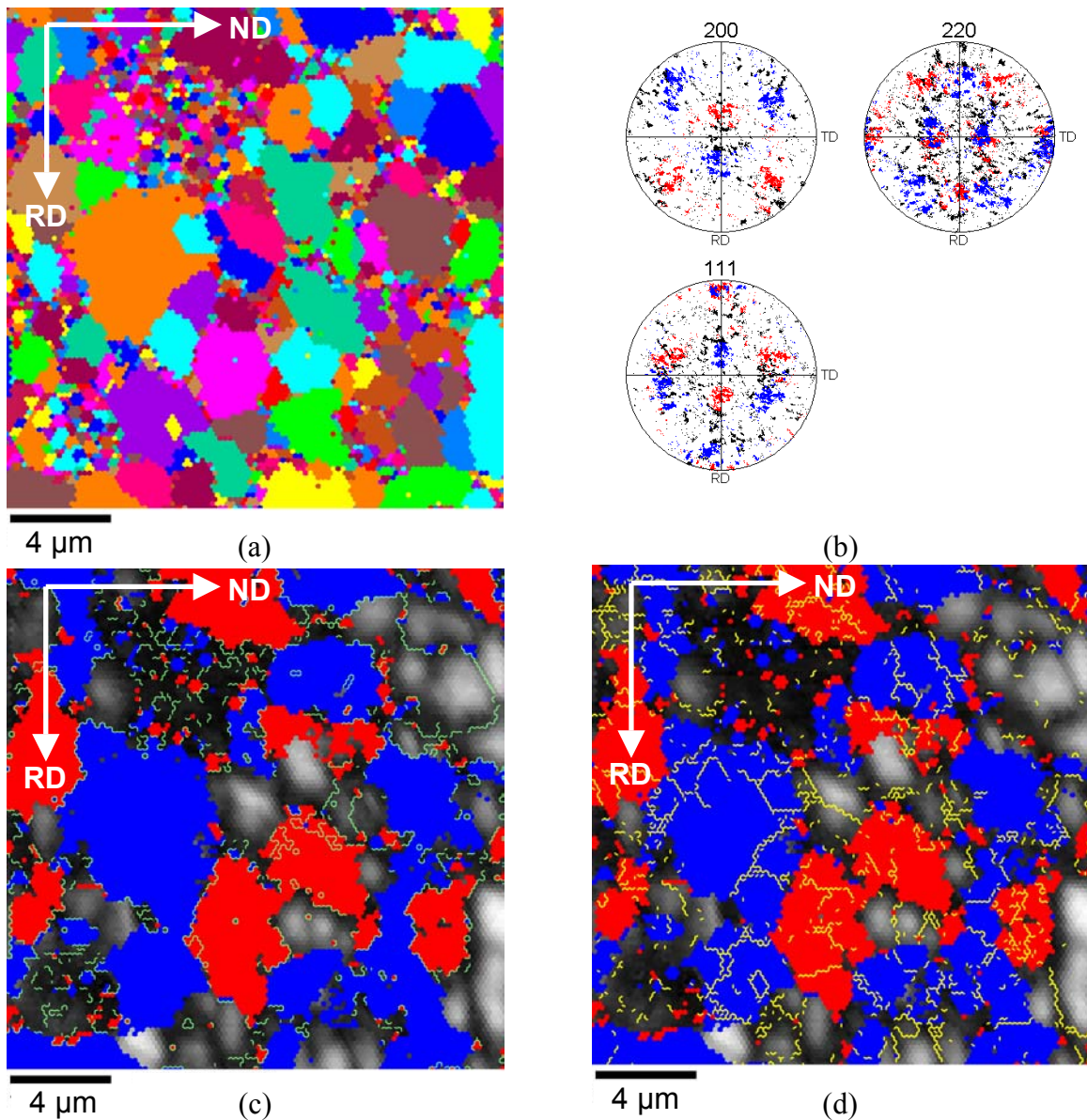
Figure 6.5. OIM data for Al-Ca-Zn deformed at 10^{-2} sec^{-1} and 400°C in the rolling direction (RD): (a), an OIM grain map for (sub)grains disoriented more than 2°; (b), discrete pole figures in which the two symmetric variants of the C texture component have been highlighted either red or blue; (c) and (d), IQ only maps illustrating the positions of the high-angle ($50° < \theta < 62.8°$) and low-angle ($2° < \theta < 15°$) boundaries have been highlighted in green and yellow respectively, along with the positions of the variants of the two C texture components.

direction (RD). This map also shows that the high-angle boundaries separate grain clusters belonging to the two different C texture variants. Figure 6.5(d) is an IQ OIM map of the same region as in Figure 6.5(a) that has been highlighted in yellow to show the spatial distribution of low-angle ($2° < \theta < 15°$) boundaries. It can be clearly seen that the

low-angle boundaries separate (sub)grains within a cluster belonging to the same texture variant.

Figure 6.6 shows OIM data corresponding to the Al-5%Ca-5%Zn alloy deformed at 400°C and 10^{-2} sec^{-1} along the transverse direction. The microstructure of this alloy under the present deformation conditions is similar to that corresponding to the test in the rolling direction. Figure 6.6(a) is an OIM grain color map illustrating an equi-axed (sub)grain structure. Figure 6.6(b) are discrete pole figures in which the two variants of the main C component have been highlighted in either blue and red. Figure 6.6(c) is an IQ OIM map of the same region as in Figure 6.6(a) showing the spatial location of these two symmetric texture variants in blue and red as well as the high-angle boundaries in white. The spatial distribution of the two variants is much more diffuse than that described for the tension test in the rolling direction. This is due to the lattice rotation away from the C texture component orientation and toward the B texture component orientation [Ref. 64]. Adjacent highlighted clusters of (sub)grains still belong to different variants. Clusters of (sub)grains are elongated along the transverse direction (TD). Again, the high-angle boundaries separate (sub)grains belonging to different variants. Figure 6.6(d) is another IQ OIM map of the same region as in Figure 6.6(a) showing the spatial location low-angle boundaries highlighted in yellow. It can be clearly seen that the low-angle boundaries separate (sub)grains within a cluster belonging to the same texture variant.
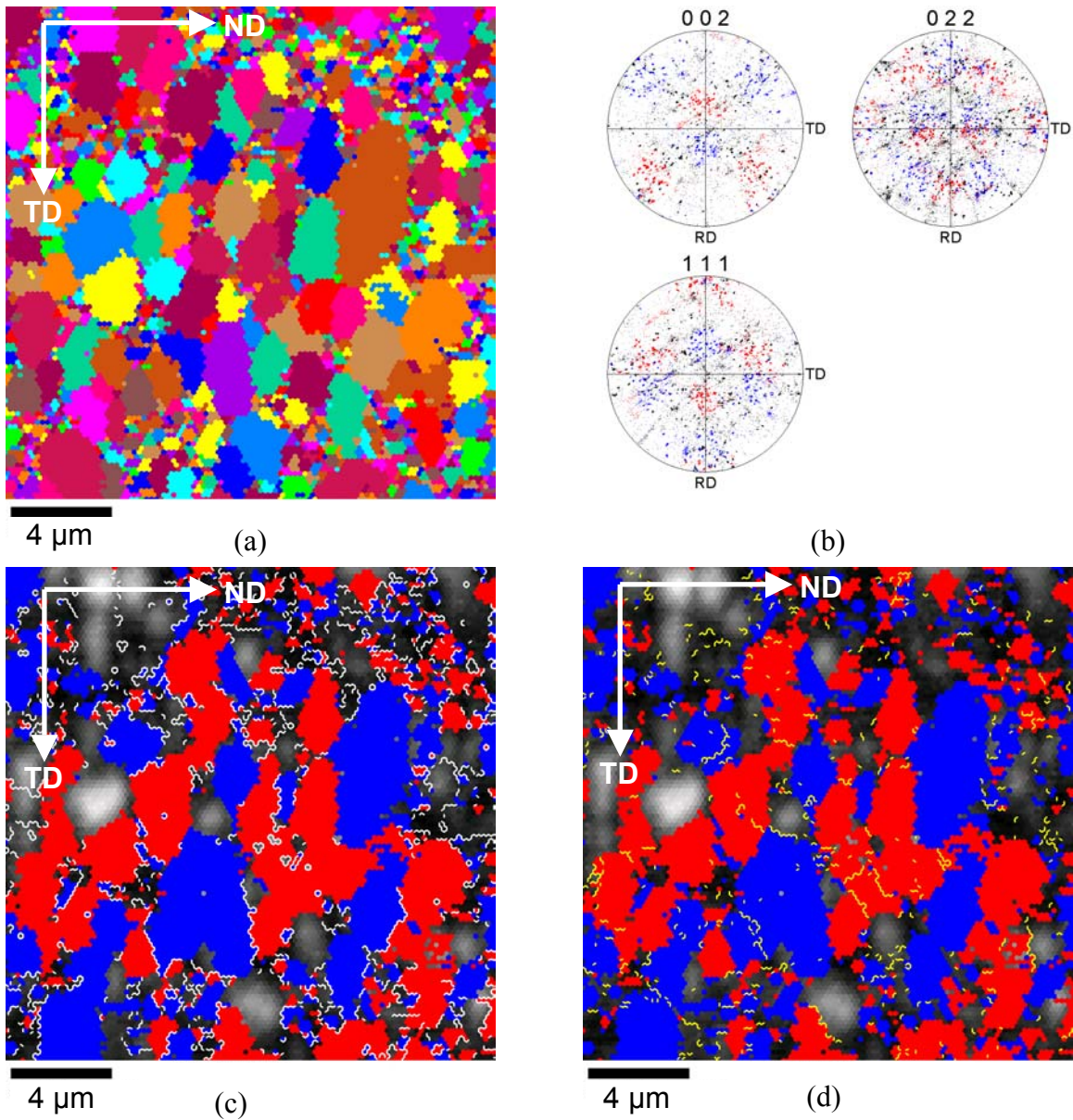
Figure 6.6. OIM data for Al-5%Ca-5%Zn deformed at 400°C at 10^{-2} sec^{-1} in the transverse direction (TD): (a) an OIM unique grain color map with a 2° disorientation tolerance, (b), discrete pole figures in which the two symmetric varints of the C texture component have been highlighted in either red or blue; (c) and (d), IQ only grain maps with the positions of the high-angle (50°<θ<62.8°) and low-angle (2°<θ<15°) boundaries highlighted in white and yellow respectively, in addition to the locations of the two C texture components shown in (b).

D.   DISCUSSION

The micro-texture and microstructural data of the Al-5%Ca-5%Zn alloy of this study correlate well with the recognized characteristics of aluminum alloys that transform by a continuous recrystallization reaction.   A model for the microstructure must be capable of explaining the development and evolution of the grain boundaries, as well as the grain size and the micro-texture, during both annealing and elevated temperature deformation. A model including deformation banding will be discussed in depth in a subsequent chapter and employed to describe, firstly, the annealing behavior and, subsequently, the elevated temperature deformation characteristics of this alloy.

1.   As-Rolled and Annealed Al-5%Ca-5%Zn Material

Altogether, previous studies [Refs. 69, 157] of this Al-5%Ca-5%Zn alloy have clearly shown that the two-phase microstructure of the as-processed material is very fine. The Al$_3$CaZn second-phase particles are homogeneously distributed, slightly elongated in the rolling direction of the sheet, and about 0.5μm in length and 0.2μm in diameter. A cellular substructure, finer than 1μm in size, is also present. The most prominent component in the texture of the as-processed material is {225}<554>, which is very close to the C orientation, a common component of deformation textures of fcc metals. The OIM data obtained for as-processed material in the present study are consistent with these previous results.

The current understanding of the evolution of deformation-induced microstructures is based mainly on studies of severely deformed pure metals [Refs. 170-171].   Thus, in the initial stages of deformation, subgrains develop and grain subdivision takes place.   This is followed by the formation, within the prior grains, of blocks or regions in which lattice rotation takes place in opposite senses.   At large strains, a banded, ribbon-like structure may develop in which the prior grain boundaries are no longer readily distinguishable.

The analyses of Hirsch and Lücke [Ref. 147] and Pérez-Prado et al. [Ref. 64] will be treated in a subsequent chapter.   Briefly, these authors describe texture development during large-strain deformation by rolling reflects lattice rotation toward stable end orientations.   For the material in this study, each variant in a C-type texture component has four slip systems with equivalent Schmid factors during plane-strain deformation

under a Tucker-type stress state ($\sigma_{RD,RD}$ = -$\sigma_{ND,ND}$) [Ref. 147]. The four slip systems having equivalent Schmid factors ($\pm$0.544) for this stress state are in conjugate pairs. The incremental strain may be calculated separately for each of the variants in tensor form assuming an identical incremental shear. Individually, each variant experiences plane strain deformation with an additional shear term, $\varepsilon_{RD,ND}$ in the strain. If the variants are arranged in an alternating manner, ..., C_1, C_2, C_1, ... etc., averaging of the incremental strains over a region comprising equal volumes of each orientation would give plane strain deformation. Such an arrangement is essentially that predicted by deformation banding models. The potential importance of deformation banding has long been recognized [Refs. 29, 174]. Due to the relaxation of constraints in individual bands, a banded structure is able to deform compatibly with the activation of less than five slip systems in each band [Refs. 34-35, 41].

Accommodation of the Al_3CaZn second-phase particles during severe plastic deformation would disrupt a tendency to form well-defined bands in the material of this investigation. The presence of such particles, as well as the need to accommodate the additional shears that arise in each band, would be reflected in the development of a cellular structure within the individual bands. In the initial stages of deformation processing the interfaces between adjacent bands may be thick, transitional regions of high dislocation density and lattice curvature, reflecting gradual lattice reorientation from the orientation of one band to that of the next. After more severe deformation such interfaces may become more sharply defined [e.g., 44]. Lattice curvature associated with the interfaces between the bands, with the cellular structure inside of the bands, and with accommodation of the Al_3CaZn particles would account for a large spread of orientations about the main texture component and the appearance of random orientations. This was evident in Figure 6.1.

Annealing, particularly at temperatures above 500°C, has been shown to result in coarsening of the matrix grains, accompanied by coarsening and spheroidization of the Al_3CaZn second-phase particles [Ref. 69]. Three additional observations lead to the conclusion that a continuous recrystallization reaction occurs during such post-TMP annealing. These were: (a) retention and progressive sharpening of the initial

deformation texture; (b), absence of formation of new texture components; and (c), development of a bimodal boundary disorientation distribution, with a high-angle boundary peak at 50º-55º and a lower-angle peak between 5º and 15º [Ref. 69]. Coarsening of the matrix grain structure and sharpening of the initial deformation texture during annealing are also evident when Figures 6.2 and 6.32 are compared to the as-received condition in Figure 6.1. The texture sharpening is consistent with a reduction in lattice curvature, and thus orientation spread about the C texture component, due to recovery during the annealing. Following annealing, the microstructure therefore consists mainly of grains of lattice orientations distributed near one or the other of the two distinct variants of this C-type texture component. The highlighting in Figures 6.2(c) and 6.3(c) clearly shows that the high-angle boundaries (50°-62.8°) are the interfaces between regions of lattice orientation near one or the other of the symmetric variants of the texture component, while low-angle boundaries (2°-15°) separate cells within such grains are seen in Figures 6.2(d) and 6.3(d).

Annealing below 500°C, has been shown to have similar effects on the microstructure and micro-texture. Specifically, the grains are seen to coarsen in Figure 6.4(a) but do not exhibit abnormal grain growth. The retention and sharpening of the as-rolled texture can be seen in Figure 6.4(b). The locations of the two texture variants are shown in Figure 6.4(c) to roughly align with RD and have high-angle boundaries separating the variants and low-angle boundaries separating the (sub)grains within each variant, Figure 6.4(d).

Processes of grain subdivision during the prior rolling of this material have resulted in the development of grain clusters of lattice orientation corresponding to the two variants near the C texture components. According to the deformation-banding model for texture development [Refs. 29, 34-35, 41, 174], the microstructure would comprise elongated, ribbon-like grains that alternate in lattice orientation. Substructure within such grains would reflect the need for accommodation of the $\varepsilon_{RD,ND}$ shear term and of the Al_3CaZn particles, although the presence of these particles would also disrupt the tendency to form well-defined bands. Thus, the disorientation of the high-angle boundaries in this material became established during the prior deformation processing as

a result of grain subdivision and lattice rotation toward the end orientations of the texture variants. The disorientation of the high-angle boundaries is the lattice rotation that relates the variants of the texture (nominally 52° in this material). Cell and substructure formation within the bands during deformation processing then accounts for the disorientation of the lower-angle boundaries. Continuous recrystallization during elevated temperature static annealing of this alloy reflects the recovery-controlled development of the boundaries within the deformation-induced microstructure. These processes would include climb-controlled rearrangement of dense dislocation arrays that separate the adjacent grain clusters, or the cells within clusters, resulting in the evolution of well-defined boundaries in place of the arrays. Grain growth during annealing results in the elimination of many boundaries developed during the prior deformation, but in a manner that maintains the texture in the material. Thus, grains or cells of initial lattice orientation near that of either variant of the texture apparently grow at the expense of nearby regions having lattice orientations in the random population due to lattice curvature associated with a high dislocation density.

2. Elevated Temperature Deformation of Al-5%Ca-5%Zn Material

The microstructure of the Al-5%Ca-5%Zn alloy of this study consists of adjacent grain clusters having lattice orientations corresponding to the symmetric variants of the main texture component. The interfaces that separate the grain clusters as well as those that separate cells within the clusters are deformation-induced boundaries that evolve from dense dislocation arrays by recovery.

A contribution of dislocation creep to the superplastic response during tensile deformation in the rolling direction at 400°C and 10^{-2} sec^{-1} is evident in the micro-texture data of Figure 6.5(b). The C texture component is distinct in the micro-texture data of Figure 6.5(b). A <111> becomes aligned with the tensile axis as lattice rotation to the exact C orientation takes place during tensile extension parallel to the RD. Grains with such a lattice orientation can deform compatibly with their neighbors during dislocation creep and without further lattice rotation. Thus, the C component is a stable end orientation in the texture for uniaxial tension parallel to the RD. The absence of fiber texture formation may be further understood by considering deformation of a fcc crystal along an axis that lays near a <111> direction, e.g. 5° from such an orientation. It is

straightforward to show by means of a stereographic projection that the lattice rotations needed to bring the tensile axis for such a crystal into alignment with the <111> in question will take place about an axis that is perpendicular to that <111> and not parallel to it. Thus, such small rotations will have the effect of stabilizing the pre-existing C component but will not produce a fiber texture. The limited extent of grain elongation apparent in the grain map of Figure 6.5(a) is consistent with a contribution of grain-boundary sliding to the total strain, but the high-angle boundaries are still predominantly the interfaces between variant grains.

Deformation of samples with tensile axes parallel to the TD resulted in the development of a B-type texture component [Ref. 64] and, again, the absence of fiber texture formation. This is evident in the micro-texture data of Figure 6.6(b). The apparent instability of the C component and subsequent lattice rotation resulting in the development of a B texture component during transverse tensile deformation requires further assessment and has been explained in detail elsewhere [Ref. 63]. In summary, lattice rotation occurs in order to align a <111> direction with the tensile axis thus distributing the deformation over equally stressed slip systems. The exact C orientation with four equally stressed slip systems may reflect a metastable condition when the material is strained in uniaxial tension along the transverse direction. Orientations initially located slightly away from C along the symmetry boundary already have higher Schmid factors for the two coplanar systems above, and therefore would tend to rotate along the symmetry boundary toward B rather than back toward the C orientation.

VII. MICROSTRUCTURE OF PURE ALUMINUM AND AN ALUMINUM ALLOY AFTER EQUAL-CHANNEL ANGULAR PRESSING

A. INTRODUCTION

The properties of metallic materials may be improved through grain refinement using processes that include severe plastic deformation (SPD). Recent studies have shown that ultra-fine grain sizes in the submicrometer or even nanometer range can be achieved by imposing extremely large plastic strains during deformation processing [Refs. 14, 175-177]. In addition to the SPD methods briefly reviewed in Chapter I, {high pressure torsion (HPT), accumulative roll bonding (ARB), asymmetric rolling and friction stir processing (FSP)}, redundant forging [Refs. 178-180], high energy ball milling [Ref. 13], sliding wear [Ref. 181] and equal-channel angular pressing (ECAP) are some processes developed in order to impart strains which are sufficiently large to produce such grain refinement. This study will concentrate on equal-channel angular pressing (ECAP) and will present results obtained by OIM methods in the SEM allowing the simultaneous determination of orientation-based images and quantitative assessment of the microtexture and the distribution of the grain-to-grain disorientation angles. Additional results from TEM methods will be provided in order to verify the results obtained in specific conditions.

A detailed introduction to the process of ECAP has been provided in Chapter II, including: process description, route definition, axis definitions, and specifics of sample sectioning. Additionally, the trace of the shear plane and the sense of the shear are indicated in Figures 7.1(a) and 7.1(b) for planes that have y-axis normals. These illustrations demonstrate the need to carefully identify the positive senses of the axes during sectioning of the ECAP billets: the apparent alignment of the shear plane as well as the sense of the shear depends on whether the section being examined has the -y or +y direction as its normal. The x-z plane is not a mirror plane and if the sense of the y direction is not correctly determined the resulting data may suggest a shear direction rotated 90º from its expected orientation.
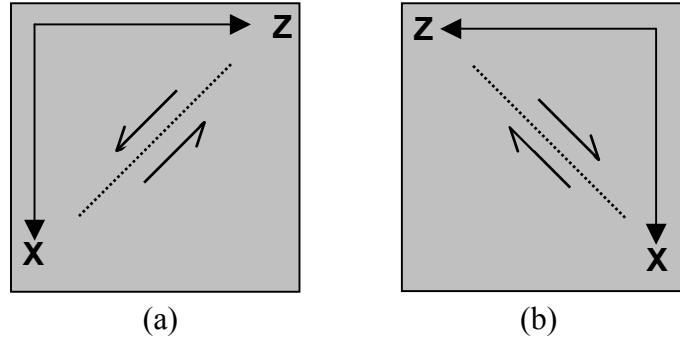
Figure 7.1. A schematic of the y plane in (a), viewed in the +y direction, indicating the shear plane and sense of shear while (b) represents a schematic of the same y plane but viewed in the -y direction with the corresponding trace of the shear plane and sense of shear indicated.

The shearing characteristics and the corresponding microstructural changes associated with the various processing routes that are possible have been analyzed for repetitive ECAP [Refs. 15, 112]. Following a single pass, TEM has revealed the presence of a cellular microstructure consisting of elongated, parallel bands of subgrains [Ref. 16, 120-121]. These bands tend to be aligned with the top and bottom edges of the pressed sample (the y direction) when viewed in the x plane. They are also roughly parallel to the direction of shear in the y plane, which in turn is inclined ideally at 45° to the top and bottom edges of the pressed sample (the x direction) when viewed in the y plane. In the z plane, the subgrain bands are arranged perpendicular to the direction of flow, which is the x direction. These microstructural features reflect the deformation occurring upon passage through the die since this requires intense shear in the shear direction on a plane inclined at 45° to both x and z.

The microstructure following repeated ECAP is dependent upon the nature of any rotation between the pressing operations. It was shown earlier by use of TEM that the evolution to a refined, equi-axed structure with an apparent presence of high-angle grain boundaries was most rapid for processing by route B_C, less rapid using route C and slowest using routes A and B_A [Ref. 100]. The evolution of the grain boundary disorientation distribution during repetitive pressing by route B_C was examined by electron backscatter diffraction (EBSD) microtexture analysis using interactive [Ref. 182] and automated acquisition [Ref. 120] methods to acquire grain-specific orientation data. A progressive increase in grain boundary disorientation and randomization of the texture

accompanied the refinement of the microstructure during repetitive ECAP [Ref. 182] via route B_C. However, the later study [Ref. 120] and comparison to other work [Ref. 122] indicated that the former material had recrystallized and developed a predominantly random texture rather than a cube recrystallization texture common to aluminum [Ref. 67]. It is considered that recrystallization occurred in the high purity aluminum due the combined influence of the metal purity and the adiabatic heating experienced by the billet upon passage through the ECAP die [Ref. 183]. Later studies [Refs. 120, 122] have shown that the population of low-angle boundaries (≤15°) remains greater than expected from texture considerations, which reflects the presence of deformation-induced boundaries after each pressing.

B.   EXPERIMENTAL PROCEDURES

The pure aluminum material was rolled into a plate at room temperature and cut to provide billets with dimensions of $25 \times 25 \times 150 mm^3$. These billets were swaged to rods of 10mm diameter, which were then cut into lengths of ~60mm. Prior to ECAP, these billets were given an annealing treatment resulting in an initial recrystallized grain size of ~1mm. X-ray investigations of the pure aluminum suggested a random initial texture [Ref. 184] and neutron diffraction methods indicated a weak fiber texture with a <111> aligned with the axis of the original unpressed material [Ref. 185]. The details of the preparation of the Al-3%Mg-0.2%Sc alloy have been provided elsewhere [Ref. 112]. The general description is the same as that of the pure aluminum except the original grain size was ~200μm and no texture data were provided.

Material conditions examined included: as-pressed billets of 99.99% pure aluminum after one, four and twelve pressing operations; and an Al-3%Mg-0.2%Sc alloy that had been pressed eight times and annealed at 400°C for ~10min. The annealing was intended to simulate heating prior to elevated temperature deformation [Ref. 112]. Both materials were pressed following the definitions of routes A, B_C and C for repetitive pressing operations.   Samples were sectioned as outlined in Chapter II.   Prior to examination in the SEM, samples were mechanically polished as detailed in Chapter II and then electropolished in the Buehler Electromet 4 apparatus using a 20% percholoric

acid - 80% ethanol electrolyte solution cooled to -25°C. The TEM thin foils were electropolished using an electrolyte consisting of 10% perchloric acid and 90% ethanol cooled to 0°C with the applied voltage set to 10V.

C. RESULTS

1. Microtexture Development of Pure Aluminum During ECAP

Results for pure aluminum after one, four and twelve ECAP passes via route B_C have been reported previously [Ref. 120]. These indicated the presence of an inhomogeneous texture after an initial ECAP operation in regions examined that were 20μm X 20μm and 100μm X 100μm. Selected examples are presented in Figure 7.2(a) and (b) for 100μm X 100μm areas for material that has been processed through one ECAP pass. These data show either a single or multiple prominent orientations. Another evaluation was conducted over a very long traverse (3.75mm) in the z direction, which represented 37.5% of the sample diameter. This microtexture data is presented in Figure 7.2(c) and shows the presence of a shear-induced deformation texture. An idealized A+B shear texture, adapted from Canova et al. [Ref. 132], is provided for comparison. The shear direction (SD) is indicated by a red arrow and shear plane normal (SPN) by a black arrow in Figure 7.2(c). Altogether, the data of Figure 7.2 indicate the presence of a shear texture in this material. However, the texture is inhomogeneous and a large volume of material must be examined before a complete shear texture is observed. Also, the shear plane and shear direction apparent in the texture do not correspond to the shear plane and shear direction expected from the ECAP die geometry. Instead, the trace of the shear plane as well as the shear direction are rotated toward the x axis by about 30º. If this discrepancy is taken into account and the resulting shear textures are represented in Euler space it is possible to calculate the relative integrated intensities of orientations along the A and B fibers. Accordingly, the A fiber component accounts for ~10 times more orientations than the B fiber component.

114
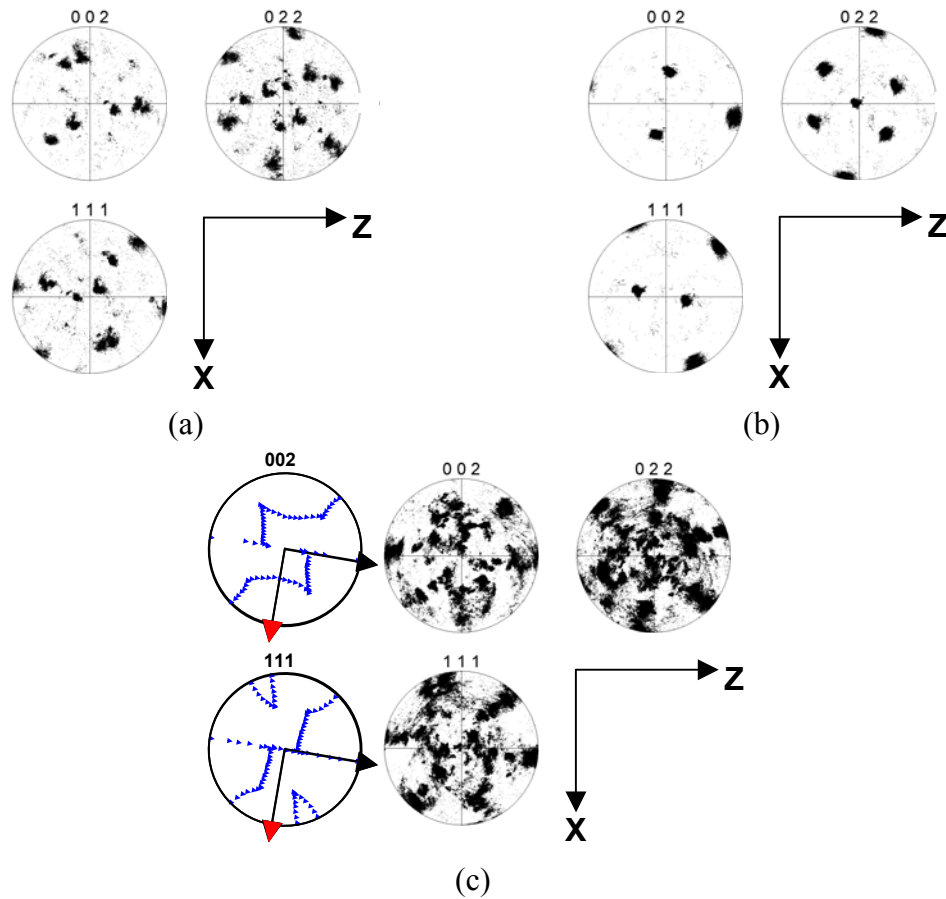
Figure 7.2. Discrete pole figures from the y plane for pure aluminum after one ECAP pass. (a) and (b) are representative examples from 100μmX100μm regions illustrating the inhomogeneous texture at that level of resolution. (c) is from a region traversing 3750μm (37.5% of the sample diameter) in the z direction, showing the presence of a shear texture and ideally represented as A+B type, with the shear direction indicated by the red arrow. The intensity for the A type shear texture is 10x the B type.

The previous study showed a results for material pressed four times via route B_C, and indicated an inhomogeneous microtexture as well [Ref. 120]. Examples of textures from 100μm X 100μm areas are provided in Figure 7.3(a) and (b). A similar approach was taken to investigate the texture over a larger dimension in the z direction. A traverse of ~10% (1.0 mm) of the sample diameter again showed the presence of a complete shear texture; again, this is compared to the idealized shear texture in Figure 7.3(c). A rotation of the shear plane trace and shear direction of almost 45° about the y axis toward the x axis is necessary in order for the observed and idealized shear textures to coincide. In the rotated reference frame the A and B components were found to have almost equal
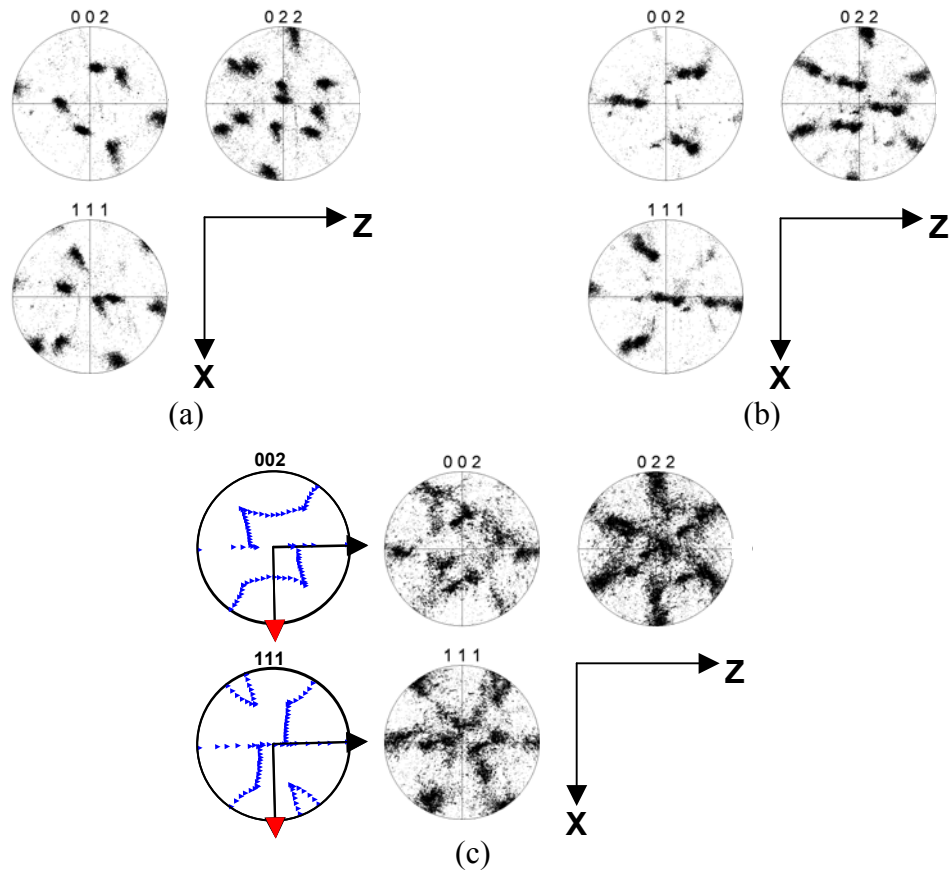
Figure 7.3. Discrete pole figures from the y plane for pure aluminum after four ECAP passes via route B_C. (a) and (b) are representative examples from 100μmX100μm regions illustrating the inhomogeneous texture at that level of resolution. (c) is from a region traversing 1000μm (10% of the sample diameter) in the z direction, showing the presence of a shear texture and ideally represented as A+B type, with the shear direction indicated by the red arrow. The intensities are the same level above random, which is ~2.5 times.

intensities of ~2.5 times random. The same comparative approach was taken to investigate material pressed four times via routes A and C. The results presented in Figure 7.4(a) and (b), for routes A and C, respectively. Route A has a dominant A type shear texture while route C contains nearly equal intensities of A and B type.

The shear texture was well developed by twelve pressings and evident in the 100μm X 100μm regions as previously investigated for route B_C [Ref. 120]. Similar results for routes A and C have also been reported [Ref. 121]. The microtexture from selected 100μm X 100μm areas and the ideal shear alignment are provided for routes A, B_C and C in Figure 7.5(a), (b) and (c), respectively. Rotations of ~30º about the y axis are needed in order for the reference axes of the ideal and observed shear textures to

116
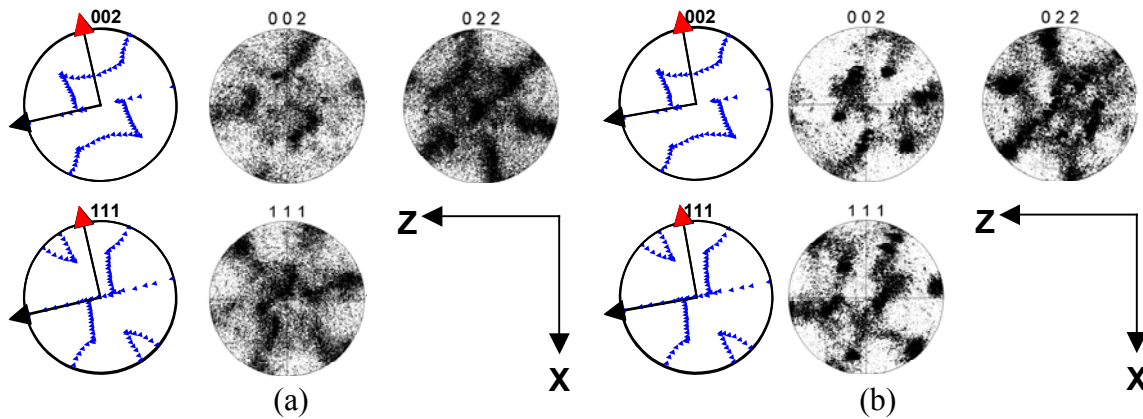
Figure 7.4. Discrete pole figures from the y plane for pure aluminum after four ECAP passes via route A (a) and C (b) from a regions traversing 1000μm (10% of the sample diameter) in the z direction. The presence of a shear texture and ideally represented as A+B type, with the shear direction indicated by the red arrow. The intensities for route A indicate a prominent A type shear texture 3x the level of the B type; route C has a equal A and B components at 1.5x random.

coincide. All routes were found to have higher concentrations of the A type shear texture while route B_C showed highest A type intensity at 14x the random. However, the microtexture for all three routes has become more diffuse, indicating the presence of more random orientations in the structure. The integrated intensities for each shear texture type for the various pressing conditions is summarized in Table 7.1.

Pure Al - 1 Pass	A type = 14		
	B type = 1.3		
Multiple Pressings	Route A	Route B_C	Route C
Pure Al - 4 Passes	A type = 3	A type = 2.5	A type = 1.2
	B type = 1	B type = 2.2	B type = 1.3
Pure Al - 12 Passes	A type = 6	A type = 14	A type = 2.8
	B type = 1.2	B type = 1.2	B type = 1.2

Table 7.1. Maximum intensity (times random) of shear texture type for various ECAP conditions.

(a)

(c)
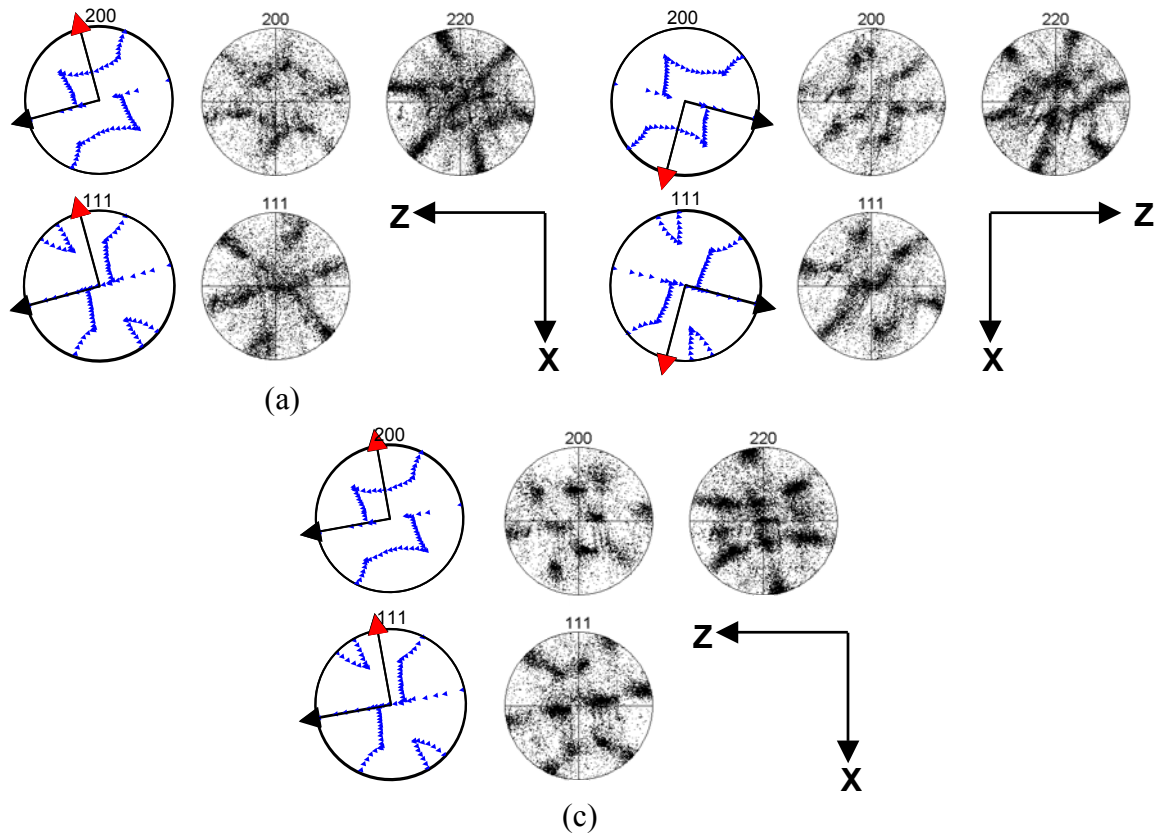
Figure 7.5. Discrete pole figures from regions on the y plane 100μmX100μm for pure aluminum after twelve ECAP passes via (a) route A, (b) route B_C and (c) route C. The ideal A+B shear texture is also shown with the shear direction indicated by the red arrow. The intensities for route A indicate a predominant A type shear at ~6x random while the B type is near random intensity; route B_C has nearly equal fractions of A and B shear textures, both slightly above random (~1.4x random A type and ~1.2x random B type; route C is also predominantly A type ~3x random while the B type is equal to the random intensity.

2.   Microstructure of Pure Aluminum After One ECAP Pass

Results for pure aluminum following one ECAP pass have already been reported [Refs. 15-16, 120]. In summary, TEM results have shown that the structure is comprised of bands of (sub)grains that are elongated and nearly aligned with the shearing direction. Within the limit of resolution of the OIM technique the OIM results were in agreement with the TEM data. Representative OIM grain maps from the y and x planes are provided in Figure 7.6 along with linear misorientation traverses showing gradual lattice rotation over long (>10μm) distances indicating the presence of the substructure below the resolution limit of OIM.

118
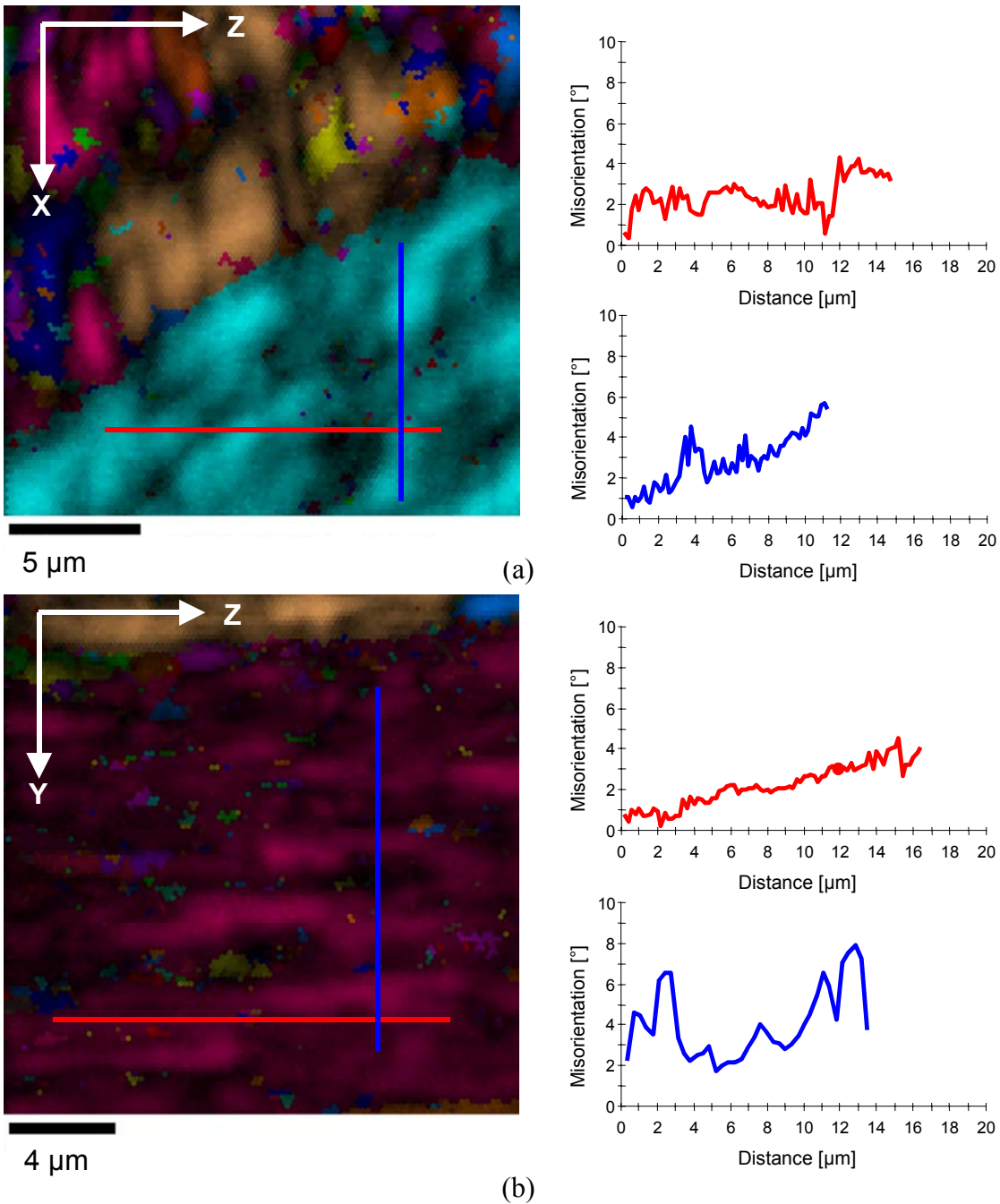
Figure 7.6. OIM data from pure aluminum after one ECAP pass. A representative example of y plane data in (a) showing a unique grain color map with IQ superimposed, the locations of the z and x linear profiles, and the associated misorientation profiles in red and blue respectively. In (b), a representative example of x plane data again showing a unique grain color map with IQ superimposed, the locations of the z and y linear profiles, and the associated misorientation profiles in red and blue respectively.

In addition, the microstructure was generally found to be inhomogeneous. The apparent grain size from the OIM unique grain color maps varied greatly from location to location. The corresponding disorientation distributions generally contained large fractions (from 40% to 70%, depending on location) of low-angle (2° - 5°) boundaries, which is consistent with the presence of a deformation-induced microstructure. The locally inhomogeneous nature of the structure reflected the coarse grain size (~1mm) prior to ECAP.

3. Microstructure of Pure Aluminum After Four ECAP Passes

Representative OIM unique grain color maps of the microstructures for pure aluminum processed either by route A, B_C or C are provided in Figures 7.7(a), (b) and (c) respectively. These maps were produced with an orientation tolerance of 2°. All routes were found to give some common characteristics to the microstructure. First, the grains tend to be aligned and elongated in the direction of shear from the last pressing operation. The grain size does not vary significantly from route to route, and all grain sizes for these data are ~1.3μm. This grain size value is also consistent with TEM examination of this material [Refs. 15-16, 120], in which a grain size of ~1.2μm was observed after four ECAP passes by route B_C. Additional results of microstructural analysis along the x and z directions (not included here) revealed that all the process routes had a similar effect on homogenizing the microstructure. Furthermore the microstructure was essentially homogeneous after four ECAP passes.

The aforementioned highlighting technique available in OIM was performed on data from larger areas (100μmX100μm) using the acquired local microtexture data, in the form of discrete pole figures, and OIM IQ maps seen in Figure 7.8(a), (b) and (c) for routes A, B_C and C, respectively. These figures indicate that alternating bands of similar orientation, separated by boundaries of high disorientation ($\theta > 40°$), are present in all processing routes. The thickness and preferred orientations vary from route to route as well as locally within each sample. These differences in microtexture are the result of the different rotations of the samples associated with the various routes and the presence of various components of the shear texture at the scale investigated. The resulting preferred

4 μm (a) **4 μm** (b) **4 μm** (c)
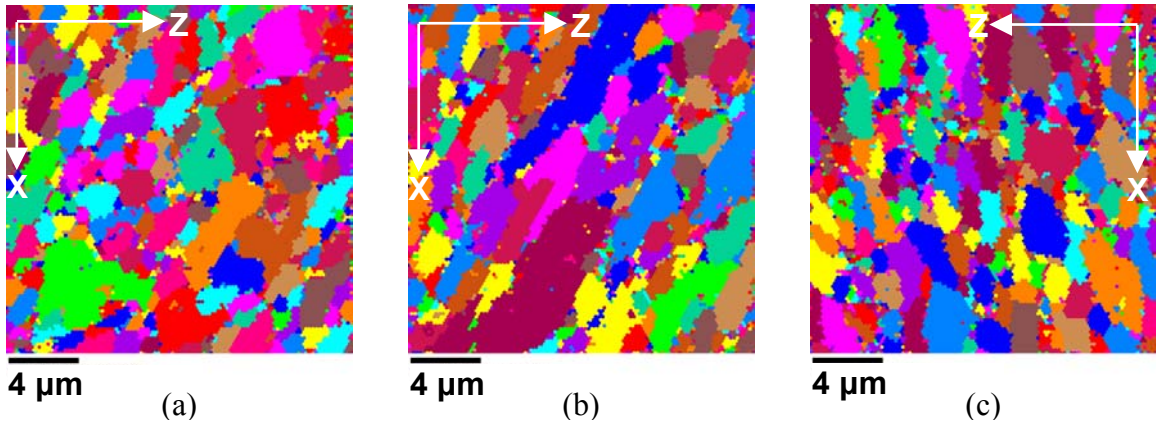
Figure 7.7. OIM unique grain color maps for pure aluminum after four repetitive ECAP pressings following (a) route A, (b) route B$_C$ and (c) rout C with the positive x and z directions indicated. All grain maps show a general tendency for the grains to elongate and align with the direction of shear in the last pressing operation while being of similar (~1.3μm) size, regardless of the process route.

local orientations tend to be alternating in nature, which may allow the greatest amount of

25 μm (a) **25 μm** (b) **25 μm** (c)

25 μm (d) **25 μm** (e) **25 μm** (f)
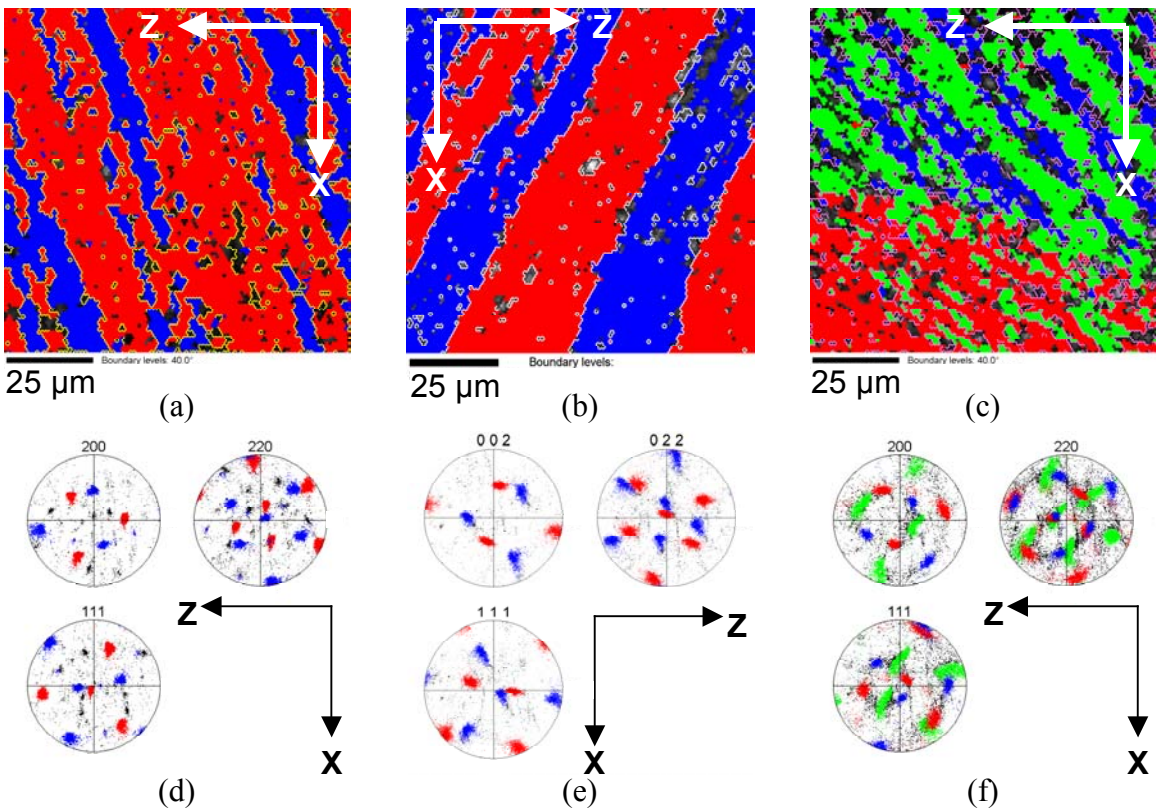
Figure 7.8. OIM IQ only maps for pure aluminum after four ECAP passes following (a) route A, (b) route B$_C$ and (c) route C with the locations of various texture components highlighted as well as boundaries with disorientation in excess of 40°. Discrete pole figures from (d) route A, (e) route B$_C$ and (f) route C with the corresponding texture components highlighted.

121

plastic deformation with a minimum of slip systems active for the local region.

TEM investigation of route B_C was conducted in order to confirm the results obtained by OIM and to ensure that micro-scale features of importance were not overlooked. The data in Figure 7.9 shows the scale of the microstructure to be similar to that reported in this and previous investigations [Refs. 15-16, 120], as well as the tendency of the grains to be slightly elongated and aligned with the direction of the last shearing operation. Furthermore, the use of the TOCA system to analyze CBED patterns and, hence, local grain orientations, confirms the presence of alternating bands of (sub)grains separated by high-angle boundaries. The exact alternating orientations obtained in the TEM are not identical to those obtained by OIM, but can still be attributed to various components of the shear texture.

The disorientation distributions for pure aluminum after four pressings by route B_C as obtained by the TEM and SEM investigations are presented in Figure 7.10(a) and (b), respectively. While not identical, the distributions of disorientations are comparable when the angular resolution of CBED pattern analysis in the TEM and the number of boundaries encountered in the OIM investigation are considered. The large fraction of boundaries in the 0°-5° bin in the TEM data is a direct result of the greater angular resolution afforded by this method. It also reflects the inability to distinguish gradual lattice curvature with the OIM system, as shown earlier. The lower total number of boundaries in the TEM analysis can be attributed to the limited area investigated in the analysis, and this, in turn, contributes significantly to the standard error in the TEM data. The similarities should also be emphasized. Both distributions show large fractions of low-angle boundaries and the presence of high-angle boundaries.

This confirmation and analysis can be extended to routes A and C. A TEM investigation would be expected show bands of (sub)grains with similar orientations, separated by low-angle boundaries roughly aligned with the shear plane of the last pressing pass. Also, these bands would alternate in orientation and be separated by boundaries of high disorientation.
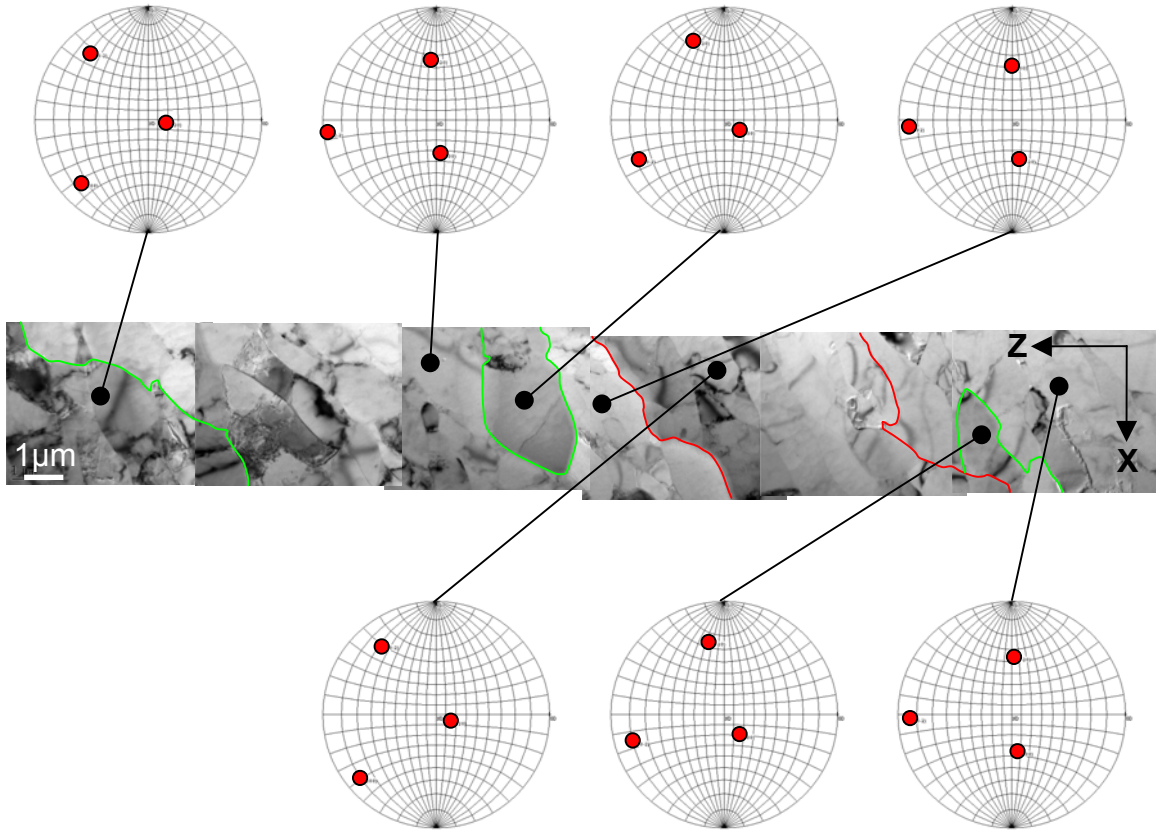
Figure 7.9. TEM montage of pure aluminum after four repetitive ECAP passes via route B_C analyzed using CBED patterns and TOCA to determine orientation and disorientations. The red highlighted boundaries correspond to disorientations in excess of 40°, while the green is from 15° to 40°. All other apparent grain boundaries are less than 15° in disorientation; most are less than 5°. The representative (200) pole figure axes coincide with the indicated sample axes and represent some of the local orientations.
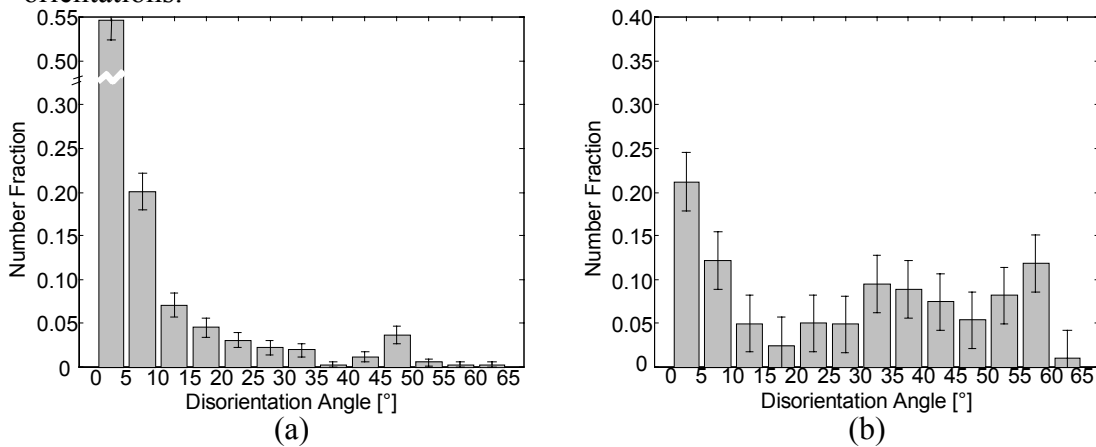
Figure 7.10. Disorientation distributions for pure aluminum after four ECAP passes via route B_C from the y plane as collected by (a) TOCA in the TEM and (b) OIM in the SEM.

123

4.   Microstructure of Pure Aluminum After Twelve ECAP Passes

Material that had undergone twelve ECAP passes was similarly examined. The OIM unique grain color maps in Figure 7.11(a), (b) and (c) correspond to material pressed twelve times by route A, B_C or C, respectively. The grain maps indicate a further slight grain refinement, to the same apparent size of ~1.0μm for all routes.   Less elongation in the shear direction of the last pressing operation is evident than in the material after four ECAP operations. However, the grains still tend to be aligned with the shear direction of the last pass.   This indicates the retention of deformation-induced features in the microstructure at this point in the processing.

Microtexture data in the form of highlighted discrete pole figures and IQ maps were used to show the locations of the various shear texture components and are presented in Figure 7.12 for routes A, B_C and C. Although there are no noticeable band-like features present at this stage in the processing, groups of (sub)grains are still clustered about a similar orientation that belongs to the shear texture, and the various orientations of the shear texture in the microstructure are separated by high-angle boundaries. Also of note is that the shear texture is now present on a scale of 100μm or less, indicating that the bands present after four pressing operations have been reduced in thickness, or cut in the course of repetitive pressing operations. As in material pressed

5 μm   (a)   4 μm   (b)   5 μm   (c)
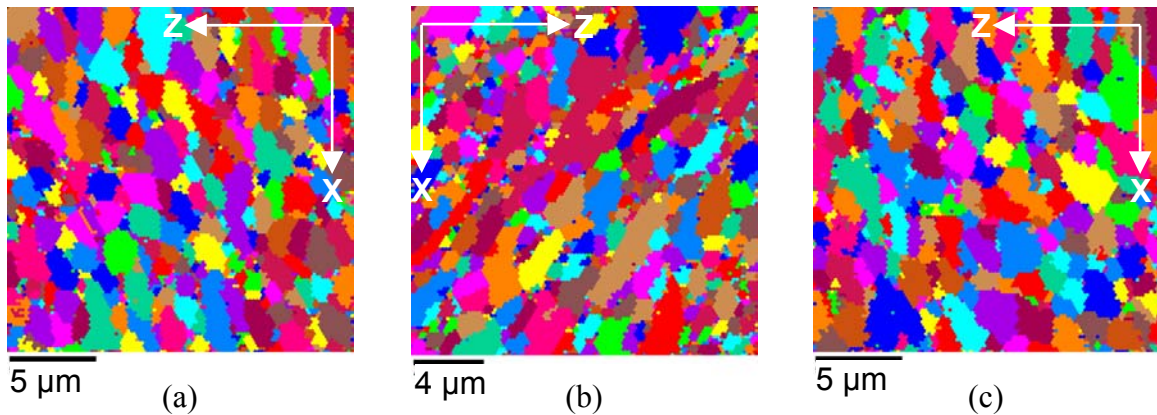
Figure 7.11. OIM unique grain color maps for pure aluminum after twelve repetitive ECAP pressings following (a) route A, (b) route B_C and (c) route C with the positive x and z directions indicated. In comparison to Figure 7.7, all grain maps again show a general tendency for the grains to elongate slightly and align with the direction of shear of the last pressing operation. The apparent grain size for all pressing conditions has been further refined to ~1.0μm, but appears to have little dependence on the process route followed.

four times, the shear texture from the final pass through the ECAP die can be discerned as the dominant texture feature, however other 'random' orientations are seen to be present in significant numbers.

TEM investigation of route B_C material was again conducted in order to confirm the results obtained by OIM, and to ensure that micro-scale features of importance had not been overlooked. The data of Figure 7.13 shows a microstructure essentially identical to that reported in this and in previous investigations [Refs. 15-16, 120], and also illustrates the tendency of the grains to be more equi-axed in shape. CBED analysis confirmed the presence of clusters of (sub)grains separated internally by low-angle boundaries and externally by high-angle boundaries. The alternating orientations obtained in four pass material are no longer predominant but instead have been replaced by the clusters resulting from the continued severe deformation of the material in shear.
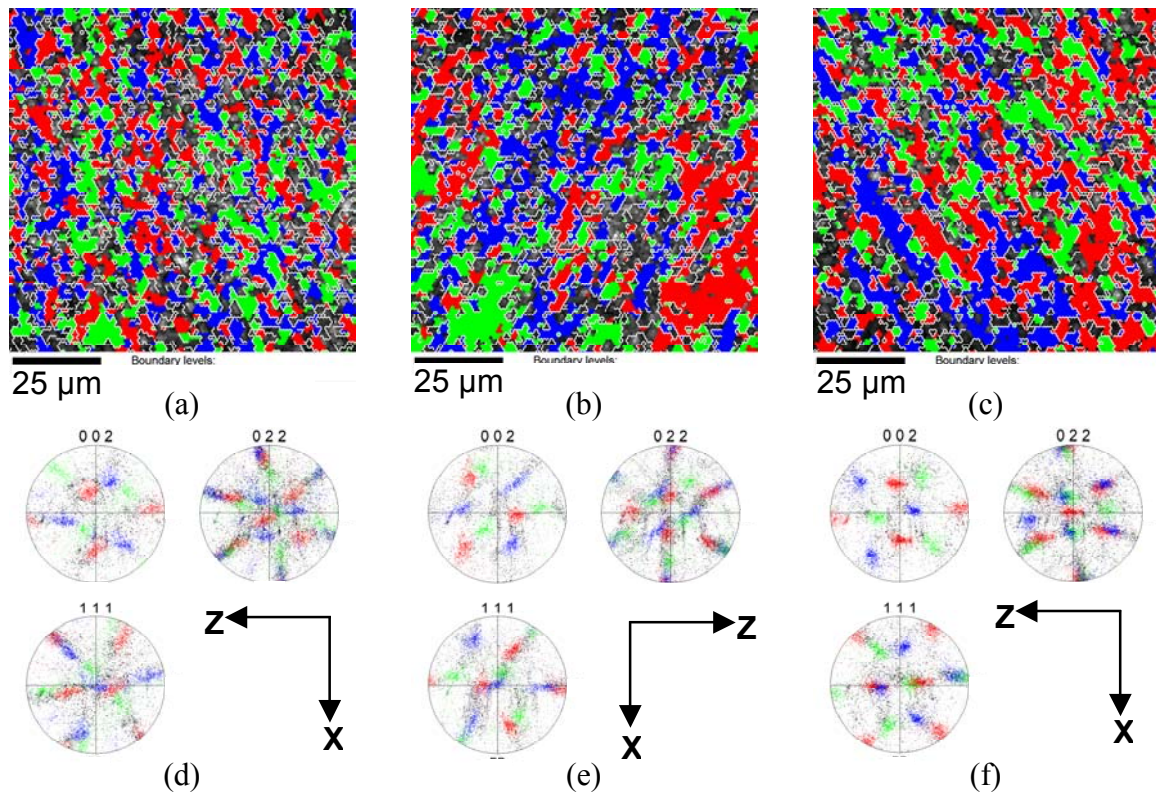
Figure 7.12. OIM IQ only maps for pure aluminum after twelve ECAP passes following (a) route A, (b) route B_C and (c) route C with the locations of various shear texture components highlighted as well as boundaries with disorientations in excess of 40°. Discrete pole figures from (d) route A, (e) route B_C and (f) route C with the corresponding shear texture components highlighted.
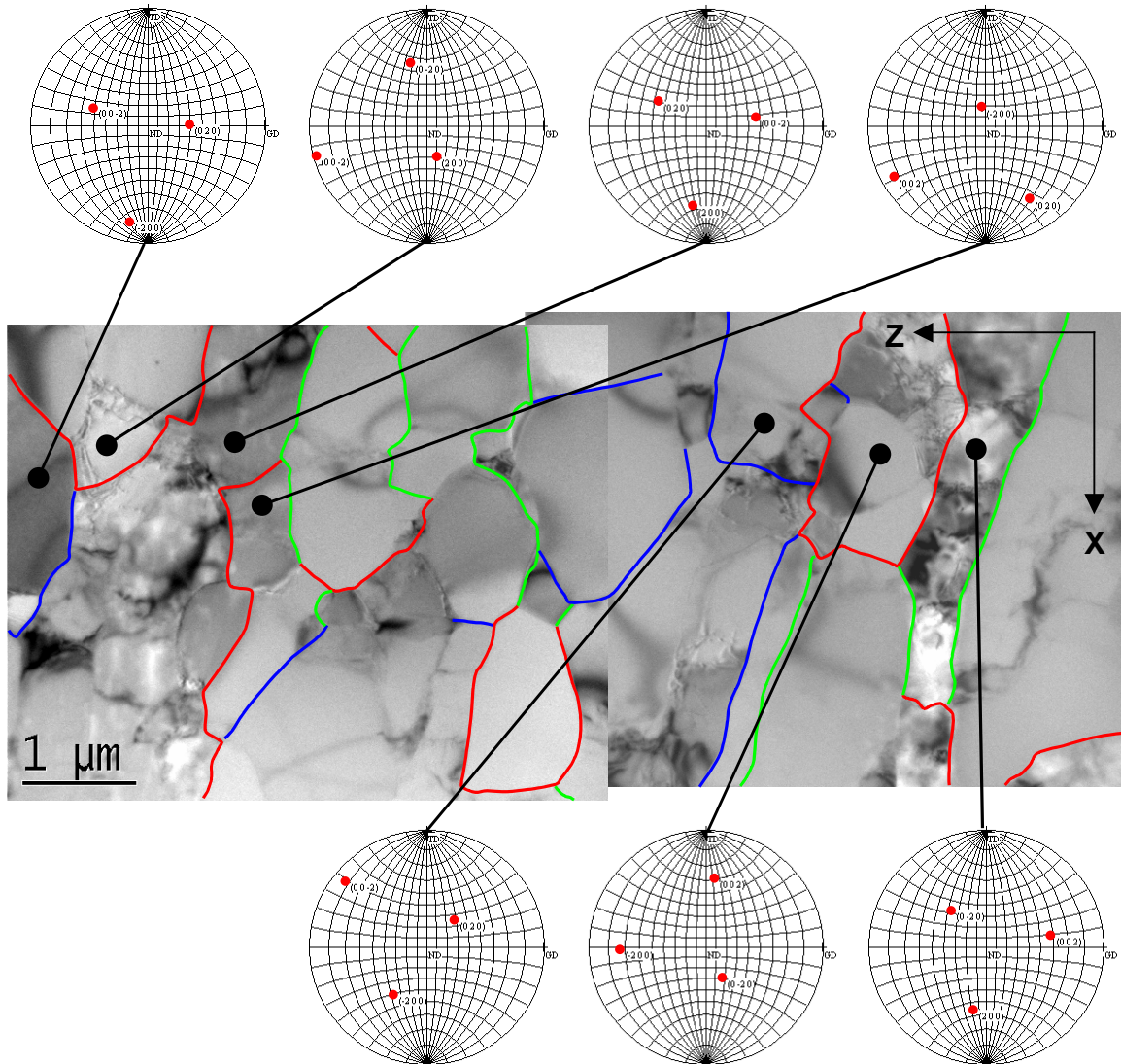
Figure 7.13. TEM montage of pure aluminum after twelve repetitive ECAP passes via route B_C analyzed using CBED patterns and TOCA to determine orientation and disorientations. The red highlighted boundaries correspond to disorientations greater than 40°, green indicates boundaries from 15° to 40° and blue highlights boundaries from 10° to 15°. All other boundaries have less than 10° disorientation. The representative (200) pole figures axes coincide with the indicated sample axes and represent some of the local orientations.

A comparison of disorientation distributions obtained by TEM and SEM methods from the pure aluminum after twelve pressings by route B_C is presented in Figure 7.14. The results are similar to those reported for material after four ECAP passes. Specifically, there is a larger fraction of boundaries in the 0°-5° bin for the TEM data {Figure 7.14(a)} due to the finer angular resolution, 0.1°, of CBED analysis as compared

126

to the 2° limit of resolution for the OIM data {Figure 7.14(b)}. Other than the 0°-5° bin the distributions are similar in all disorientation ranges when the standard error is considered. Both distributions show large fractions of low-angle boundaries indicating the presence of a deformation induced microstructure and an overall increase in the fraction of high-angle boundaries when compared to material processed by four ECAP passes. Again, it may be inferred that Routes A and C will also demonstrate the same characteristics if investigated using TEM methods. Specifically, a TEM investigation would be expected show (sub)grain clusters of similar orientation, low-angle boundaries separating the (sub)grains, and high-angle boundaries separating the clusters.

(a)
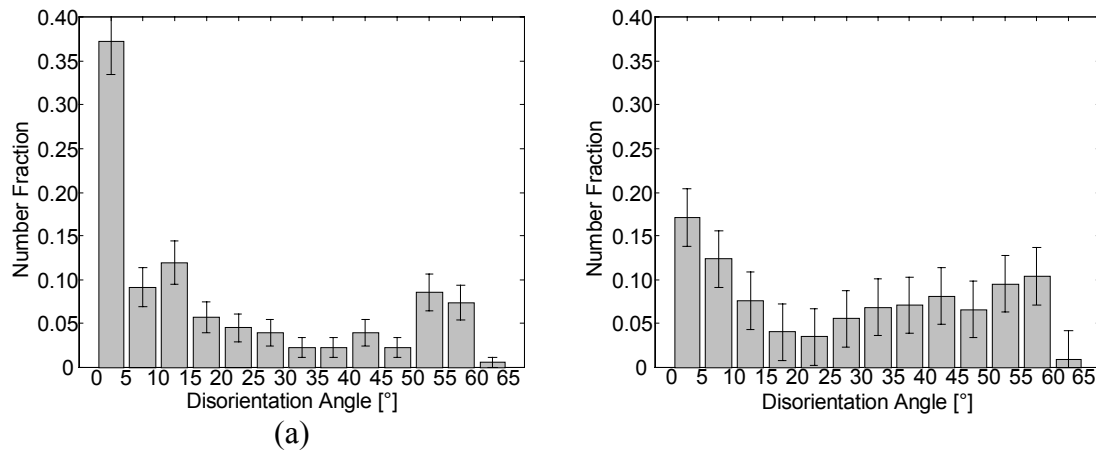
Figure 7.14. Disorientation distributions for pure aluminum after twelve ECAP passes via route B_C from the y plane as collected by (a) TOCA in the TEM and (b) OIM in the SEM.

5. Microstructure and Microtexture of Al-3%Mg-0.2%Sc After Eight ECAP Passes

Al-3%Mg-0.2%Sc material that had undergone eight ECAP passes and subsequent annealing at 400°C for ~10min, was examined using these same techniques. The OIM analysis revealed a grain size of ~1.0μm, which is similar to that reported earlier [Ref. 112]. The locations of the various shear texture components and are presented in Figure 7.15 for routes A, B_C and C using highlighted IQ maps along with the corresponding discrete pole figures. Groups of (sub)grains are again found in clusters corresponding to the various shear texture orientations and the clusters are separated by high-angle boundaries. The shear texture is now present on a fine scale after eight pressing operations, indicating that the band-like features observed in the pure aluminum

127
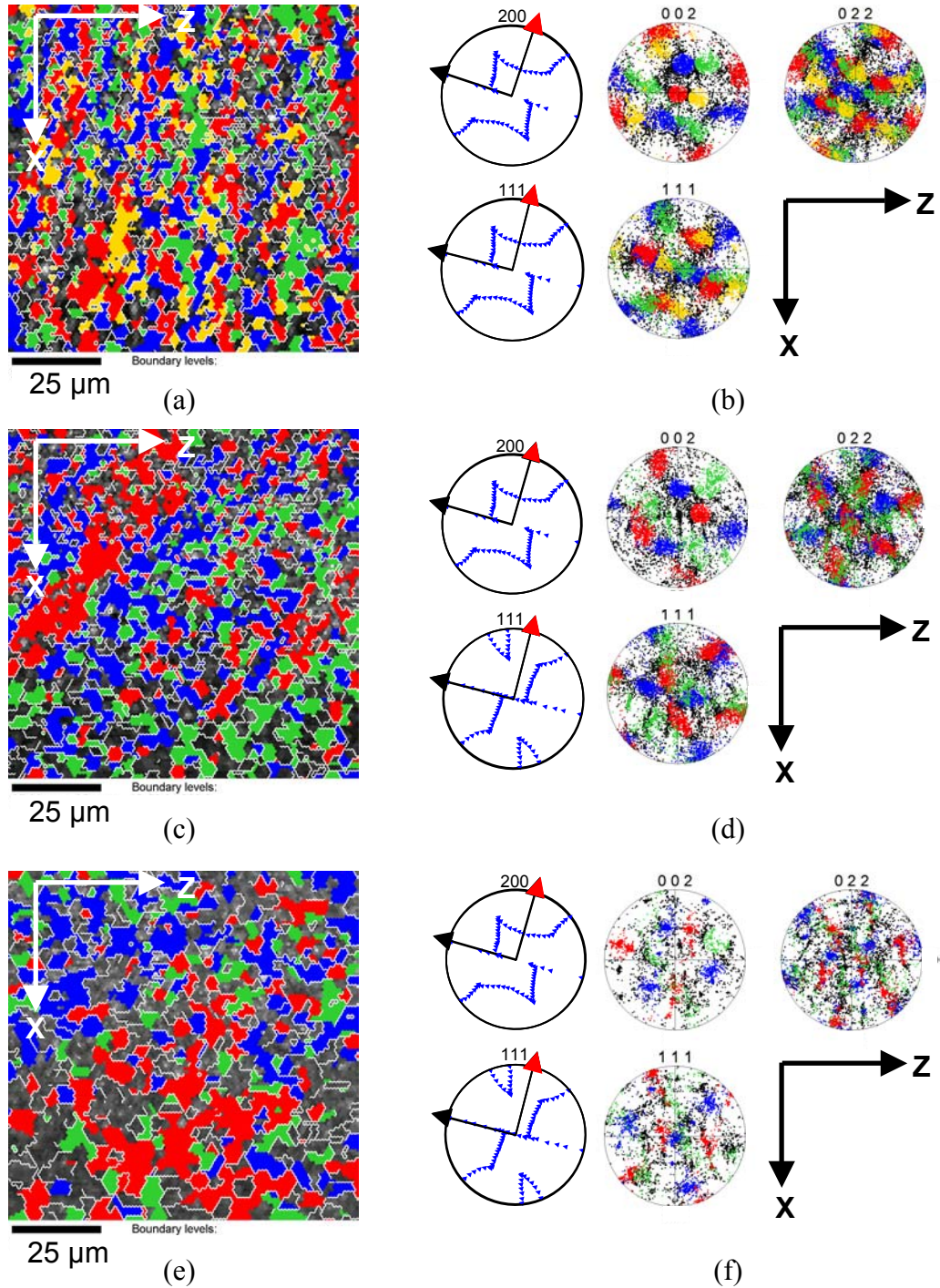
Figure 7.15. OIM IQ only maps with regions corresponding to the associated discrete pole figures highlighted along with boundaries in excess of 40° (in white) from regions 100µm^2 of Al-3%Mg-0.2%Sc after eight ECAP passes and a 400°C anneal to simulate times encountered during superplastic deformation via route A in (a) and (b), route B_C in (c) and (d) and route C in (e) and (f). The shear texture intensities are as follows: in route A, A type 4.5x random, B type 8.5x random; route B_C, A type 1.5x random, B type 3x random; and route C, A type 13x random, B type equal to random.

128

have been broken up into clusters more readily as a result of the alloying additions. As in material pure aluminum pressed twelve times, the shear from the final pass through the ECAP die can be discerned as the dominant texture, however random orientations are present in significant numbers.

D.   DISCUSSION

It has been well established that severe plastic deformation (SPD) by repetitive ECAP may be employed to produce grain sizes at the micron or sub-micron scale. However, predictive models for the process of grain refinement remain to be developed. Processing nominally pure aluminum through a single ECAP pass at room temperature leads to the development of elongated bands of (sub)grains. It has been shown elsewhere [Refs. 15-16, 120] that the bands are ~1.2μm in width, ~4μm in length and nominally aligned with the trace of the shear plane. A banded microstructure is also evident in the OIM results excepting that the bands are not of uniform size throughout the sample. OIM results also indicate the presence of similar orientations over large regions of the sample and accompanying lattice curvature, indicating a buildup of dislocations that are arranged to form low-angle boundaries. The micro-texture varies from location to location at a micro level but at each location is part of a macroscopic shear texture present in the material. A band-like sequence of orientations was not readily apparent in material after one ECAP pass. However, regions of different orientations that are separated by high-angle boundaries were encountered in this investigation. It can be inferred that the band structure may have existed on a scale larger than that investigated in 100μm X 100 μm regions and the probable width of the bands was on the order of a few 100's of microns.

Pure aluminum pressed four times by various ECAP routes exhibited similar general characteristics irrespective of route. The apparent grain size was refined to ~1.2μm. The (sub)grains tended to be elongated and aligned with the shear direction of the last pressing pass. A previous study [Ref. 121] indicated that there was no substantial difference in the relative fraction of disorientation distributions to within the error associated with the data collection method, and that the fraction of low-angle boundaries significantly decreased after four pressing operations. The textures developed after four

pressing operations remain inhomogeneous when examined at a scale less than ~10% of the sample diameter. The macro-texture for all routes contain elements of the A and B shear textures to varying degrees. The presence of an alternating band-like structure is seen in all routes with the alternating orientations belonging to various parts of the overall shear texture. It has been reported elsewhere [Ref. 122] that elongated, lamellar structures separated by high-angle boundaries are observed in material after ECAP.

Pure aluminum pressed twelve times and an aluminum alloy pressed eight times by the various ECAP routes indicate the break-up of the alternating band-like features and are subsequently replaced by (sub)grain clusters belonging to shear texture components. The disorientation distributions in the previous study of pure aluminum after twelve ECAP passes by McNelley et al. [Ref. 121] indicate a further reduction in the population of low-angle boundaries without the appearance of a random distribution, predicted by MacKenzie [Ref. 135] for randomly oriented cubes. The disorientation distribution tends to flatten significantly, as would be the case for a pure fiber texture. The difference arise from the incomplete fiber textures developed during shear and the presence of a random texture component that probably results from the rotation of the billet between passes, and the associated reoriented shear direction - shear plane. The microstructure still contains a large fraction of low-angle boundaries, indicating a deformation-induced microstructure.

The formation and subsequent elimination of the alternating band-like features observed here can be explained with a deformation-banding model along with the apparent grain refinement of the material. Plastic deformation will create dislocations and, in turn, generate dislocation pile-ups. This will result in dislocation rearrangement to a minimize the amount of stored energy, i.e. recovery. This recovery process can be aided by the adiabatic heating encountered during plastic deformation. The rearrangement of the like-sign dislocations into low-angle dislocation boundaries may result in lattice curvature over an extended region. In order to minimize the amount of energy expended during subsequent deformation, these regions will be oriented so as to minimize the number of active slip systems and hence reduce the probability of dislocation entanglement and pinning. In order to accommodate the macroscopic plastic

deformation, bands of alternating orientation develop as a result of the combination of lattice curvature and the minimization of active slip systems. The orientation of these regions must be such that the overall macroscopic plastic deformation can be accounted for when all regions are summed together. In other words, a single small region may form bands consisting of one alternating sequence due to the local stress-strain state while another region may form bands with a different set of alternating orientations to accommodate different local stress-strain conditions. The bands would tend to be highly disoriented but still related through a symmetric variant type of orientation difference. If the degree of recovery were sufficient, dislocations may annihilate and the regions separating the band variants could develop into a high-angle grain boundary with a thickness of a few nanometers. The internal structure of the bands would consist of low-angle dislocation boundaries formed to minimize the internal energy and still accommodate the lattice curvature within each band. After one ECAP operation, these bands are probably on the order of the original grain size and the prior grain boundaries may be indistinguishable from the band-band interfaces.

Upon subsequent deformation, the band structure formed in the previous pass would be broken up by the same mechanisms and a new band structure, on a finer scale would become evident. This would result from the existing bands not being amenable to accommodate the new plastic deformation, i.e. different macroscopic stress-strain state, while minimizing the stored energy and utilizing the existing slip systems. The deformation processes previously described (dislocation formation, motion and entanglement, lattice curvature, etc.) would be accounted for by the break-up of the bands into finer bands meeting the criteria outlined above. As shown in this research, the band thickness after four ECAP passes in pure aluminum varied from a few micrometers up to ~25µm depending on the process route and location examined.

This process would be repeated through subsequent pressing operations until the bands are of the same thickness as the (sub)grains within each band. The final ultimate size of these grain-clusters is most likely a function of the alloying content and other material specific parameters.

THIS PAGE INTENTIONALLY LEFT BLANK

VIII. MODELING OF PLASTIC DEFORMATION

A.   INTRODUCTION

Texture modeling was accomplished using the Visco-Plastic Self-Consistent (VPSC) code provided by Dr. C.N. Tomé and written at Los Alamos National Laboratory. The following description is based on the VPSC manual [Ref. 186] for this code, which is written in the FORTRAN77 programming language. The code was written to simulate the plastic deformation of polycrystalline aggregates. VPSC can account for full anisotropy in properties and response of both the individual crystals and the aggregate, where applicable. It simulates the plastic deformation of aggregates subjected to external strains and stresses. VPSC is based on the physical deformation mechanisms of slip and twinning. Grain interactions were not taken into account in the current study although the program is capable of treating grain-grain interactions in a limited way. In addition to providing the macroscopic stress-strain response, it accounts for hardening, reorientation and the shape change of individual grains and it can predict the evolution of hardening and texture associated with plastic forming. The simulation procedure was applied here to the deformation of fcc metals, but can be used to simulate intermetallics and geologic materials as well.

The formal theory upon which the code is based is explained in detail by Lebensohn and Tomé [Ref. 187], and also in Chapter 11 of the book by Kocks et al. [Ref. 188]. Extensions of the theory can be found in the papers by Lebensohn et al. [Ref. 189] and Tomé [Ref. 190].

The polycrystal is represented by means of weighted orientations. The orientations represent grains and the weights represent volume fractions of material corresponding to these orientations. The latter are chosen to reproduce the initial texture of the material. Each grain is treated as an ellipsoidal visco-plastic inclusion embedded in an effective visco-plastic medium. Both inclusion and medium have fully anisotropic properties, if applicable. The effective medium represents the 'average' environment 'seen' by each grain. Deformation is based on the crystal plasticity mechanisms of slip and twinning, each activated by the appropriate resolved shear stress.

133

The main FORTRAN77-based code that calls all input files and subroutines was not modified in the current work. The input parameter file 'vpsc5.in' was the file employed to specify input parameters such as: textures, grain shapes, grain elongations, the type and extent of deformation, and the imposed boundary conditions. The velocity gradient tensor was modified to impose the macroscopic deformation conditions. Plane strain, uniaxial tension and pure shear were investigated in this study. The amount of macroscopic deformation was controlled by specifying a deformation incremental step for one component of the velocity gradient (udot in the code) tensor and subsequently defining a prescribed number of deformation steps to be evaluated. The total amount of deformation was recorded in an output file in a tabular form that listed for each step of the deformation the total equivalent von Mises strain and the individual tensorial strain and stress components. Another output file included the texture in the form of Euler angles to describe the final orientation of each grain. The output as well as the input texture files could be adapted for use with the OIM software, thus allowing pole figure representations to be created and used for comparison.

The initial (or input) textures used in this study are schematically represented in the pole figures of Figure 8.1. The four 'ideal' starting textures used in this study include the following: equal volume fractions of the B variants; equal volume fractions of the C variants; a random texture; and equal volume fractions of the symmetric B, S and C variants to roughly simulate a deformation induced texture along the β fiber of an fcc metal.

B.   EXPERIMENTAL PROCDURES

The analysis was conducted using the aforementioned input textures and controlling input parameters to model the texture development after various subsequent deformations. The VPSC input code was modified to model plane strain, uniaxial tension and pure shear. The modeling was conducted for comparison with results obtained from the material systems studied during this research.

Representative examples for the velocity gradients, udot, during various deformation conditions are provided in Equations 8.1 through 8.3. Equation 8.1
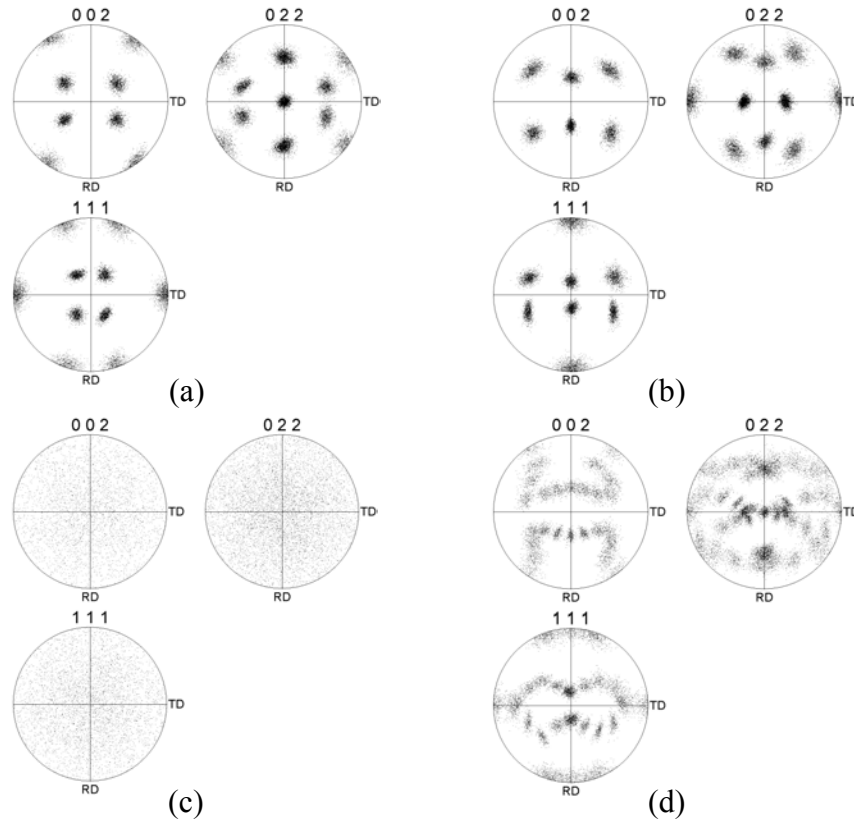
Figure 8.1. Constructed ideal starting textures. In (a), equal volume fractions of the B type variants; (b), equal volume fractions of the C variants; (c) random texture; and (d) equal volume fractions of the two B and C variants and four S variants to simulate a deformation texture (β fiber) encountered after rolling an fcc material.

represents plane strain deformation with compression occurring in ND and elongation in RD. Equation 8.2 presents the velocity gradient used during uniaxial tension deformation with the tensile axis aligned with RD. Finally, Equation 8.3 is the tensor representing a state of pure shear having the shear direction aligned with RD and the shear plane normal aligned with TD.

$$udot_{PlaneStrain} = \begin{pmatrix} -1 & 0 & 0 \\ 0 & 0 & 0 \\ 0 & 0 & 1 \end{pmatrix} \qquad \text{Equation 8.1}$$

$$udot_{UniaxialTension} = \begin{pmatrix} 1 & 0 & 0 \\ 0 & -0.5 & 0 \\ 0 & 0 & -0.5 \end{pmatrix} \qquad \text{Equation 8.2}$$

$$udot_{PureShear} = \begin{pmatrix} 0 & 1 & 0 \\ 0 & 0 & 0 \\ 0 & 0 & 0 \end{pmatrix}$$
<div align="right">Equation 8.3</div>

C. RESULTS

1. Modeling of Plane Strain Deformation

Plane strain conditions were examined utilizing the VPSC code to simulate a rolling reduction of ~92% on fcc materials with equi-axed grains and various starting textures. Figure 8.2 presents data for the various starting textures after plastic deformation. An initially random starting texture is seen to converge rapidly to a plane strain deformation-induced texture in Figure 8.2(a) after straining to ε_{true}~2.5. This simulated deformation texture is composed predominantly of the β fiber variants but with extra components connecting the B and Goss texture variants. These extra orientations are part of the α fiber and are also observed during rolling of fcc metals.

Initial starting textures consisting of the either the B or C texture variants were deformed by modeling in order to confirm their stability during plane strain deformation. Figures 8.2(b) and (c) present data for a simulated rolling reduction of ~92% for materials having either an initial B or C type texture, respectively. Both the B and C orientations are stable during plane strain reduction although both texture types exhibit a

<div align="center">(a)   (b)   (c)</div>
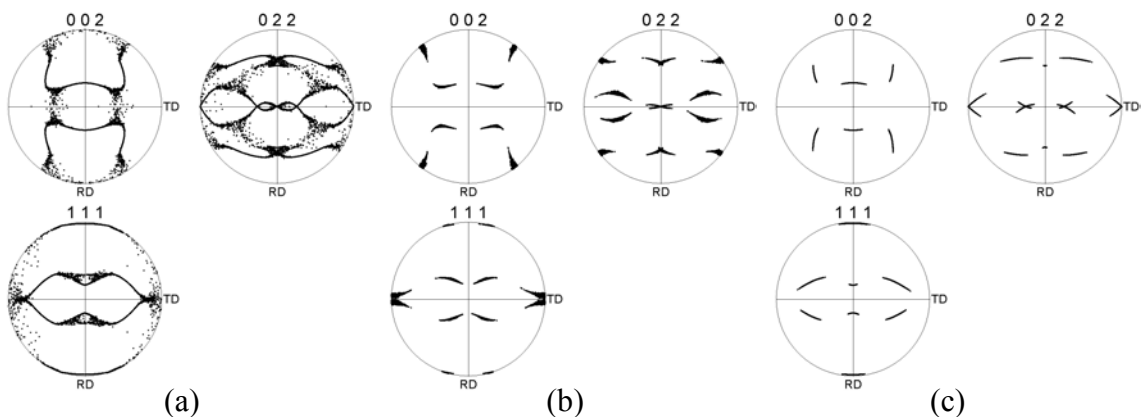
Figure 8.2. Macro-texture predicted after a rolling reduction of 92% (ε_{true}~2.5) from various original starting textures; (a) random, (b) B variants, and (c) C variants. This shows the predictive capability of the VPSC model and the stability of the B and C texture variants during plane strain deformation for equi-axed grains.

tendency for the end orientations to spread somewhat about the RD and, in the case of the C texture, to spread about the TD as well. This may reflect the assumption of initially equi-axed grains. Both the B and the C orientations will give plane strain deformation with the activation of only two slip systems although there will be an additional shear in either case that is averaged out over large numbers of grains. The spreading of these initial textures may reflect the assumption of initially equi-axed grains and the contribution of the additional shear term.

2. Modeling of Uniaxial Tension

The B, C, random and β fiber textures were deformed in a state of uniaxial tension along either the rolling or transverse directions to a nominal 100% plastic elongation ($\varepsilon_{VM} \sim 0.69$). Additionally, the effects of grain aspect ratios were investigated for selected cases. The resulting textures are presented in Figures 8.3 through 8.5.

Results for the B texture variants deformed in uniaxial tension are provided in Figure 8.3. The resulting macrotexture after deformation with the tensile axis parallel to the rolling direction are seen in Figure 8.3(a) for grains with an initial aspect ratio of 10:1 (RD:ND) and Figure 8.3(b) for initially equi-axed grains. In both cases, a partial fiber texture can be seen to result from the tensile deformation. Comparison with the initial B texture shows that there is lattice rotation about ND such that a <111> from each variant tends to align with RD. Such lattice rotation during deformation results in a <111> aligned with the tensile axis thus allowing six independent slip systems to become active in each grain. The elongated grain shape appears to stabilize the transition to a <111> partial fiber by accommodating rapid reorientation of each grain to a stable end orientation. This end orientation is very near the initial individual grain orientations in the B texture variants. Equi-axed grains allow a greater spread in orientations. This is the result of the ability of these grains to rotate more freely, not being constrained by their shape, into other alignments that will also accommodate deformation by uniaxial tension. Inspection of Figure 8.3(b) reveals concentrations of grains near the Goss orientation. The spreading of these orientations along the TD axis would represent a partial <002> fiber. This orientation grouping is also stable in uniaxial tension by having eight equally stressed slip systems of the <110>(111) type.

Analysis of deformation of the B texture in the transverse direction is similar in that a partial <111> fiber is seen to result. This is a direct consequence of the initial B texture having a <111> aligned with TD, as seen in Figure 8.1(a). Figure 8.3(c) represents initially elongated grains. The elongated grains appear to hinder the rapid sharpening of the <111> partial fiber. This can be accounted for by the inability of the elongated grain to freely rotate and thus align and accommodate all plastic deformation. This is in contrast to the rapid texture sharpening of the equi-axed grains observed in Figure 8.3(d). If grain sub-division were incorporated into the model, it would be expected to produce a similar sharpening of the <111> partial fiber.
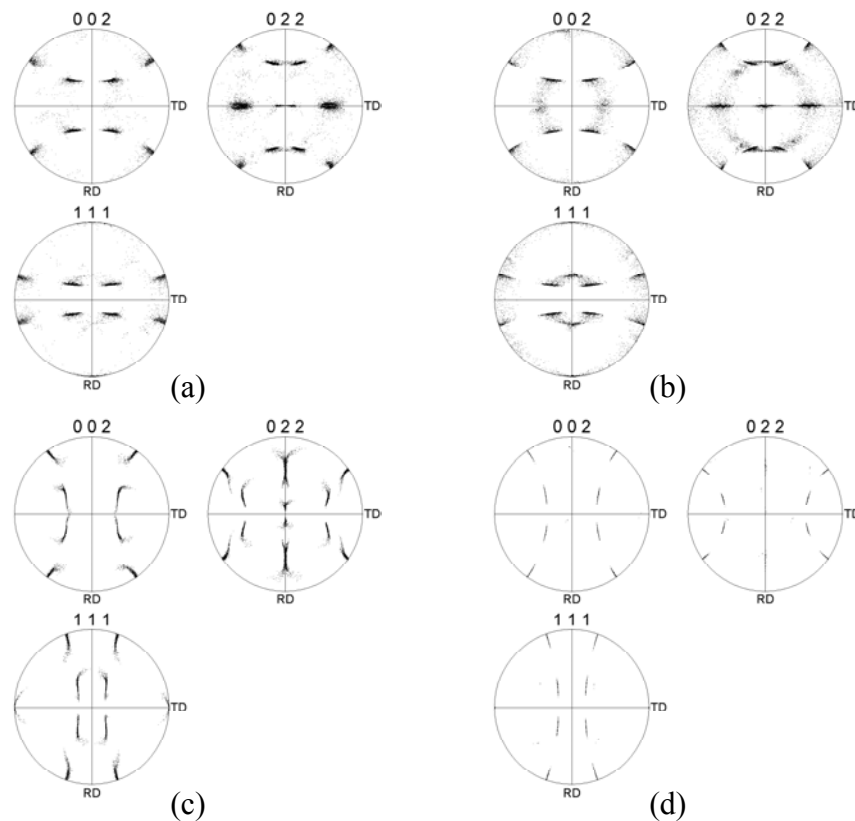
Figure 8.3. B texture variants deformed under uniaxial tension to 100% elongation for the following conditions: (a) and (b) tensile axis is RD; (c) and (d) tensile axis is TD; (a) and (c) 10:1 (tensile axis:ND) grain aspect ratio; (b) and (d) equi-axed grains.

Results of the macrotexture from similar analysis of deformation of an initial C type texture are presented in Figure 8.4. The tensile deformation aligned with RD produces the expected partial <111> fiber from the rapid sharpening of the <111> already nearly aligned with RD in the initial condition. This will allow deformation in both

conditions, with elongated and equi-axed grains. Deformation in the transverse direction for both conditions results in a more diffuse texture. This results from the lack of readily available orientations requiring little grain rotation that will allow a maximum number of slip systems to be equally stressed and hence accommodate uniaxial tension. It can be seen that <111> fibers are in the early stages of formation in both cases. The equi-axed grains are allowed to rotate more easily and hence the fiber formation is more advanced in this case.
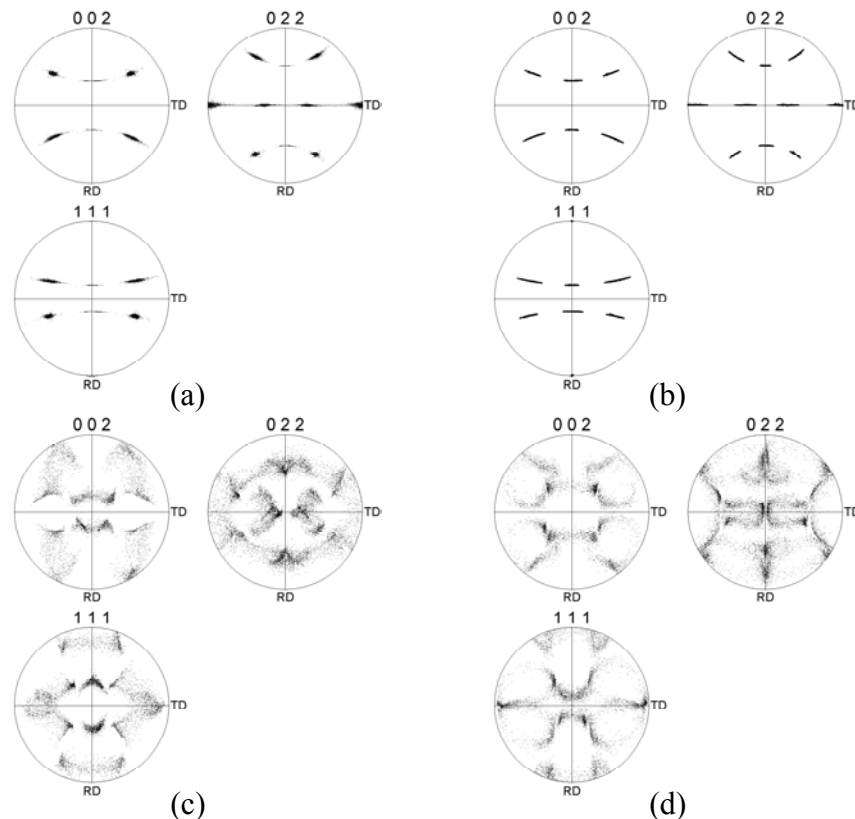
Figure 8.4. C texture variants deformed under uniaxial tension to 100% elongation for the following conditions: (a) and (b) tensile axis is RD; (c) and (d) tensile axis is TD; (a) and (c) 10:1 (tensile axis:ND) grain aspect ratio; (b) and (d) equi-axed grains.

Uniaxial tension in RD was also examined for materials with initial random and plane strain induced textures. Deformation of the initially random textured material can be seen to result in a double fiber consisting of a <111> and <002> aligning with the tensile axis, RD, in Figure 8.5(a). The initial deformation induced texture, when deformed in tension in RD, resulted in a near <111> single fiber in both the elongated and equi-axed grain conditions seen in Figures 8.5(b) and (c) respectively. This results from the concentration of <111> poles near RD in the initial texture of Figure 8.1(d).

Both grain shape conditions require only slight grain rotation to align a <111> with the tensile axis.

(a)   (b)   (c)
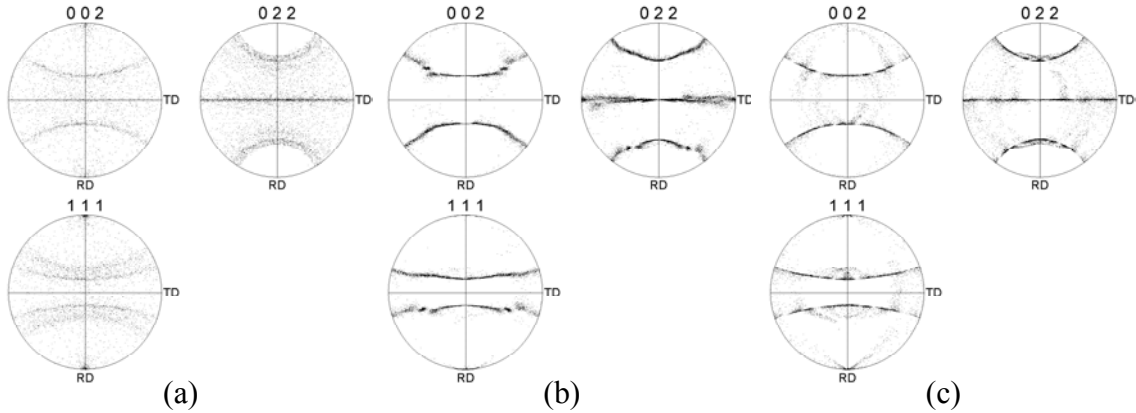
Figure 8.5. Macro-textures predicted by VPSC for uniaxial tension to 100% elongation in RD with the following initial conditions: (a) random texture with equi-axed grains; (b) deformation texture with a 10:1 (RD:ND) grain shape aspect ratio; (c) deformation texture with initially equi-axed grains. All show the formation of a <111> fiber texture aligning with the tensile axis (RD); (a) shows and additional <002> fiber aligned with RD.

3.   Modeling of Pure Shear

An initially random texture was subjected to pure shear via VPSC modeling to ε_{VM}~1.0, which is approximately the strain encountered during one equal-channel pressing operation with a 90° die. The resulting textures are presented in Figures 8.6(a) and (c). Figure 8.6(b) is the same data as (a) but rotated 45° anti-clockwise in order to allow ease of comparison to the shear modeled in (c). The shear deformation resulting in

(a)   (b)   (c)
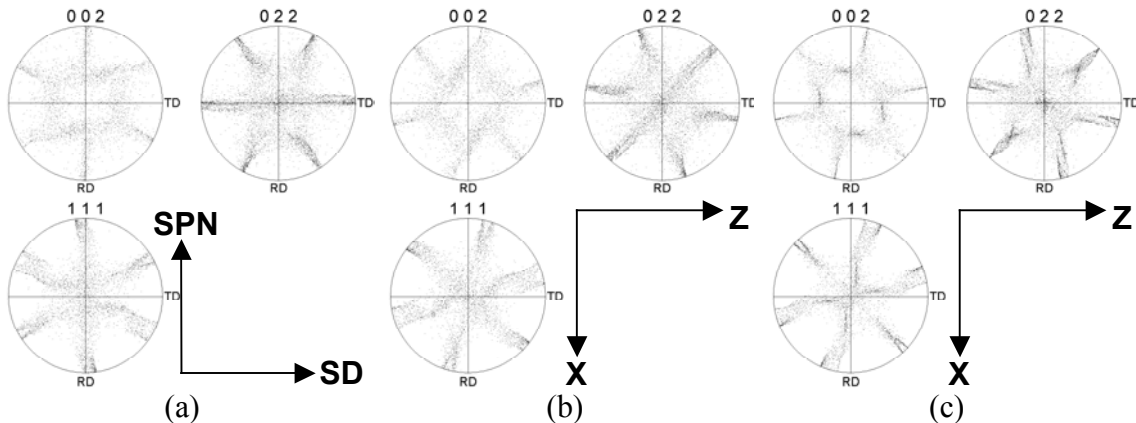
Figure 8.6. VPSC modeled texture in pure shear in (a), rotated 45° clockwise in (b) and texture after modeling shear at a 45° angle by coupling two shearing operations. The single shear case in (a) and (b) indicate a predominance of A type component (6x random) while the B type is only just above the random density (1.2x random). The shear case in (c) indicates a prominent A type (8x random) and stronger B type (2x random).

140

the texture seen in Figure 8.6(a) was modeled using the skew symmetric velocity gradient tensor provided in Equation 8.3. This deformation condition imposed a shear direction parallel to TD acting on the plane whose normal is RD. The resulting texture is very close to that predicted by Canova et al. [Ref. 132]. The shear was also modeled using a symmetric velocity gradient tensor and the resultant texture is provided in Figure 8.6(c). The results are similar to an imposed single shear rotated 45° anti-clockwise with slight differences in the resulting texture. These texture differences imply path dependence within the VPSC model.

D.   DISCUSSION

Accurate modeling of deformation processes at all characteristic length scales will aid in the predictive capability currently in use, which is based mainly on empirical data. The visco-plastic self-consistent (VPSC) model, and others like it, are an important step towards the accurate predictive modeling necessary to evaluate emerging technology, specifically with respect to severe plastic deformation (SPD) processing. Innovative SPD techniques must be able to be modeled and evaluated. This predictive capability, lacking as of yet, will afford users insight into grain refinement mechanisms and the degree to which grain refinement may be obtained with SPD processing.

The VPSC modeling of plane strain deformation demonstrated the accuracy in predicting the macroscopic texture that would evolve from randomly oriented, equi-axed grains. VPSC converges very rapidly and predicts a much sharper final texture than observed in real rolling textures. Figure 8.2(a) represents 1000 random starting point that have converged to form lines with no spread about the ideal orientations. An actual plane strain deformation texture from a comparable final strain condition, will show significant spreading about the ideal orientations, e.g., as can be seen in Figure 3.29(b).

The modeling of the B and C texture variants in plane strain demonstrates the stability of these orientations when deformed in such a manner. This stability is evidenced by the lack of lattice rotation to new orientations and the breakup of the existing texture. The stability of the texture is also the result of slip systems being present and aligned in the input texture that capable of supporting this type of

deformation. This constitutes a direct comparison to the Supral 2004 material of Chapter V and the Al-%5Ca-5%Zn material of Chapter VI. The Supral 2004 and Al-5%Ca-5%Zn exhibit prominent B and C single texture components, respectively, after the thermomechanical processing (i.e. rolling) of each alloy. The thermomechanical processing route and alloy composition are sure to affect the final texture in the as-rolled condition. The current level of modeling available can not predict the formation of these observed single component textures. However, the modeling of this study was capable of and used to evaluate the stability of the single component textures during further plane strain deformation, assuming the pre-existing or starting texture was one of those stated.

The modeling of uniaxial tension was used to evaluate VPSC for comparison to the experimental data obtained in this research. The single component textures relating to the Supral 2004 and Al-5%Ca-5%Zn again, were shown to have compatible deformation in certain deformation modes due only to the alignment, or lack thereof, of the slip systems in the pre-existing texture variants. The B texture variants sharpened when the tensile axis aligned with either the RD or TD while the C texture variant sharpened when deformed in tension along RD. The transverse deformation of the C texture variant resulted in the break-up of the texture while attempting to align a <111> with the tensile axis. The Al-5%Ca-5%Zn exhibited a similar trend. The C texture became more diffuse and there was a sharpening of the B texture components, which would have a <111> aligned with the tensile axis and therefore be part of a <111> fiber.

The uniaxial tension deformation of an initially random texture resulted in a <111> <002> double fiber aligning with the tensile axis. The results of rolled copper subsequently deformed in uniaxial tension slightly above the recrystallization temperature resulted in a similar macrotexture and was presented in Chapter III. A previously studied [Ref. 137] aluminum 5083 material also exhibited the formation of a <111> fiber aligned with the tensile axis. The 5083 material exhibited a random recrystallization texture along with a very fine grain size resulting from particle-stimulated nucleation of recrystallization during prior processing. The copper of this study was allowed to recrystallize but annealing at a low temperature minimized the grain growth. As seen in the heavily annealed samples, distinct recrystallization textures

142

developed at the expense of the random component of the texture. The retardation of grain growth allowed the random texture component to remain present and significantly contribute to the accommodation of plastic deformation through the formation of the fiber textures.

The simulated rolling texture for an fcc metal quickly evolved into a distinct <111> single fiber aligned with the tensile axis regardless of the grain shape. This evolution is similar to that described for the single component B and C texture deformations where the deformation induced <111> directions aligned near a tensile axis. This initial alignment will easily accommodate slight grain rotation in order to bring the <111> in line with the imposed tension and thus have six equally stressed slip systems available to accommodate deformation.

The shear deformation studies do predict the formation of the A and B type shear textures as defined by Canova et al. [Ref. 132] from randomly oriented initial grains after deformation by pure shear to $\varepsilon_{VM} \sim 1$ or nearly equivalent to the ECAP material after one pass presented in this study. The VPSC code also predicts, to varying degrees, similar shear texture developments irrespective of the starting texture, though this result is not included here. The shear textures developed were partial in nature, much like the partial fiber textures developed during uniaxial tension, although with considerably more spreading to encompass nearly the entire shear texture. It can be concluded that VPSC will predict a shear texture after each ECAP pass, however with no length scale.

It should be noted that VPSC is capable of being coupled to a finite element program also set up for the modeling of plastic deformation. This was not accomplished during this study. As a consequence, all data provided by the modeling exercises are lacking a characteristic length scale. If the processes of grain sub-division are to be accurately modeled, a plastic deformation code such as VPSC and a finite element code must both be able to account for interactions at the micro-, meso-, and macro-level.

THIS PAGE INTENTIONALLY LEFT BLANK

IX. SUMMARY OF RESULTS AND CONCLUSIONS

A. DEFORMATION BANDING DURING PLANE STRAIN DEFORMATION

Bands of alternating lattice orientation have been shown to exist in metals deformed by rolling, a process that results in approximately plane strain deformation conditions. It was also shown that the bands are ribbon-like in shape and become aligned with the rolling direction (RD). For the case of pure metals, the bands comprised orientations located along the β fiber, which may be as defined in Euler space as connecting one or the other of the B, S and C orientation variants. For aluminum alloys, the bands consisted of alternating single-component variants. In both cases, the interface between the bands was shown to be one of high angular disorientation.

The addition of alloying elements appears to be responsible for the stabilization of specific texture components resulting in a regular, repeating pattern of alternating texture components. One hypothesis for the origin of the single component texture is that anisotropy may result from these alloy additions. The effect would be a 'soft' direction in the lattice. The bands may then form and align in such a manner as to deform readily by slip processes utilizing slip systems containing that 'soft' direction. However, the specifics regarding anisotropy in these alloys and the associated origin of preferred individual single component orientations as a function of alloying remain to be investigated.

Second-phase particles containing the alloying elements were also observed to result in the break-up of the distinctive alternating bands into clusters of similarly oriented grains that roughly align with RD. Additionally, some alloying elements, such as Sc and Zr, may contribute to the stabilization of the microstructure by retarding the migration of high-angle grain boundaries during elevated temperature deformation.

These observations indicate that structures containing high-angle interfaces form during large-strain plastic deformation. Then, during controlled annealing of the material under recovery dominated conditions high-angle grain boundaries may form by dislocation re-arrangement within the high-angle interfaces while a distinct sub-structure evolves within each band. High-angle grain boundaries, when combined with a fine

grain size, are desired for improved mechanical properties such as those provided in Chapter I.

B.   DEFORMATION BANDING DURING SHEAR DEFORMATION

Equal-Channel Angular Pressing (ECAP) is a process that may give approximately pure shear conditions during straining and is capable of imposing giving very large plastic strains, i.e. ECAP results in severe plastic deformation (SPD). The ECAP deformation of pure aluminum and an aluminum alloy has been shown to result in the formation of regions with bands of alternating orientation separated by high-angle interfaces. The bands are observed at various length scales, which, in turn, are a function of the total amount of plastic deformation. These orientations were subsequently shown to be part of a shear texture that had developed throughout the bulk of the material. As the amount of plastic strain was increased using ECAP, the widths of the bands were seen to decrease until the resulting microstructure was one in which 'clusters' of grains of similar orientation had replaced the 'bands'. This refinement of the microstructure is apparently a function of processing route and total amount of plastic deformation. The resulting microstructure and microtexture showed evidence of grain refinement while maintaining aspects of a deformation induced microstructure, namely a large population of low-angle boundaries and a distinct shear texture. Again, with controlled annealing treatments, the high-angle interfaces and sub-structure may be converted into a microstructure containing high-angle grain boundaries.

C.   PROPOSED DEFORMATION BANDING MODEL

The analyses of Hirsch and Lücke [Ref. 9.1], McNelley et al. [Ref. 9.2] and Pérez-Prado et al. [Ref. 9.3] will be incorporated into a qualitative model describing the role of deformation banding in microstructure evolution. Briefly, these authors all describe texture development during large-strain deformation by rolling. The straining results in lattice rotation toward stable end orientations. For the materials in the study by McNelley et al. [Ref 9.2] and Pérez-Prado et al. [Ref. 9.3], each variant in a B or C texture variant component has four slip systems with equivalent Schmid factors during

plane-strain deformation under a Tucker-type stress state ($\sigma_{RD,RD} = -\sigma_{ND,ND}$) [Ref. 9.1]. The Schmid factors for the B and C texture components have been previously analyzed and summarized [Refs. 9.2 and 9.3]. A similar analysis could be extended to the S texture variants along with all variants along the β fibers formed during plane strain deformation. The slip systems in all variants having equivalent Schmid factors occur in conjugate pairs for a state of plane strain. The incremental strain, dε, may be calculated separately for each of the variants in tensor form assuming an identical incremental shear, dγ, on each of these slip systems as was done for the C texture variants by Perez-Prado et al. [Ref. 9.4] and is presented in Equations 9.1 and 9.2 for the those texture variants.

$$d\varepsilon^{C_1} = d\gamma \begin{pmatrix} 1.088 & 0 & -0.962 \\ 0 & 0 & 0 \\ -0.962 & 0 & -1.088 \end{pmatrix} \qquad \text{Equation 9.1}$$

$$d\varepsilon^{C_2} = d\gamma \begin{pmatrix} 1.088 & 0 & 0.962 \\ 0 & 0 & 0 \\ 0.962 & 0 & -1.088 \end{pmatrix} \qquad \text{Equation 9.2}$$

Where C_1 and C_2 refer to the texture variants. Individually, each variant experiences plane strain deformation with an additional shear term, $\varepsilon_{RD,ND}$ in the strain. The texture variants were shown to occur in an alternating manner. For such an arrangement, averaging of the incremental strains over a region comprising equal volumes of each orientation, would result in the overall incremental strain for the C component, $d\varepsilon_C^{ave}$, and is represented for the C texture variants only in Equation 9.3 for plane strain deformation.

$$d\varepsilon_C^{ave} = d\gamma \begin{pmatrix} 1.088 & 0 & 0 \\ 0 & 0 & 0 \\ 0 & 0 & -1.088 \end{pmatrix} \qquad \text{Equation 9.3}$$

Such an analysis may be extended to a generalized state of plane strain and can be represented by Equation 9.4 to determine the average total incremental strain, $d\varepsilon_{Total}^{ave}$, over a volume of material containing several orientations. The subscript i would be assigned a value from 1 to N, corresponding to a particular texture variant found along the β fiber (i.e. B orientation $(110)[1\bar{1}2]$ $i=1$, B orientation $(011)[2\bar{1}1]$ $i=2$, etc.), V_i is the

volume fraction of the ith component, γ is the incremental shear strain and SF$_i$ is the tensor representation of the Schmid Factor for the ith component. This type of arrangement would allow individual bands corresponding to a single orientation component to deform with at most four active slip systems. An averaging over the entire volume, thus allowing the entire banded structure to deform in plane strain, would accommodate the residual shear term present in each individual orientation.

$$\mathrm{d}\varepsilon_{\mathrm{Total}}^{\mathrm{ave}} = \sum_{i=1}^{N} V_i \mathrm{d}\varepsilon_i^{\mathrm{ave}}$$

Equation 9.4

Such an arrangement is essentially that predicted by deformation banding models and has long been recognized [Refs. 9.5-9.7]. Due to the relaxation of constraints in individual bands, a banded structure is able to deform compatibly with the activation of less than five slip systems in each band [Refs. 9.8-9.10].

A further extension of this analysis to a general state of imposed strain is possible through the following approach in which dislocation build-up and lattice curvature may be included. At the onset of deformation, dislocations will form in each grain. Dislocations of like sign will arrange into low-energy configurations (low-angle tilt boundaries). Other dislocations may become part of large dislocation tangles. Within each grain, regions of similar orientation, separated by low-angle boundaries, form in band-like features with orientations related to the local stress-strain state, as illustrated in the schematic of Figure 9.1(a). These bands can then deform with fewer active slip systems active than required by the Taylor model [Ref. 9.11]. The network of dislocation tangles would accommodate the local reorientations within each band, as needed to average out the residual shear term in each band. It is suggested that the lattice orientation change from one band to the next is accommodated by dislocation structures that constitute the interface. Furthermore, the alternating character of the lattice orientation suggests that the dislocation structures themselves have alternating senses of rotation, that is, they are correlated. The interfaces between the evolving band features would then become the high-angle interfaces by incorporating new dislocations generated during continued deformation. Based upon the type of imposed deformation (plane strain, uniaxial tension, shear, etc.), the banded structure will thereby continue to evolve

as a function of the imposed plastic deformation. Continued plastic deformation may also result in the further reduction of the average width of the bands, defined as the distance between high angle interfaces, or in the creation of new bands within preexisting bands.

Rolling reduction would result in the rotation and alignment of the bands with the RD and ultimately producing long, ribbon-like structures containing low-angle boundaries and separated by high-angle boundaries. The dislocations would continue to
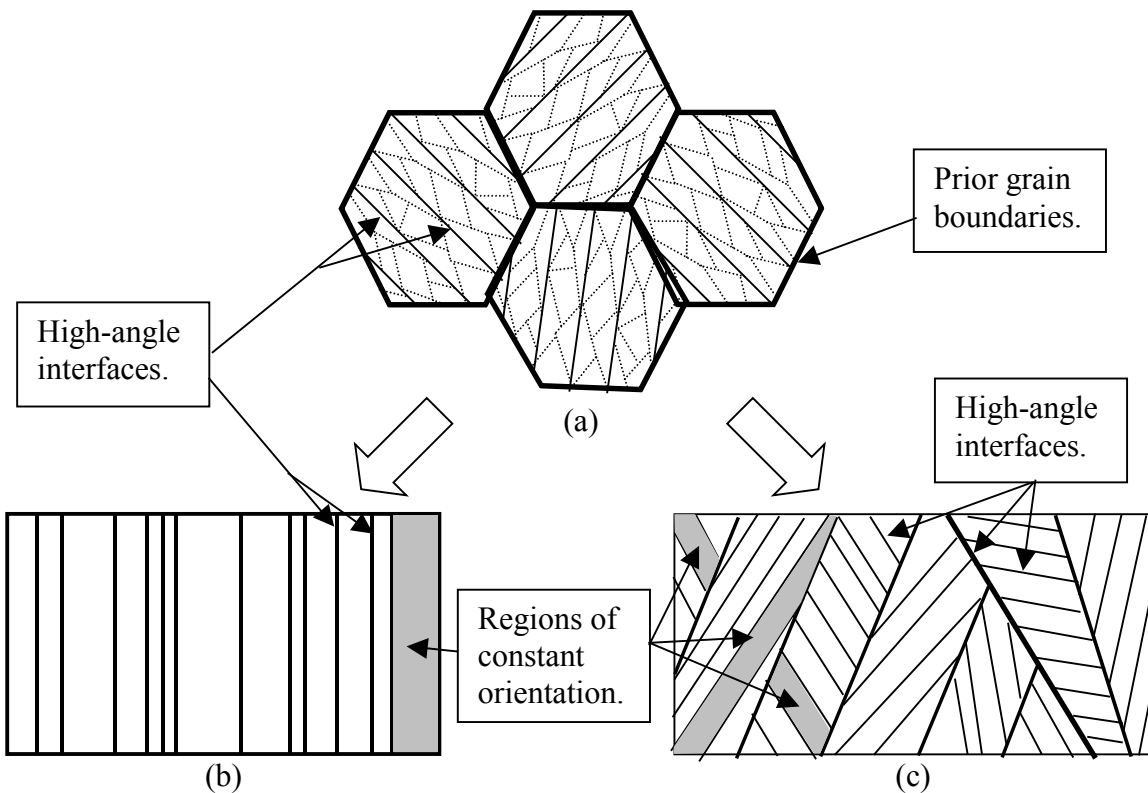
Figure 9.1.   Schematic representation of deformation banding occurring during deformation. In (a), the prior grain boundaries are evident along with the high-angle interfaces separating the bands and the low-angle boundaries within each band, all formed during the early stages of processing.   In (b), the band alignment in one direction results from each band orienting to deform with a minimum of active slip systems.   The prior grain boundaries are indistinguishable from the high-angle interfaces formed during deformation. Also present, though not shown schematically, would be the presence of low-angle boundaries within each band.   In (c), varying strain paths cause local variations of stress and strain resulting in the formation of high-angle interfaces within each band. Also implied are the low-angle boundaries within each band but not depicted here.

form and contribute to lattice rotation toward an end orientation capable of supporting the imposed deformation with a minimum number of slip systems active in each band, i.e. orientations along the β fibers. The prior grain boundaries would also align with the RD and become indistinguishable from the high-angle interfaces created through the dislocation mechanism previously described. This is illustrated schematically in Figure 9.1(b).

More complex stress-strain states resulting from various deformation paths may result in the formation of new bands to accommodate the more complex deformation imposed. ECAP, for example, imposes a new strain state, with respect to the reference global axis system, for each follow-on pressing operation during repetitive pressing. Due to the new imposed macroscopic state of strain, the prior deformation bands are unable to deform with a minimum number of slip systems possible. The formation and accumulation of dislocations, within each prior band, will result in another band structure on a finer scale. Again, the prior grain boundaries would become indistinguishable from the high-angle interfaces formed during deformation. This is represented schematically in Figure 9.1(c). An advantage of this complex deformation condition is the 'cutting' of prior bands with each subsequent pressing operation. This will result in retention of some of the high-angle interfaces from previous deformation, and the formation of new high-angle interfaces to accommodate the local stress-strain state in each band.

Addition of alloying elements and the formation of second phase particles may also be a factor affecting the size and orientation of each band. The rolled Supral 2004 and Al-5%Ca-5%Zn materials exhibited different single component textures with second phase particles near the high-angle interfaces. The addition of Mg and Sc to material subjected to ECAP resulted in an extremely refined microstructure after eight pressing operations. This material was of the same grain size after a brief anneal as compared to the pure aluminum processed through twelve ECAP passes.

**D.	CONCLUSIONS**

The following conclusions can be made regarding this research:

1.	Deformation banding has been demonstrated in several fcc metals and alloys. The deformation bands form as the result of thermomechanical processing and are not the result of microstructural and microtextural changes occurring during to post-processing annealing.	With proper control, the deformation bands and the associated high-angle interfaces can, through recovery dominated mechanisms, evolve into high-angle grain boundaries. It is possible that grains of nanometer scale may be produced if the deformation bands can be reduced to nanometer thickness.	These boundaries will then be able to support continued deformation and enhance the mechanical properties of the material.

2.	The deformation bands are influenced by alloy constitution. Solutes in solution as well as second-phase particles influence the bands and the scale at which bands form in the material.	Alloying also affects the specific preferred orientations that are associated with the bands.	However, all bands modeled in plane strain were found to be stable during continued deformation.

3.	Grain refinement as a result of severe plastic deformation via deformation banding is possible, with the retention of characteristics of deformation induced microstructures.	The strain path followed by a material greatly influences the amount of grain refinement possible with respect to the formation and alignment of the high-angle interfaces.

4.	The modeling of plastic deformation must incorporate deformation banding in order to bridge the gap between the atomistic and macro-scale models currently in use and, potentially, to provide the capability to accurately predict the grain refinement capability of innovative plastic deformation processes.

E. RECOMMENDATIONS FOR FURTHER STUDY

The following are some recommended areas of further research to be conducted regarding deformation banding and its role in the formation and retention of high-angle grain boundaries.

1. The effects of specific alloying elements on deformation band widths and continuity require further evaluation.

2. Lattice curvature from dislocation-dislocation interactions requires further evaluation.

3. The viability of a meso-scale plasticity model through the incorporation of finite element techniques should be evaluated.

LIST OF REFERENCES

1.   *Materials*, 1st ed., pp. 1-19, W.H. Freeman and Company, 1967.

2.   R.D. Doherty, D.A. Hughes, F.J. Humphreys, J.J. Jonas, D. Juul Jensen, M.E. Kasner, W.E. King, T.R. McNelley, H.J. McQueen and A.D. Rollett, "Current Issues in Recrystallization: A Review" *Materials Science and Engineering A*, vol. A238, pp. 219-274, 1997.

3.   J.M. Bijvoet, W.G. Burgers and G. Hagg., Eds. "Early Papers on Diffraction of X-Rays" published for the *International Union on Crystallography*, N.V.A. Ossthoek's Uitgeversmaatschappij, Utrecht, The Netherlands, 1969.

4.   P.P. Ewald, Ed. "Fifty Years of X-Ray Diffraction" published for the *International Union on Crystallography*, N.V.A. Ossthoek's Uitgeversmaatschappij, Utrecht, The Netherlands, 1962.

5.   D.D. Cullity, *Elements of X-Ray Diffraction*, Addison-Wesley, 1978.

6.   C. Suryanarayana and M.G. Norton, *X-Ray Diffraction A Practical Approach*, Plenum Press, 1998.

7.   R.E. Smallman, *Modern Physical Metallurgy*, 4th ed., Butterworths, 1985.

8.   E.O. Hall, "The Deformation and Ageing of Mild Steel: II Characteristics of the Luders Deformation" *Proceedings of the Physical Society B*, vol. 64B, pp. 742-753, 1951.

9.   N.J. Petch, "The Cleavage Strength of Polycrystals" *Journal of the Iron and Steel Institute*, vol. 174, pp. 25-28, 1953.

10. P. Haasen, "How are New Orientations Generated During Primary Recrystallization" *Metallurgical Transactions A*, vol. 24A, pp. 1001-1025, 1993.

11. H. Gleiter, "Materials with Ultrafine Microstructures: Retrospectives and Perspectives" *NanoStructured Materials*, vol. 1, pp. 1-19, 1992.

12. V. Provenzano, N.P. Louat, M.A. Imam and K. Sadananda, "Ultrafine Superstrength Materials" *NanoStructured Materials*, vol. 1, pp. 89-94, 1992.

13. C.C. Koch and Y.S. Cho, "Nanocrystals by High Energy Ball Milling" *NanoStructured Materials*, vol. 1, pp. 207-212, 1992.

14. N.A. Akhmadeev, V.I. Kopylov, R.R. Mulyoukov and R.Z. Valiev, "Formation of Submicro Grain Structure in Copper and Nickel by Extensive Shear Deformation" *Izvestija Akademii nauk SSSR, Metally; "Russian Metallurgy"*, vol. 5, pp. 96-101, 1992.

15. Y. Iwahashi, Z. Horita, M. Nemoto and T.G. Langdon, "An Investigation of Microstructural Evolution During Equal-Channel Angular Pressing" *Acta Materialia*, vol. 45, pp. 4733-4741, 1997.

16. Y. Iwahashi, Z. Horita, M. Nemoto and T.G. Langdon, "The Process of Grain Refinement in Equal-Channel Angular Pressing" *Acta Materialia*, vol. 46, pp. 3317-3331, 1998.

17. R.Z. Valiev, A.V. Korznikov and R.R. Mulyukov, "Structure and Properties of Ultrafine-Grained Materials Produced by Severe Plastic-Deformation" *Materials Science and Engineering A*, vol. A168, pp. 141-148, 1993.

18. Y. Saito, N. Tsuji, H. Utsunomiya, T. Sakai and R.G. Hong, "Ultra-Fine Grained Bulk Aluminum Produced by Accumulative Roll-Bonding (ARB) Process" *Scripta Materialia*, vol. 39, pp. 1221-1227, 1998.

19. C.H. Choi, K.H. Kim and D.N. Lee, "The Effect of Shear Texture Development on the Formability in Rolled Aluminum Alloy Sheets" *Materials Science Forum*, vol. 273-275, pp. 391-396, 1998.

20. D. Kuhlmann-Wilsdorf, "The Theory of Dislocation-Based Crystal Plasticity" *Philosophical Magazine A*, vol. 79, pp. 955-1008, 1999.

21. D. Kuhlmann-Wilsdorf and N. Hansen, "Geometrically Necessary, Incidental and Subgrain Boundaries" *Scripta Metallurgica et Materialia*, vol. 25, pp. 1557-1562, 1991.

22. Q. Liu and N. Hansen, "Geometrically Necessary Boundaries and Incidental Dislocation Boundaries Formed During Cold Deformation" *Scripta Metallurgica et Materialia*, vol. 32, pp. 1289-1295, 1995.

23. J.A. Wert, Q. Liu and N. Hansen, "Dislocation Boundaries and Active Slip Systems" *Acta Metallurgica et Materialia*, vol. 43, pp. 4153-4163, 1995.

24. D.A. Hughes, S.M.A. Khan, A. Godfrey and H.M. Zbib, "Internal Structures of Deformation Induced Planar Dislocation Boundaries" *Materials Science and Engineering A*, vol. A309-310, pp. 220-226, 2001.

25. D.A. Hughes, N. Hansen and D.J. Bammann, "Geometrically Necessary Boundaries, Incidental Dislocation Boundaries and Geometrically Necessary Dislocations" *Scripta Materialia*, vol. 48, pp. 147-153, 2003.

26. H.J. McQueen, O. Knustad, N. Ryum and J.K. Solberg, "Microstructural Evolution in Al Deformed to Strains of 60 at 400-Degrees-C" *Scripta Metallurgica*, vol. 19, pp. 73-78, 1985.

27. J.K. Solberg, H.J. McQueen, N. Ryum and E. Nes, "Influence of Ultrahigh Strains at Elevated-Temperatures on the Microstructure of Aluminum 1" *Philosophical Magazine A*, vol. 60, pp. 447-471, 1989.

28. H.J. McQueen, J.K. Solberg, N. Ryum and E. Nes, "Evolution of Flow-Stress in Aluminum During Ultrahigh Straining at Elevated-Temperatures 2" *Philosophical Magazine A*, vol. 60, pp. 473-485, 1989.

29. C.S. Barrett, "The Structure of Iron after Compression" *Transactions of the American Institute of Mining Engineers*, vol. 135, pp. 296-326, 1939.

30. C.S. Barrett and L.H. Levenson, "The Structure of Aluminum after Compression" *Transactions of the American Institute of Mining Engineers*, vol. 137, pp. 112-127, 1940.

31. G.Y. Chin and B.C. Wonsiewicz, *Transactions of the American Institute of Mining Engineers*, vol. 245, pp. 871-872, 1969.

32. B.J. Duggan and C.S. Lee, "Deformation Banding, Original Grain Size and Recrystallization in FCC Intermediate-to-High SFE Metals" *Scripta Metallurgica et Materialia*, vol. 27, pp. 1503-1507, 1992.

33. C.S. Lee, R.E. Smallman and B.J. Duggan, "Deformation Banding and Formation of Cube Volumes in Cold-Rolled FCC Metals" *Materials Science and Technology*, vol. 10, pp. 862-868, 1994.

34. C.S. Lee, B.J. Duggan and R.E. Smallman, "A Theory of Deformation Banding in Cold Rolling" *Acta Metallurgica et Materialia,* vol. 41, pp. 2265-2270, 1993.

35. C.S. Lee and B.J. Duggan, "Deformation Banding and Copper-Type Rolling Textures" *Acta Metallurgica et Materialia,* vol. 41, pp. 2691-2699, 1993.

36. C.S. Lee, B.J. Duggan and R.E. Smallman, "Deformation Banding and its Influence on Deformation Textures Formation" *Journal de Physique IV, Colloque,* vol. C7, pp. 2027-2332, 1993.

37. C.S. Lee, R.E. Smallman and B.J. Duggan, "A Simplified Criterion for Deformation Banding Applied to Deformation Texture Simulation" *Scripta Metallurgica et Materialia,* vol. 33, pp. 727-733, 1995.

38. J.R. Hirsch, "Correlation of Deformation Texture and Microstructure" *Materials Science and Technology*, vol. 6, pp. 1048-1057, 1990.

39. A. Godfrey, D. Juul Jensen and N. Hansen, "Slip Pattern, Microstructure and Local Crystallography in an Aluminium Single Crystal of Brass Orientation {110}< 112 >" *Acta Materialia*, vol.46, pp. 823-833, 1998.

40. G.I. Taylor, "Plastic Strain in Metals" *Journal of the Institute of Metals*, vol. 63, pp. 307-324, 1938.

41. K. Kulkarni, E.A. Starke Jr. and D. Kuhlmann-Wilsdorf, "Some Observations on Deformation Banding and Correlated Microstructures of Two Aluminum Alloys Compressed at Different Temperatures and Strain Rates" *Acta Materialia,* vol. 46, pp. 5283-5301, 1998.

42. J. Liu, M. Mato, and R.D. Doherty, "Shear Banding in Rolled Dispersion Hardened Al-Mg2Si Alloys" *Scripta Metallurgica*, vol. 23, pp. 1811-1816, 1989.

43. P. Cizek, B.A. Parker and B.J. Wynne, "Dense Dislocation Walls and Deformation Banding in Commercial Purity Aluminum" *Scripta Metallurgica et Materialia*, vol. 32, pp. 319-323, 1995.

44. P. Wagner, O. Engler and K. Lücke, "Formation of the Cu-Type Shear Bands and Their Influence on Deformation and Texture of Rolled f.c.c. {112}<111> Singal Crystals" *Acta Metallurgica et Materialia*, vol. 43, pp. 3799-3812, 1995.

45. S.P. Bellier and R.D. Doherty, "The Structure of Deformed Aluminum and Its Recrystallization - Investigations with Transmission Kossel Diffraction" *Acta Metallurgica*, vol. 25, pp. 521-538, 1977.

46. S. Li, B. Gong and Z. Wang, "On The Formation of Deformation Bands in Fatigued Copper Single-Crystal with Double Slip" *Scripta Metallurgica et Materialia*, vol. 31, pp.1729-1734, 1994.

47. K. Kashihara, M. Tagami and F. Inoko, "Deformed Structure and Crystal Orientation at Deformation Bands in <011>Aluminum Single Crystals" *Materials Transactions, JIM*, vol. 37, pp. 564-571, 1996.

48. K. Kashihara, M. Tagami and F. Inoko, "Recrystallization Behavior at Deformation Bands in <011>Aluminum Single Crystals" *Materials Transactions, JIM*, vol. 37, pp. 572-578, 1996.

49. B. Gong, Z. Wang, D. Chen and Z. Wang, "Investigation of Macro Deformation Bands in Fatigued [001] Cu Single Crystals by Electron Channeling Contrast Technique" *Scripta Materialia*, vol. 37, pp. 1605-1610, 1997.

50. Y. Inokuti and R.D. Doherty, "Transmission Kossel Study of the Structure of Compressed Iron and Its Recrystallization Behaviour" *Acta Metallurgica*, vol. 26, pp. 61-80, 1978.

51. J.H. Driver, D. Juul Jensen and N. Hansen, "Large-Strain Deformation Structures in Aluminum Crystals with Rolling Texture Orientations" *Acta Metallurgica et Materialia*, vol. 42, pp. 3105-3114, 1994.

52. T. Wang, B.L. Adams and P.R. Morris, "Development of Orientation Coherence in Plane-Strain Deformation" *Metallurgical Transactions A*, vol. 21A, pp. 2223-2236, 1990.

53. F. Li and P.S. Bate, "Strain Path Change Effects in Cube Textured Aluminum Sheet" *Acta Metallurgica et Materialia*, vol. 39, pp. 2639-2650, 1991.

54. R. Becker, J.F. Butler Jr., H. Hu and L.A. Lalli, "Analysis of an Aluminum Single-Crystal With Unstable Initial Orientation (001) [110] in Channel Die Compression" *Metallurgical Transactions A*, vol. 22A, pp. 45-58, 1991.

55. A. Akef and J.H. Driver, "Orientation Splitting of Cube-Oriented Face-Centered Cubic-Crystals in Plane-Strain Compression" *Materials Science and Engineering A*, vol. A132, pp. 245-255, 1991.

56. P. Cizek, B.P. Wynne, H. Lu and B.A. Parker, "Deformation Banding in (001)[110] Textured Aluminium Sheet Deformed in Tension" *Materials Science and Engineering A*, vol. A219, pp. 44-55, 1996.

57. Y. Inokuti, F. Saito and C. Gotoh, "Computer Color Mapping Analyses of Deformation Bands and Recrystallized Grains Inside Elongated Grains Near

Surface of Hot-Rolled Silicon Steel Sheet" *Materials Transactions, JIM*, vol. 37, pp. 203-209, 1996.

58. A. Korbel, J.D. Embury, M. Hatherly, P.L. Martin and H.W. Erbsloh, "Microstructural Aspects of Strain Localization in Al-Mg Alloys" *Acta Metallurgica*, vol. 34, pp. 1999-2009, 1986.

59. H. Hu, "Microbands in a Rolled Si-Fe Crystal and Their Role in Recrystallization" *Acta Metallurgica*, vol. 10, pp. 1112-1116, 1962.

60. P. Bate and A. Oscarsson, "Deformation Banding and Texture In Hot Rolled Al-1.0Mn-1.2Mg Alloy" *Materials Science and Technology*, vol. 6, pp. 520-527, 1990.

61. B. Bay, N. Hansen, D.A. Hughes and D. Kuhlmann-Wilsdorf, "Overview No-96 - Evolution of fcc Deformation Structures in Polyslip" *Acta Metallurgica et Materialia*, vol. 40, pp. 205-219, 1992.

62. M. Eddahbi, T.R. McNelley and O.A. Ruano, "The Evolution of Grain Boundary Character During Superplastic Deformation of an Al-6Cu-0.4Zr Alloy" *Metallurgical and Materials Transactions A*, vol. 32A, pp. 1093-1102, 2001.

63. T.R. McNelley, D.L. Swisher and M.T. Pérez-Prado, "Deformation Bands and the Formation of Grain Boundaries in a Superplastic Aluminum Alloy" *Metallurgical and Materials Transactions A*, vol. 33A, pp. 279-290, 2001.

64. M.T. Pérez-Prado, T.R. McNelley, D.L. Swisher, G. González-Doncel and O.A. Ruano, "Texture Analysis of the Transition from Slip to Grain Boundary Sliding in a Continuously Recrystallized Superplastic Aluminum Alloy" *Materials Science and Engineering A*, vol. A342, pp. 216-230, 2003.

65. J. Gil-Sevillano, P.V. Houtte and E. Aernoudt, *Progress in Materials Science*, vol. 25, pp. 69-412, 1980.

66. W.F. Hosford, *The Mechanics of Crystals and Textured Polycrystals*, pp. 128-138, Oxford University Press, 1993.

67. U.F. Kocks, C.N. Tomé and H.-R. Wenk, *Texture and Anisotropy- Preferred Orientations in Polycrystals and Their Effect on Materials Properties*, Cambridge University Press, 1998.

68. F.J. Humphreys, "A Unified Theory of Recovery, Recrystallization and Grain Growth, Based on the Stability and Growth of Cellular Microstructures - I. The Basic Model" *Acta Materialia*, vol. 45, pp. 4231-4240, 1997.

69. M.T. Pérez-Prado, T.R. McNelley, O.A. Ruano and G. González-Doncel, "Microtexture Evolution during Annealing and Superplastic Deformation of Al-5%Ca-5%Zn" *Metallurgical and Materials Transactions A*, vol. 29A, pp. 485-492, 1998.

70. T.R. McNelley and M.E. McMahon, "Microtexture and Grain Boundary Evolution During Microstructural Refinement Processes in SUPRAL 2004" *Metallurgical and Materials Transactions A*, vol. 28A, pp. 1879-1887, 1997.

71. T.R. McNelley, M.E. McMahon and M.T. Pérez-Prado, "Grain Boundary Evolution and Continuous Recrystallization of a Superplastic Al-Cu-Zr Alloy" *Philosophical Transactions of the Royal Society A,* vol. 357, pp. 1683-1705, 1999.

72. E. Nes, *Superplasticité,* Eds. B. Baudelet and M. Suèry, Centre National de la Recherche Scientifique, París, pp. 71, 1985.

73. E. Hornbogen, "Combined Reactions" *Metallurgical Transactions A,* vol. 10, pp. 947-972, 1979.

74. H. Gudmundsson, D. Brooks and J.A. Wert, "Mechanisms of Continuous Recrystallization in an Al-Zr-Si Alloy" *Acta Metallurgica et Materialia,* vol. 39, pp. 19-35, 1991.

75. M.T. Lyttle and J.A. Wert, "Modelling of Continuous Recrystallization in Aluminum Alloys" *Journal of Materials Science,* vol. 29. pp. 3342-3350, 1994.

76. S.J. Hales, T.R. McNelley and H.J. McQueen, "Recrystallization and Superplasticity at 300C in an Aluminum-Magnesium Alloy" *Metallurgical Transactions A,* vol. 22, pp. 1037-1047, 1991.

77. K. Tsuzaki, H. Xiaoxu and T. Maki, "Mechanism of Dynamic Continuous Recrystallization During Superplastic Deformation in a Microduplex Stainless Steel" *Acta Materialia,* vol. 44, pp. 4491-4499, 1996.

78. V.M. Segal, "Materials Processing by Simple Shear" *Materials Science and Engineering A,* vol. A197, pp. 157-164, 1995.

79. V.Y. Gertsman, R. Birringer, R.Z. Valiev and H. Gleiter, "On the Structure and Strength of Ultrafine-Grained Copper Produced by Severe Plastic-Deformation" *Scripta Metallurgica et Materialia,* vol. 30, pp. 229-234, 1994.

80. R.Z. Valiev, Y.V. Ivanisenko, E.F. rauch and B. Baudelet, "Structure and Deformation Behaviour of Armco Iron Subjected to Severe Plastic Deformation" *Acta Materialia,* vol. 44, pp. 4705-4712, 1996.

81. R.Z. Valiev, "Structure and Mechanical Properties of Ultrafine-Grained Metals" *Materials Science and Engineering A,* vol. A234-236, pp. 59-66, 1997.

82. R.Z. Valiev, R.K. Islamgaliev and I.V. Alexandrov, "Bulk Nanostructured Materials from Severe Plastic Deformation" *Progress in Materials Science,* vol. 45, pp. 103-189, 2000.

83. R.Z. Valiev, R.S. Mishral, J. Grozal and A.K. Mukherjee, "Processing of Nanostructured Nickel by Severe Plastic Deformation Consolidation of Ball-Milled Powder" *Scripta Materialia,* vol. 34, pp. 1443-1448, 1996.

84. Y. Saito, H. Utsunomiya, N. Tsuji and T. Saki, "Novel Ultra-High Straining Process for Bulk Materials-Development of the Accumulative Roll-Bonding (ARB) Process" *Acta Materialia,* vol. 47, pp. 579-583, 1999.

85. N. Tsuji, Y. Ito, Y. Saito and Y. Minamino, "Strength and Ductility of Ultrafine Grained Aluminum and Iron Produced by ARB and Annealing" *Scripta Materialia*, vol. 47, pp. 893-899, 2002.

86. S.B. Kang, H.W. Kim, C.Y. Lim and Z.P. Xing, "Microstructure and Mechanical Properties of Non-Heat Treatable Aluminum Alloys Produced by Accumulative Roll Bonding Process" *Ultrafine Grained Materials II*, Edited by: Y.T. Zhu, T.G. Langdon, R.S. Mishar, S.L. Semiatin, MlJ. Saran and T.C. Lowe, pp. 661-667, TMS (The Minerals, Metals and Materials Society), 2002.

87. K.H. Kim and D.N. Lee, "Analysis of Deformation Textures of Asymmetrically Rolled Aluminum Sheets" *Acta Materialia*, vol. 49, pp. 2583-2595, 2001.

88. S.H. Kim, J.K. Lee and D.N. Lee, "Grain Refinement and Texture Development in Asymmetrically Rolled Aluminum Alloy Sheets" *Ultrafine Grained Materials II*, Edited by: Y.T. Zhu, T.G. Langdon, R.S. Mishar, S.L. Semiatin, MlJ. Saran and T.C. Lowe, pp. 55-63, TMS (The Minerals, Metals and Materials Society), 2002.

89. W.M. Thomas, E.D. Nicholas, J.C. Needham, M.G. Murch, P. Templesmith and C.J. Dawes, "Friction Stir Butt Welding," Great Britain Patent Application No. 9125978.8, Dec. 1991; U.S. Patent No. 5460317, Oct. 1995.

90. R.S. Mishra and M.W. Mahoney, "Friction Stir Processing: A New Grain Refinement Technique to Achieve High Strain Rate Superplasticity in Commercial Alloys" *Materials Science Forum,* vol. 357-359, pp. 507-514, 2001.

91. P.B. Berbon, W.H. Bingel, R.S. Mishra, C.C. Bampton and M.W. Mahoney, "Friction Stir Processing: A Tool to Homogenize Nanocomposite Aluminum Alloys" *Scripta Materialia*, vol. 44, pp. 61-66, 2001.

92. R.S. Mishra, M.W. Mahoney, S.X. McFadden, N.A. Mara and A.K. Mukherjee, "High Strain Rate Superplasticity In A Friction Stir Processed 7075 Al Alloy" *Scripta Materialia*, vol. 42, pp. 163-168, 2000.

93. D.S. Schnur and D. Lee, "Determination of Strain Distributions in Machined Chips" *Metallurgical and Materials Transactions A*, vol. 15, pp. 1777-1779, 1984.

94. M. Mabuchi, K. Kubota and K. Higashi, "New Recycling Process by Extrusion for Machined Chips of AZ91 Magnesium and Mechanical Properties of Extruded Bars" *Materials Transactions JIM*, vol. 36, pp. 1249-1254, 1995.

95. H. Watanabe, K. Moriwaki, T. Mukai, K. Ishikawa, M. Kohzu and K. Higashi, "Consolidation of Machined Magnesium Alloy Chips by Hot Extrusion Utilizing Superplastic Flow" *Journal of Materials Science*, vol. 36, pp. 5007-5011, 2001.

96. Y. Chino, R. Kishihara, K. Shimojima, H. Hosokawa, Y. Yamada, C. Wen, H. Iwasaki and M. Mabuchi, "Superplasticity and Cavitation of Recycled AZ31 Magnesium Alloy Fabricated by Solid Recycling Process" *Materials Transactions*, vol. 43, pp. 2437-2442, 2002.

97.   J.P. Hirth and J. Lothe, *Theory of Dislocations*, John Wiley and Sons, 2nd ed., 1982.

98.   R. Hill, *The Mathematical Theory of Plasticity*, Oxford University Press, 1998.

99.   Y. Iwahashi, J. Wang, Z. Horita, M. Nemoto and T.G. Langdon, "Principle of Equal-Channel Angular Pressing for the Processing of Ultra-Fine Grained Materials" *Scripta Materialia*, vol. 35, pp. 143-146, 1996.

100. K. Oh-ishi, Z. Horita, M. Furukawa, M. Nemoto and T.G. Langdon, "Optimizing the Rotation Conditions for Grain Refinement in Equal-Channel Angular Pressing" *Metallurgical and Materials Transactions A*, vol. 29A, pp. 2011-2013, 1998.

101. Z. Horita, M. Furukawa, K. Oh-ishi, M. Nemoto and T.G. Langdon, "Equal-Channel Angular Pressing for Grain Refinement of Metallic Materials" published for *The Fourth International Conference on Recrystallization and Related Phenomena*, The Japan Institute of Metals, pp. 301-308, 1999.

102. A. Gholinia, P.B. Prangnell and M.V. Markushev, "The Effect of Strain Path on the Development of Deformation Structures in Severely Deformed Aluminum Alloys Processed by ECAE" *Acta Materialia*, vol. 48, pp. 1115-1130, 2000.

103. V.V. Stolyarov, Y.T. Zhu, I.V. Alexandrov, T.C. Lowe and R.Z. Valiev, "Influence of ECAP Routes on the Microstructure and Properties of Pure Ti" *Materials Science and Engineering A*, vol. A299, pp. 59-67, 2001.

104. W.H. Huang, L. Chang, P.W. Kao and C.P. Chang, "Effect of Die Angle on the Deformation Texture of Copper Processed by Equal Channel Angular Extrusion" *Materials Science and Engineering A*, vol. A307, pp. 113-118, 2001.

105. A. Gholina, P. Bate and P.B. Prangnell, "Modelling Texture Development Durign Equal Channel Angular Extrusion of Aluminum" *Acta Materialia*, vol. 50, pp. 2121-2136, 2002.

106. K. Nakashima, Z. Horita, M. Nemoto and T.G. Langdon, "Influence of Channel Angle on the Development of Ultrafine Grains in Equal-Channel Angular Pressing" *Acta Materialia*, vol. 46, pp. 1589-1599, 1998.

107. D.N. Lee, "An Upper-Bound Solution of Channel Angular Deformation" *Scripta Materialia*, vol. 43, pp. 115-118, 2000.

108. T. Aida, K. Matsuki, Z. Horita and T.G. Langdon, "Estimating the Equivalent Strain in Equal-Channel Angular Pressing" *Scripta Materialia*, vol. 44, pp. 575-579, 2000.

109. J.R. Bowen, A. Gholinia, S.M. Roberts and P.B. Prangnell, "Analysis of the Billet Deformation Behaviour in Equal-Channel Angular Extrusion" *Materials Science and Engineering A*, vol. A287, pp. 87-99, 2000.

110. H.S. Kim, M.H. Seo and S.I. Hong, "On The Die Corner Gap Formation in Equal-Channel Angular Pressing" *Materials Science and Engineering A*, vol. A291, pp. 86-90, 2000.

111. D. Yamaguchi, Z. Horita, M. Nemoto and T.G. Langdon, "Significance of Adiabatic Heating in Equal-Channel Angular Pressing" *Scripta Materialia*, vol. 41, pp. 791-796, 1999.

112. Z. Horita, M. Furukawa, M. Nemoto, A.J. Barnes and T.G. Langdon, "Superplastic Forming at High Strain Rates After Severe Plastic Deformation" *Acta Materialia*, vol. 48, pp. 3633-3640, 2000.

113. Z. Horita, S. Lee, S. Ota, K. Neishi and T.G. Langdon, "Equal-Channel Angular Pressing as a Production Tool for Superplastic Materials" *Materials Science Forum*, vols. 357-359, pp. 471-476, 2001.

114. K. Neishi, T. Uchida, A. Yamauchi, K. Nakamura, Z. Horita and T.G. Langdon, "Low-Temperature Superplasticity in a Cu-Zn Alloy Processed by Severe Plastic Deformation" *Materials Science and Engineering A*, vol. A307, pp. 23-28, 2001.

115. Komura, M. Furukawa, Z. Horita, M. Nemoto and T.G. Langdon, "Optimizing the Procedure of Equal-Channel Angular Pressing for Maximum Superplasticity" *Materials Science and Engineering A*, vol. A297, pp. 111-118, 2001.

116. Y. Iwahashi, M. Furukawa, Z. Horita, M. Nemoto and T.G. Langdon, "Microstructural Characteristics of Ultrafine Grained Aluminum Produced Using Equal-Channel Angular Pressing" *Metallurgical and Materials Transactions A*, vol. 29A, pp. 2245-2252, 1998.

117. Z. Horita, T. Fujinami, M. Nemoto and T.G. Langdon, "Equal-Channel Angular Pressing of Commercial Aluminum Alloys: Grain Refinement, Thermal Stability and Tensile Properties" *Metallurgical and Materials Transactions A*, vol. 31A, pp. 691-701, 2000.

118. D.H. Shin, I. Kim, J. Kim and K. Park, "Grain Refinement Mechanism During Equal-Channel Angular Pressing of a Low-Carbon Steel" *Acta Materialia*, vol. 49, pp. 1285-1292, 2001.

119. C.P. Chang, P.L. Sun and P.W. Kao, "Deformation Induced Grain Boundaries in Commercially Pure Aluminum" *Acta Materialia*, vol. 48, pp. 3377-3385, 2000.

120. S.D. Terhune, D.L. Swisher, K. Oh-Ishi, Z. Horita, T.G. Langdon and T.R. McNelley, "An Investigation of Microstructure and Grain-Boundary Evolution During ECA Pressing of Pure Aluminum" *Metallurgical and Materials Transactions A*, vol. 33A, pp. 2173-2184, 2002.

121. T.R. McNelley, D.L. Swisher, Z. Horita and T.G. Langdon, "Influence of Processing Route on Microstructure and Grain Boundary Development During Equal-Channel Angular Pressing of Pure Aluminum" *Ultrafine Grained Materials II*, Edited by; Y.T. Zhu, T.G. Langdon, R.S. Mishra, S.L. Semiatin, M.J. Saran and T.C. Lowe, pp. 15-24, TMS (The Minerals, Metals and Materials Society), 2002.

122. O.V. Mishin, D. Juul Jensen and N. Hansen, "Microstructures and Boundary Populations in Materials Produced by Equal Channel Angular Extrusion" *Materials Science and Engineering A*, vol. A342, pp. 320-328, 2003.

123. I.J. Beyerlein, R.A. Lebensohn, C.N. Tomé, "Modeling Texture and Microstructural Evolution in the Equal Channnel Angular Extrusion Process" *Materials Science and Engineering A*, vol. A345, pp. 122-138, 2003.

124. V. Randle and O. Engler, *Introduction to Texture Analysis Macrotexture, Microtexture and Orientation Mapping*, Gordon and Breach Science Publishers, 2000.

125. *OIM Analysis Users Manual*, January 3, 2001 edition, TSL, Draper, UT, 2001.

126. H.J. Bunge., *Texture Analysis in Materials Science Mathematical Methods*, Butterworths, 1982.

127. W.T. Read, Jr., *Dislocations in Crystals*, McGraw-Hill, 1953.

128. D.B. Williams and C.B. Carter, *Transmission Electron Microscopy*, Plenum Press, 1996.

129. L. Solymar and D. Walsh, *Electrical Properties of Materials*, pp. 23-24, Oxford University Press, 1998.

130. S. Kikuchi, *Japan Journal of Physics*, vol. 5, pp. 23, 1928.

131. M.N. Alam, M. Blackman and D.W. Pashley, "High-Angle Kikuchi Patterns" *Proceedings of the Royal Society*, vol. 221A, pp. 224-242, 1954.

132. G.R. Canova, U.F. Kocks and J.J. Jonas, "Theory of Torsion Texture Development" *Acta Metallurgica*, vol. 32, pp. 211-226, 1984.

133. American Society for Metals, *Metals Handbook, Properties & Selections: Nonferrous Alloys and Pure Metals*, 9th Ed., vol. 2., pp. 237-490, American Society for Metals, 1979.

134. American Society for Metals, *Metals Handbook, Properties & Selections: Nonferrous Alloys and Pure Metals*, 9th Ed., vol. 9., pp. 399-414, American Society for Metals, 1979.

135. J.K. MacKenzie, "Second Paper on Statistics Associated with the Random Disorientation of Cubes" *Biometrika*, vol. 45, pp. 229-240, 1958.

136. B.J. Duggan, K. Luecke, G. Kohlhoff and C.S. Lee, "On the Origin of Cube Texture in Copper" *Acta Metallurgica et Materialia*, vol. 41, pp. 1921-1927, 1993.

137. M.T. Pérez-Prado, G. González-Doncel, O.A. Ruano and T.R. McNelley, "Texture Analysis of the Transition from Slip to Grain Boundary Sliding in a Discontinuously Recrystallized Superplastic Aluminum Alloy" *Acta Materialia*, vol.49, pp. 2259-2268, 2001.

138. American Society for Metals, *Metals Handbook, Properties & Selections: Nonferrous Alloys and Pure Metals*, 9th Ed., vol. 2., pp. 1-236, American Society for Metals, 1979.

139. R. Grimes, *Superplasticity,* NATO-Advisory Group for Aerospace Research and Development (AGARD)*, Lecture Series No. 168, pp. 8.1-8.16, 1988.

140. B.M. Watts, M.J. Stowell, B.L. Baike, and D.G.E. Owen, *Journal of Metal Science*, vol. 10, pp. 189-197, 1976.

141. T.G. Nieh, J. Wadsworth and O.D. Sherby: *Superplasticity in Metals and Ceramics*, D.R. Clarke, S. Suresh and I.M. Ward, eds., Cambridge University Press, Cambridge, UK, 1997.

142. A.H. Chokshi, A.K. Mukherjee and T.G. Langdon, "Superplasticity in Advanced Materials" *Materials Science and Engineering R*, vol. R10, pp. 237-274, 1993.

143. O.A. Kaibyshev, *Superplasticity of Alloys, Intermetallics and Ceramics*, Springer-Verlag, Berlin, 1992.

144. O.D. Sherby and J. Wadsworth, *Deformation Processing and Microstructure*, G. Krauss, ed., American Society for Metals, Metals Park, OH, pp. 355-389, 1982.

145. F. Weinberg, *Transactions of the American Institute of Mining Engineers*, vol. 212, pp. 808-817, 1958.

146. R. Orsund, and E. Nes, "Subgrain Growth During Annealing of Heavily Deformed Metals" *Scripta Metallurgica*, vol. 23, pp. 1187-1192, 1989.

147. J. Hirsch and K. Lücke, "Mechanism of Deformation and Development of Rolling Textures in Polycrystalline FCC Metals - II. Simulation and Interpretation of Experiments on the Basis of Taylor-Type Theories" *Acta Metallurgica*, vol. 36, pp. 2883-2904, 1988.

148. J.W. Edington, K.N. Melton, and C.P. Cutler, "Superplasticity" *Progress in Materials Science,* vol. 21, pp. 63-170, 1976.

149. O.A. Kaibyshev, B.V. Rodionov, and R.Z. Valiev, "Peculiarities of Dislocation Slip During Superplastic Deformation of Zn-Al Alloys" *Acta Metallurgica,* vol. 26, pp. 1877-1886, 1978.

150. O.A. Kaibyshev, I.V. Kazachkov, and R.M. Galeev, "The Influence of Texture on Superplasticity of the Titanium Alloy VT6" *Journal of Materials Science,* vol. 16, pp. 2501-2506, 1981.

151. K. Matsuki, H. Morita, M. Yamada, and Y. Murakami, "Relative Motion of Grains During Superplastic Flow in an Al-9Zn-1Mg Alloy" *Metal Science,* vol. 6, pp. 156-163, 1977.

152. C.P. Cutler, J.W. Edington, J.S. Kallend and K.N. Melton, "Quantitative Texture Studies of the Superplastically Deformed Al-Cu Eutectic Alloy" *Acta Metallurgica,* vol. 22, pp. 665-671, 1974.

153. K.N. Melton and J.W. Edington, "Crystallographic Slip During Superplastic Deformation of the Zn-Al Eutectoid Alloy" *Scripta Metallurgica,* vol. 8, pp. 1141-1144, 1974.

154. R.H. Bricknell and J.W. Edington, "Textures in a Superplastic Al-6Cu-0.3Zr Alloy" *Acta Metallurgica,* vol. 27, pp. 1303-1311, 1979.

155. R.H. Bricknell and J.W. Edington, "Mechanical Anisotropy and Deformation Mechanisms in an Al-Cu-Zr Superplastic Alloy" *Acta Metallurgica,* vol. 27, pp. 1313-1318, 1979.

156. K.N. Melton, J.W. Edington, J.S. Kallend and C.P. Cutler, "Textures in Superplastic Zn-40%Al" *Acta Metallurgica,* vol. 22, pp. 165-170, 1974.

157. M.T. Pérez-Prado, M.C. Cristina, O.A. Ruano and G. González-Doncel, "Grain Boundary Sliding and Crystallographic Slip During Superplasticity of Al-5%Ca-5%Zn as Studied by Texture Analysis" *Materials Science and Engineering A,* vol. A244, pp. 216-223, 1998.

158. K. Tsuzaki, H. Matsuyama, M. Nagao and T. Maki, "High-Strain Rate Superplasticity and Role of Dynamic Recrystallization in a Superplastic Duplex Stainless Steel" *Materials Transactions, JIM,* vol. 31, pp. 983-994 , 1990.

159. L. Qing, H. Xiaoxu, Y. Mei and Y. Jinfeng, "On Deformation-Induced Continuous Recrystallization in a Superplastic Al-Li-Cu-Mg-Zr Alloy" *Acta Metallurgica et Materialia*, vol. 40, pp. 1753-1762 , 1992.

160. J. Liu and D.J. Chakrabarti, "Grain Structure and Microtexture Evolution During Superplastic Forming of a High Strength Al-Zn-Mg-Cu Alloy" *Acta Materialia,* vol. 44, pp. 4647-4661, 1996.

161. P.L. Blackwell and P.S. Bate, "The Absence of Relative Grain Translation During Superplastic Deformation of an Al-Li-Mg-Cu-Zr Alloy" *Metallurgical Transactions A.,* vol. 24A, pp. 1085-1093, 1993.

162. P.S. Bate, "Plastic Anisotropy in a Superplastic Al-Li-Mg-Cu Alloy" *Metallurgical Transactions A*, vol. 23A, pp. 1467-1478, 1992.

163. P.L. Blackwell and P.S. Bate, *Superplasticity: 60 years after Pearson*, Ed. N. Ridley, The Institute of Materials, Manchester, UK, pp. 183, 1994.

164. R. H. Johnson, C.M. Parker, L. Anderson and O.D. Sherby, "Microstructure of Superplastic Alloys" *Philosophical Magazine*, vol. 18, pp. 1309-1314, 1968.

165. N. Naziri and R. Pearce, "Anisotropic Effects in Superplastic Zn-0.4%Al Sheet" *Journal of the Institute of Metals*, vol. 98, pp. 71-77, 1970.

166. D.S. McDarmaid, A.W. Bowen and P.G. Partridge, "Tensile Properties of Strongly Textured Ti-6Al-4V After Superplastic Deformation" *Materials Science and Engineering,* vol. 64, pp. 105-111, 1984.

167. L.C.A. Samuelsson, K.N. Melton, and J.W. Edington, "Dislocation Structures in a Superplastic Zn-40%Al Alloy" *Acta Metallurgica,* vol. 24, pp. 1017-1026, 1976.

168. B.P. Kashyap, A. Arieli, and A.K. Mukherjee, "Review: Microstructural Aspects of Superplasticity" *Journal of Materials Science,* vol. 20, pp. 2661-2686, 1985.

169. L.K.L. Falk, P.R. Howell, G.L. Dunlop and T.G. Langdon, "Role of Matrix Dislocations in the Superplastic Deformation of a Copper Alloy" *Acta Metallurgica,* vol. 4, pp. 1203-1214, 1986.

170. F.J. Humphreys, "A Unified Theory of Recovery, Recrystallization and Grain Growth, Based on the Stability and Growth of Cellular Microstructures - II. The Effect of Second-Phase Particles" *Acta Materialia,* vol. 45, pp. 5031-5039, 1997.

171. D.A. Hughes and N. Hansen, "High Angle Boundaries Formed by Grain Subdivision Mechanisms" *Acta Materialia,* vol. 45, pp. 3871-3886, 1997.

172. D.M. Moore and L.R. Morris, "A New Superplastic Aluminum Sheet Alloy" *Materials Science and Engineering*, vol. 43, pp. 85-92, 1980.

173. M.T. Pérez-Prado, M.C. Cristina, O.A. Ruano and G. González-Doncel, "Microstructural Evolution of Annealed Al-5 Wt% Ca-5 Wt% Zn Sheet Alloy" *Journal of Materials Science,* vol. 32, pp. 1313-1318, 1997.

174. C.S. Barret and H. Levenson, "Structure of Iron after Drawing, Swaging, and Elongation in Tension" *Transactions of the American Institute of Mining Engineers,* vol. 137, pp. 327-352, 1940.

175. R.Z. Valiev, R.R. Mulyukov, V.V. Ovchinnikov, and V.A. Shabashov, "Mossbauer Analysis of Submicrometer Grained Iron" *Scripta Metallurgica Materialia*, vol. 25, pp. 2717-2722, 1991.

176. J. Wang, Z. Horita, M. Furukawa, M. Nemoto, N.K Tsenev, R.Z. Valiev, Y. Ma, and T.G. Langdon, "An Investigation of Ductility and Microstructural Evolution in an Al-3-Percent Mg Alloy with Submicron Grain-Size" *Journal of Materials Research*, vol. 8, pp. 2810-2818, 1993.

177. T.G. Langdon, M. Furukawa, M. Nemoto and Z. Horita, "Using Equal Channel Angular Pressing for Refining Grain Size" *JOM*, vol. 52, pp. 30-33, 2000.

178. R.Z. Valiev, O.A. Kaibyshev, R.I. Kuznetsov, R. Sh. Musalimov, and N. K. Tsenev, "The Low-Temperature Superplasticity of Metallic Materials" *Doklady Akademii Nauk SSSR*, vol. 301, pp. 864-866, 1988.

179. O.A. Kaibyshev, R. Kaibyshev, and G. Salishchev, "Formation of Submicrocrystalline Structure in Materials During Dynamic Recrystallization" *Materials Science Forum*, vols. 113-115, pp. 423-428, 1993.

180. G.A. Salishchev, R.M. Imayev, V.M. Imayev, and N.K. Gabdullin, "Dynamic Recrystallization in TiAl and Ti3Al Intermetallic Compounds" *Materials Science Forum*, vols. 113-115, pp. 613-618, 1993.

181. D.A. Rigney, "Sliding Wear of Metals" *Annual Review of Materials Science*, vol. 18, pp. 141-163, 1988.

182. S.D. Terhune, Z. Horita, M. Nemoto, Y. Li, T.G. Langdon and T.R. McNelley, "The Evolution of Microtexture and Grain Boundary Character During ECA Pressing of Pure Aluminum" *Proceedings from ReX'99, 4th International Conference on Recrystallization and Related Phenomena*, Edited by; T. Sakai and H.G. Suzuki, pp. 515-522, Japan Institute of Metals, 1999.

183. H.J. McQueen and W. Blum, "Dynamic Recovery: Sufficient Mechanism in the Hot Deformation of Al (<99.99)" *Materials Science and Engineering* A, vol. A290, pp. 95-107, 2000.

184. Telephone conversation and e-mail between Z. Horita, Kyushu University, Japan and the author, November 21, 2001.

185. Telephone conversation and e-mail between S. Vogel, Los Alamos National Laboratories, New Mexico, USA and the author, March 19, 2002.

186. R.A. Lebensohn and C.N. Tomé, *Manual for Code Visco-Plastic Self-Consistent (VPSC)*, Version 5, Los Alamos National Laboratory, December 2000.

187. R.A. Lebensohn and C.N. Tomé, "A Self-Consistent Anisotropic Approach for the Simulation of Plastic Deformation and Texture Development of Polycrystals – Application to Zirconium Alloys" *Acta Metallurgica et Materialia*, vol. 41, pp. 2611-2624, 1993.

188. U.F. Kocks, C.N. Tomé and H.-R. Wenk, *Texture and Anisotropy*, Cambridge University Press, 2nd ed., 2000.

189. R.A. Lebensohn, D. Solas, G.R. Canova and Y. Brecht, "Modelling Damage of Al-Zn-Mg Alloys" *Acta Materialia*, vol. 44, pp. 315-325, 1996.

190. C.N. Tomé, "Self-Consistent Polycrystal Models: A Directional Compliance Criterion to Describe Grain Interactions" *Modelling and Simulation in Materials Science and Engineering*, vol. 7, pp. 723-738, 1999.

INITIAL DISTRIBUTION LIST

1. Defense Technical Information Center
    Ft. Belvoir, Virginia

2. Dudley Knox Library
    Naval Postgraduate School
    Monterey, California

3. Professor Terry R. McNelley
    Department of Mechanical Engineering
    Naval Postgraduate School
    Monterey, California

4. Douglas L. Swisher
    Supervisor of Shipbuilding, Construction and Repair
    Bath, Maine

5. Keiichiro Oh-Ishi
    Department of Mechanical Engineering
    Naval Postgraduate School
    Monterey, California

6. Zenji Horita
    Kyushu Univeristy
    Fukuoka, Japan

7. Maria Teresa Pérez-Prado
    Centro Nacional de Investigaciones Metalúrgicas (CENIM)
    Madrid, Spain

8. Professor Terrence G. Langdon
    University of Southern California
    Los Angeles, California